THE UNIVERSITY OF QUEENSLAND

A U S T R A L I A

Simulation and Analysis of Surface Wind Fields during Landfalling Tropical Cyclones

Thomas Kloetzke

M.Sc., B.Sc. Meteorology

A thesis submitted for the degree of Doctor of Philosophy at

The University of Queensland in 2019

School of Civil Engineering

Abstract

Tropical cyclones (TCs) are rotating atmospheric vortices characterised by high wind speeds that pose a major threat to people and infrastructure in coastal communities. To minimise their impacts, the winds in the lowest part of the TC boundary layer (TCBL) must be adequately understood. This understanding enables engineers to make rational decisions around building design in these regions and allows meteorologists to improve their forecasts. Of particular importance is how the TCBL is modified when abrupt changes in surface terrain conditions occur, such as during landfall, which can significantly alter the physical structure of a TC. Although near-surface TC wind data has begun to be captured through coordinated field campaigns in, for example, the USA and Australia, there is little explicit information on how the TCBL is modified during landfall or in the vicinity of other sudden changes in land surface conditions. This thesis sets out to investigate this process through, 1) analysis of near-surface wind observations, and 2) numerical simulation of idealised TCs.

To explore how near-surface turbulence is modified, the present study analysed observational TC wind records at measurement heights of 2.25 m, 3 m, 5 m, and 10 m collected during 11 TCs from the Florida Coastal Monitoring Program (FCMP), StickNet, and the Surface Weather Information Relay and Logging network (SWIRLnet). These low-level records will be analysed to assess their turbulent characteristics and the response of these characteristics to sudden changes in land surface. Results were compared with traditional engineering models (AS/NZS1170.2, ESDU) predicting turbulence transition in non-TC environments to assess their efficacy in TC environments. Results show that turbulence statistics require about 2 km to reach equilibrium with the underlying terrain, independent of measurement height and upstream terrain. Engineering models tested were found to over predict turbulence intensities in a TC environment. A simple empirical model for estimating the transition of turbulence intensity following a single change in terrain is proposed.

Exploring more broadly how the mean TCBL structure is modified during TC landfall, this thesis also uses hybrid real-idealised Weather Research and Forecasting (WRF) numerical simulations to investigate the mean TCBL response during landfall. This numerical modelling method combines an idealised spun-up TC and a real world environment to undertake a series of parametric simulations where idealised TCs impact coastlines with a range of terrain conditions. These tests systematically explore how sudden changes in terrain (e.g. sea to different land surfaces) influence bulk storm characteristics (e.g. TC size, radius of maximum wind), surface wind footprints, and vertical TC wind profiles in different parts of simulated TCs. Generated TC wind profiles are also compared with observational dropsonde data as well as one existing analytical model. Increased surface roughness over land was found not to deflect the TC track prior to landfall, but was shown to lower TC intensity. Increased surface roughness was also found to reduce maximum surface level wind speeds by up to 70% within 12 hours after TC landfall. Modelled TCBL profiles over water follow a logarithmic wind profile up to the height of maximum wind speed, which increases with TC radius. TCBL profiles over land also exhibit a logarithmic wind profile but wind speeds decay faster particularly closer to the surface.

Declaration by author

This thesis is composed of my original work, and contains no material previously published or written by another person except where due reference has been made in the text. I have clearly stated the contribution by others to jointly-authored works that I have included in my thesis.

I have clearly stated the contribution of others to my thesis as a whole, including statistical assistance, survey design, data analysis, significant technical procedures, professional editorial advice, and any other original research work used or reported in my thesis. The content of my thesis is the result of work I have carried out since the commencement of my research higher degree candidature and does not include a substantial part of work that has been submitted to qualify for the award of any other degree or diploma in any university or other tertiary institution. I have clearly stated which parts of my thesis, if any, have been submitted to qualify for another award.

I acknowledge that an electronic copy of my thesis must be lodged with the University Library and, subject to the policy and procedures of The University of Queensland, the thesis be made available for research and study in accordance with the *Copyright Act 1968* unless a period of embargo has been approved by the Dean of the Graduate School.

I acknowledge that copyright of all material contained in my thesis resides with the copyright holder(s) of that material. Where appropriate I have obtained copyright permission from the copyright holder to reproduce material in this thesis.

Publications included in this thesis

No publications included.

Submitted manuscripts included in this thesis

No manuscripts submitted for publication.

Other publications during candidature

[1] Vigh, J., Arthur, C., Done, J., Ge, M., Wang, C., **Kloetzke, T.**, M. Rozoff, C., Brown, B., Ellingwood, B. (2018) The Hurricane Risk Calculator: Translating Potential Wind Impacts for Coastal and Inland Residents, 33rd Conference on Hurricanes and Tropical Meteorology, At Ponte Vedra Beach, FL.

[2] **Kloetzke, T.**, Mason, M.S., Krupar III, R.J. (2016), Sensitivity of WRF-ARW simulations to the choice of physics parameterisation schemes when reconstructing Tropical Cyclone Ita (2014), 18th Australasian Wind Engineering Society Workshop, McLaren Vale, South Australia 6-8 July, 2016.

[3] **Kloetzke, T.**, Mason, M. S., Krupar, III, R.J. (2016), Evaluating topographic influences on the near-surface wind field of Tropical Cyclone Ita (2014) using WRF-ARW, AFAC16 (Bushfire and Natural Hazards CRC, 2016).

[4] **Kloetzke, T.**, Parackal, K., Smith, D.J., Krupar III, R.J., Leblais, A., Humphreys, M., Spassiani, A., Mason, M.S., Henderson, D.J., Boughton, G.N. (2017), Severe Wind Hazard Preliminary Assessment: Tropical Cyclone Debbie, Whitsunday Coast, Queensland, Australia, James Cook University.

[5] Boughton, G.N., Falck, D.J., Henderson, D.J., Smith, D.J., Parackal, K., **Kloetzke, T.**, Mason, M.S., Krupar III, R.J., Humphreys, M., Navaratnam, S., Bodhinayake, G., Ingham, S., and Ginger, J.D. (2017), Tropical Cyclone Debbie: Damage to buildings in the Whitsunday Region, Technical Report No. 63, Cyclone Testing Station, James Cook University, 3 June 2017.

Contributions by others to the thesis

No contributions by others.

Statement of parts of the thesis submitted to qualify for the award of another degree

No works submitted towards another degree have been included in this thesis.

Research Involving Human or Animal Subjects

No animal or human subjects were involved in this research.

Acknowledgements

First and foremost I want to thank my God and heavenly Father, who made all things work together for my good and gave me the intelligence to study Meteorology with a particular focus on tropical cyclones. God's love and grace in my life has accompanied me particularly throughout my PhD, which I am truly thankful for. The verse "I can do all things through Christ who strengthens me" in Philippians 4:13 has proven to be true in so many ways.

My wife Nicole deserves outstanding recognition due to her tremendous support, love, patience, perseverance, and constant encouragement during the PhD project. Her unshakable belief in me combined with her incredible ability to fully envision our life journey has led us to explore this adventure in Australia. I would like to thank my parents, Liane and Manfred, my sister Katharina and her husband Tobias, as well as Nicole's parents Dorothea and Winfried, along with my in-laws Nadine and Markus including their children Jakob and Lena, for their unconditional love and support during the entire PhD project. A special thank you is dedicated to my grandfather Johannes Barthel, who has been an inspiring personality for me.

Of note is the outstanding supervision by my doctoral advisor Dr. Matthew S. Mason, who introduced me into the world of wind engineering and provided deep insights and guidance along the PhD research project. I am very thankful that he has given me the chance to work on and further build up on my understanding on tropical cyclones. He taught me a variety of research techniques, as well as independent and critical thinking to conduct research on a high level. I am deeply grateful to him for the opportunity to participate in tropical cyclone SWIRLnet deployments along with researchers from the James Cook University. I would also like to thank my associate advisor Dr. Richard J. Krupar III for providing knowledge and valuable suggestions that helped me completing my dissertation. In addition, I would like to thank my university mates Massi, Aaron, and Alessio for their support and countless research-related as well as personal conversations. Financial support by the University of Queensland and the Bushfire & Natural Hazards CRC was provided, which is also highly appreciated.

Last but not least, I am very thankful for the opportunity to work on my PhD project at the National Center for Atmospheric Research (NCAR) in Boulder, Colorado, USA. A special thank you goes to Cindy Bruyere and Dave Gill for supporting my research and adding tremendous value to my thesis. I would like to acknowledge high-performance computing support from Cheyenne (doi:10.5065/D6RX99HX) provided by NCAR's Computational and Information Systems Laboratory, sponsored by the National Science Foundation.

Keywords

Wind, tropical cyclones, tropical cyclone boundary layer, near-surface wind field, turbulence, surface roughness, terrain changes, field campaigns, WRF model, idealised TC simulations

Australian and New Zealand Standard Research Classifications (ANZSRC)

ANZSRC code: 040107, Meteorology, 75%
ANZSRC code: 091507, Risk Engineering, 25%

Fields of Research (FoR) Classification

FoR code: 0401, Atmospheric Sciences, 75%
FoR code: 0915, Interdisciplinary Engineering, 25%

Contents

List of Figures

xiv

List of Tables

List of Abbreviations

ABL	Atmospheric Boundary Layer
AS/NZS1170.2	Australian/New Zealand Structural Design Standard 1170.2
ESDU	Engineering Sciences Data Unit
FCMP	Florida Coastal Monitoring Program
HWCM	Hybrid WRF Cyclone Model
MBL	Mean Boundary Layer
PBL	Planetary Boundary Layer
RMW	Radius Of Maximum Winds
SST	Sea Surface Temperature (°C)
SWIRLnet	Surface Weather Information Relay And Logging Network
TC	Tropical Cyclone
TCBL	Tropical Cyclone Boundary Layer
WRF	Weather Research And Forecasting Model

List of Symbols

All the symbols are defined in the locations where they first appear in the text. The following is a list for the important symbols.

$\bar{U}$	Mean wind speed	m/s
γ_{ku}	Across-wind kurtosis	
γ_{ku}	Along-wind kurtosis	
γ_{su}	Along-wind skewness	
γ_{sv}	Across-wind skewness	
κ	von-Karman coefficient	
σ_u	Standard deviation	
f	Coriolis parameter	$1/s$
g	Gravity acceleration	m/s^2
G_u	Along-wind gust factor	
g_u	Along-wind peak factor	
G_v	Across-wind gust factor	
g_v	Across-wind peak factor	
I_u	Along-wind turbulence intensity	
I_v	Across-wind turbulence intensity	
L_u	Along-wind integral length scale	m
L_v	Across-wind integral length scale	m
M_a	Absolute angular momentum	$m^2 s^{-1}$
r	Radius	m
r_0	Outer vortex radius	m

r_m	Radius of maximum wind	m
u_*	Friction velocity	m/s
v_m	Maximum wind	m/s
x	Distance from measurement site to roughness change	m
x_1	Fetch of upwind terrain	m
z	Measurement height	m
z_0	Aerodynamic roughness length	m
z_{01}	Aerodynamic roughness length of upwind terrain	m

Chapter 1

Introduction and Motivation

Tropical cyclones (TCs) are fast, rotating atmospheric low pressure systems characterised by high wind speeds throughout their depth. TCs form over tropical oceans in weakly sheared environments with enhanced vorticity and high levels of moisture. They are, in essence, thermal heat engines that intensify through the release of latent heat due to the condensation of water and can vary significantly with respect to their intensity, size and structure. When these storms make landfall they have the potential to impact large, densely populated coastal regions and must therefore be forecasted adequately and considered in the design of buildings and infrastructure in these areas.

TCs impact people and infrastructure through the concomitant hazards of wind, rain and coastal or inland inundation. Based on Munich RE NatCatSERVICE's worldwide damage records since 2001[1], overall losses associated with TCs exceed at least 10 billion US Dollar (USD) each year and reach almost 250 billion USD in years with catastrophic TC events such as 2005 (e.g. Hurricanes Katrina, Rita, Wilma) and 2017 (Hurricanes Harvey, Irma, Maria). If structures are to be built in a way that better protects their inhabitants or ensures their survivability, it is important that wind hazards are adequately understood. This is true with respect to understanding physical TC characteristics (e.g. mean and turbulent wind profiles) as well as the probability that a given structure or region will be impacted by these events. A detailed understanding of both these aspects allows decisions around engineering design to be well informed and cost effective.

TCs interact with people and structures within the lowest 1-2 km of the atmosphere, which is referred to as the tropical cyclone boundary layer (TCBL) [*Holland*, 1987; *Zhang et al.*, 2011; *Kepert et al.*, 2016]. It is characterised by the exchange of heat, moisture, and momentum at the earth's surface and is considered almost continuously turbulent throughout its whole depth [*Zhang et al.*, 2011]. The TCBL is responsible for the inflow of moist air that favours TC spin-up processes and maintains or strengthens TC intensity [*Ooyama*, 1969; *Stull*, 1988; *Smith and Montgomery*, 2010; *Montgomery and Smith*, 2014]. Thus, it is important to understand TCBL processes (i.e. TC force-balance) so that the effects that landfall, interactions with abrupt changes in terrain, and movement over changing sea surface temperatures have on TC structure can be better understood [*Holland*, 1987; *Hirth et al.*,

---

[1] https://tinyurl.com/ybt3wyqr - accessed on 9 January 9:30 AM UTC

1

2012]. Characteristics such as the TCBL height and vertical wind structure, have been discussed in various studies [*Franklin et al.*, 2003; *Kepert*, 2006a,b, 2010b; *Lorsolo et al.*, 2010; *Zhang et al.*, 2011]. The TCBL height is typically below 1 km [*Smith and Montgomery*, 2010], with the location of the maximum wind speed found near the eyewall at elevations typically between 300-800 m [*Franklin et al.*, 2003; *Kepert*, 2010b]. The height of the wind maxima, however, becomes greater as the storm radius increases. Below these maxima, mean wind speeds increase logarithmically when over the ocean, but terrain has a significant impact on TCBL structure when over land and the logarithmic assumption may break down, as observed in *Krupar* [2015].

To better understand TCBL structure, wind field measurements have been collected using GPS drop-sondes, radiosondes, Doppler radar and portable weather towers [e.g. *Franklin et al.*, 2003; *Schroeder and Smith*, 2003; *Yu and Gan Chowdhury*, 2009; *Vickery et al.*, 2009; *Lorsolo et al.*, 2010; *Masters et al.*, 2010; *Balderrama et al.*, 2011, 2012; *Henderson et al.*, 2013; *Miller et al.*, 2015; *Song et al.*, 2016]. Through coordinated observational studies in the USA [e.g. *Balderrama et al.*, 2011; *Weiss and Schroeder*, 2008] and Australia [*Henderson et al.*, 2013] information has begun to be captured, but substantially more needs to be collected and analysed so these highly complex wind fields can be more adequately understood. While some information about the wind structure in the very near-surface region can be inferred from upper level wind data [e.g. *Vickery et al.*, 2009], there is little explicit information on the characteristics of the spatio-temporal mean and turbulence in near-surface TC wind fields over land. This is particularly the case within the roughness canopy, at terrain change interfaces (e.g. sea to land transition) and in the presence of complex terrain. Without this information, operational forecasters cannot generate accurate TC wind speed forecasts. In addition, wind profiles used by design engineers cannot be validated and the reliability of coastal structures cannot be quantified.

To complement these observational studies, increased computational capacity over the last few decades has allowed numerical models to become viable tools for understanding the complex near-surface structure of the TCBL. As an example, the Weather Research and Forecasting Model (WRF) [*Skamarock et al.*, 2005, 2008] has been used to reconstruct historic TCs, and conduct more fundamental studies through idealised TC simulations [e.g. *Hill and Lackmann*, 2009; *Gentry and Lackmann*, 2010; *Lin et al.*, 2010; *Dodla et al.*, 2011; *Parker et al.*, 2013; *Mallik et al.*, 2015]. The WRF model is versatile in its configuration, with regards to initial and boundary conditions, and the different physical pa-rameterisation schemes, such as cumulus, microphysics, planetary boundary layer (PBL), and surface parameterisations that can be implemented. Such models have also been used to investigate TC wind field modification by terrain and topography [e.g. *Ramsay and Leslie*, 2008; *Lin et al.*, 1999, 2010]. For example, *Lin et al.* [1999] studied the interaction of an idealised TC with the Central Mountain Range of Taiwan. While such studies showed evidence of localized wind blocking and channelling processes through mountain ranges, more recent research found topography to also impact TC track, intensity, and structure, even prior to landfall [*Ramsay and Leslie*, 2008]. However, the fundamental understanding of these interactions in a highly turbulent rotational flow field still remains unresolved. This lack of understanding can in part be attributed to the one-sided usage of the term "complex terrain", which has been interpreted solely as mountainous or hilly terrain in the bulk of previous

research conducted. In fact, "complex terrain" also refers to variations of land surface characteristics such as rural, urban, bare, and forested, according to the American Meteorological Society [2].

Considering limitations in current atmospheric science- and engineering-based literature, this thesis seeks to explore how changes in terrain (surface roughness) influence the TCBL structure and its evolution throughout the TC landfall process. This will be studied throughout the boundary layer depth, with particular attention paid to evolution and variability in the near-surface layer, where structures reside. To achieve this, the present study will incorporate observational analysis of near-surface TC wind records at measurement heights of 2.25 m, 3 m, 5 m, and 10 m. In addition, this thesis uses numerical modelling techniques including the adoption of a hybrid real-idealised simulation method conceptualised by [*Bruyere et al.*, 2016]. The observational analysis includes the acquisition and aggregation of surface wind records at or below 10 m captured during field campaigns in Australia (Surface Weather Information Relay and Logging Network or SWIRLnet) and the USA (Florida Coastal Monitoring Program or FCMP, StickNet). These low-level records will be analysed to assess their turbulent characteristics and their response to sudden changes in land surface characteristics. The numerical modelling method combines an idealised spun up TC and a real world environment (hybrid WRF [*Bruyere et al.*, 2016]) to undertake a series of parametric simulations where idealised TCs impact coastlines with a range of terrain conditions. These tests will systematically explore how sudden changes in terrain (i. e. sea to different land surface characteristics) will influence the surface wind field and the structure of the TCBL.

Specific objectives for observational and numerical analyses include:

- Observational objectives

    1. Aggregate and categorise observational wind records from FCMP, StickNet, and SWIRLnet at measured elevations of 2.25 m, 3.2 m, 5 m, and 10 m.

    2. Assess equilibrium characteristics of near-surface TC turbulence, e.g., turbulence intensity, gust and peak factors, skewness, kurtosis, integral length scale and upwind fetch requirements, based on the observational data listed in Objective 1.

    3. Explore the effect of upwind distance between measurement tower and roughness change on measured turbulent characteristics following single and multiple changes in surface roughness.

    4. Assess the validity of traditional engineering terrain transition models (e.g. AS/NZS1170.2, ESDU) in a TC environment.

- Numerical modelling objectives

    1. Numerically simulate an idealised TC within a real-world environment.

---

[2] http://glossary.ametsoc.org/wiki/Complex_terrain - accessed on 7 January 2019, 10:45 AM UTC

2. Analyse vertical TC wind profiles in different parts of simulated TCs and assess whether these simulated profiles reflect observed TC wind profiles measured by dropsondes.

3. Model and analyse vertical TC wind profiles at a fixed storm-relative position throughout the landfall process over different land surfaces with different roughness characteristics.

In order to build context for the proposed study, Chapter 2 provides a review of historical literature concerning the TCBL and how it is numerically modelled. Existing gaps in the research are identified and the major research questions are presented. Chapter 3 discusses the origin of TC surface observations used in this dissertation, while data processing techniques and steps to generate real and idealised TC simulations are described in Chapter 4 and 5, respectively. Chapter 6 details and discusses observational results in the context of the research questions expressed in Chapter 2. Chapter 7 discusses the results of the TCBL structure changes during TC landfall. Finally, Chapter 8 concludes the dissertation with a summary of the key findings and discusses multiple avenues for future research related to near-surface wind field modification resulting from sudden changes in terrain.

Chapter 2

Literature Review

A review of existing literature on the TCBL, observations of near-surface TC wind field characteristics, and numerical modelling of TCs is presented in this chapter. It begins with a review of the TCBL structure, covering its height and vertical wind profile, followed by a review of landfalling TC near-surface turbulence processes and characteristics. The evolution of numerical TC modelling and idealised TC simulations are then discussed before a short summary of the chapter is presented and research gaps are identified.

2.1 Tropical Cyclone Boundary Layer

The planetary boundary layer (PBL) is defined as the lowest 3 km of the atmosphere layer, where the exchange of heat, moisture and momentum between the earth's surface and the atmosphere occurs [*Stull*, 1988]. The primary source of energy for all atmospheric motion is provided through short-wave radiation from the sun, which reaches the surface and results in thermal generation of turbulence. Heating of the PBL through molecular and turbulent thermal conduction also results in pressure contrasts, which cause air parcels to move [*Etling*, 2008]. Friction reduces the flow velocity through the depth of the PBL to the height of the gradient winds, which induces the exchange of heat and momentum between the earth's surface and the atmosphere [*Etling*, 2008].

Similarly, the TCBL is defined by its interactions with the underlying surface. In particular, heat, momentum and moisture transfer regulate the physical processes needed for TC maintenance and intensification [*Ooyama*, 1969; *Smith and Montgomery*, 2010; *Montgomery and Smith*, 2014]. The TCBL is distinct from the typical atmospheric boundary layer because of the strong effect of an overlaying rotational wind field [*Kepert*, 2012]. This is true not just for TCs over homogeneous surfaces, but also for interactions with non-homogeneous terrain and topography, such as during TC landfall. Thus, any (sudden) change in surface terrain will influence the horizontal and vertical TCBL structure [*Holland*, 1987; *Ramsay and Leslie*, 2008]. A better understanding of TCBL processes therefore becomes a prerequisite to adequately and accurately forecast TCs and their impacts.

2.1.1 Vertical Wind Structure over Water

The introduction of reconnaissance aircraft flights in the early 1940's [*Sumner*, 1943] pioneered quantitative observations in TCs to contribute to a better understanding of their structure, dynamics and formation [*Dorst*, 2007]. First attempts to describe the vertical TCBL structure were made by *Palmen* [1948] and *Bergeron* [1954], but were based on limited observations. These scarce observations led to many misconceptions regarding TC formation and structure [*Dorst*, 2007]. To increase the number of observations, Robert Simpson from the U.S. Weather Bureau espoused the benefits of regular reconnaissance after participating in numerous Air Force flights in the 1950's [*Dorst*, 2007]. Simpson's efforts were rewarded and along with technological improvements to aircraft instrumentation during the 1970's, the first detailed insights into eyewall [*Jorgensen*, 1984] and rainband dynamics [*Willoughby et al.*, 1984] were possible. New instruments such as the airborne Doppler radar advanced the measurement of horizontal wind fields with high vertical resolution, with the first documented use in Hurricane Debby (1982) [*Marks and Houze*, 1984]. This study provided insight into the vertical wind field of a developing eyewall with mesoscale wind maxima occurring at 1, 3 and 5 km height. In a follow-up study by *Marks and Houze* [1987], airborne Doppler radar measurements were utilised to estimate horizontal and vertical winds within 40 km of the eye of Hurricane Alicia (1983). Peak winds were found between 1.5 - 2.5 km height at the leading side of the storm.

Further technological advances during the 1990's led to the development of new observational equipment that would provide highly resolved horizontal and vertical TC wind profiles. Numerous wind profile observations have since been measured in TCs and TC eyewalls using Global Positioning System (GPS) dropsondes [*Franklin et al.*, 2003; *Powell et al.*, 2003; *Kepert*, 2006a,b; *Vickery et al.*, 2009], Doppler radar [*Marks and Houze*, 1987], wind profiler [*Knupp et al.*, 2000, 2006], and weather towers [e.g. *Schroeder and Smith*, 2003; *Yu and Gan Chowdhury*, 2009; *Masters et al.*, 2010; *Balderrama et al.*, 2011, 2012; *Henderson et al.*, 2013; *Miller et al.*, 2015; *Song et al.*, 2016]. These studies showed that the maximum wind speed occurs in the lowest 300-800 m of the TCBL near the eyewall, but this increases up to 2 km at larger radii [*Franklin et al.*, 2003; *Kepert*, 2006a,b; *Schwendike and Kepert*, 2008; *Kepert*, 2010b]. *Franklin et al.* [2003] analysed mean eyewall and outer-vortex mean wind speed profiles using 630 GPS dropsondes in 17 TCs. Figure 2.1 shows seven observed mean eyewall wind speed profiles normalised by wind speeds at aircraft flight level height of 700 hPa (i.e. 3 km).
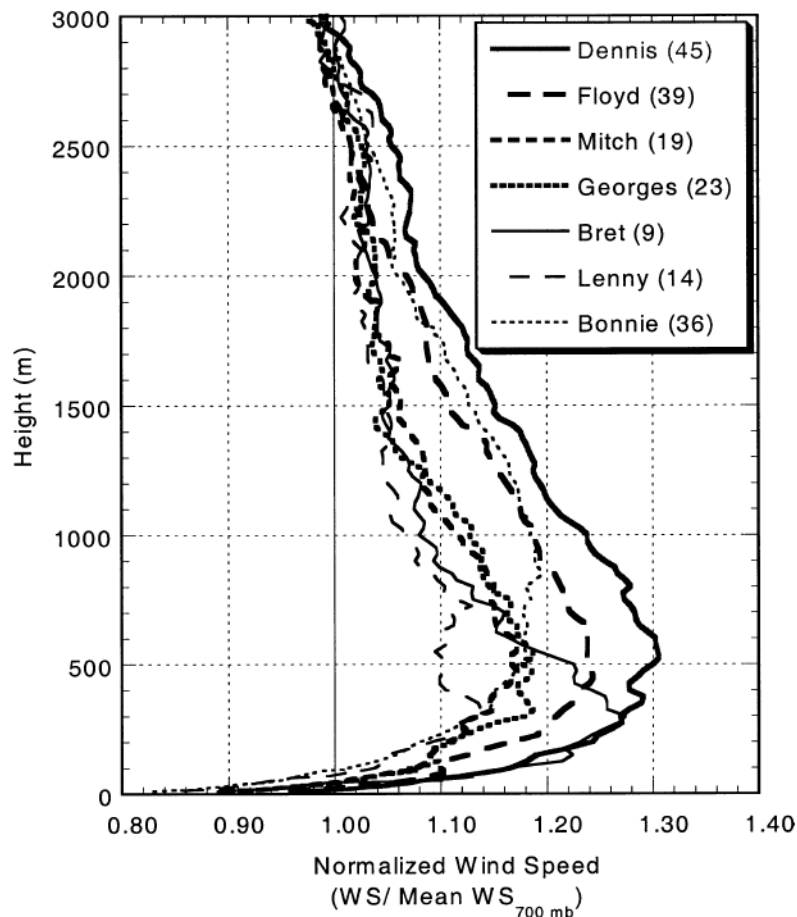
Figure 2.1: Mean wind speed profiles measured in different hurricane eyewalls normalized by the wind speed at 700 hPa [*Franklin et al.*, 2003]

The authors noted that the mean eyewall wind speed maximum was located at about 500 m above the surface in the eyewall. Within the lowest 100-200 m, the wind speed increased nearly logarithmically due to the influence of frictional forces within the TCBL surface layer [*Franklin et al.*, 2003; *Kepert*, 2010b]. Above the wind maximum, wind speeds decreased due to the warm core nature of TCs and prevalent gradient wind balance [*Franklin et al.*, 2003; *Kepert*, 2010b]. The authors emphasise that these dropsonde results only hold true for TCs over water and in the immediate vicinity of the coast.

Powell et al. [2003] also analysed dropsonde data using 331 measured wind profiles in 15 TCs from 1997-1999. In agreement with *Franklin et al.* [2003] it was found that wind speeds increase logarithmically over the lower 200 m of the marine boundary layer. In addition, wind speeds at 10 m height were found to be equal to approximately 78% of the mean average wind speed over the lower 500 m and equal to approximately 71% of the maximum wind speed. *Vickery et al.* [2009] confirmed the logarithmic wind increase over the lower 200-300 m through the examination of the same dropsonde data. The authors categorised the wind records by TC size and wind speed and combined their analysis with a linearised TCBL model developed by *Kepert* [2001] to derive mean TCBL profiles for various storm radii. These profiles taken at or near the radius of maximum wind (RMW) are illustrated in Figure 2.2.
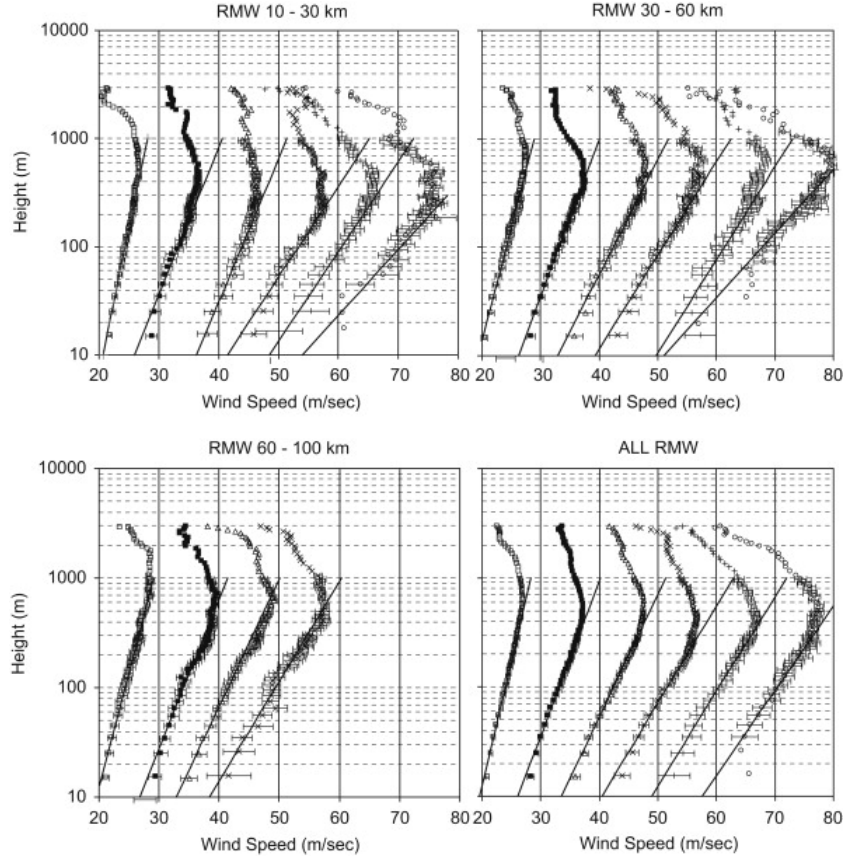
Figure 2.2: Variation of mean wind speed with height and radius of maximum wind (RMW). Horizontal error bars represent the 95th percentile error on the estimate of the mean wind speed [*Vickery et al.*, 2009].

Using the vertical profiles of the mean horizontal wind speed in Figure 2.2, *Vickery et al.* [2009] inferred a decreasing trend in the height of the mean horizontal wind speed maxima as RMW decreased and as wind speeds increased. This, they empirically modelled using

$$H^* = 343.7 + 0.26/I \tag{2.1}$$

$$I = \sqrt{\left(f + \frac{2V}{r}\right)\left(f + \frac{V}{r} + \frac{\partial V}{\partial r}\right)} \tag{2.2}$$

where H^* is a TCBL height parameter decreasing with increasing inertial stability I, f the Coriolis parameter, V the azimuthally averaged tangential gradient wind speed, and r the radial distance from the center of the storm [*Vickery et al.*, 2009]. The authors also empirically modelled the mean wind speed variation $U(z)$ in the TCBL using the following equation:

$$U(z) = \frac{u_*}{\kappa}\left[ln\left(\frac{z}{z_0}\right) - 0.4\left(\frac{z}{H^*}\right)^2\right] \tag{2.3}$$

In Eq. 2.3 u_* is the friction velocity, κ is the von-Karman coefficient of 0.4, and z_0 the aerodynamic roughness length.

As observations of vertical wind profiles by dropsondes are scarce over land, TCBL changes after landfall need to be described through similar empirical models. However, such models for this process do not exist, but engineering models do. Therefore, *Vickery et al.* [2009] describes the usage of a classic engineering approach [e.g. *Deaves*, 1981], in which the wind speed at the ABL top remains unchanged when the flow transitions to a new roughness regime. Moreover, the underlying surface roughness controls the variation of the horizontal wind speed with height as described by the Log Law [*Vickery et al.*, 2009]. The authors assume this principle to hold true in hurricane winds over land. To determine the height of the TCBL, the authors used a modified approach of the linearised TCBL theory by *Kepert* [2001]. In general, the TCBL height is a fundamental parameter characterising the vertical extent of atmospheric mixing below where the turbulent flow becomes negligible [*Zhang et al.*, 2011]. *Vickery et al.* [2009] determined TCBL height increases between 60-100% to about 800-1500 m after the TC transitions from water onto open terrain.

Kepert [2001] and *Kepert and Wang* [2001] described TCBL structure including its height from a dynamical perspective. The former study presents a three-dimensional linear model to describe the processes that generate a low-level wind speed maximum in the TCBL. These processes are strongly linked with the advection of absolute angular momentum M_a defined as

$$M_a = rv + \frac{1}{2}fr^2 \tag{2.4}$$

where r is the radius, v the azimuthal wind component, and f the Coriolis parameter. The change of M_a is described through

$$\frac{dM_a}{dt} = -\frac{\partial \phi}{\partial \lambda} + K\left[\nabla^2 M_a + \frac{2}{r}\left(\frac{\partial u}{\partial \lambda} - \frac{\partial M_a}{\partial r}\right)\right] \tag{2.5}$$

where u is the radial wind component, ϕ the geopotential, $d/dt = \partial/\partial t + u\partial/\partial r + v/r\,\partial/\partial \lambda + w\partial/\partial z$ the rate of change following the parcel, K the turbulent diffusivity for momentum and $\nabla^2 = \partial^2/\partial r^2 + 1/r\,\partial/\partial r + 1/r^2\,\partial^2/\partial \lambda^2 + \partial^2/\partial z^2$ in a storm-centered cylindrical coordinate system (r, λ, z) [*Kepert*, 2001]. Thus, M_a varies through horizontal advection, azimuthal pressure gradients, and frictional torques [*Kepert*, 2001]. For a steady-state, symmetric, stationary storm in a quiescent environment a balance between radial and vertical advection, and turbulent diffusion of M_a exists at all levels [*Kepert*, 2001]. In an inertially stable storm M_a increases with increasing r, while the radial gradient of M_a equals zero in an inertially neutral storm. *Kepert* [2001] hypothesises that supergradient flow (i.e. TC low-level jet) can occur once a strong combination of inertial stability and inflow exists. To assess the validity of the theory, *Kepert* [2001] investigated the importance of radial inflow. If radial winds are accelerated outwards due to the imbalance between pressure, Coriolis and centripetal terms, supergradient flow occurs. This outward acceleration of the radial wind will reverse the radial inflow and disturb the gradient wind balance, which eventually leads to a weakening of the jet. *Kepert* [2001] proposed two possibilities for maintenance of the radial inflow against the imbalance in the gradient wind. First, inflow increases outward from the storm center and is therefore sustained by

self-advection. Second, radial inflow is believed to be greater below the jet level and through processes of upward diffusion and upward advection, the jet is being maintained [*Kepert*, 2001]. These two proposed mechanisms were transferred into a linear analytic model of the TCBL applied for a stationary and a moving TC, respectively.

The *Kepert* [2001] linear model consists of asymmetric components for translating TCs, whereas for stationary storms his theory reduces to the solution in the axisymmetric case provided by *Eliassen and Lystad* [1977]. Along with the asymmetric components, the height δ_k for supergradient flow is introduced as

$$\delta_k = \sqrt{\frac{2K}{I}}. \tag{2.6}$$

With the linear model, *Kepert* [2001] examined the variation of diffusivity K, drag coefficient C, gradient wind speed V, radius r, and inertial stability I. The inertial stability I was further parameterised through a variable x, given by $\partial V/\partial r = xV/r$. Aforementioned parameters were varied about $K = 50 m^2 s^{-1}$, $C = 0.002$, $V = 50 ms^{-1}$, $f = 3.77 \cdot 10^{-5} s^{-1}$ (15° latitude), $r = 40 km$, and $x = -0.5$, with results shown in Figure 2.3.
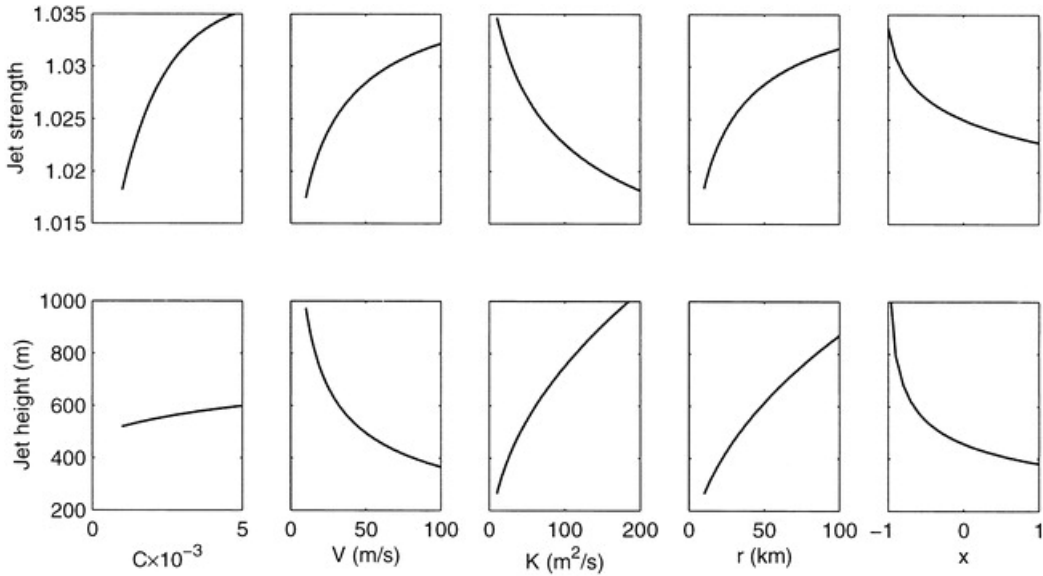
Figure 2.3: Variation of relative jet strength (top) and jet height (bottom) with various parameters drag coefficient, gradient wind speed, turbulent diffusivity, radius, and inertial stability in the linear model [*Kepert*, 2001].

The variation of the parameters revealed that an increased drag coefficient C enhanced the jet strength, with little effects on the jet height δ_k. The author explains that enhanced surface friction causes stronger inflow in the TCBL associated with higher inwards advection of angular momentum. An increase in gradient wind speed leads to a lower and stronger jet. A shallower but weaker jet was observed for lower radii, as the inertial stability is modified (Eq. 2.2). In general, it was found that the mean degree to which flow is supergradient was about 3%. This result was noticeably weaker than in the observations [*Kepert*, 2001]. In a moving storm supergradient flow was evident in the

left forward quadrant for a TC in the Northern Hemisphere as opposed to the right forward quadrant, where the strongest near-surface winds occur [*Kepert*, 2001]. Using surface azimuthal and gradient wind speeds, surface wind reduction factors were calculated for stationary and moving storms. In good agreement with previous observations [e.g. *Powell*, 1990], a surface wind reduction factor of 0.81 was calculated near the radius of maximum winds and on the left (weaker) side of the storm (Northern Hemisphere).

In part II of the study, *Kepert and Wang* [2001] expanded on the linear model through the implementation of nonlinear terms, a sophisticated turbulence closure and surface layer parameterisation in their three-dimensional, high-resolution, dry, hydrostatic, numerical model. The inclusion of nonlinear terms and the vertical advection of radial wind in particular enhanced inflow and strengthened the supergradient flow, which tend to be more realistic than predicted by the linear model. Wind maxima were between 10% and 25% supergradient in a stationary TC, whereas the jet was found to be more supergradient in a more intense TC. In conclusion, *Kepert and Wang* [2001] state that magnitude and height of the jet were in agreement with observations. With regards to the location of the jet, the authors found the jet to be near the eyewall in case of a non-moving, axisymmetric storm for a relatively rapid decrease in wind speed outside of the RMW. In contrast, the jet was more widely distributed when the TC exhibited a more inertially stable radial profile [*Kepert and Wang*, 2001]. In a moving storm, the study revealed that the location of the jet was generally located in the left forward quadrant for a Northern Hemisphere TC.

Zhang et al. [2011] also studied the TCBL structure analysing observations of 13 hurricanes using 794 GPS dropsondes. Here, the authors apply dynamic and thermodynamic parameters to estimate the height of the TCBL throughout each of these storms. In particular, one such parameter suggested to represent the TCBL height is the nearly constant virtual temperature layer referred to as the mixed layer depth z_i [*Zhang et al.*, 2011]. Another thermodynamic parameter introduced is the bulk Richardson number Ri_{cr}, which combines buoyancy and shear forcing processes responsible for reducing and generating turbulence, respectively [*Zhang et al.*, 2011]. In addition to the two thermodynamic parameters defining the TCBL height, two dynamical height scales were proposed, first being the height of the maximum wind speed h_{vmax} and second, the inflow layer depth h_{infl}. The latter parameter is defined by the height where the radial velocity is 10% of the peak inflow that is directly induced by surface friction [*Zhang et al.*, 2011]. All height scales introduced are shown as a function of distance from the storm center resulting from the analysis of all dropsonde data in Figure 2.4.
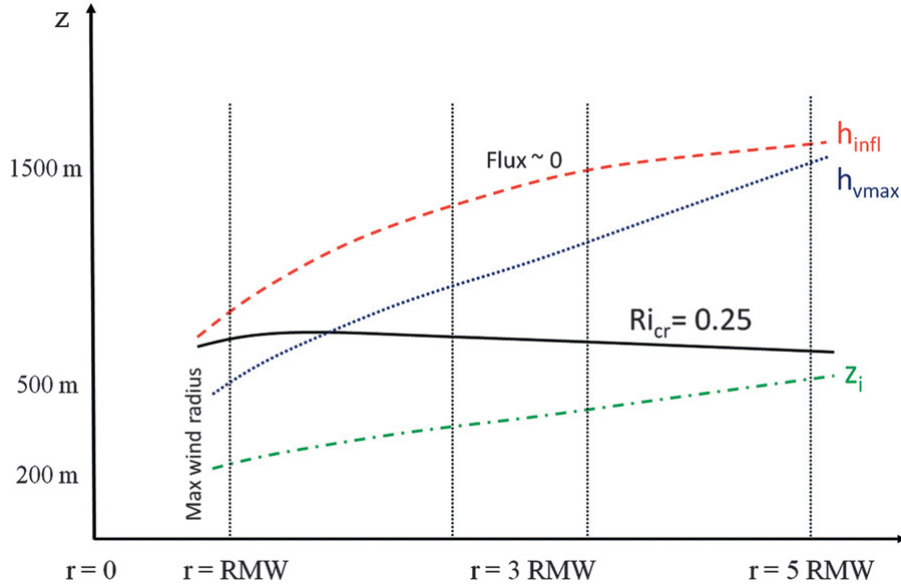
Figure 2.4: Characteristic TCBL height scales as a function of distance from storm centre. The red dashed line is the inflow layer depth h_{infl}, h_{vmax} (blue dotted line) denotes the height of the maximum wind speed, the boundary layer depth is visualised through the solid black line where the bulk Richardson number equals 0.25, and z_i (green dashed-dotted line) illustrates the mixed layer depth [*Zhang et al.*, 2011].

Both dynamical parameters h_{infl} and h_{vmax}, and the mixed layer depth z_i show a decrease in height with lower storm radius, while Ri_{cr} slightly increases toward the eyewall [*Zhang et al.*, 2011]. The height h_{vmax}, however, exhibits the sharpest decrease. Similar results were found by *Montgomery et al.* [2006], who investigated GPS dropsonde and flight-level aircraft data recorded during Hurricane Isabel (2003). The observed decrease in h_{infl}, h_{vmax} and z_i [e.g. *Kepert*, 2006a,b; *Schwendike and Kepert*, 2008; *Sitkowski and Barnes*, 2009] have been shown in the theory of rotating boundary layers [e.g. *Eliassen and Lystad*, 1977; *Montgomery et al.*, 2001]. *Zhang et al.* [2011] discusses the different TCBL heights and suggest that h_{infl} might represent the TCBL height better than thermodynamic approaches because the studies of *Kepert and Wang* [2001], *Zhang et al.* [2009] and *Kepert* [2010a] show the momentum flux is an essential part of the TCBL dynamics above the inflow. *Zhang et al.* [2011] does, however, concede that the use of h_{infl} to define the TCBL top has its weaknesses due to asymmetric inflow layers.

Another approach to estimate the height of the TCBL has been suggested by *Lorsolo et al.* [2010], who used the turbulent kinetic energy (TKE) derived from aircraft Doppler radar measurements. TKE is an important measure that describes the generation and destruction of turbulence and is recognised to be the central energetic base equation of the PBL [*Etling*, 2008]. Furthermore, it identifies where turbulence-generating processes are occurring and unifies the interaction between the synoptic, turbulent and molecular scale. It holds that:

$$\underbrace{\frac{\partial \overline{TKE}}{\partial t}}_{\substack{local\ change \\ of\ TKE}} = \underbrace{\frac{\vec{\tau}}{\rho} \cdot \frac{\partial \overline{u}_h}{\partial z}}_{\substack{turbulent \\ momentum\ flux}} + \underbrace{\frac{H}{\rho \cdot c_p} \cdot \frac{g}{\overline{\overline{\theta}}}}_{\substack{turbulent \\ heat\ flux}} - \underbrace{\varepsilon}_{dissipation} - \underbrace{D}_{divergence} \qquad (2.7)$$

where $\overline{TKE}$ is the mass-specific turbulent kinetic energy, $\vec{\tau}$ the shear stress vector, ρ the air density, $\vec{u_h}$ the horizontal wind vector, H the enthalpy, c_p the specific heat capacity of air, g the gravity acceleration, and $\bar{\theta}$ the potential temperature according to the base equation of the Prandtl layer [*Lange*, 2002]. Local changes of TKE are governed by four major processes, the turbulent momentum flux, turbulent heat flux, the turbulent kinetic energy dissipation through molecular friction and the divergence of TKE. Following these terms, it becomes apparent that energy transport in the PBL is directly related to TKE [*Stull*, 1988; *Lorsolo et al.*, 2010]. Closing this TKE equation is an important part of PBL schemes [e.g. *Janjić*, 1994] within numerical models such as the Weather Research and Forecasting Model (WRF).

Within the TCBL, *Lorsolo et al.* [2010] identified maximum TKE values at the RMW, particularly in the eyewall, which exhibit a strong correlation with gradients of radial and vertical wind (see Figure 2.5).
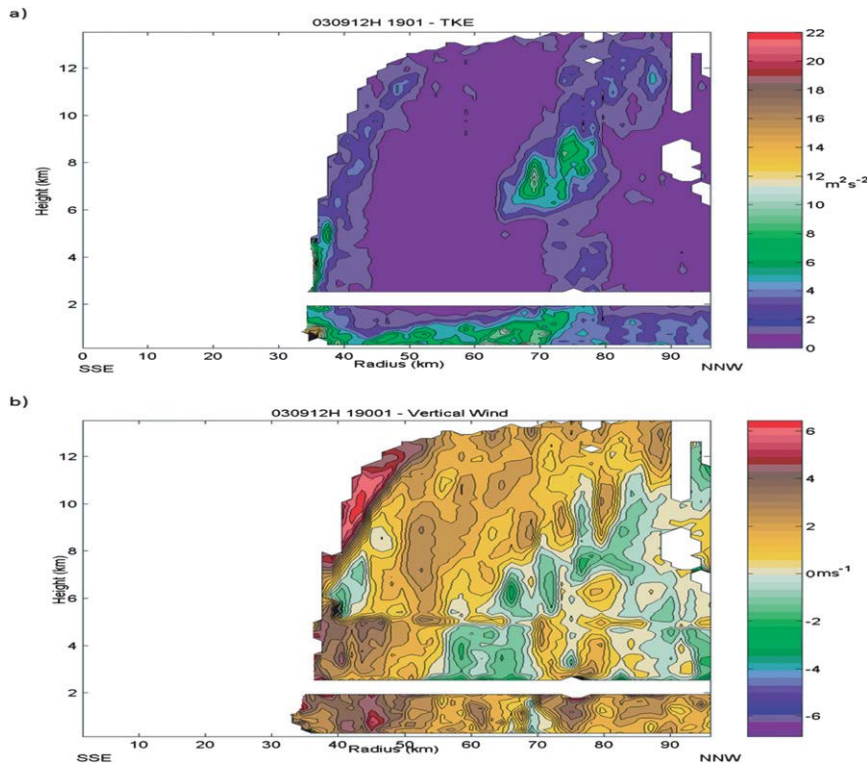
Figure 2.5: 2D profiles of TKE (a) and vertical wind speed (b) for Hurricane Isabel on 12 Sep 2003, 1901 UTC [*Lorsolo et al.*, 2010].
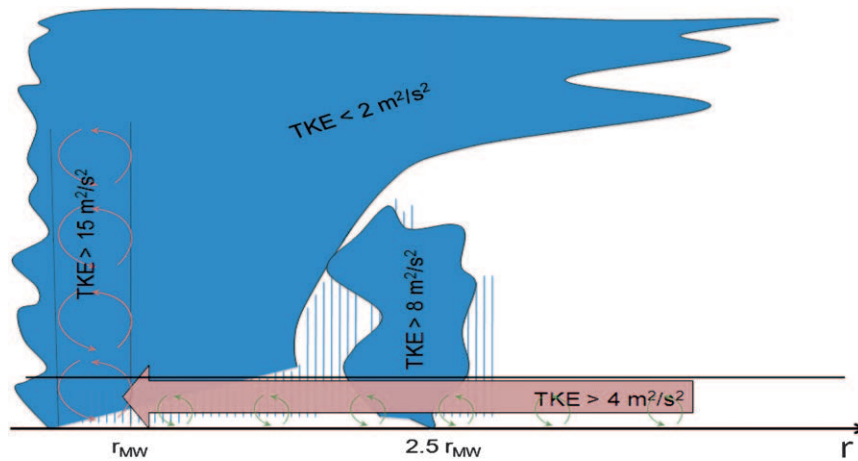
Figure 2.6: Conceptual model of TKE distribution in a TC over water [*Lorsolo et al.*, 2010].

Using this information, *Lorsolo et al.* [2010] suggested a simple conceptual model, illustrated in Figure 2.6. It depicts the strongest TKE signal exists inside the RMW (rotating red arrows) due to strong horizontal shear, and in the TCBL (green arrows) where the vertical gradient in the radial flow causes high wind shear [*Lorsolo et al.*, 2010]. Overall, the authors emphasise that the TKE exhibits locally high values, especially in the eyewall, whereas the other regions show a low TKE signal. However, the study focused primarily on hurricanes prior to landfall, which will lead to smaller TKE values when compared with storms over land [*Zhu*, 2008]. The calculation of the TCBL height turned out to be very difficult to compute using TKE as it does not vanish in those heights where the turbulent fluxes become zero (near the top of the inflow layer) [*Zhang et al.*, 2011].

2.1.2 Tropical Cyclone Interaction with Land

The aforementioned research highlighted the horizontal and vertical wind structure of the TCBL over water. However, the TCBL structure changes if the low level flow is subjected to changes in underlying terrain and topography during TC landfall. Numerous studies have already explored the changes to the near-surface wind structure within the TCBL during the landfall phase [e.g. *Powell*, 1982; *Schneider and Barnes*, 2005; *Hirth et al.*, 2012; *Krupar*, 2015]. Work during the 1950s [e.g. *Johnson*, 1954; *Hubert*, 1959; *Myers*, 1959] and 1960s [*Miller*, 1963, 1964] first investigated the influence of friction on landfalling TCs. In particular, *Johnson* [1954] and *Myers* [1959] introduced a method to calculate surface friction in a TC by analysing surface winds in the region of Lake Okeechobee based on measurements by 10 anemometers at elevations between 14 m and 18 m. *Johnson* [1954] derived his model by reformulating the equations of horizontal motion and modifying these into equations appropriate for modelling a TC, as shown in Figure 2.7.
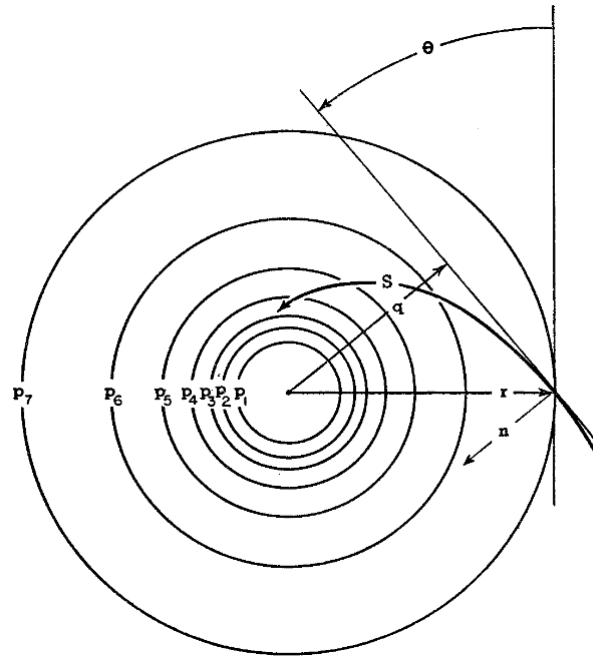
Figure 2.7: Hurricane model by *Johnson* [1954] with p_i = value of circular isobar, r = radius, s = path of air particle, directed positive in the direction of motion, θ = Deflection angle of wind across a circular isobar, n = Normal to s, q = normal to tangent of path originating from the center.

The tangential and normal friction components F_s and F_n for a given distance from the center in a model TC were calculated by

$$F_s = sin\,\theta \left(\alpha \frac{\partial p}{\partial r} + v_s \frac{\partial v_s}{\partial r} \right) \tag{2.8}$$

$$F_n = \left(\alpha \frac{\partial p}{\partial r} \right) cos\,\theta - v_s^2 \left(\frac{cos\,\theta}{r} - sin\,\theta\,\frac{\partial \theta}{\partial r} \right) - fv_s \tag{2.9}$$

where θ is the deflection angle of wind across a circular isobar p_i, v_i the wind speed, r the radius, f the Coriolis parameter, and α the specific volume. Application of this model by *Johnson* [1954] to the observed data revealed a greater tangential component F_s in the rear of the center, while the normal component F_n appeared to be greater in the front of the center. *Myers* [1959] extended the work of *Johnson* [1954] and determined a relationship between frictional forces and anemometer-height wind flow. He found that both frictional components outside the eye were almost proportional to the square of the wind speed over water, while friction over land appeared to be the same at all TC radii. In general, both noted a pressure increase over land which they associated with a wind speed decrease. *Hubert* [1959] also provided insight into the effect of surface friction on the TCBL of landfalling TCs through the analysis of surface wind records captured during Hurricanes Hazel (1954), Connie (1955), and Diane (1955). Unlike *Myers* [1959], *Hubert* [1959] found an increase in friction was evident toward the TC center, but confirmed many of the other findings related to the behaviour of frictional components by *Johnson* [1954].

Further research highlighting TC interactions with land was conducted by *Miller* [1963, 1964] through

a composite study of Hurricane Donna (1960). Research data was drawn from wind records captured by surface weather stations, rawinsondes, reconnaissance aircraft flights, radar, lighthouse stations and ship reports. Both studies utilised the data to calculate changes in energy supply to the TCBL during TC landfall, away from the warm ocean. *Miller* [1963, 1964] showed that the TC core is subjected to cooling during landfall and collapses eventually due to the absence of the oceanic heat source. Cooling also causes radial gradients of heights of constant pressure surfaces near the TC core to decrease to approximately 50% of their value during landfall. *Miller* [1963, 1964] concluded that the absence of oceanic heat at landfall led to the weakening of Hurricane Donna (1960), whereas increased surface roughness over land also contributed to the weakening through a reduction in surface wind speeds.

Numerous studies from the 1980s onwards have identified discontinuities in the (near-) surface winds through increased surface roughness during TC landfall. *Powell* [1982] recorded the landfall phase of Hurricane Frederic (1979) in the Gulf of Mexico using 152 data sources, which included surface observations from 91 stations over land, 3 buoys, 54 ships, and 4 reconnaissance aircraft flights. His results showed that measured 10 m wind speeds were 20% lower than those measured over water. *Powell* [1982] also showed that near-surface winds were approximately half the magnitude of winds recorded by a reconnaissance aircraft flying at 500 m height. He inferred the near-surface flow to be discontinuous and suggested that terrain features extract energy from the flow through friction, which induces higher vertical shear over land. He emphasised that this process induces higher turbulence, reduces the mean wind speed, and changes inflow angles. Figure 2.8 illustrates wind speed contours for Hurricane Frederic (1979) during its landfall [*Powell*, 1982].
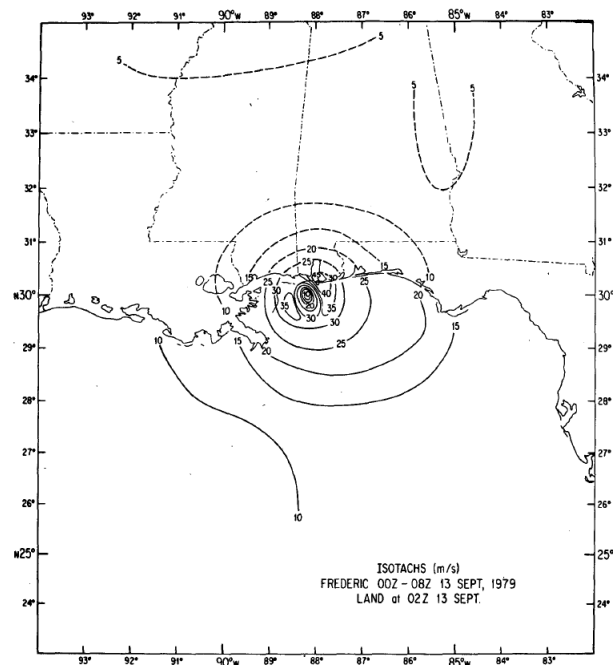
Figure 2.8: Isotach analyses at landfall for Hurricane Frederic (1979) with dashed flow over land [*Powell*, 1982].

When near-surface TC flow is subjected to increased surface roughness it experiences deceleration. Moreover, the inner vortex loses its gradient wind balance because of a wind speed reduction in the

low-levels that leads to a decrease of the outward directed Coriolis and centrifugal force and inward directed pressure gradient force. This drives the flow inward [*Powell*, 1982]. Similar observations were made by *Powell* [1987] during the investigation of the kinematic structure of Hurricane Alicia (1983) using 85 weather stations over land, two reconnaissance aircraft flight data, and two oil rig platforms. He observed land-sea asymmetries in the surface wind field during landfall, with winds over water being greater than over land. In contrast to his previous findings in Hurricane Frederic [*Powell*, 1982], Hurricane Alicia (1983) exhibited surface convergence, higher radar reflectivity, and a maximum in inflow angle in the offshore flow. *Powell* [1987] attributed these features to asymmetries associated with southwesterly environmental flow, which paralleled the southwest-northeast oriented coastline. In subsequent TC wind field analyses during Hurricane Hugo (1989) [*Powell et al.*, 1991] and Andrew (1992) [*Powell and Houston*, 1996], isotach discontinuities were also present. *Powell and Houston* [1996] described the coastline as a transition zone, where oceanic flow near the surface adjusts to land surface conditions. In an attempt to include these land surface conditions to standardise Hurricane Andrew (1992) wind measurements, the authors roughly categorised measurements recorded either over land or marine exposure. Here, *Powell and Houston* [1996] highlighted the importance of the wind direction, classifying it as on-, off-, or alongshore winds, using this to determine the fetch (distance between measurement site and roughness change) for coastal weather stations. Onshore winds decelerate due to increased surface roughness, while offshore winds accelerate [*Powell and Houston*, 1996]. The authors identify great variability in recorded TC surface winds, which they link directly to upstream terrain roughness and the size of upwind obstacles. Knowledge about the upstream terrain roughness was important for properly adjusting wind records at different heights down to 10 m [*Powell and Houston*, 1996]. The correction of mean surface wind speeds $\bar{U}$ at a height z to 10 m mean wind speeds $\bar{U}_{10}$ dependent on the upstream roughness z_0 was calculated through

$$\frac{\bar{U}_{10}}{\bar{U}} = \frac{ln[(10 - z_D)/z_0]}{ln[(z - z_D)/z_0]} \tag{2.10}$$

where z_D is the zero-plane displacement height [*Powell and Houston*, 1996]. The zero-plane displacement height z_D is utilised to determine an effective height $z - z_0$ of the anemometer above surrounding roughness elements given those are large relative to the height of the anemometer [*Powell and Houston*, 1996]. However, as design standards or building codes typically prescribe open exposure, *Powell and Houston* [1996] converted all surface wind measurements over land to a standard $z_0 = 0.03$ m. This conversion was realised through the relationship between the friction velocity u_* and the gradient wind. Moreover, *Simiu and Scanlan* [1986] determined an equation that relates two different roughness values to the same gradient wind. It holds that

$$\frac{u_{*s}}{u_*} = \left(\frac{z_{0s}}{z_0}\right)^{0.0706} \tag{2.11}$$

where u_{*s} is the friction velocity for standardised terrain and z_{0s} the standard open-terrain exposure roughness of 0.03 m. Using their standardisation approach, *Powell et al.* [1996] noted that the wind flow is not in equilibrium with the underlying surface until 30 km or even beyond downwind of a

terrain change, which is also supported by observations made by *Sempreviva et al.* [1990] in non-tropical cyclone conditions on the North Sea coast of Jutland. However, traditional approaches [e.g. *Businger*, 1986] suggest 10 m winds reach equilibrium between 1-3 km.

Attempts to examine the TC wind field modification over flat terrain were also made by *Kaplan and DeMaria* [1995]. Their development of a simple, two parameter empirical model was based on wind speed observations of 67 landfalling TCs between 1967 and 1993 [e.g. *Powell*, 1982; *Powell et al.*, 1991]. *Kaplan and DeMaria* [1995] assumed an exponential decay of TC wind speeds with time after landfall, which includes a reduction factor that accounts for increased roughness over land. The increased roughness is, in turn, responsible for the rapid decrease in wind speed [*Powell et al.*, 1991]. Increased roughness over land has also been found to alter the wind field prior to landfall. *Kepert* [2002] analysed 30 dropwindsondes in Hurricane Mitch (1998) when the eye was 85 km off the Honduran coast. He noted large asymmetries close to the eyewall, with the strongest inflow evident in the left-rear quadrant in the TCBL contrary to previous findings. These asymmetries were attributed to the proximity of land, which was verified with a model run [*Kepert*, 2002]. Asymmetries in landfalling TCs were also investigated by *Schneider and Barnes* [2005]. The authors used 85 dropwindsondes in Hurricane Bonnie (1998) to study the kinematic and thermodynamic structure. During landfall, Bonnie (1998) underwent an eyewall decrease of 28 km within 9 hours. Further analysis of the kinematic structure revealed offshore tangential winds to be 5 m/s weaker than onshore flow, with increased roughness attributed to reductions in tangential winds over land. The analyses of radial winds showed a wind variation up to 20 m/s between onshore and offshore flow. These discontinuities arose because of the higher roughness over land, which induced an increased, drier inflow, which produced a flow asymmetry extending to the eyewall [*Kepert*, 2010b].

To further assess these wind field asymmetries, *Giammanco et al.* [2012] studied the characteristics of observed low-level wind maxima and their accompanying vertical profiles before and during landfall. Wind field observations over open water were obtained from 1080 dropwindsondes, while a modified velocity azimuth display (VAD) technique was combined to WSR-88D Doppler velocity data to produce over 300 vertical wind profiles over land during landfalling TCs. The VAD technique invented by *Browning and Wexler* [1968] describes a method to determine horizontal wind speeds and direction at a specific height and has been widely used by subsequent studies [e.g. *Giammanco et al.*, 2013; *Krupar*, 2015; *Krupar et al.*, 2016]. The calculation of horizontal wind speed v_h and direction θ uses first order Fourier coefficients a_1 and b_1 and it holds that

$$v_h = -\frac{\sqrt{a_1^2 + b_1^2}}{cos\ \alpha} \tag{2.12}$$

$$\theta = \begin{cases} \frac{\pi}{2} - tan^{-1}\frac{a_1}{b_1} & b_1 < 0 \\ \frac{\pi}{2} - tan^{-1}\frac{a_1}{b_1} & b_1 > 0 \end{cases} \tag{2.13}$$

where α is the elevation angle [*Browning and Wexler*, 1968; *Krupar*, 2015; *Krupar et al.*, 2016]. Based on that technique, *Giammanco et al.* [2012] derived a composite vertical wind speed profile

using all generated VAD profiles. This derived composite vertical wind speed profile exhibited a logarithmic increase up to 400 m height, as displayed in Figure 2.9.
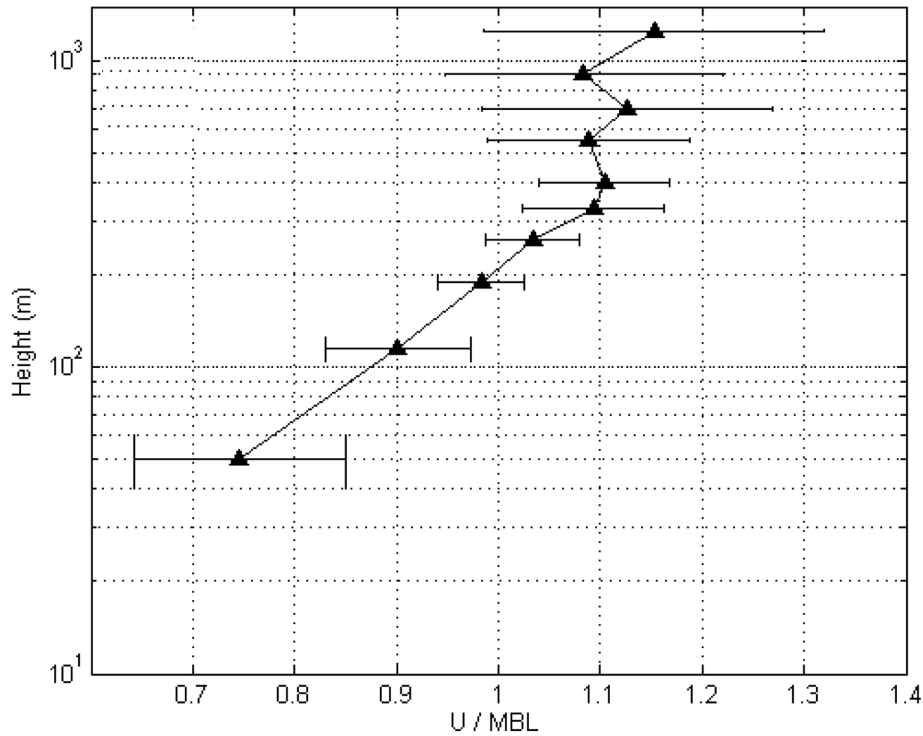
Figure 2.9: Composite VAD vertical wind profile over land normalised by the mean boundary layer wind (MBL). Error bars denote ± 1 standard deviation from the mean for each height bin [*Giammanco et al.*, 2012].

The authors noted a more rapid increase in wind speed over the same height when compared with GPS dropsonde composite vertical wind profiles over water. This difference has been attributed to increased roughness over land (i.e. at the radar site) rather than over water [*Giammanco et al.*, 2012]. The authors also found the radial wind component to become zero above 500 m with large variations above 300 m likely arising from internal boundary layer (IBL) formation and storm-scale variability. In a subsequent study, *Giammanco et al.* [2013] found differences in the slope of the VAD composite wind profiles in the offshore and onshore flow, however, the contribution of land surface conditions remained unknown as it is difficult to assess roughness captured within a VAD profile. *Krupar* [2015] and *Krupar et al.* [2016] extended this research and created a WSR-88D VAD wind profile database including roughly 21,000 VAD profiles, which were compared to Automated Surface Observing System (ASOS) mean wind speeds. This approach was used to formulate empirical relationships for determining near-surface wind fields during TC landfall. Multiple methods included log law, power law, mean/gust wind speed ratio method, and curve fitting with linear regression and polynomial fits. *Krupar* [2015] and *Krupar et al.* [2016] showed the most accurate predictions (up to 97%) of ASOS 10 m standardised mean wind speeds resulted from radar site-specific linear regression equations using a VAD 0–200-m layer average wind speed. Non-site specific linear regression equations described 83% of the variation in the ASOS 10-m nonstandardised maximum 3-s gust wind speeds.

Vertical wind profiles in landfalling TCs were further examined using WSR-88D and GPS dropsonde data in more recent research conducted by *Snaiki and Wu* [2018]. A total of 2120 dropsonde observa-

tions from 1996 to 2012 and 19 WSR-88D Doppler radar wind measurements were used to calculate vertical wind profiles over water and over land, respectively. Resulting dropsonde profiles over water shown in Figure 2.10 were grouped into mean boundary layer (MBL) wind speeds of 20-29, 30-39, 40-49, 50-59, 60-69, and 70-85 m/s, vertical heights bins of 10 m up below 300 m, 20 m from 300 m to 500 m, 50 m from 500 m to 1000 m, and 100 m bins for heights above 1000 m, and storm radius bins [*Snaiki and Wu*, 2018]. The MBL is defined by a wind speed average over the lowest 500 m following the method of *Powell et al.* [2003].
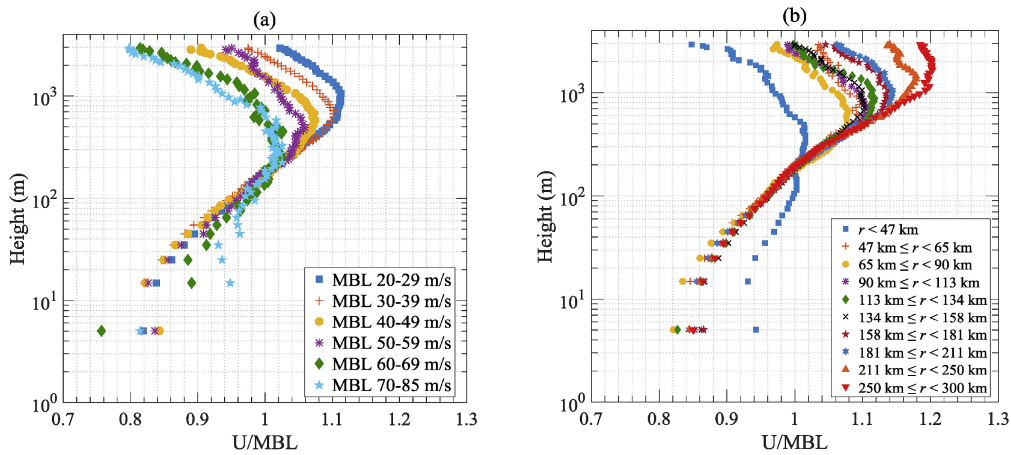
Figure 2.10: (a) Composite dropsonde vertical wind profiles over water grouped by MBL wind speed and (b) storm radius [*Snaiki and Wu*, 2018].

Snaiki and Wu [2018] found logarithmic behaviour of composite VAD vertical wind profiles measured over land up to the maximum wind speed, while its height lowers with increasing MBL wind speed (Figure 2.10). The investigation of dropsonde vertical wind profiles (over water) grouped by storm radius revealed that the maximum wind height increases with larger radii. The authors conducted the same analysis for VAD composite WSR-88D wind profiles over land, as illustrated in Figure 2.11.
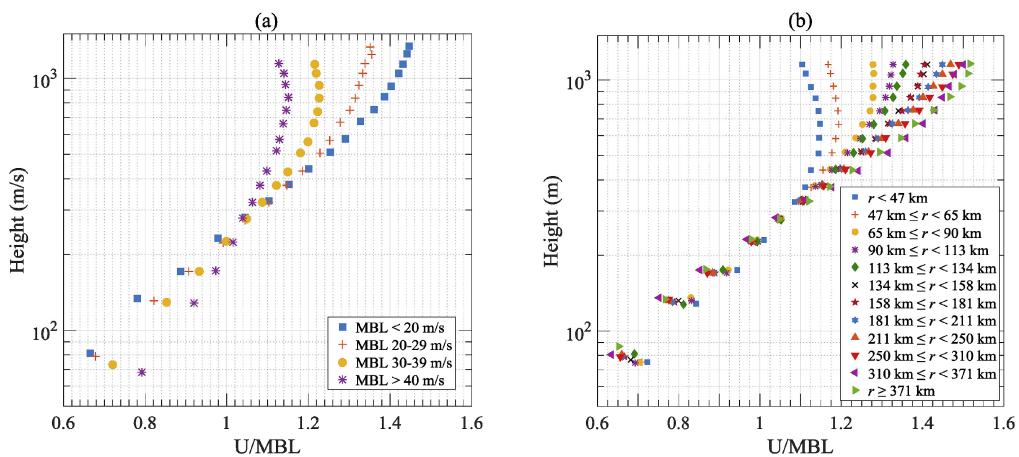
Figure 2.11: (a) Composite VAD vertical wind profiles over land grouped by MBL wind speed and (b) storm radius [*Snaiki and Wu*, 2018].

Composite VAD vertical wind profiles showed a more rapid decrease in wind speeds below the wind maxima compared to those over water, which was attributed to the increased roughness over land [*Giammanco et al.*, 2012; *Snaiki and Wu*, 2018]. In addition, the height of maximum wind, δ, increases

with greater storm radius. Evaluating the results from Figures 2.10 and 2.11, the authors hypothesise that the TCBL wind structure is defined by surface shear stress τ_ω, roughness length z_0, and height of maximum wind δ. Based on this, *Snaiki and Wu* [2018] proposed a semi-empirical model for mean vertical wind profiles in landfalling TCs. The proposed model includes a logarithmic part and an empirical height function, where height z is normalised by surface roughness z_0 and the height of maximum wind δ, respectively. The proposed semi-empirical approach to obtain vertical wind speed profiles is defined by

$$U_m(z) = \frac{u_*}{\kappa} \left[ln \left(\frac{z}{z_0} \right) + \eta_0 \, sin \left(\frac{z}{\delta} \right) exp \left(-\frac{z}{\delta} \right) \right] \tag{2.14}$$

where $U_m(z)$ is the mean wind speed at a specific height z, κ the von Karman constant, u_* the friction velocity, and $\eta_0 \approx 9.026$. This model was validated by wind observations from Hurricanes Wilma (2005) and Katrina (2005), where computed vertical wind profiles were in close agreement with observed profiles. After successful model validation, *Snaiki and Wu* [2018] applied their method to general cases of TC wind fields over water and over land. With roughness values of $z_0 = 0.001$ m and $z_0 = 0.1$ m representing marine and land exposure, respectively, the study showed the height of the maximum wind over ocean to be lower than over land. Furthermore, the authors show the model accurately predicts supergradient flow inside the eyewall region, while a logarithmic profile was evident in the outer vortex zone, as indicated in Figure 2.12.
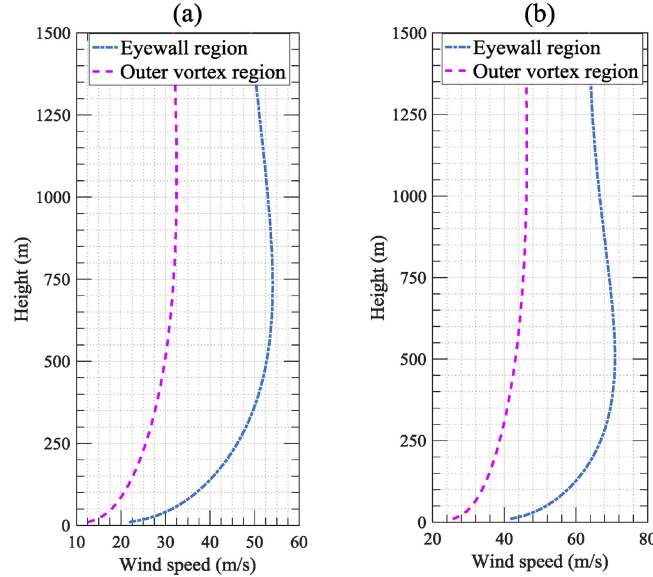
Figure 2.12: (a) Vertical profile of eyewall and outer regions for land exposure and (b) marine exposure [*Snaiki and Wu*, 2018].

2.1.3 Tropical Cyclone Near-Surface Wind Characteristics

Chapter 2.1.2 highlighted that changes in surface roughness during TC landfall alter TCBL structure. In those studies though, land surface conditions were assigned a constant roughness z_0, which implies homogeneous terrain to be present after landfall. The existence of such conditions is rare in reality

due to the largely inhomogeneous surface properties of the earth. Examples of different surface types include water bodies, flat grasslands, bushlands, scattered and dense forests and (sub-) urban terrain. These distinct surface types differ with respect to their canopy height, unevenness, vegetation, and roughness [*Foken*, 2008]. Aerodynamic roughness is the main parameter used to characterise the texture of the surface [*Wieringa*, 1993]. Throughout this thesis, aerodynamic roughness will be generalised and simply referred to as roughness.

According to *Wieringa* [1993] and *Foken* [2008], there are two common methods for defining surface roughness. First, solving the Log Law Eq. 2.21 for z_0. This, however, requires information of the friction velocity u_*. Second, roughness values can be estimated through characterisation of the geometric surface structure [*Foken*, 2008]. The second approach has been extensively studied by *Wieringa* [1993] who reviewed roughness values used in previous research [e.g. *Davenport*, 1960; *Oke*, 1978; *Cook*, 1985; *Troen et al.*, 1987] and found differences of up to a factor of three for similarly classified surface conditions. To overcome these inconsistencies, he summarised homogeneous surface types into groups using ranges of roughness, which are displayed in Table 2.1.

Surface type	z_0 [m]
Sea, loose sand and snow	≈ 0.0002
Concrete, flat desert, tidal flat	0.0002-0.0005
Flat snow field	0.0001-0.0007
Rough ice field	0.001-0.012
Fallow ground	0.001-0.004
Short grass and moss	0.008-0.03
Long grass and heather	0.02-0.06
Low mature agricultural crops	0.04-0.09
High mature crops ("grain")	0.12-0.18
Continuous bushland	0.35-0.45
Mature pine forest	0.8-1.6
Tropical forest	1.7-2.3
Dense low buildings ("suburb")	0.4-0.7
Regularly-built large town	0.7-1.5

Table 2.1: Roughness lengths of homogeneous surface types, Table VIII [*Wieringa*, 1993]

If horizontal flow across a step change in surface roughness occurs, a transition zone of limited height develops in which the flow adjusts to the new underlying roughness. Above this transition zone, the wind structure is determined by upwind roughness [*Wieringa*, 1993; *Hirth et al.*, 2012]. This transition zone was described by *Elliott* [1958] and is commonly known as the internal boundary layer (IBL). The general theory of the IBL and its growth relies on initial flow being in equilibrium with the underlying surface [*Elliott*, 1958]. The rate of IBL growth depends on surface roughness, with the IBL growing continuously until the entire boundary layer has adjusted to the underlying terrain [*Hirth*

et al., 2012]. The IBL height was determined by previous researchers through the identification of kinks in the vertical wind profile [e.g. *Deaves*, 1981]. These kinks (Figure 2.13) denote the intersect between upwind flow and modified flow after the roughness change. The area below the intersect is characterised as a transitional zone, with the lowest 10% believed to be in equilibrium with the underlying surface [*Wieringa*, 1993; *Hirth et al.*, 2012]. A simplified schematic overview of IBL growth is illustrated in Figure 2.13.
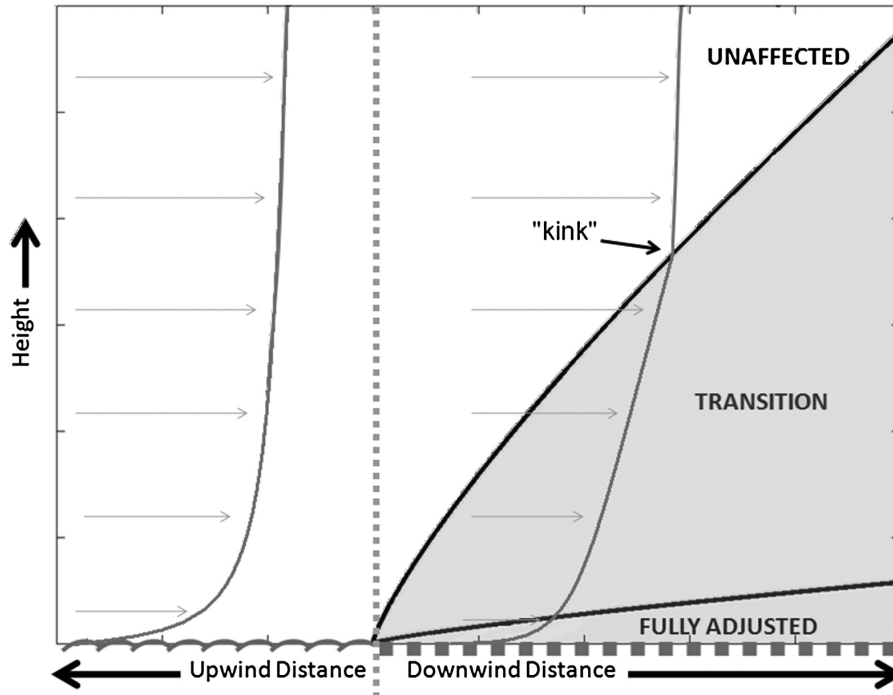
Figure 2.13: Schematic illustration of IBL development after a step change in surface roughness (dashed grey line) [*Hirth et al.*, 2012]

Equilibrium conditions or fully adjusted flow occurs when the downwind distance, referred to as fetch x, is sufficiently long that wind speeds at a given height are only dependent on the underlying terrain conditions [*Stull*, 1988]. To calculate fetch requirements for equilibrium conditions, *Wieringa* [1993] substituted the height of the IBL with $10z$ in the model of *Miyake* [1965], who originally conceptualised an approach that is based on the downwind diffusion of a pollutant plume from a surface source. It holds that

$$x = 2z_0 \left(\frac{10z}{z_0} \left[ln \frac{10z}{z_0} - 1 \right] + 1 \right) \qquad (2.15)$$

where a sufficient x is necessary to ensure that at a particular height z the flow is fully adjusted the underlying roughness z_0. However, *Wieringa* [1993] highlighted that simplifying Eq. 2.15 leads to the observation $x \approx 100z$. In reviewing earlier work, *Wieringa* [1993] also noted that the results of several wind field experiments conducted by *Gash* [e.g. 1986] aligned well with Eq. 2.15. *Gash* [1986] measured wind speeds at three 3.5 m towers deployed on heather ($z_0 = 0.05$ m) to infer the growth of the equilibrium layer downwind of a forest. He found that a fetch of about 400 m was

necessary for the flow to satisfy equilibrium conditions. As Eq. 2.15 also agreed reasonably well with several other studies [e.g. *Brooks*, 1961; *Hupfer*, 1978], *Wieringa* [1993] calculated pairs of height and surface roughness to easily infer the necessary fetch required for equilibrium conditions to be met, as shown in Figure 2.14.
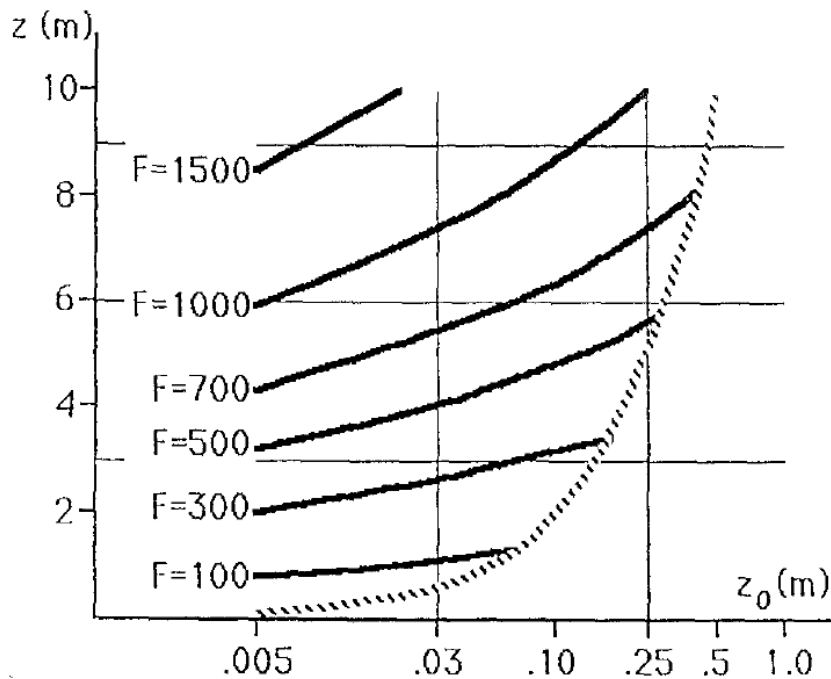
Figure 2.14: Minimum required fetch x (same as F above) for given height z and roughness z_0 [*Wieringa*, 1993]

At measurement heights of 10 m, calculations by *Wieringa* [1993] suggest about 1000 m of uniform fetch are required until equilibrium is reached. However, this method disregards influence of surface roughness upwind of the uniform fetch, which *Businger* [1986] showed to be important. Beyond the aforementioned studies, the impact of upstream roughness and fetch on turbulence characteristics has drawn very little attention, particularly in a TC environment. However, a recent study by *Miller et al.* [2015] investigated how variations in upstream roughness alter turbulence characteristics in a TC environment. Their quantitative approach included 11 towers deployed in open terrain with varying distances to rough upwind terrain during landfalling TCs between 1999 and 2008. *Miller et al.* [2015] found flow characteristics over a rough surface require about 1000 m to adjust to the new surface at 10 m measurement height, which matches the suggestion by *Wieringa* [1993]. More detail on this study is presented in Chapters 2.1.3.1 and 2.1.3.2. Following aforementioned studies, it is crucial to understand the relationship between upwind terrain features of the tower and measured turbulence in order to describe the near-surface wind field precisely.

For a precise description of near-surface winds, more detail on the wind and its components is required. *Stull* [1988] (among others) suggests the wind can be decomposed into three components - mean wind, waves, and turbulence (Figure 2.15). Each can exist in the PBL, but the mean wind dominates transport of moisture, heat, and momentum horizontally, while turbulence transmits these quantities vertically through the PBL [*Stull*, 1988].
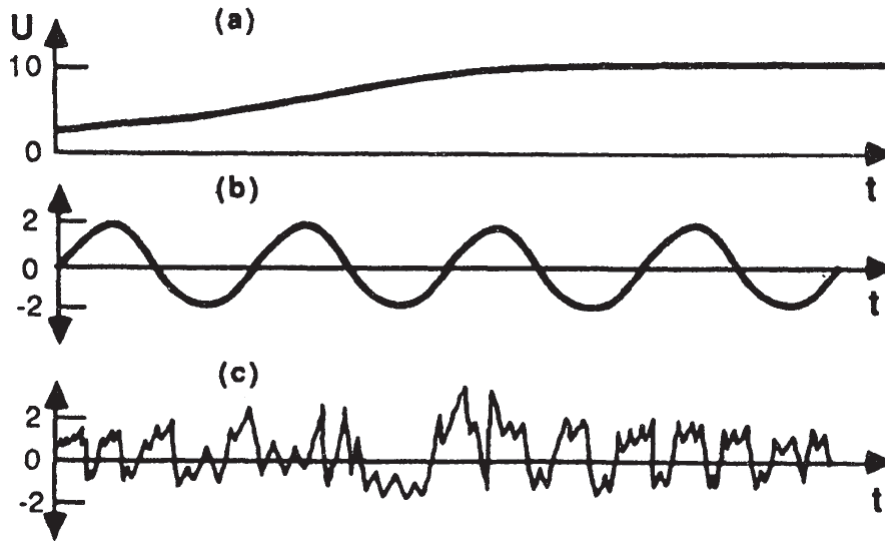
Figure 2.15: Three wind categories by *Stull* [1988]: a) mean wind, b) waves, c) turbulence. U denotes the wind component in x-direction.

Horizontal transport, or advection, primarily occurs through the mean wind, given stable conditions, vertical mean winds are small. Waves are responsible for transport quantities such as heat, humidity, momentum, and energy and they are generated locally through wind shear and flow over obstacles [*Stull*, 1988]. As friction slows mean winds near the surface, a high frequency of turbulence occurs at the ground which makes the PBL unique. *Stull* [1988] and *Holmes* [2015] both describe turbulence as "gustiness" superimposed on the mean wind, which consists of irregular swirls of motion referred to as eddies. Eddies vary in size, ranging from a few millimetres to the depth of the PBL, and strength. The superposition of these eddies characterises turbulence. In the study of turbulence, wind is mathematically expressed as a random atmospheric process that can be described through the sum of its time averaged mean $\bar{U}$, and fluctuating components $U'(t)$, as shown in Eq 2.16. Here, the fluctuating component is assumed to represent the turbulent fluctuations and the contribution of waves is assumed negligible [*Stull*, 1988].

$$U(t) = \bar{U} + U'(t) \tag{2.16}$$

The bulk of PBL turbulence originates from forcings near the surface, e.g. solar heating or wind shear. Trees and buildings also act as obstacles that deflect the wind flow causing turbulent wakes. It is through the process of turbulence that the PBL responds to changes in surface forcings.

It is difficult to accurately define eddy size and their scale of motion in the PBL. Therefore, *Taylor* [1938] proposed that given the advection velocity of an eddy is greater than the turbulence velocity itself, changes in wind speed (or temperature, Figure 2.16) at a fixed point occur due to the passage of an unmodified pattern of turbulent motion over the point. This principle is known as *frozen turbulence*.
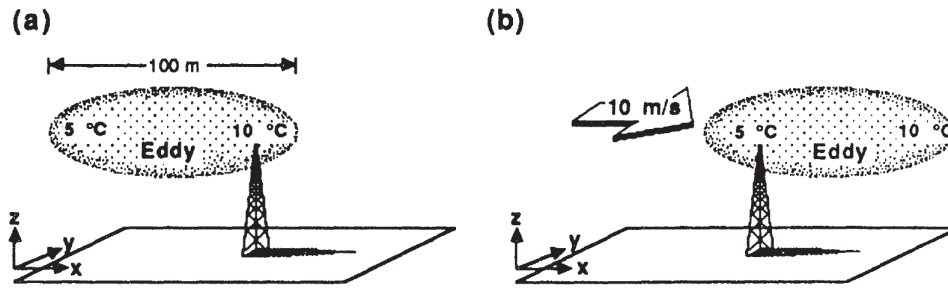
Figure 2.16: Taylor's hypothesis of a *frozen* eddy. a) A 100 m in diameter eddy with a 5 K temperature difference. b) The same eddy moved to the right 10 s later with a wind speed of 10 m/s [*Stull*, 1988].

Using this conceptual framework, wind speed could then be used to translate turbulence measurements as a function of time to their corresponding measurements in space [*Stull*, 1988]. An example of Taylor's hypothesis is shown in Figure 2.16 [*Stull*, 1988], where a 100 m diameter eddy exhibits 10°C at the front side. Given a wind speed of 10 m/s, a sensor would measure 5°C at the trailing side 10 s later, assuming the eddy is advected while its size and characteristic parameters remain constant. This fundamental work allows to directly infer turbulence characteristics from wind speed recording and is applied in this work as well.

To better understand the influence of land surface conditions on the near-surface turbulent flow, the following subsections examine literature that describes and quantifies turbulence statistics, including turbulence intensity, gust factor, peak factor, skewness, kurtosis, and integral length scale measured during landfalling TCs. The mechanisms by which varying terrain conditions and storm-scale dynamics impact the aforementioned statistics is also explored.

2.1.3.1 Turbulence intensity

Standard deviation of wind speed, σ, as described in Eq. 2.17 is an important parameter used for describing turbulence [*Holmes*, 2015]:

$$\sigma = \sqrt{\frac{1}{T} \int_0^T \left(U(t) - \bar{U}\right)^2 dt} \tag{2.17}$$

This variable is then typically divided by the signal mean, $\bar{U}$, to provide a measure of turbulence, termed the turbulence intensity I. This parameter is typically divided into its three vectorial components

$$I_u = \sigma_u/\bar{U} \tag{2.18}$$

$$I_v = \sigma_v/\bar{U} \tag{2.19}$$

$$I_w = \sigma_w/\bar{U}, \tag{2.20}$$

where I_u, I_v, and I_w are the longitudinal, lateral, and vertical turbulence intensities, respectively [*Holmes*, 2015]. The magnitude of turbulence intensity at any given location is dependent on the local and upwind roughness and elevations [*Stull*, 1988; *Holmes*, 2015]. This can be shown mathematically by substituting the logarithmic law (Eq. 2.21)

$$\bar{U}(z) = \frac{u_*}{\kappa} \, log_e(z/z_0) \tag{2.21}$$

into Eq. 2.18. In Eq. 2.21 u_* is the friction velocity, κ the von-Karman constant, which has been found experimentally to be about 0.4, z_0 the roughness length and z the height above the ground [*Holmes*, 2015]. Under the condition of neutral atmospheric stability one can assume $\sigma_u \approx 2.5u_*$ [*Schroeder and Smith*, 2003], leading to the relationship

$$I_u = \frac{1}{ln(z/z_0)}. \tag{2.22}$$

While $\sigma_u \approx 2.5u_*$ is commonly used in reviewed literature, analysis by *Miller et al.* [2015] revealed considerable σ_u/u_* variations ranging from 2.00 to 5.24 for FCMP measurements at 5 m and 10 m heights. Using Eq. 2.22 it is clear that higher surface roughness values z_0 will induce higher turbulence intensities and similarly an increase in elevation z will decrease this value [*Schroeder and Smith*, 2003; *Yu and Gan Chowdhury*, 2009; *Holmes*, 2015].

Early studies of the turbulence intensity in landfalling TCs have been limited largely to the last two decades. Some researchers investigated TCBL near-surface wind flow characteristics before this [e.g. *Choi*, 1978; *Ishizaki*, 1983; *Wu and Chiu*, 1983; *Schroeder et al.*, 1998] and observed an inverse relationship between turbulence intensity and mean wind speed. *Choi* [1978] found about 50% higher longitudinal turbulence intensities in the vicinity of a TC compared to those measured in extratropical regions. Longitudinal and lateral turbulence intensities were also examined by *Schroeder et al.* [1998] during the passage of Hurricane Bob (1991). The authors defined three separate flow regimes, offshore, transitional, and onshore when analysing wind measurements at 19 m height from a Field Research Facility. Here, the term "transitional" refers to measurements at a site that has insufficient distance between it and a change in roughness for an IBL to grow to the measurement height [*Schroeder et al.*, 1998]. In the offshore flow, I_u values reached up to 16.9%, while I_v exhibited values up to 13.7%. Both components were found to be around 4% and 5% lower for transitional and onshore flow, respectively. In subsequent research, *Schroeder and Smith* [2003] analysed horizontal and vertical wind speeds measured at elevations of approximately 3 m, 6 m, and 11 m by a Wind Engineering Mobile Instrumented Tower Experiment (WEMITE) site during Hurricane Bonnie (1998). Both longitudinal and lateral turbulence intensities exhibited a peak of 35% and 42% at 11 m elevation, respectively, caused during a temporary change in wind speed and direction. Furthermore, a ratio of $I_v/I_u = 0.92$ was found during the first part of the storm for airport exposure. Further study of the type of exposure and underlying roughness was undertaken by *Schroeder et al.* [2009]. The authors examined turbulence intensities relative to changes in surface roughness using 10 m observations from 8 individual tower deployments during 1998-2005 Atlantic Hurricane Seasons. To

explore the importance of surface roughness, four z_0 groups shown in Table 2.2 were introduced using a combined method of calculated turbulence intensities and areal imagery [*Wieringa*, 1993].

Roughness Regime	z_0 [m]
Smooth	$0.005 \leq z_0 \leq 0.0199$
Open	$0.020 \leq z_0 \leq 0.0499$
Roughly Open	$0.050 \leq z_0 \leq 0.0899$
Rough	$0.090 \leq z_0 \leq 0.1899$

Table 2.2: Roughness regimes and their associated roughness length [*Schroeder et al.*, 2002, 2009]

The authors noted increasing longitudinal turbulence intensities with increasing roughness, while I_u decreased with higher wind speeds. Similar results were obtained by *Masters et al.* [2010] who utilised the Florida Coastal Monitoring Program (FCMP, *Balderrama et al.* [2011]) dataset to investigate the turbulence intensity behaviour during three notable hurricanes in 2005, namely Katrina, Rita, and Wilma. This study revealed that the eyewall passage did not significantly affect turbulence intensities. In fact, this work showed that irrespective of position within the storm, turbulence intensity primarily depends on the roughness of the upwind terrain. In particular, mean I_u and I_v were found to reach 16.8% and 12.4% in relatively smooth terrain (0.01 m $\leq z_0 \leq$ 0.03 m), and 23.2% and 17.8% in rougher exposure (0.07 m $\leq z_0 \leq$ 0.13 m).

Similar results were found by *Miller et al.* [2015], who again showed that upstream surface roughness is the prevailing contributor to the observed variability of turbulence intensities noted for sites with similar roughness regimes. To explore this further, *Miller et al.* [2015] chose one tower deployed in a car park near to the beach during tropical storm Irene (1999). At this site, *Miller et al.* [2015] identified three 30° wide wind direction bins with varying distances to the coastline, whereas the distances were based on areal imagery. Figure 2.17 shows the variation of along- and across-wind component of the turbulence intensity I_u, I_v at 10 m measurement height with respect to the distance from the coastline.
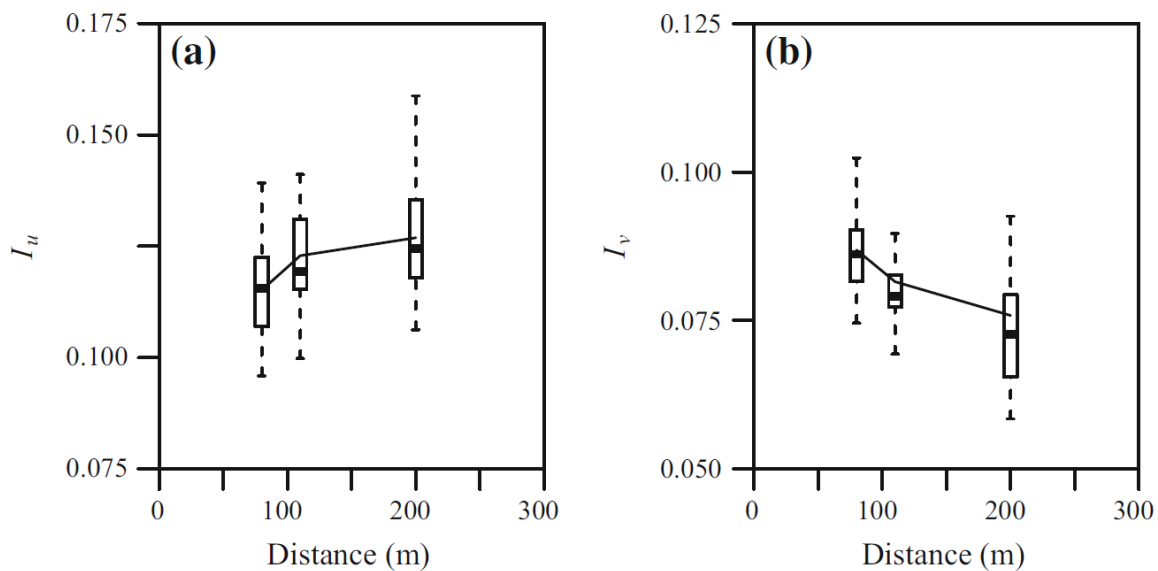
Figure 2.17: Variation of 10 m (a) I_u and (b) I_v with distance from open water. Mean values are represented by solid lines and the variability by boxplots [*Miller et al.*, 2015]

In exploring the upstream terrain impacts on I_u, I_v, *Miller et al.* [2015] noted increasing I_u with longer distances as the flow transitioned from a smooth to a rough surface. However, I_v showed a decreasing trend over the same distance. The authors expanded their investigation of upstream terrain impacts on turbulent characteristics by including 11 more measurement sites. These measurement sites were near an airfield in open grassland with varying distances (for each 30° wind direction bin) to rougher upwind terrain, which was composed of either tall trees or suburban terrain based on areal imagery [*Miller et al.*, 2015]. Figure 2.18 shows the variation of I_u and I_v with distance over the transition from (sub-) urban terrain to open grassland.
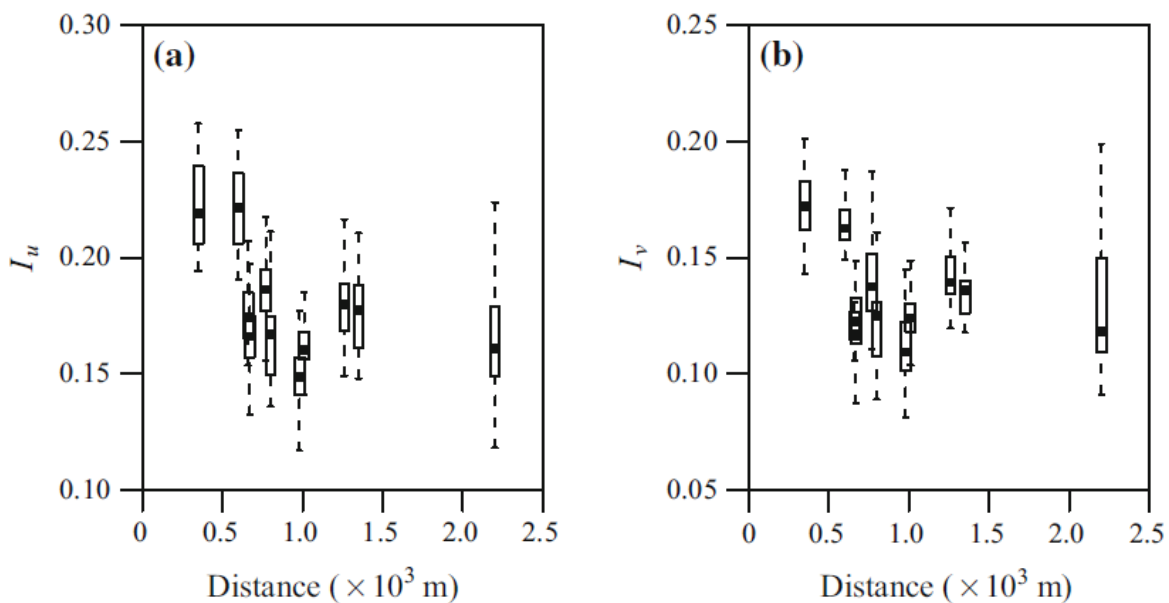
Figure 2.18: Variation of (a) I_u and (b) I_v with distance for the transition from (sub-) urban terrain to open terrain. Mean values are represented by solid lines and the variability by boxplots [*Miller et al.*, 2015].

29

As expected, both turbulence intensity components decrease with increasing distance to the roughness change as transition occurs from a rough to a smooth terrain [*Miller et al.*, 2015]. The authors further noted that turbulence intensities seem to be in equilibrium with the underlying terrain at a distance of 1000 m between tower and roughness change, which agrees with previous findings by *Wieringa* [1993].

2.1.3.2 Gust Wind Speed Parameters

In 1960, *Durst* [1960] introduced the so-called gust factor G. It is now widely used in the wind engineering community to describe the ratio between a maximum gust $\hat{U}$ within a given time period and its mean $\bar{U}$ [*Miller*, 2011].

$$G = \frac{\hat{U}}{\bar{U}}. \tag{2.23}$$

The magnitude of gust factor varies in different environments as both its components are dependent on height, topography and underlying terrain conditions [*Schroeder and Smith*, 2003; *Paulsen and Schroeder*, 2005; *Balderrama et al.*, 2012]. Moreover, *Schroeder and Smith* [2003] found 10-min mean 2-sec gust factors to be around 1.55 in open exposure ($z_0 \approx 0.04$ based on turbulence calculations) and 1.85 in rougher regime. *Paulsen and Schroeder* [2005] and *Schroeder et al.* [2009] confirmed these results by categorising gust factors into the four roughness regimes as shown in Table 2.2. Mean 2-sec Gust factors were 1.49 in open terrain ($0.020 \leq z_0 \leq 0.0499$), whereas G reached higher values in rougher terrain as indicated by Figure 2.19 [*Paulsen and Schroeder*, 2005].
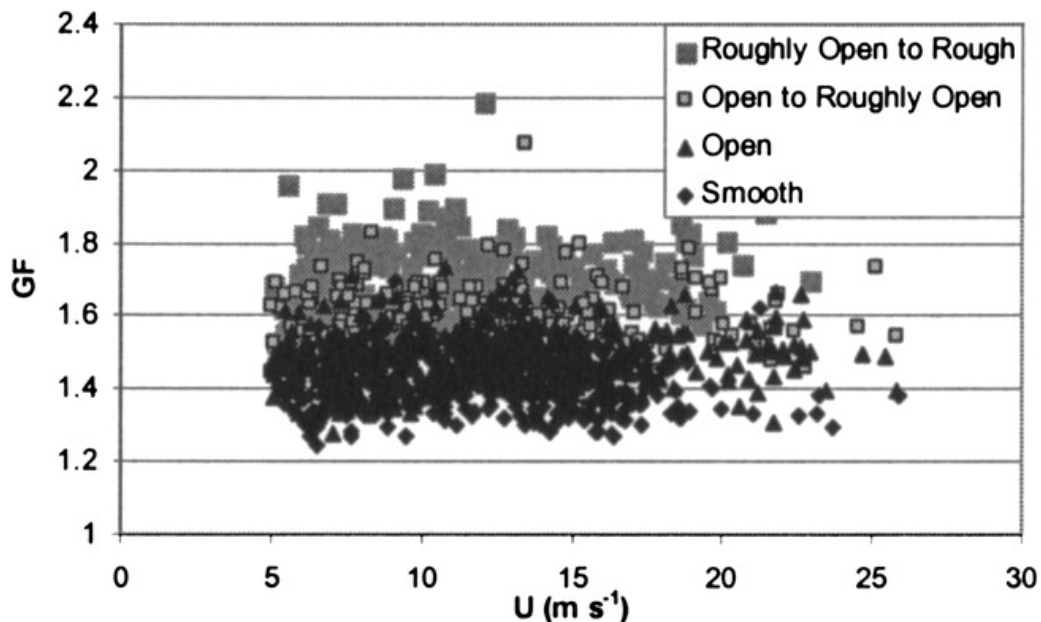
Figure 2.19: Variation of mean G with mean wind speed for different roughness regimes [*Paulsen and Schroeder*, 2005].

Within each roughness regime, gust factors were found to show minor variations with increasing mean wind speed [*Paulsen and Schroeder*, 2005; *Schroeder et al.*, 2009]. Furthermore, *Masters et al.*

[2010] examined the relationship between gust factors and turbulence intensities from surface TC wind observations at 10 m height. The authors showed increasing 15-min mean 3-sec gust factors with increasing turbulence intensities and thus inferred a linear relationship.

As well as investigating turbulence intensity (Chapter 2.1.3.1), *Miller et al.* [2015] investigated the influence of upstream surface roughness on changes in the observed gust factors. Figure 2.20 shows the 3-sec moving average along- and across-wind gust factor G_u, G_v for one tower deployed in a car park in close proximity to the beach during tropical storm Irene (1999).
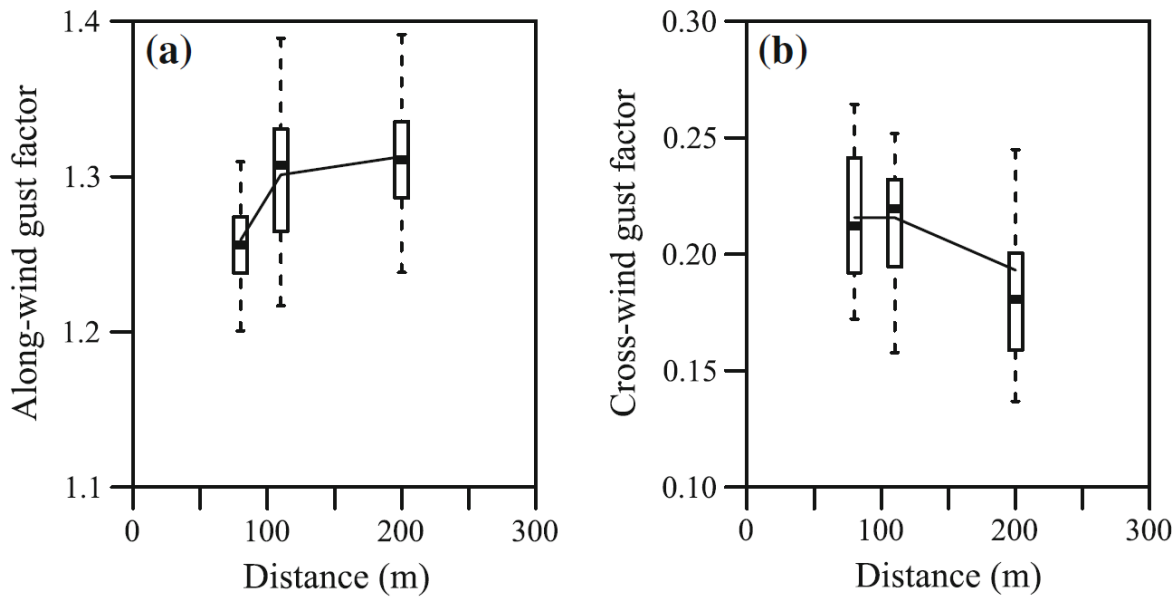
Figure 2.20: Variation of (a) G_u and (b) G_v with distance from open water. Mean values are represented by solid lines and the variability by boxplots [*Miller et al.*, 2015]

Along-wind gust factors G_u in Figure 2.20 exhibited an increase as distance to the coastline become greater, while G_v remained almost constant up to 110 m before decreasing. In good agreement with results presented in Figure 2.20, *Giammanco et al.* [2016] found gust factors to be below 2.00 in open terrain. Similar to the investigation of turbulence intensities at varying distances, *Miller et al.* [2015] expanded their research on the influence of different distances to the roughness change on gust factors. Figure 2.21 shows the variation of 3-sec G_u and G_v with distance over the transition from (sub-) urban terrain to open grassland.
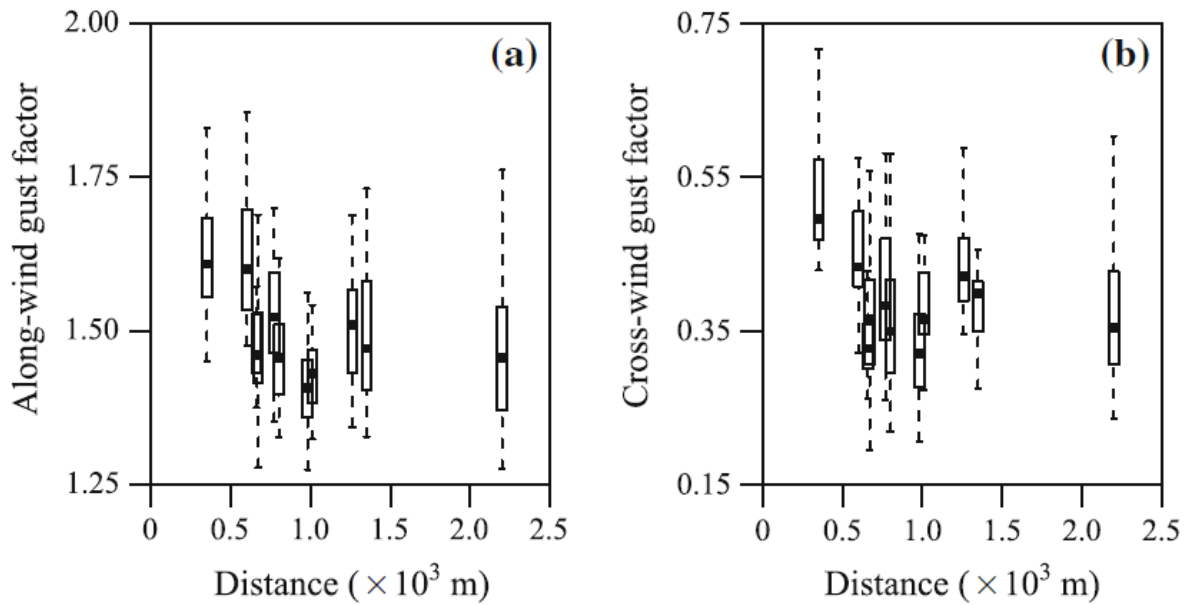
Figure 2.21: Variation of (a) G_u and (b) G_v with distance for the transition from (sub-) urban terrain to open terrain. Mean values are represented by solid lines and the variability by boxplots [*Miller et al.*, 2015].

Observed along- and across-wind components with increasing distance to the change in roughness exhibit a similar pattern to that observed for turbulence intensities (Figure 2.18) with smaller G_u and G_v being evident with increasing distance.

In an attempt to investigate gust factors based on the gust averaging time, *Durst* [1960], *Deacon* [1965], *Schroeder and Smith* [2003], and *Masters et al.* [2010] showed that G varies with respect to both peak and mean averaging time windows employed. The gust factor behaviour in TCs has been reviewed in great detail by *Harper et al.* [2010] who considered numerous studies that give credence to the dependency on height, topography and surface roughness. Figure 2.22 illustrates the gust factor dependency on the turbulence intensity and the gust duration.
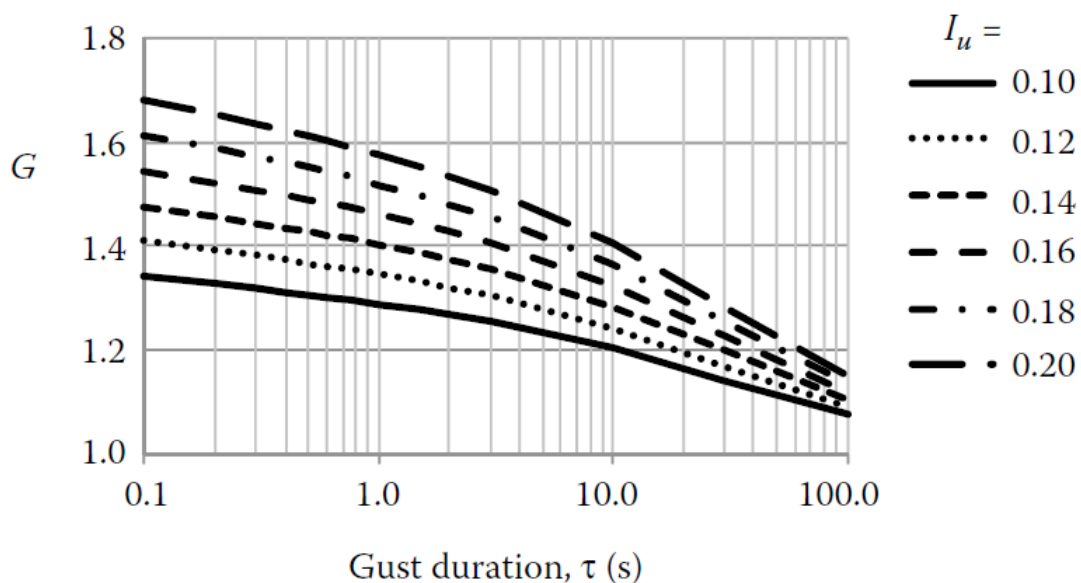
Figure 2.22: Gust factor (G) dependency for different turbulence intensities (I_u) and gust durations τ for a sample time T of 600 s [*Holmes*, 2015]

Figure 2.22 shows the selection of τ determines the magnitude of G as higher frequency gusts are "averaged out" for longer gust durations. It is also evident that as I_u increases, so too does the gust factor [*Harper et al.*, 2010]. The two can be linked using Eqs. 2.23 and 2.24

$$\hat{U} = \bar{U} + g\sigma_u \tag{2.24}$$

$$G = 1 + gI_u \tag{2.25}$$

where g is the peak factor introduced by *Davenport* [1964]. By definition, g is the expected number of standard deviations that the largest peak within a time period T is statistically expected to lie above the mean wind speed [*Harper et al.*, 2010; *Balderrama et al.*, 2012]. Similar to the gust factor, g varies with respect to averaging time, anemometer response characteristics, turbulence intensity, wind speed distribution, and terrain [*Masters et al.*, 2010; *Balderrama et al.*, 2012].

Only a small number of studies addressed the behaviour of g in landfalling TCs. *Balderrama et al.* [2012] conducted an extensive investigation of the nature of extreme gust values during 64 deployments in 19 storms from 1999-2008. A key objective of their work was to assess theoretical model approaches of a Gaussian [*Davenport*, 1961] and non-Gaussian peak factor distribution [*Kareem and Zhao*, 1994]. Using random process theory, *Davenport* [1961] originally proposed a Gaussian peak factor relationship for a moving average gust duration that approaches zero, which can be written as

$$g(\tau \to 0, T \geq 1h) = \sqrt{2ln(\nu T)} + \frac{\gamma}{\sqrt{2ln(\nu T)}} \tag{2.26}$$

where $\gamma = 0.5772$ denotes the Euler constant, ν is the zero up-crossing rate, which can be estimated using Eq. 2.27, and T is the duration of the averaging block.

$$\nu^2(\tau, T) = \frac{\int_0^\infty f^2 S_{uu}(f)\chi^2(f)df}{\int_0^\infty S_{uu}(f)\chi^2(f)df} \tag{2.27}$$

$$\chi^2(f) = \left(\frac{1}{1 + (2\pi f\gamma/U)^2}\right)\left(\left[\frac{sin(\pi f\tau)}{\pi f\tau}\right]^2 - \left[\frac{sin(\pi fT)}{\pi fT}\right]^2\right) \tag{2.28}$$

In Eq. 2.27, f is the frequency, S_{uu} is the one-sided power spectral density function, and χ^2 denotes a filter function that covers mechanical filtering and segmental or moving gust filtering [*Balderrama et al.*, 2012]. Recent work by *Balderrama et al.* [2012] used these equations to show that the Gaussian peak factor assumption at 5 m and 10 m elevations does not hold as skewness and kurtosis increase with longitudinal turbulence intensity and therefore causes errors into peak gust estimation when using the method of *Davenport* [1961]. Better estimates of g were found when incorporating values of skewness γ_s, and kurtosis γ_k into the non-Gaussian model of *Kareem and Zhao* [1994]. The non-Gaussian model approach involves a moment-based Hermite transformation and depends on crossing

rate ν, skewness γ_s and kurtosis γ_k. For $\gamma_s = 0$ and $\gamma_k = 3$ (i.e. a Guassian distribution) Eq. 2.29 collapses to Eq. 2.26.

$$g_{NG} = \alpha \left[(\beta + \gamma/\beta) + h_3(\beta^3 + 2\gamma - 1) + h_4[\beta^3 + 3\beta(\gamma - 1) + (3/\beta)((\pi^2/12) - \gamma + \gamma^2/2))] \right] \tag{2.29}$$

along with

$$\alpha = \frac{1}{\sqrt{1 + h_3^2 + 6h_4^2}} \tag{2.30}$$

$$\beta = \sqrt{2ln(\nu T)} \tag{2.31}$$

$$h_3 = \frac{\gamma_s}{4 + 2\sqrt{1 + 1.5(\gamma_k - 3)}} \tag{2.32}$$

$$h_4 = \frac{\sqrt{1 + 1.5(\gamma_k - 3)} - 1}{18} \tag{2.33}$$

Balderrama et al. [2012] focused on open terrain exposed wind measurements. However, to understand higher turbulence intensity regimes, additional wind field measurements in suburban terrain are required.

2.1.3.3   Skewness and Kurtosis

The distribution of the fluctuating wind component can be characterised by the statistical moments, skewness and kurtosis. The traditional approach to calculate the skewness γ_s [*Wilks*, 2005] is given

$$\gamma_s = \frac{\frac{1}{n-1} \sum_{i=1}^{n} (x_i - \bar{x})^3}{\sigma^3}, \tag{2.34}$$

with n denoting the sample size, x_i the sample data, and $\bar{x}$ the sample mean. The same nomenclature applies to the fourth standardised moment, also referred to as kurtosis γ_k:

$$\gamma_k = \frac{\frac{1}{n-1} \sum_{i=1}^{n} (x_i - \bar{x})^4}{\sigma^4} \tag{2.35}$$

In case of a normal distribution, expected skewness and kurtosis values are 0 and 3, respectively.

As wind speed is physically constrained to non-negative values, wind data is often positively skewed [*Wilks*, 2005]. A positively skewed wind distribution is more likely to contain more extreme gusts in comparison to a Gaussian distribution [*Balderrama et al.*, 2012]. With σ included in both statistical parameters (Eq. 2.34, 2.35), *Balderrama et al.* [2012] found that skewness and kurtosis exhibit an upwind terrain roughness dependency. Thus, both wind distribution parameters increased with I_u.

Average skewness and kurtosis values were shown to be $\gamma_s = 0.26$ and 0.32 and $\gamma_k = 2.90$ and 2.96 for open and suburban terrain, respectively [*Balderrama et al.*, 2012]. In a subsequent study, *Fernández-Cabán and Masters* [2017] expanded the work of *Balderrama et al.* [2012] through the inclusion of field measurements in suburban terrain during landfalling TCs at five levels ranging from 5-15 m and boundary layer wind tunnel (BLWT) flow data. Figures 2.23 and 2.24 show boxplots of 15-min block-averaged longitudinal skewness γ_{su} and kurtosis γ_{ku} at 5 m and 10 m for three wind speed bins obtained from TC surface wind measurements. The letters inside the boxes denote the roughness regime, whereas B = suburban (0.15 m $> z_0 \geq 0.7$ m), C = open country (0.01 m $> z_0 \geq 0.15$ m), and D = very smooth ($z_0 < 0.01$ m).
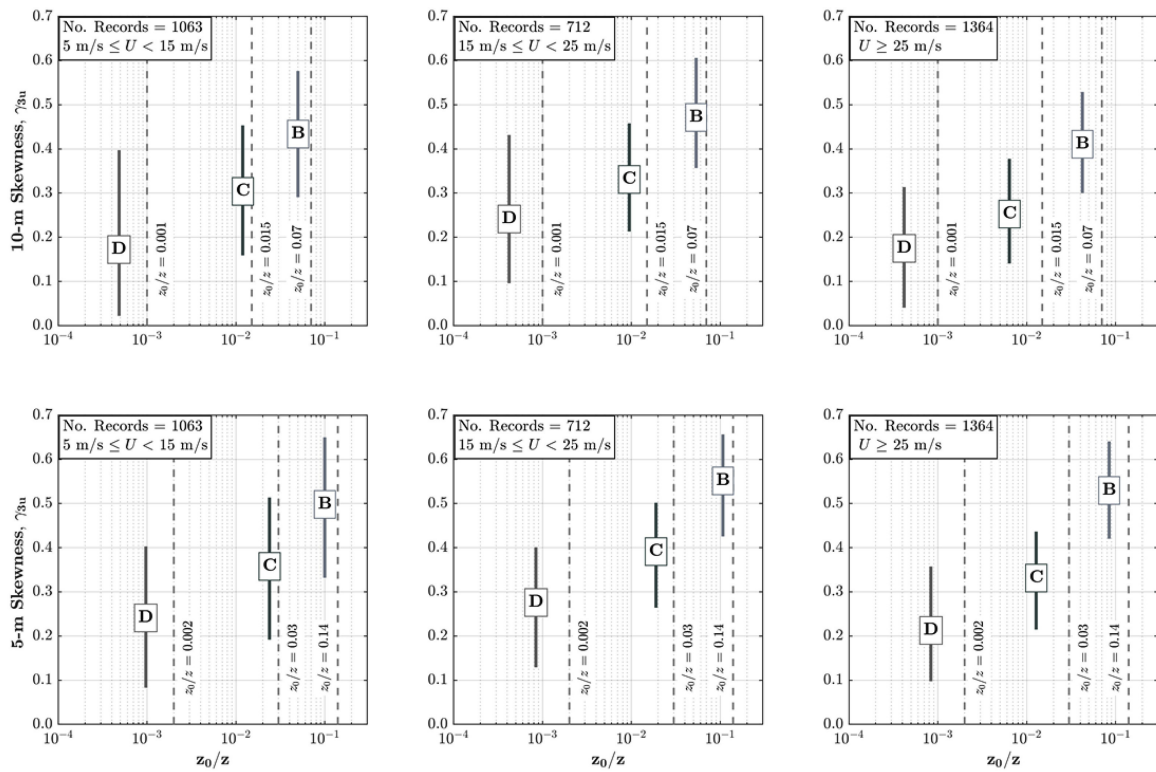
Figure 2.23: Observed mean longitudinal skewness segregated into wind speed bin and roughness regime at 10 m and 5 m [*Fernández-Cabán and Masters*, 2017]
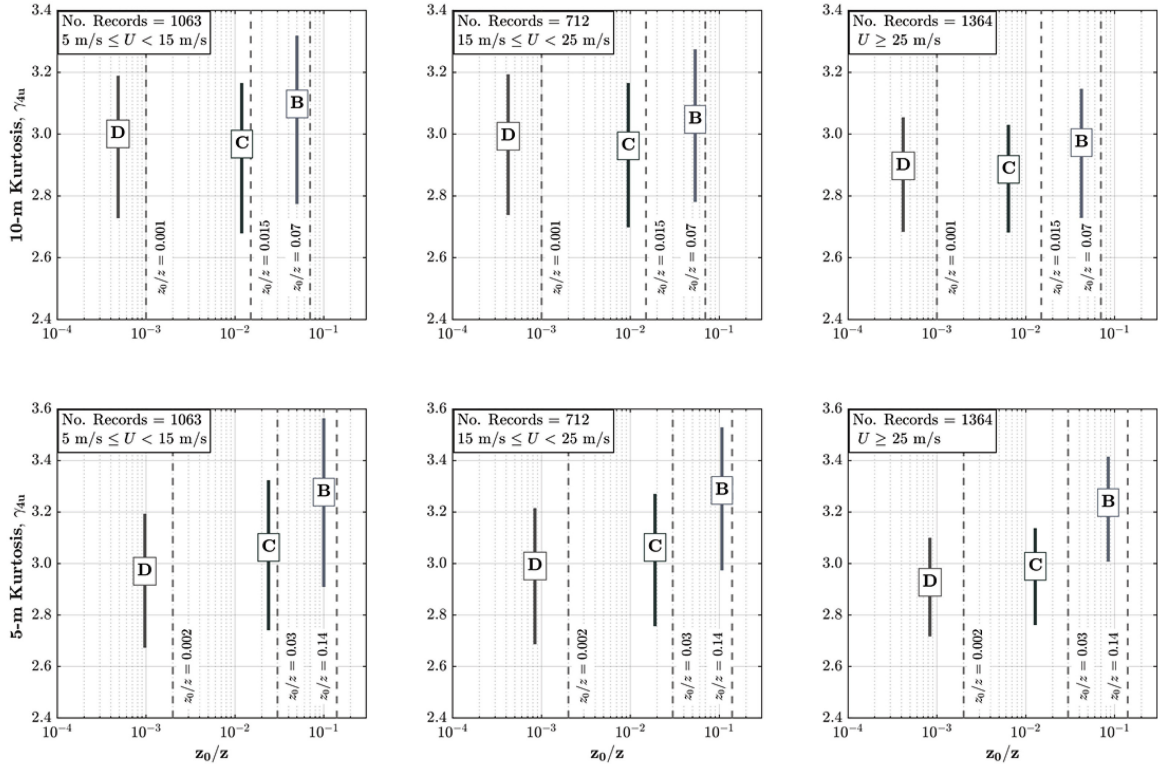
Figure 2.24: Observed mean longitudinal kurtosis segregated into wind speed bin and roughness regime at 10 m and 5 m [*Fernández-Cabán and Masters*, 2017]

Fernández-Cabán and Masters [2017] found measured TC wind speeds to be positively skewed independent of the magnitude of the wind speed and the underlying terrain. However, skewness values decrease with smoother terrain. Larger skewness values were observed at 5 m compared to those obtained at 10 m measurement height for all roughness regimes [*Fernández-Cabán and Masters*, 2017]. The kurtosis fluctuates around a value of 3.0 with no significant trend evident at both measurement height.

In the discussion of non-Gaussian trends within the roughness sublayer, *Fernández-Cabán and Masters* [2017] introduced an equivalent exposure coefficient K_{zNG} defined as

$$K_{zNG} = \left(\frac{U_{gNG}(z)}{U_{g,ref}} \right) \text{ with} \tag{2.36}$$

$$U_{gNG}(z) = U(z) \left[1 + g_{NG} I_u \right]. \tag{2.37}$$

In these equations, $U_{gNG}(z)$ is the gust velocity profile, $U_{g,ref}$ the 3-sec gust velocity at 10 m in open exposure ($z_0 = 0.02$ m), $U(z)$ the mean velocity profile, and g_{NG} the non-Gaussian peak factor as defined in Eq. 2.29. Skewness values measured in TCs and the BLWT were then combined with the non-Gaussian model approach to calculate the exposure coefficient. Figure 2.25 shows the vertical K_{zNG}-profile along with mean FCMP skewness observations over suburban terrain (horizontal grey lines) and BLWT skewness measurements. BLWT skewness values range between 0.2 and 0.5 up to 5 m with noticeably lower skewness values trending towards zero with higher elevations [*Fernández-Cabán and Masters*, 2017]. The authors further identified a $\sim 14\%$ increase in suburban exposure

coefficient values at 10 m height compared to those provided in the Minimum Design Loads for Buildings and Other Structures by the American Society of Civil Engineers (ASCE 7-10).
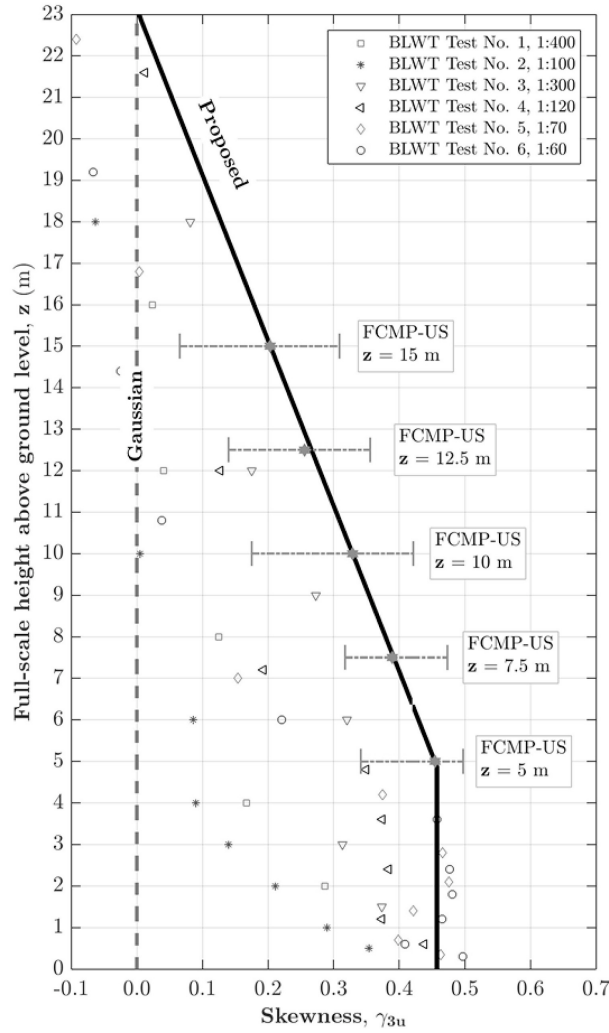
Figure 2.25: Non-gaussian exposure coefficient K_{zNG} versus height z [*Fernández-Cabán and Masters*, 2017].

2.1.3.4 Integral Length Scale

Following *Kolmogorov* [1941], turbulent flow can be thought of containing a range of different eddy sizes. The mean size of these eddies in the along-wind direction is referred to as its integral length scale L. Literature provides several approaches to calculate L, with the most common approach, as presented in *Yu et al.* [2008] and *Masters et al.* [2010],

$$L = \bar{U} \int_0^\infty \rho_{uu}(t_l) dt_l \tag{2.38}$$

where ρ_{uu} is the autocorrelation function of the wind speed sample with the mean wind speed $\bar{U}$ and time lag t_l [*Yu et al.*, 2008]. The longitudinal, lateral and vertical integral length scales (L_u,L_v,L_w) can be determined using Eq. 2.38 for each wind speed component.

Estimates of L during landfalling TC events were made using measurements from the FCMP [*Balderrama et al.*, 2011] and StickNet [*Weiss and Schroeder*, 2008] platforms. *Yu et al.* [2008] and *Masters et al.* [2010] both found that L increases with increasing averaging time and measurement height and exhibits larger values over the sea than over open terrain [*Yu et al.*, 2008]. *Masters et al.* [2010] calculated maximum horizontal length scales of up to 1200 m at 10 m measurement height. Also, *Masters et al.* [2010] results indicate no significant relationship between the longitudinal integral length scale and the gust wind speed.

2.1.4 Engineering Models

Understanding variability of wind in the PBL is important for building design requirements [*ESDU*, 1982]. As such, a number of models have been developed to estimate how both mean wind and its associate turbulence is modified in response to changes in underlying surface roughness. Although these models were originally developed for the PBL, this thesis sets out to explore how they perform in a TC environment.

2.1.4.1 The Engineering Sciences Data Unit Model

The ESDU model estimates maximum gust speed, turbulence intensity, and gust components at a site downwind of changes in surface roughness. To achieve this, the ESDU model determines a maximum expected gust with averaging time τ for a given hourly-mean wind speed V_z in a neutral boundary layer [*ESDU*, 1982, 1983]. The expected hourly-mean wind speed is dependent on the height above the ground (at the deployed tower), the surface roughness, and any roughness changes in the upwind direction [*ESDU*, 1982]. Combined with the mean observation interval T_0, turbulence intensity, gust factor, and the maximum expected gust at a site can also be calculated [*ESDU*, 1983]. Determined wind statistics are notionally valid for heights from the ground level to the upper edge of the PBL [*ESDU*, 1983]. Furthermore, the ESDU procedure is suitable for wind speeds greater than 10 m/s in fully-developed weather systems assuming neutral atmospheric conditions. The neutral approximation implies turbulent fluctuations in the PBL are modified only by changes in surface roughness rather than thermal effects [*Powell et al.*, 2003].

Calculation Procedure for Single Terrain Changes

Figure 2.26 illustrates the transition at step change B from upwind surface roughness z_{01} to surface roughness z_0 at site A. Calculations given in *ESDU* [1982] and *ESDU* [1983] provide a method for estimating smooth-to-rough and rough-to-smooth transitions. It is assumed that the wind flow is in equilibrium with the underlying surface upwind (z_{01}) of the step change B. The ESDU model postulates equilibrium conditions to hold true only once $F > 50$ km of uniform terrain [*ESDU*, 1983].
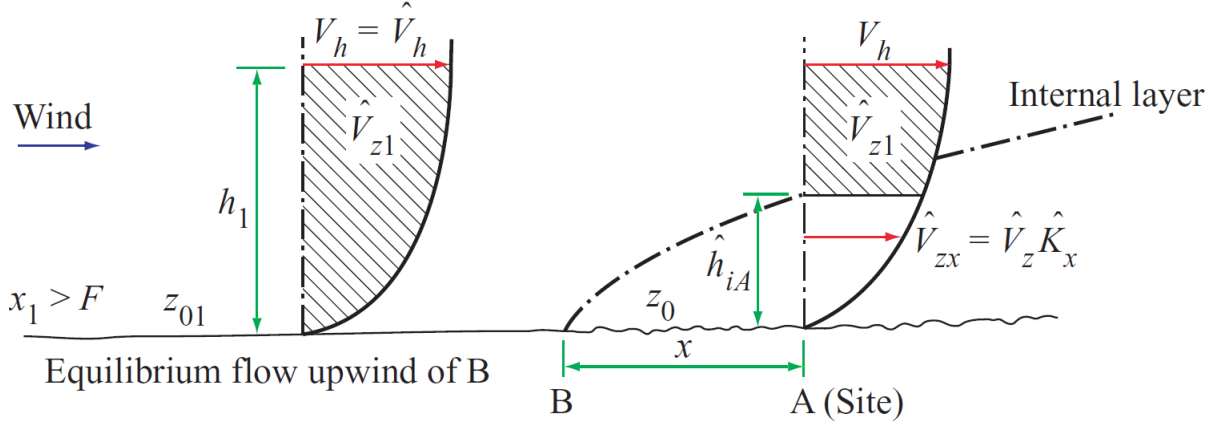
Figure 2.26: Single terrain change wind profiles at the site and upwind [*ESDU*, 1983].

Upwind of B, the vertical wind speed profile follows a logarithmic pattern to the top of the PBL h_1, which can extend up to 3 km [*Stull*, 1988], but is considerably lower in the TCBL (see Chapter 2.1). At h_1 the gradient wind speed V_h equals the maximum gust speed $\hat{V}_h$ because the influence of turbulence vanishes. The maximum gust speed $\hat{V}_{z1}$ below h_1 however, is influenced by turbulence. At B, an IBL forms below, where the turbulent characteristics are influenced by the underlying terrain. Above the IBL height $\hat{h}_{iA}$ the wind flow is assumed to be the same as upwind of the terrain change [*ESDU*, 1983]. Within the IBL, the expected maximum gust speed $\hat{V}_{zx}$ is dependent on an "equilibrium maximum gust" $\hat{V}_z$ and the gust fetch factor $\hat{K}_x$ that considers the previous roughness change and its effect on the mean-hourly wind speed (Eq. 2.39). It holds that

$$\hat{V}_{zx} = \hat{V}_z \hat{K}_x = V_z G \hat{K}_x \tag{2.39}$$

with the expected hourly-mean wind speed V_z

$$V_z = u * K_{z*} \text{, with} \tag{2.40}$$

$$K_{z*} = 2.5 \left[ln(z/z0) + 34.5 fz/u_* \right] \tag{2.41}$$

at the site and the gust factor G (compare to Eq. 2.23). The calculation of the gust fetch factor $\hat{K}_x$ is defined by

$$\frac{\hat{K}_x - 1}{K_x - 1} = 1 - a \cdot exp \left[-0.05 \tau^{0.65} \right] \tag{2.42}$$

where $a = 0.595$ or $a = 0.502$ for smooth-to-rough or rough-to-smooth transitions, respectively [*ESDU*, 1983]. Eq. 2.42 arises as a result from the fetch factor K_x (ratio between wind speed at the site and upwind wind speed given $x > F$), which is based on a method by *Deaves* [1980, 1981] assuming an eddy-viscosity closure for the full elliptic form of the Navier-Stokes equations [*ESDU*,

39

1982]. Deaves' procedure was applied to numerous roughness changes and obtained a range of universal curves, which were fitted with simple equations. These equations were further simplified in the ESDU model to account for non-equilibrium conditions due to changes in roughness upstream of a site. One simplification included correlating K_x values with changes in upwind roughness summarised in a parameter R, which is defined as

$$R = \frac{|ln(z_0/z_{01})|}{[u_*/fz_0]^n} \tag{2.43}$$

with Coriolis parameter $f = 1.458 \times 10^{-4} sin(\phi)$ (for a site at latitude ϕ) and $n = 0.23$ or $n = 0.14$ for smooth-to-rough (sr) or rough-to-smooth (rs) transitions, respectively [*ESDU*, 1982]. With the introduction of parameter R, K_x just depends on the fetch x using the equations

$$K_x = 1 + 0.67R^{0.85}f_{sr} \qquad \text{smooth-to-rough} \tag{2.44}$$

$$K_x = 1 - 0.41Rf_{rs} \qquad \text{rough-to-smooth} \tag{2.45}$$

with fetch-dependent parameters f_{sr} and f_{rs} given (in terms of $X = log_{10} x$ meters) by

$$f_{sr} = \begin{cases} 0.1143X^2 - 1.372X + 4.087 & \text{for X} \leq 5.5 \\ 0 & \text{for X} > 5.5 \end{cases} \tag{2.46}$$

$$f_{rs} = \begin{cases} 0.0192X^2 - 0.550X + 2.477 & \text{for X} \leq 5.6 \\ 0 & \text{for X} > 5.6 \end{cases} \tag{2.47}$$

Considering parameters used in equations 2.44 and 2.45, the fetch factor K_x is height-independent up to height $\hat{h}_{iA}$, where V_{zx} equals V_{z1} (see Fig 2.26). Above $\hat{h}_{iA}$, it is believed that upwind changes in surface roughness do not affect the velocity profile [*ESDU*, 1982]. In ESDU model, V_{zx} is defined by

$$V_{zx} = V_z K_x \tag{2.48}$$

and describes the mean velocity at the tower. To obtain the turbulence intensity I_u at the tower, the gust and peak factor G and g are required. For a specific gust averaging time τ and observation period $T_0 < 3600$ s the gust factor is calculated through

$$G_{T_0} = \frac{[G_\tau]_{T_0}}{[G_\tau]_{T_0=1hr}}. \tag{2.49}$$

With respect to the peak factor g, *ESDU* [1983] uses the formulation by *Davenport* [1961] and a further simplification by *Wood* [1983] to determine

$$\frac{\hat{u}(\tau, T_0)}{\sigma_u(\tau, T_0)} = \sqrt{2ln\left[T_0\nu(\tau, T_0)\right]} + \frac{0.577}{\sqrt{2ln\left[T_0\nu(\tau, T_0)\right]}} \tag{2.50}$$

$$\frac{\sigma_u(\tau, T_0 = 1hr)}{\sigma_u} = 1 - 0.193 \left[\frac{T_u}{\tau} + 0.1\right]^{-0.68}, \text{ with} \tag{2.51}$$

$$\nu(\tau, T_0 = 1hr) = \left[0.007 + 0.213(T_u/\tau)^{0.654}\right]/T_u \text{ and} \tag{2.52}$$

$$T_u = 3.13z^{0.2}, \tag{2.53}$$

which leads to an equation of the peak factor g

$$g = \frac{\hat{u}(\tau, T_0)}{\sigma_u(\tau, T_0)} \frac{\sigma_u(\tau, T_0 = 1hr)}{\sigma_u}. \tag{2.54}$$

through the combination of Eqs. 2.50 and 2.51. Finally, the turbulence intensity at a given location is defined by

$$I_u = \frac{1}{g}\left[\frac{\hat{V}_{zx}}{V_{zx}G_{T_0}} - 1\right]. \tag{2.55}$$

The turbulence intensity estimation for multiple terrain changes also follows Eq. 2.55, however, the peak velocity $\hat{V}_{zx}$ at the measurement site (Eq. 2.39) changes due a different gust fetch factor $\hat{K}_x$, which is described below.

Calculation Procedure for Multiple Terrain Changes

In reality multiple roughness changes often occur in the immediate vicinity of a tower site. Thus, at each roughness change a new IBL forms that influences wind profile and gust speeds downwind of the change [*ESDU*, 1982]. To quantify this influence on wind profile and turbulence characteristics, the method for single terrain changes is expanded to multiple terrain changes in *ESDU* [1983].

The calculation procedure for an expected gust speed downwind of multiple roughness changes follows a multiplication of all gust fetch factors calculated for each terrain change. This procedure is based on the simplification that each roughness change and its effect on the wind profile can be examined separately and independently [*ESDU*, 1982]. Assuming equilibrium conditions at each roughness change, the downwind wind profile and gust speed are then calculated by using the procedure for single terrain changes. It holds that

$$\hat{V}_{xA} = V_z G \hat{K}_{x1} \hat{K}_x \tag{2.56}$$

where $\hat{K}_{x1}$ denotes the gust fetch factor for the roughness change z_{02} to z_{01}. Following the method for a single terrain change, R_j parameters have to be calculated given j roughness changes. In case of two roughness changes

$$R_1 = \frac{|ln(z_{02}/z_{01})}{[u_{*1}/fz_{01}]^n} \tag{2.57}$$

whereas the friction velocity u_{*1} is different after each j-th change in terrain by an additional factor of $[K_x]_{j-1}$ [*ESDU*, 1982].

The entire calculation procedure for multiple terrain changes involves 58 steps and can be found on page 22 of amendment C in *ESDU* [1983].

2.1.4.2 The Australian Standard AS/NZS1170.2 (2011)

Another wind engineering model that describes the transition of wind speed and turbulence intensity when flow moves from z_{01} to z_0 is provided in the Australian/New Zealand Structural Design Standard [*AS/NZS 1170.2:2011*, 2011]. This standard provides a simple fetch-weighted approach to estimating how these variables transition. To do this, a terrain/height multiplier $M_{z,cat}$ is introduced based on the following terrain categories shown in Table 2.3 [*AS/NZS 1170.2:2011*, 2011].

Terrain Category	z_0 [m]	Description
1	0.002	Exposed, open terrain with almost no obstructions
2	0.02	Water surfaces, open terrain, grassland with few, well-scattered obstructions having heights generally from 1.5 m to 10 m.
3	0.2	Terrain with numerous closely spaced obstructions of 3 m to 5 m high, such as areas of suburban housing.
4	2.0	Terrain with numerous large, 10 m to 30 m high and closely spaced obstructions, such as large city centres and well-developed industrial complexes.

Table 2.3: Roughness lengths and descriptions for terrain categories in AS/NZS1170.2 [*AS/NZS 1170.2:2011*, 2011]

The conversion between z_0 and the terrain category is defined by

$$z_0 = 2 \times 10^{\text{(Terrain category number - 4)}} \tag{2.58}$$

which allows intermediate z_0 and terrain categories not listed in Table 2.3 to be calculated. For each of the terrain categories the design standard provides specific $M_{z,cat}$ values for various measurement heights up to 200 m in cyclone-prone regions in Australia. Relevant for this thesis are $M_{z,cat}$ up to 10 m height, which are presented in Table 2.4.

z [m]	$M_{z,cat}$ **Cat 1**	$M_{z,cat}$ **Cat 2**	$M_{z,cat}$ **Cat 3**	$M_{z,cat}$ **Cat 4**
≤ 3	0.99	0.91	0.83	0.75
5	1.05	0.91	0.83	0.75
10	1.12	1.00	0.83	0.75

Table 2.4: Roughness lengths and descriptions for terrain categories in AS/NZS1170.2 [*AS/NZS 1170.2:2011*, 2011]

$M_{z,cat}$ values in Table 2.4 are valid for fully developed profiles. When flow transitions over surface conditions with different roughness values that lie within the averaging distance of 500 m, AS/NZS1170.2 prescribes $M_{z,cat}$ to be weighted by the length of each upwind terrain including the lag distance at each terrain change. The lag distance is defined by $20z$ in AS/NZS1170.2 [*AS/NZS 1170.2:2011*, 2011]. To determine the weighted $M_{z,cat}$, the following Eq. 2.59 is used:

$$M_{z,cat} = \frac{\sum_{i=1}^{n} M_{z,cat(i)} x_i}{\sum_{i=1}^{n} x_i} \tag{2.59}$$

where x_i is the length for each terrain category. To relate $M_{z,cat}$ to the turbulence intensity, AS/NZS1170.2 provides an overview of appropriate turbulence intensities depending on measurement height z and terrain category following Table 2.5 [*AS/NZS 1170.2:2011*, 2011].

z [m]	**TerCat 1**	**TerCat 2**	**TerCat 3**	**TerCat 4**
≤ 3	0.171	0.207	0.271	0.342
5	0.165	0.196	0.271	0.342
10	0.157	0.183	0.239	0.342

Table 2.5: Appropriate turbulence intensities for terrain categories 1-4 and measurement heights z as in AS/NZS1170.2 [*AS/NZS 1170.2:2011*, 2011]

To automate the process of calculating turbulence intensities using AS/NZS1170.2, information from Tables 2.3- 2.5 are connected through simple equations. This conversion procedure is described in more detail in Chapter 4.5.

2.2 Tropical Cyclone Numerical Modelling

2.2.1 Development of The Weather Research and Forecasting Model

TC numerical model development commenced in the early 1950's and 60's [e.g. *Eliassen*, 1949; *Haque*, 1952; *Syono*, 1953; *Charney*, 1955; *Charney and Eliassen*, 1964; *Ooyama*, 1964, 1969] in response to the technical revolution of reconnaissance aircraft flights that officially started on 17 July

in 1943 [*Sumner*, 1943]. During this time, the fundamental mathematics behind TC simulations were formulated and a solid foundation for the first two major TC genesis and intensification theories (conditional instability of the second kind (CISK) [*Charney and Eliassen*, 1964] and Ooyama's co-operative intensification theory [*Ooyama*, 1964]), were produced. Although these theories are similar (Figure 2.27), they were in fact developed independently. The main aim of both *Charney and Eliassen* [1964] and *Ooyama* [1964] was to explain storm development from a tropical depression into an intense TC with a focus on the role of surface friction. *Charney and Eliassen* [1964] focused on the mutual-supporting interaction between a cumulus cell and a tropical depression, which encompasses the heat energy provided by the cell while the vortex supplies low-level moisture convergence into the cumulus cell through friction. Although friction is usually recognised to inhibit vortex intensification through kinetic energy dissipation, *Charney and Eliassen* [1964] showed that frictional convergence in the moist surface layer acts to supply latent heat to the system. Figure 2.27 illustrates the primary mechanism of the CISK theory.
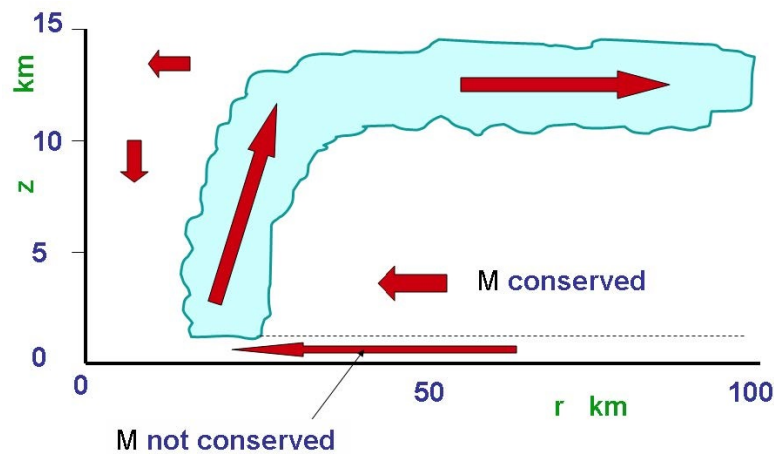
Figure 2.27: Schematic CISK TC intensification theory [*Montgomery and Smith*, 2014]

Figure 2.27 and Eq. 2.4 describe the basic principle of vortex spin-up as the absolute angular momentum based on the assumption that M_a is conserved above 1 km. Hence, v is inversely proportional to r, which means that an increase in v occurs if r decreases and vice versa. Therefore, for an axisymmetric vortex to spin-up, radial inflow above the frictional layer is required. This inflow conserves M_a and transports moist air that is subjected to frictional convergence in the TCBL. The strong convergence of moist air is a response to diabatic heating within a convective regime because the latent heat release leads to an upward flux that requires inflow below the middle to upper troposphere and outflow above [*Montgomery and Smith*, 2014]. In regions of inflow, the tangential wind is amplified by the Coriolis force at the top of the boundary layer [*Charney and Eliassen*, 1964; *Montgomery and Smith*, 2014]. Thus, the frictional inflow in the TCBL increases and is accompanied by an increase of moisture convergence. Basically, the CISK paradigm expresses that deep convection in a vortex environment produces inflow into the TCBL [*Charney and Eliassen*, 1964; *Montgomery and Smith*, 2014]. Ooyama's "cooperative intensification theory" [*Ooyama*, 1964, 1969] follows the same scheme, but the so-called closure problem, which is "the control of the convection by the vortex-scale flow" [*Craig and Gray*, 1996], was expressed differently. Ooyama expressed the closure problem in

terms of a convective mass flux (instead of convective heating as in *Charney and Eliassen* [1964]), which is proportional to the frictional convergence in the TCBL.

Using the concepts discussed above, *Charney and Eliassen* [1964] and *Ooyama* [1964] established the first two-dimensional numerical models of TCs. These were, however, unable to simulate the full life cycle of a TC. Building on the CISK TC intensification theory, *Anthes* [1972] introduced the first hydrostatic three-layer TC numerical model in the early 1970s. This model included the implementation of a water vapour cycle and the addition of a horizontally staggered grid, which allowed simulations on a 30 km horizontal grid of horizontal diffusion processes, spiral rain bands, and outflow layer asymmetries, supported by the implementation of a cumulus convection scheme. These improvements led to new insight into the TC water vapour budget and its role in TC development [*Anthes*, 1972]. Furthermore, the three-layer numerical model was more versatile, and its use was extended to study topics like air pollution and other mesometeorological studies valid on different scales [*Anthes and Warner*, 1978].

Subsequent research has improved the original three-dimensional, hydrostatic, predictive model of *Anthes and Warner* [1978]. Examples include the incorporation of an updated cumulus convection scheme [*Anthes*, 1977a,b], a description of mesoscale flows over complex terrain [*Anthes and Warner*, 1974; *Freeman*, 1974], modelling of PBL processes [*Busch et al.*, 1976; *O'Lenic*, 1976; *Chang*, 1977; *Blackadar*, 1978; *Oliger and Sundström*, 1978], and the first implementation of nested grids [*Harrison and Elsberry*, 1972; *Phillips and Shukla*, 1973; *Sobel*, 1976; *Miyakoda and Rosati*, 1977]. During the late 1970's, numerous tests of TC forecast skill, PBL scheme behaviour, and terrain influence on the (sub-) synoptic scale [e.g. *Warner et al.*, 1978; *Anthes and Keyser*, 1979; *Anthes et al.*, 1982, 1983; *Hsie and Anthes*, 1984; *Benjamin and Carlson*, 1986] were conducted to further refine the model. Developments at this time resulted in the formulation of the Penn State/National Center for Atmospheric Research (NCAR) Mesoscale Model Version 4 (hereafter MM4, *Anthes and Warner* [1987]).

Even in its early implementations, MM4 exhibited similarities to modern numerical models (e.g. WRF) [*Skamarock et al.*, 2008]. However, it came with a three-dimensional, hydrostatic, primitive equation version and was written in terrain dependent σ - coordinates to cover different topography and land use types on all meteorological scales. Furthermore, MM4 included a moisture, PBL and radiation scheme on a staggered horizontal Arakawa B grid and 16 vertical levels [*Anthes and Warner*, 1987]. Although considerable success was achieved in simulating realistic events with MM4 [e.g. *Dudhia*, 1989] a major weakness was its inability to be run at high resolution.

Due to rapid development of computational resources during the 1990s, an improved MM4, called MM5 (version 2), was published by NCAR/Penn State in 1994. The key changes, described by *Dudhia* [1993], encompassed the extension of a fully compressible nonhydrostatic capacity that maintained physical consistency on highly resolved grids. Furthermore, improvements to moisture, PBL processes, radiation and cumulus parameterisations were included [*Otte*, 1999]. Over the next decade, multiple versions of MM5 [*Dudhia et al.*, 1999, 2002, 2005] were released with emphasis on continuous implementation of more sophisticated physical parameterisation schemes that leverage more

robust computational resources. *Dudhia et al.* [2005] provides an overview of pertinent changes implemented since the first formulation of MM5 by *Anthes* [1972] and *Anthes and Warner* [1978] which included multiple nests, nonhydrostatic extension , four-dimensional data assimilation (Newtonian nudging) capability, enhanced quantity and quality of physics options, and better usability on a broad range of computer platforms. MM5 was originally designed to be a pure research model but with time the demand for a research and operational model became greater [*Knievel*, 2006].

Since the early 2000's, The Weather Research and Forecasting Model (WRF) was developed to replace MM5 through a collaboration between NCAR, National Oceanic and Atmospheric Administration (represented by the National Centers for Environmental Prediction (NCEP) and the (then) Forecast Systems Laboratory (FSL)), the Air Force Weather Agency (AFWA), the Naval Research Laboratory (NRL), the University of Oklahoma, and the Federal Aviation Administration (FAA)[1]. With its first official release in 2004 (version 2.0, [*Skamarock et al.*, 2005]), the cloud-scale WRF model was capable of conserving mass, momentum, and energy [*Knievel*, 2006], through two main dynamical solvers that were associated with WRF:

- ARW - Advanced Research WRF maintained by NCAR [*Skamarock et al.*, 2005, 2008]

- NMM - Nonhydrostatic Mesoscale Model maintained by NCEP [*Janjic*, 2003]

The WRF numerics are based on recent computational technology that allows highly resolved meteorological outputs and a better performance of local effects. This was achieved through recent developments in physics parameterisations, which include cumulus convection, microphysics of clouds and precipitation, short-wave and long-wave radiation, turbulence and diffusion, PBL and surface layer, and the interaction with Earth's surface [*Knievel*, 2006]. Since 2005, NCAR has been publishing annual WRF updates. Version 3.9 (May 2017) will be employed throughout this thesis. A more detailed description of WRF-ARW including its numerics can be found in Chapter 5.1.

2.2.2 Idealised Tropical Cyclone Modelling

During the development of the WRF model, the concept of creating an idealised TC vortex in a numerical environment were explored [*Anthes*, 1972; *Anthes and Warner*, 1978]. In particular, idealised TC simulations were improved through the development of a time-dependent nonhydrostatic axisymmetric numerical model by *Emanuel* [1986] and *Rotunno and Emanuel* [1987] that is now part of the versatile and complex WRF model (see Chapter 5.2.1). These authors based their research on the improved understanding of previous TC formation theories such as CISK [*Charney and Eliassen*, 1964] (see also Section 2.2.1). Moreover, they hypothesised that the interaction between air and ocean is predominant in the early formation phase of a TC, which is opposed to the classic CISK theory. Their understanding of the air-sea interaction process was based on the Carnot engine (see Figure 2.28) acquiring enthalpy through warm sea surface temperatures (A) and releasing heat near the relatively

---

[1]http://www.wrf-model.org/index.php

cold stratosphere (C), which is realised through convection (B to C). Air slowly descends isothermally in the lower stratosphere (C to D) and then further back down to A [*Emanuel*, 2018].
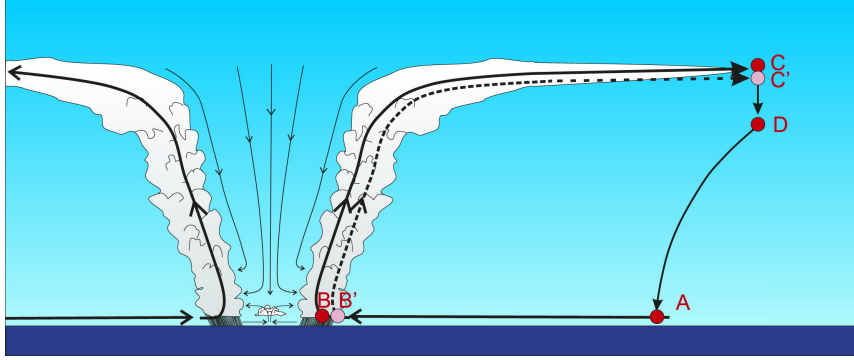
Figure 2.28: Energy cycle of a mature, steady, axisymmetric tropical cyclone [*Emanuel*, 2018].

The Carnot engine effectively describes a heat redistribution process that is determined by the organisation of surface heat flux [*Rotunno and Emanuel*, 1987]. Their theory gained wide acceptance in the following decades and became commonly known as "wind-induced surface heat exchange" (WISHE) [*Smith and Montgomery*, 2015]. The numerical model by *Emanuel* [1986] and *Rotunno and Emanuel* [1987] itself is based on the assumptions of gradient wind balance as well as a neutrally conditioned boundary layer. In addition, the model is time-dependent, nonhydrostatic and axisymmetric with an explicit solution for convection, whereas all turbulent flow is parameterised [*Rotunno and Emanuel*, 1987]. Their basic model setup included a domain size of r_{outer} = 1500 km and a domain top z_{top} = 25 km, with grid spacing of 15 km in the horizontal and 1.25 km in the vertical direction, respectively. Near the top of the domain and above the tropopause, *Rotunno and Emanuel* [1987] introduced a "sponge" layer z_{sponge} = 19.375 km to create a zone, in which convection is limited in height and gravity waves are damped out to prevent them from reflecting back into the lower troposphere. To validate their idealised TC model approach, the authors conducted a range of sensitivity tests using neutral atmospheric soundings and a finite-amplitude vortex specified by the vortex tangential velocity

$$v(r, z, 0) = \frac{z_{sponge} - z}{z_{sponge}} \left[\sqrt{v_m^2 \left(\frac{r}{r_m}\right)^2 \left[\left(\frac{2r_m}{r + r_m}\right)^3 - \left(\frac{2r_m}{r_0 + r_m}\right)^3 \right] + \frac{f^2 r^2}{4}} - \frac{fr}{2} \right] \quad (2.60)$$

where r_0 is the outer vortex radius, f the Coriolis parameter, and v_m and r_m are the maximum wind and the radius of maximum wind, respectively [*Rotunno and Emanuel*, 1987]. These sensitivity tests were carried out to study the sensitivity to the initial vortex, sea surface temperature and tropopause height, and the initial relative humidity. In the control run (experiment A), r_0 = 412.5 km, r_m = 82.5 km, and v_m = 15 m/s, whereas these parameters were changed in further simulations B to E as shown in Table 2.6.

Exp	v_m [m/s]	r_m [km]	r_0 [km]	SST [C]	Tropopause (mb)	Comments
A	12	82.5	412.5	26.3	100	Control run
B	2	82.5	412.5	26.3	100	Weak vortex
C	12	160.0	800.0	26.3	100	Large vortex
D	12	41.0	206.0	26.3	100	Small vortex
E	12	82.5	412.5	26.3	100	Dry to 30% RH above boundary layer

Table 2.6: Numerical vortex simulations A-E [*Rotunno and Emanuel*, 1987]

Numerical results of the simulations in Table 2.6 are displayed in Figure 2.29 plotting the maximum wind speed v_m over the simulation time.
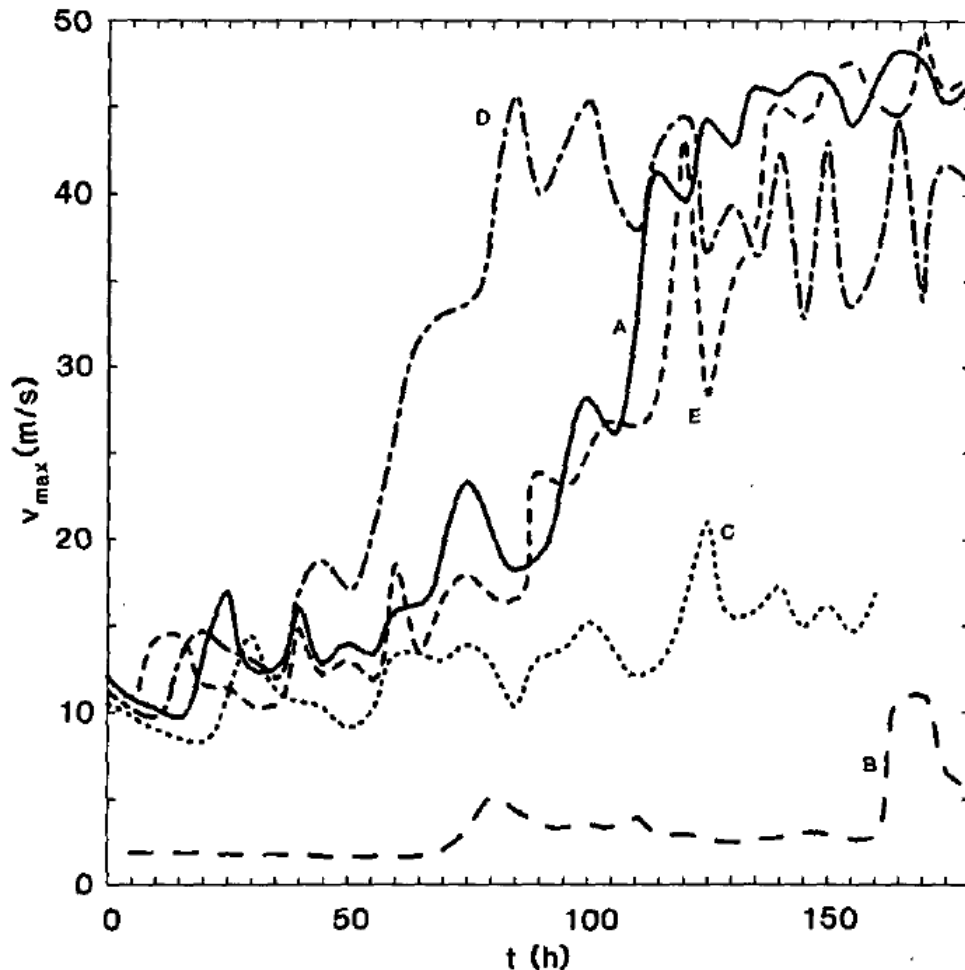
Figure 2.29: Time series of v_m for Experiments A-E [*Rotunno and Emanuel*, 1987].

Figure 2.29 visualises the sensitivity of the experiments A to E to the vortex intensity. The control run A in Figure 2.29 is conceptualised so that the initial vortex is in thermal wind balance. The vortex develops from a neutral state into a hurricane-intensity vortex at around 100 h in the simulation. In

experiment B, the maximum initial velocity v_m was set to 2 m/s with other parameters being equal to those in run A. *Rotunno and Emanuel* [1987] found that the low velocity slows the latent heat transfer and thus cumulus convection is largely suppressed throughout the entire simulation time. In conclusion, a weak vortex in experiment B does not reach hurricane intensity. The authors also investigated a vortex that covers a large area by almost doubling r_0 and r_m in experiment C. Because convection is spread over a large area, the central part of the vortex does not become moist enough to become a TC [*Rotunno and Emanuel*, 1987]. In contrast, the horizontal size r_0 and r_m were reduced by 50% in experiment D. The authors noted a more rapid TC development but a slightly less intense storm than the vortex in the base experiment A. Furthermore, the general structure seemed to be similar to the control run besides the 50% reduction in size. *Rotunno and Emanuel* [1987] concluded that the size of a severe TC is determined by the size of the initial vortex. Experiment E exhibits the same initial parameters, however, the relative humidity everywhere above the lowest grid level was reduced to 30%. The vortex in experiment E gains hurricane strength similar to the control experiment but at different timesteps. With experiment E *Rotunno and Emanuel* [1987] showed that the supply of high moisture in the lower levels is crucial for TC intensification. In general, the choice of initial parameters determines the strength of a spun up TC. These numerical experiments will become important in Chapter 5.2.1 of this thesis, as an idealised TC is spun up and included in a real world environment using a hybrid WRF model approach [*Bruyere et al.*, 2016].

2.2.3 Idealised Tropical Cyclone Modelling during Landfall

In the late 60's, *Ooyama* [1969] conducted the first successful numerical simulation of an entire TC life cycle using a three-layer axisymmetric model. Its vertical structure was characterised by a bottom layer surmounted by two further layers representing the TCBL and the stable, free atmosphere, respectively. The use of this simple approach allowed the importance of latent heat for TC development and maintenance to be highlighted. From this work *Ooyama* [1969] also showed that a modelled TC could not maintain its intensity for more than 15 hours when surface characteristics changed from ocean to land and the supply of latent heat from the ocean ceased. However, if coastal temperatures reach a sufficient temperature, the presence of land had very little effect on the intensity of a TC staying at least 100 km offshore. *Ooyama* [1969] conducted, in essence, the first set of idealised TC simulations to highlight the importance of underlying terrain during TC landfall. A deeper physical understanding of the landfall processes was provided by *Kurihara and Tuleya* [1974] and *Tuleya and Kurihara* [1978], who divided the TCBL into four vertical levels into a three-dimensional, primitive equation model with 11 model levels in total. In order to simulate TC landfall, the coastline was moved through a 4000 km square domain with minimum horizontal grid spacing of 20 km and no background flow. Overall, two simulations were carried out to examine the role of surface roughness during TC landfall. The land surface in the basic experiment (*basic*) was set to $z_0 = 0.25$ m and no evaporation was permitted. Simulation S1 assumed the land surface to be entirely smooth and the same as over ocean. However, *Tuleya and Kurihara* [1978] calculate surface roughness through Charnock's relation $z_0 = 0.032 \cdot u_*^2 / g$ with no indication given which roughness values were used

over the ocean. In Charnock's relation, u_* is the friction velocity and g the acceleration of gravity [*Kurihara and Tuleya*, 1974]. A further run S2 was conducted to study the impact of evaporation during TC landfall, which shall not be discussed further here. Numerical results for both *basic*, *S1* and *S2* runs are shown in Figure 2.30.
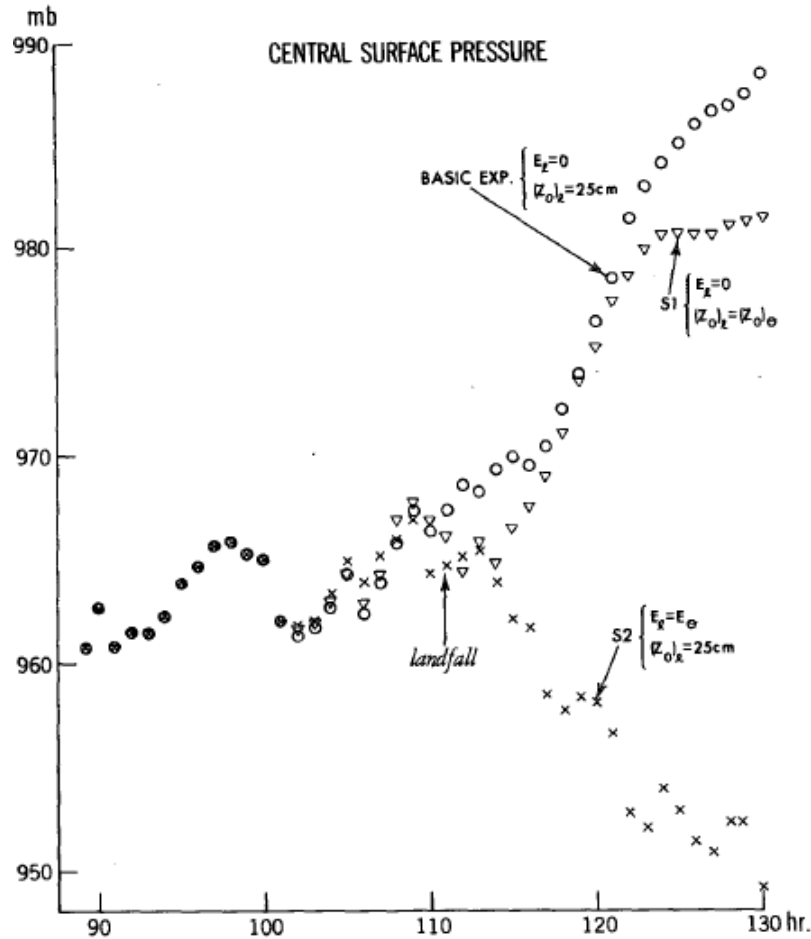
Figure 2.30: Central pressure variation for TC landfall (at hour 111) experiments: basic (circles, $z_0 = 0.25$ m, no evaporation), S1 (triangles, roughness the same as over water, no evaporation), and S2 (crosses, $z_0 = 0.25$ m, evaporation included) experiments [*Tuleya and Kurihara*, 1978].

Figure 2.30 displays the central pressure variation for the basic experiment and the S1 run. Both runs exhibit a similar central pressure decay rate within the first 10 hours after landfall. Immediately after simulation hour 121, TC intensity over the rougher terrain (*basic*) decreases more rapidly than over smooth land in simulation S1. More specifically, TC central pressure in the run with ocean roughness was 3.4 hPa and 6.9 hPa lower four and 19 hours after landfall, respectively. In addition, maximum surface winds in S1 were about 9 m/s higher during the same numerical timesteps. However, while *Tuleya and Kurihara* [1978] concluded that increased land surface roughness leads to a reduction of the tangential wind component in the TCBL, and to an increase of the radial wind component with minor impact on TC intensity, they suggest TC decay after landfall was largely caused by evaporation depletion.

Using a more sophisticated modelling framework, *Tuleya et al.* [1984] briefly examined the effect of surface roughness variation on TC decay in the landfall phase. Their experiments were performed on

a triply-nested domain with a grid resolution of 1/6 ° using 22 grid points in both x- and y-direction. To investigate the impact of heterogeneous roughness conditions on TC surface winds, a simulation was run with roughness variations from $z_0 = 0.1$ m at the coast to $z_0 = 1$ m at 1.5° inland, as illustrated in Figure 2.31.
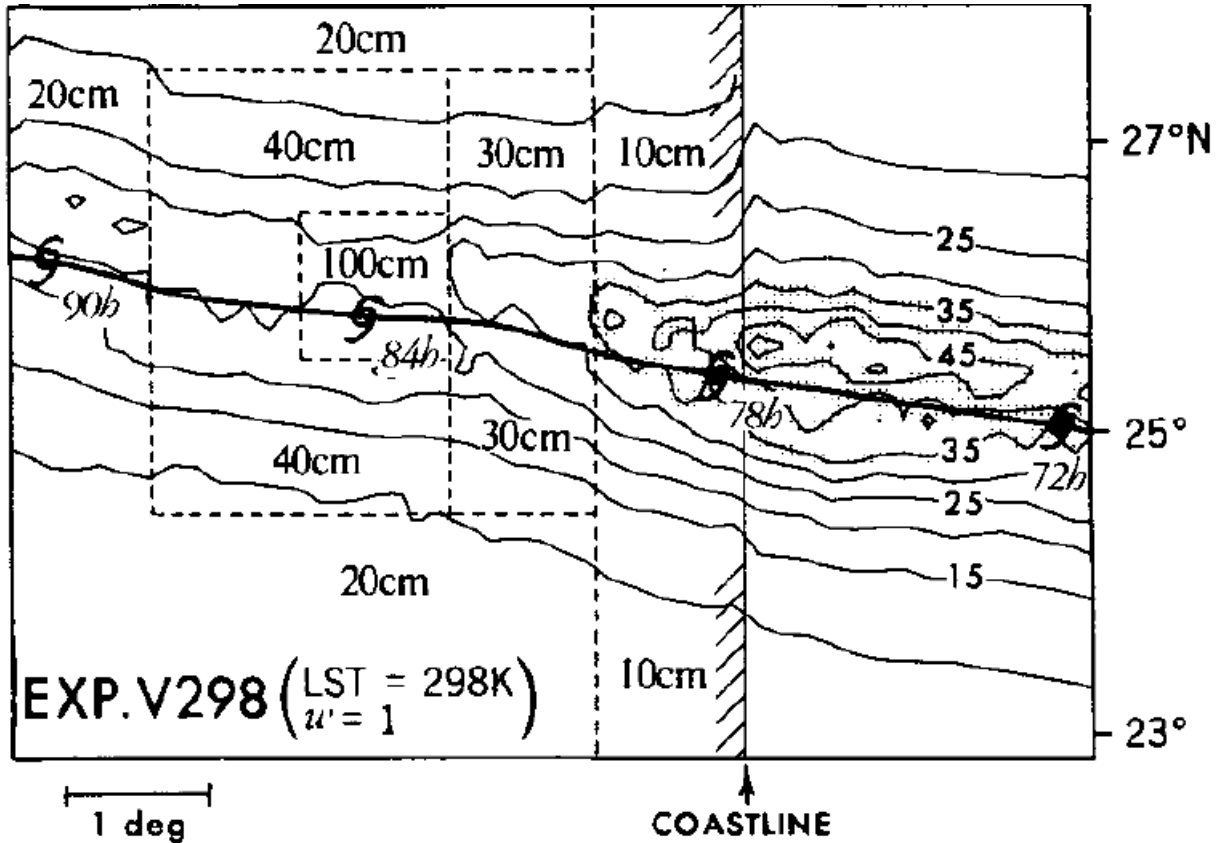
Figure 2.31: Maximum surface wind distribution during TC passage (right to left) with horizontal z_0 variations in cm [*Tuleya et al.*, 1984].

Tuleya et al. [1984] noted a rapid adjustment of the near-surface wind field after the occurrence of a roughness change, as indicated by the isotachs progression. Furthermore, increased roughness leads to a 3 hPa increase in the central pressure and a modification of the upper level winds (not shown). Unfortunately, the authors do not give any further information on how upper-level winds changed. Instead, *Tuleya et al.* [1984] indicate that the inclusion of topography will have a greater impact than roughness variations. Such simulations, including the presence of topography, were carried out in the proximity of the Central Mountain Range over Taiwan [*Chang*, 1982; *Bender et al.*, 1985]. In these simulations it was shown that when a storm approached, the air flows mostly around the mountain range instead of over it, while a ridge on the windside and a trough on the leeside slopes was formed [*Chang*, 1982]. *Bender et al.* [1985] confirmed these results and added that topographic features also influence the decay rate and precipitation distribution of landfalling TCs.

As improvements were made to TC numerical models by *Rotunno and Emanuel* [1987] and computing capacity increased rapidly, the research community began to use these idealised models to simulate the TC landfall phase in more detail, and learned how the wind flow in the low levels is modified by the underlying surface. Over the last two decades, studies have addressed the land-ocean

contrast and its contribution to TC weakening and modification throughout landfall using the WRF predecessor MM5 [e.g. *Zhang et al.*, 1999; *Chen and Yau*, 2003; *Wong and Chan*, 2006, 2007; *Ramsay and Leslie*, 2008] and WRF [e.g. *Li et al.*, 2014]. *Zhang et al.* [1999] ascribed the reduction of RMW intensity to increased frictional forces over land that also causes large cross-isobaric flows in the eyewall. This was also found in the study by *Chen and Yau* [2003], who noted a 19 m/s decrease in low-level winds and a surface pressure increase of 27 hPa within six hours after landfall. These low-level winds start to weaken one hour prior to landfall, hence the authors suggest that the TCBL reacts faster to surface properties (i.e. land) than to the reduced heat source over land. Furthermore, TCBL changes due to increased friction over land can lead to asymmetries in the mean TC circulation. The same phenomenon was observed in idealised TC simulations of *Wong and Chan* [2006], who suggested the roughness contrast between ocean and land was responsible for inducing asymmetries in the near-surface wind field in two ways. First, wind speeds over land decrease and second, winds need time to adjust to the new surface when transitioning from water to land and vice versa. In a follow-up study, *Wong and Chan* [2007] conducted idealised TC experiments in the Northern Hemisphere where the storm is located at 50, 100, 150 km inland and at the coastline. In all simulations land surface was characterised by a roughness length $z_0 = 0.5$ m, while roughness over ocean depended on wind strength. Their results show a weaker radial inflow on the rear-right side for post-landfall simulations and a strong radial inflow to the rear left at landfall.

TC wind speed asymmetries have also been found in vortices in the Southern Hemisphere [*Ramsay and Leslie*, 2008]. This study is considered to be the first to investigate the complex terrain interactions over northeast Australia through an event reconstruction of TC Larry (2006). *Ramsay and Leslie* [2008] showed that the presence of mountainous terrain altered the TCBL structure as well as storm parameters such as track, intensity, forward speed, size, and wind field characteristics. This was found through idealised simulations with and without topography. Regarding track, the simulation considering flat topography followed a more southerly track resulting in a landfall location about 80 km south due to an increased mid-to-upper-level flow on the left rearward side of the storm relative to the observed track that induced a greater advection of potential vorticity toward the south *Ramsay and Leslie* [2008]. Apart from track differences, the authors revealed a more intense storm with weaker wind shear at landfall when topography was removed. It is found, that topography induces higher vertical wind shear in the simulated track with non-zero topography, which is known to be hostile for TC development and intensification [e.g. *DeMaria*, 1996]. Without topography, 10 m wind speeds were around 10 m/s higher over land than with non-zero terrain [*Ramsay and Leslie*, 2008]. Hence, topography interactions alter the near-surface wind field during the TC landfall phase as increased roughness led to a fast deceleration of the flow onshore from 50 m/s to 34 m/s over 3 km distance.

The effect of increased roughness over land was also investigated on TC precipitation patterns [e.g. *Li et al.*, 2014]. Similar to a previous study by *Wong and Chan* [2007], the rough land surface was set to $z_0 = 0.5$ m. It was shown that increased roughness over land induces surface convergence, which favours convection.

Driven by the question of what would have happened if TC Yasi (2011) came from a different direction and how would wind, precipitation, and damages be affected when the storm had a different size, a

new TC modelling approach was conceptualised by *Bruyere et al.* [2016] that will be utilised in this dissertation. An answer to this question is not easy, as there is only one observed storm. To artificially increase the number of storms for one event, *Bruyere et al.* [2016] combined idealised spun up TCs with a real environment, which is referred to as Hybrid WRF Cyclone Model (HWCM). In particular, the real world environment includes land-water distribution, land surface information, such as terrain and topography, and weather information such as temperature, pressure, and humidity. The idealised component involves the numerical spin up of a TC [*Rotunno and Emanuel*, 1987] over water without terrain information. Hence, the idealised component allows the generation of various TCs that are different in size, structure and intensity but the entire simulation is generally undertaken over a water surface with a constant Coriolis parameter f. On the other hand, the real component runs on a dynamical model adding terrain information. The great advantage of this approach lies in its versatility to create a range of scenarios in different real-world environments. For example, dynamic and thermodynamic parameters like steering flow, land surface information, temperatures, and boundary conditions can be modified arbitrarily to create a large number of TC scenarios. This approach is further modified to serve the purpose of investigating different surface roughnesses and the effect on near-surface wind field and on the TCBL. A detailed description of how this method is utilised in this thesis is found in Chapter 5.2.

In previous idealised experiments, TC landfall was simulated by spinning up a vortex in a quiescent environment and dragging the coastline below the storm. This approach limits the interactions TCs may have with the environment prior, during, and after landfall. Using the HWCM model allows a TC to be set up in an evolving meteorological environment, with the versatility of also allowing initial thermodynamic parameters over land such as temperature and relative humidity to be modified explicitly. In addition, poleward TC movement increases the β-drift through the variation of Coriolis force with latitude, which can be indirectly associated with TC structure changes [*Elsberry*, 1987]. Traditional approaches to simulate idealised TCs usually run in a domain with a constant Coriolis parameter and thus neglect the β-drift.

2.3 Summary and Research Questions

2.3.1 Tropical Cyclone Observations

The first half of this Chapter contains a review of existing literature on the TCBL and near-surface wind characteristics within landfalling TCs. To better understand the TCs and TCBL at landfall, various measurement techniques such as satellite retrievals, dropsonde data, radar data, buoys, and portable weather towers have been employed. Portable weather towers were part of coordinated field campaigns (such as FCMP, StickNet, and SWIRLnet), which provided information about the near-surface wind field in a range of different terrain exposure [*Balderrama et al.*, 2011; *Weiss and Schroeder*, 2008; *Balderrama et al.*, 2012; *Henderson et al.*, 2013; *Miller et al.*, 2015; *Giammanco*

et al., 2016]. Although near-surface wind records in landfalling TCs are limited, US and Australian field campaigns collected a sufficient amount of data that is analysed in this thesis (see Chapter 3).

To better understand these highly complex wind fields, previous research has addressed turbulent characteristics behaviour near terrain changes [e.g. *Paulsen and Schroeder*, 2005; *Schroeder et al.*, 2009; *Yu et al.*, 2008; *Yu and Gan Chowdhury*, 2009; *Miller et al.*, 2015; *Giammanco et al.*, 2016]. However, gust components, turbulence intensity and length scales were typically analysed with the assumption that these turbulent parameters are in equilibrium with the underlying terrain, irrespective of the upstream surface roughness [e.g. *Paulsen and Schroeder*, 2005]. This assumption may have influenced their findings given equilibrium conditions may not be achieved for distances less than 100 times the measurement height downwind of a terrain change [*Businger*, 1986; *Wieringa*, 1993; *Jegede and Foken*, 1999].

Only limited attempts have been made to explicitly incorporate upstream roughness changes and non-equilibrium conditions into the analysis of turbulence statistics in the vicinity of terrain changes [*Miller et al.*, 2015; *Giammanco et al.*, 2016]. As such, it remains unclear how changes in terrain alter the near-surface TC wind profile and their turbulent characteristics in non-equilibrium environments. Hence, the following research questions arise:

1. Can observational data be used to empirically quantify the relationship between upwind fetch, x, and the turbulent parameters, turbulence intensity, gust and peak factors, skewness, kurtosis, and eddy sizes, following a single terrain change within a landfalling TC environment?

2. Is the prevailing belief that an upwind distance of $x \approx 100z$ supported by observations within landfalling TCs?

3. Are the ESDU or AS/NZS1170.2 models appropriate for estimating turbulence intensity and gust factors transitioning in a TC environment?

Observational data methods described in Chapter 4 will address how the above listed research questions are going to be answered.

2.3.2 Numerical Tropical Cyclone Simulations

Although only a limited number of studies have undertaken research on the TCBL during landfall, the general consensus of these works is that increased surface roughness during landfall alters the TCBL structure and hence effects the main TC circulation. Almost all studies, apart from *Tuleya et al.* [1984], reviewed simulated land with a constant surface roughness. In particular, a differentiation between terrain characteristics such as sand, grassland, or trees and how the surface wind field and the TCBL respond have not been investigated.

In all reviewed studies, the common method was to generate idealised TCs in a constrained domain on an f-plane without the inclusion of advection. To simulate landfall, TCs were spun up until

they reached a quasi steady state. After a steady state was accomplished, a "moving" coastline was dragged below the TC. In essence, past numerical simulations included a position-fixed TC with a moving coastline. So far, no studies attempted to simulate TCs in a real environment including β-drift (changing f), steering flow and flexible land surface properties. However, *Wong and Chan* [2006] already highlighted that the inclusion of these parameters might contribute to a better understanding of landfalling TCs. Therefore, in the numerical part of this thesis, the HWCM approach by *Bruyere et al.* [2016] will be utilised to examine how the landfalling TCBL is modified by different land surface roughnesses.

Considering the research gaps identified above, the research questions to be addressed by this thesis are stated as follows:

1. How do TCBL profiles in different parts of numerically simulated TCs prior to and during landfall compare to observed TC wind profiles measured by dropsondes and radars?

2. How does the time dependent mean TCBL respond as TCs move from ocean to land?

3. How do different land surface conditions influence the TCBL response during landfall?

Chapter 3

Data Sources

The aim of this chapter is to describe the data used to analyse the near-surface wind field observations of landfalling TCs and data used to drive the numerical WRF-ARW simulations. Observations from USA TCs were acquired through the Florida Coastal Monitoring Program (FCMP) and StickNet archives, as discussed in Chapter 3.1.1 and 3.1.2, respectively. Australian surface weather data were acquired through a tower deployment during TC Debbie (2017) in line with the Surface Weather Information Relay and Logging Network (SWIRLnet), as described in Chapter 3.1.3.

3.1 Wind Observations from Field Campaigns

3.1.1 The Florida Coastal Monitoring Program (FCMP)

Observational datasets of landfalling TCs in US coastal regions will be analysed throughout this thesis. Available wind records from the Florida Coastal Monitoring Program (FCMP) campaign include the hurricane seasons from 2004 to 2012, whereas meteorological data such as wind speed at three heights, temperature, rainfall, pressure, and relative humidity were captured. The main purpose of these deployments was to investigate the near-surface wind and rain characteristics of Atlantic hurricanes and their threat to coastal infrastructure [*Balderrama et al.*, 2011].

FCMP towers are designed for rapid deployment in various terrain conditions and to resist wind gust speeds up to 90 m/s (Figure 3.1). They are equipped with a 10 m steel lattice tower mounted on a tandem axle trailer [*Balderrama et al.*, 2011]. Numerous sensors are mounted at elevations of 3 m, 5 m, and 10 m. Two arrays of three fixed axis anemometers (RM Young Model Number 27106R) record three-dimensional wind speed and direction at 5 m and 10 m and a further anemometer (RM Young Model Number 08234) is located at 10 m height. All mounted anemometers exhibit a 2.7 m and 63% recovery distance constant. The sensors at the lowest elevation monitor temperature, precipitation, pressure, and relative humidity.

Figure 3.1: FCMP tower (http://fcmp.ce.ufl.edu/)

High-frequency 10 Hz wind measurements at 10 m and 5 m are available for Hurricanes Frances (2004), Katrina (2005), Rita (2005), Wilma (2005), Ike (2008), Isaac (2012), and Sandy (2012), all of which will be incorporated in the analysis for this thesis. For the validation of the method to analyse near-surface wind field characteristics, 10 m wind records for T1 deployed in Hurricane Irene (1999) were included also.

3.1.2 StickNet

The second observational dataset considered in this thesis was acquired with the Texas Tech University (TTU) StickNet platform. This platform was developed in 2005 at TTU to measure surface weather conditions in the vicinity of supercell thunderstorms and hurricanes[1]. At the time, the StickNet network included 24 rapidly deployable towers of 2.25 m height collecting temperature, relative humidity, barometric pressure, wind speed, and wind direction at sampling rates from 1 - 10 Hz using a RM Young 05103V anemometer (Figure 3.2). All towers are designed to withstand 3-second gusts of 63 m/s, with the option of an additional earth screw that provides more stability [*Weiss and Schroeder*, 2008]. Hurricane Dolly (2008) along the Southern Gulf Coast of Texas was the first storm where StickNet recorded meteorological data.

---

[1] https://www.depts.ttu.edu/ttuhrt/Instrumentation/StickNet.php

Figure 3.2: StickNet 0101A tower (Photo credit: Dr. Richard J. Krupar III)

Wind observations at 2.25 m were available from Hurricanes Bill (2015), Dolly (2008), Ike (2008), Irene (2011), Isaac (2012), and Sandy (2012).

3.1.3 The Surface Weather Information Relay and Logging Network (SWIRLnet)

Due to the lack of permanent weather stations capable of measuring winds during landfalling TCs in Australia, a ruggedized network of portable weather stations called Surface Weather Information Relay and Logging Network (SWIRLnet) was developed at the Cyclone Testing Station (James Cook University) in 2013 [*Henderson et al.*, 2013; *Mason and Henderson*, 2015]. The current network of six portable weather stations is deployed in front of landfalling TCs in Queensland, Australia, to capture near-surface weather data (wind speed, pressure, temperature, relative humidity) at approximately 3.2 m above ground level in a variety of surface terrain conditions (e.g. open and suburban exposure). In particular, information about the peak wind speeds contribute to an important understanding of the vulnerability of structures and the effectiveness of current standards and building regulations [*Henderson et al.*, 2013].

SWIRLnet towers were deployed by myself along with a team of researchers from the James Cook University during TC Debbie (2017) and successfully captured high-fidelity records of the turbulent winds produced by this event. The six 3.2 m SWIRLnet towers (Figure 3.3) are designed for rapid deployment 24 to 48 hours prior to TC landfall and to withstand gust wind speeds up to 90 m/s. Towers are built upon a freestanding tripod which is fixed through anchoring on each of the tower leg footpads and at its centre [*Henderson et al.*, 2013]. Each tower is equipped with an anemometer that captures wind speed and direction data at 10 Hz. In addition, clamped and shrouded sensors at a height of 1 m measure 1-minute mean values of temperature, relative humidity and pressure once every 10 minutes.

Figure 3.3: SWIRLnet Tower with RM Young anemometer deployed during TC Ita [*Mason and Henderson*, 2015]

As shown in figure 3.3 each tower uses an R.M. Young anemometer (Wind Monitor-MA Model 05106) to measure the horizontal wind speed and direction over the range 0 to 100 m/s and from 0° to 360° [*R.M. Young*, 2000] using a 18 cm diameter 4-blade helicoid propeller molded of polypropylene. Considering the distant constant of this instrument (2.7 m), despite the sampling frequency of 10 Hz, it can only effectively respond at a rate of around 1 Hz.

3.2   Land Cover Data

In order to obtain the underlying surface roughness for each tower, land cover data provided by the Coastal Change Analysis Program (C-CAP) [*NOAA*, 2010] was utilised. Land cover data is available at a 30 m spatial resolution for all US coastal regions and covers intertidal areas, wetlands, and adjacent uplands (see Figure 3.4). Coloured areas in Fig. 3.4 represent 25 different land cover types, which are explained in more detail in Table 3.1.
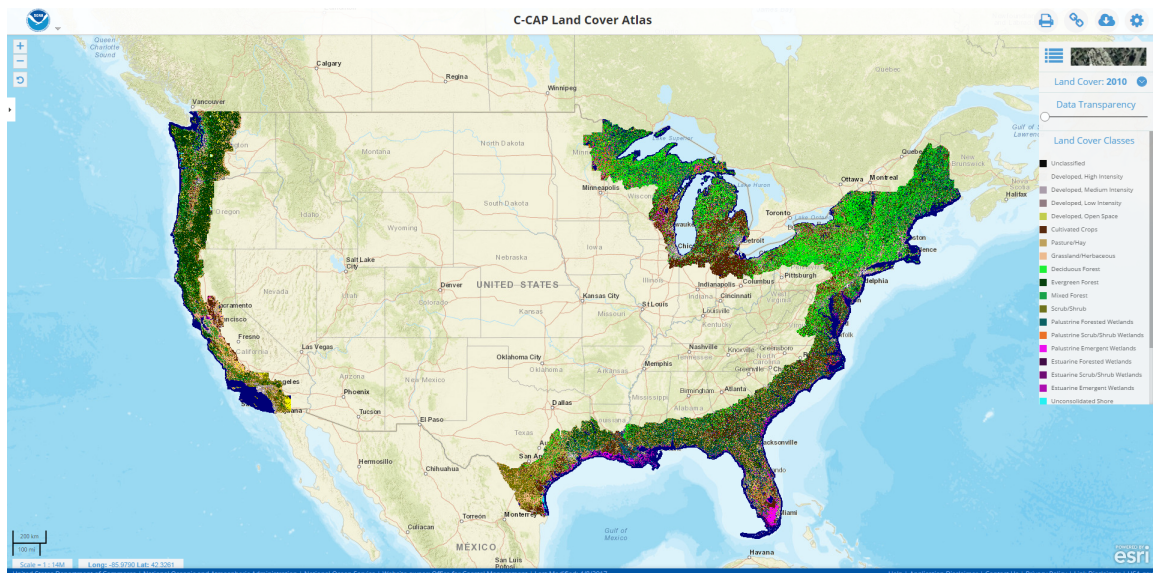
Figure 3.4: C-CAP Land Cover Atlas Data Overview: Land cover for US coastal areas
(https://coast.noaa.gov/ccapatlas/).

Land cover	Description
High Intensity Developed	Little or no vegetation, heavily built-up urban centers, large constructed surfaces in suburban and rural areas, large buildings (such as multiple family housing, hangars, and large barns), interstate highways, and runways.
Medium Intensity Developed	Substantial amounts of constructed surface mixed with substantial amounts of vegetated surface and small buildings (such as single family housing, farm outbuildings, and large sheds).
Low Intensity Developed	Contains constructed surface mixed with vegetated surface with streets and roads with associated trees and grasses.
Open Space Developed	Includes areas with a mixture of some constructed materials, but mostly vegetation in the form of lawn grasses. Includes parks, lawns, athletic fields, golf courses, and natural grasses occurring around airports and industrial sites.
Cultivated Land	Includes herbaceous (cropland) and woody (e.g., orchards, nurseries, and vineyards) cultivated lands.
Pasture/Hay	Characterized by grasses, legumes or grass-legume mixtures planted for livestock grazing.
Grassland	Dominated by naturally occurring grasses and non-grasses (forbs) that are not fertilized, cut, tilled, or planted regularly.
Deciduous Forest	Includes areas dominated by single stemmed, woody vegetation unbranched 0.6 to 1 meter above the ground and having a height greater than 5 meters.
Evergreen Forest	Includes areas in which more than 67 percent of the trees remain green throughout the year. Trees must be taller than 5 meters.
Mixed Forest	Contains all forested areas in which both evergreen and deciduous trees are growing. Trees must be taller than 5 meters.
Scrub/Shrub	Areas dominated by woody vegetation less than 5 meters in height, including shrubs and young trees.

Palustrine Forested Wetland	Includes all non-tidal wetlands dominated by woody vegetation greater than or equal to 5 meters in height, and all such wetlands that occur in tidal areas.
Palustrine Scrub/Shrub Wetland	Includes all non-tidal wetlands dominated by woody vegetation less than or equal to 5 meters in height, and all such wetlands that occur in tidal areas.
Palustrine Emergent Wetland	Includes all non-tidal wetlands dominated by persistent emergents, emergent mosses, or lichens, and all such wetlands that occur in tidal areas.
Estuarine Forested Wetland	Includes all tidal wetlands dominated by woody vegetation greater than or equal to 5 meters in height, and all such wetlands that occur in tidal areas.
Estuarine Scrub/Shrub Wetland	Includes all tidal wetlands dominated by woody vegetation less than or equal to 5 meters in height, and all such wetlands that occur in tidal areas.
Estuarine Emergent Wetland	Characterized by erect, rooted, herbaceous hydrophytes (excluding mosses and lichens) that are present for most of the growing season in most years.
Unconsolidated Shore	Characterized by substrates lacking vegetation except for pioneering plants that become established during brief periods when growing conditions are favorable. Erosion and deposition by waves and currents produce a number of landforms, such as beaches, bars, and flats.
Bare Land	Composed of bare soil, rock, sand, silt, gravel, or other earthen material with little or no vegetation.
Water	Includes all areas of open water with less than 25% cover of vegetation or soil.
Palustrine Aquatic Bed	Includes wetlands and deepwater habitats dominated by plants that grow principally on or below the surface of the water for most of the growing season in most years.
Estuarine Aquatic Bed	Includes widespread and diverse Algal Beds in the Marine and Estuarine Systems, where they occupy substrates characterized by a wide range of sediment depths and textures.

Table 3.1: C-CAP land cover classes and description.[2]

Data from measurements taken in the following states are included in the thesis: Delaware, Florida, Louisiana, Maryland, Mississippi, North Carolina, New Jersey, New York, Texas, and Virginia. All listed C-CAP land cover classes listed above were also assigned a surface roughness z_0 shown in Table 4.2 in Chapter 4.2.

---

[2]https://coast.noaa.gov/data/digitalcoast/pdf/ccap-class-scheme-regional.pdf

Chapter 4

Surface Wind and Roughness Aggregation Methodology

This chapter describes the general method implemented to combine observed near-surface wind data with upstream roughness characteristics. To achieve this, the following three steps were undertaken:

1. **Aggregation of Wind Data and Turbulent Statistics:** Wind data from all campaigns were aggregated, quality-controlled and turbulent characteristics derived.

2. **Determination of Tower Upstream Roughness Profiles:** Upstream terrain roughness characteristics were determined in 10° segments surrounding all towers.

3. **Aggregation of Events:** Available turbulent characteristics were assigned to upwind terrain profiles of the same wind cone independent of the storm and tower location relative to the storm.

The outline procedure described above combines TC wind measurements from all three field campaigns (see Chapter 3) at four different elevations.

4.1 Aggregation of Wind Data and Turbulent Statistics

The present thesis analyses recorded near-surface wind observations by portable weather towers in a range of different terrain exposures. To prepare data for further analysis, wind records were aggregated and turbulent statistics calculated. In particular, wind data were obtained from TCs that occurred between 2004 and 2017 using three different field campaigns, including US-based FCMP (Section 3.1.1) and StickNet (Section 3.1.2), and the Australian SWIRLnet (Section 3.1.3). The combined archive contains 11 TCs with wind data available at elevations of 2.25 m (StickNet), 3.2 m (SWIRLnet), 5 m and 10 m (FCMP). Analysis of wind measurements at all four elevations provides new insight over much of the research to date, which has focused largely on single elevations of 10 m,

5 m and/or 2.25 m [e.g. *Paulsen and Schroeder*, 2005; *Schroeder et al.*, 2009; *Masters et al.*, 2010; *Balderrama et al.*, 2012; *Miller et al.*, 2015; *Giammanco et al.*, 2016].

First, high-frequency wind speed and direction observations were separated for each storm individually and segmented into 10-min blocks. During this segmentation process, all wind observations were quality-controlled through a modified reverse arrangement stationary test [*Siegel and Castellan*, 1988], which has been used in previous research [e.g. *Schroeder et al.*, 2009; *Giammanco et al.*, 2016]. This stationarity test checks whether a significant trend underlies these samples using a z-score z_{MA} for ten 1-min segments within the 10-min means through

$$z_{MA} = \frac{A_r - \left[\frac{N(N-1)}{4}\right]}{\sqrt{\frac{2n^3 + 3N^2 - 5N}{72}}}. \tag{4.1}$$

In Eq. 4.1 A_r is the total number of reverse arrangements in the segments and N denotes their lengths. The null hypothesis for this test includes an underlying trend for the observations. Therefore, independent observations with no obvious trend mark the alternative hypothesis. To reject the null hypothesis at $p \leq 0.05$ (95% confidence interval), a z-score of $z_{MA} \geq 1.96$ and $z_{MA} \leq 1.96$ is required. If a given 10-min sample is classified as stationary it is considered further for analysis. Future work is required to analyse non-stationary segments, which are important to understand in more detail because these exist near the eyewall region, where wind speeds change rapidly.

A second quality control measure was then imposed. Recorded wind speed and direction observations were required to fall inside of $\pm$ three standard deviations. Wind data, which failed to satisfy the $\pm$ three standard deviations requirement were disregarded for further calculations. Table 4.1 lists the remaining data following this quality control procedure, which consists of 11 TCs along with 129 towers.

Storm	Year	Campaign	Elevation [m]	Number of Towers
Hurricane Bill	2015	StickNet	2.25	12
Hurricane Dolly	2008	StickNet	2.25	22
Hurricane Frances	2004	FCMP	10	3
			5	2*
Hurricane Katrina	2005	FCMP	10	5
			5	5
Hurricane Ike	2008	FCMP	10	6
			5	6
		StickNet	2.25	20
Hurricane Irene	2011	StickNet	2.25	19
Hurricane Isaac	2012	FCMP	10	1
			5	1
		StickNet	2.25	17
Hurricane Rita	2005	FCMP	10	4
			5	4
Hurricane Sandy	2012	FCMP	10	1
			5	1
		StickNet	2.25	9
Hurricane Wilma	2005	FCMP	10	4
			5	4
Tropical Cyclone Debbie	2017	SWIRLnet	3.2	6

Table 4.1: List of available storms and towers considered in the observational analysis. *Wind measurements at 5 m from T0 during Hurricane Francis (2004) were faulty and therefore not included in the analysis.

A total number of 19913, 2968, 1868, 1996 10-min wind observations $\geq$ 5 m/s are available at 2.25 m, 3.2 m, 5 m, and 10 m elevation, respectively. These quality-controlled 10-minute mean wind segments were then used to determine along- and across-wind turbulent statistics based on 3-sec block-averaged gust data. Statistics calculated were,

- Turbulence intensity I_u, I_v (Eq. 2.18),

- Gust factor G_u, G_v (Eq. 2.23),

- Peak factor g_u, g_v (Eq. 2.24),

- Skewness γ_{su}, γ_{sv} (Eq. 2.34),

- Kurtosis γ_{ku}, γ_{kv} (Eq. 2.35), and

- Integral length scale L_u, L_v (Eq. 2.38).

In an additional step, the magnitude of the gusts was corrected to account for effects of instrument response (distance constant = 2.7 m for all anemometers). Following *Balderrama et al.* [2012], the filter function in Eq. 2.28 was utilised.

Unlike previous research [e.g. *Giammanco et al.*, 2016], turbulent parameters were not used to calculate the underlying and surrounding roughness for each site. Instead, a manual approach was taken to determine z_0 using historical areal imagery available in Google Earth.

4.2 Determination of Tower Upstream Roughness Profiles

The choice of how to determine the surface roughness upstream of a site is significant [*Barthelmie et al.*, 1993]. *Barthelmie et al.* [1993] compares four techniques for estimating roughness lengths, which are the wind speed profile method, the gust method [*Wieringa*, 1976, 1983], the standard deviation measurement method [*Beljaars*, 1987], and the terrain method [*Wieringa*, 1992] using wind speed and direction data at 12.7 m, 20.0 m, 28.5 m and 33.8 m over a three-year period. In their comparison, *Barthelmie et al.* [1993] emphasises that terrain-derived mean roughness values are similar to those determined by the wind profile method. Roughness values calculated by standard deviations and gusts were found to be much lower. In this thesis, data will be aggregated based on similar underlying terrain of a tower site without the use of available wind speeds.

For each tower with usable data, the terrain present along the centreline of each 10° wind direction bin was identified. Obtained terrain information included surface roughness, distance from the tower to the roughness changes, and upstream fetches (length of the upstream terrain). In the analysis, only towers located in flat terrain were considered so as to avoid any influence of topographic speed up. Here, the term "flat" was defined as the slope of the underlying surface of 5° and below. Slope data provided by the Environmental Systems Research Institute (ESRI)[1] was then identified at each tower location. All towers listed in Table 4.1 were found to satisfy the 5° threshold and were considered for further analysis.

In an attempt to automatically determine terrain information for all 129 towers, surrounding surface terrain was obtained from the C-CAP land cover data atlas [*NOAA*, 2010] within a 10 km radius of each US-based tower latitude/longitude location. The 10 km radius was chosen in order to include multiple terrain changes of long fetches. Terrain and roughness information for the Australian-based towers were purely derived from aerial imagery, as the resolution of available datasets was too coarse (250 m at the lowest). The method of obtaining terrain information from aerial imagery is described in section 4.2.1.

For all US-based towers listed in Table 4.1, a profile of roughness values z_0 was assigned to the underlying and upstream C-CAP land cover using previous literature [*Wieringa*, 1993; *Hirth et al.*, 2012; *Kosiba et al.*, 2013]. The assigned roughness values for 22 C-CAP land cover classes were then grouped into five roughness regimes A, B, C, D, and E to minimise the spectrum of z_0 values and

---

[1]https://www.arcgis.com/home/item.html?id=a1ba14d09df14f42ad6ca3c4bcebf3b4

transitions. Each roughness regime represents a different range of land surface conditions found in the immediate vicinity of deployed towers. Developed roughness regimes A-E and their characteristics are listed in Table 4.2.

Regime	Classification	z_0-range [m]	C-CAP Land Cover	assigned z_0 [m]
A	Water Bodies	< 0.01	Open Water	0.0005
			Estuarine Aquatic Bed	0.001
			Palustrine Aquatic Bed	0.001
B	Open Land	≥ 0.01 - < 0.051	Bare Land	0.01
			Unconsolidated Shore	0.01
			Pasture/Hay	0.02
			Cultivated Crops	0.03
			Grassland/Herbaceous	0.03
			Estuarine Emergent Wetland	0.05
			Palustrine Emergent Wetland	0.05
C	Roughly Open	≥ 0.051 - < 0.31	Developed, Open Space	0.25
			Estuarine Scrub/Shrub Wetland	0.3
			Palustrine Scrub/Shrub Wetland	0.3
			Scrub/Shrub	0.3
D	Dense Suburban	≥ 0.31 - < 0.61	Developed, Low Intensity	0.35
			Developed, Medium Intensity	0.5
			Deciduous Forest	0.6
			Estuarine Forested Wetland	0.6
			Palustrine Forested Wetland	0.6
E	High Intensity / Forested	≥ 0.61	Evergreen Forest	0.8
			Mixed Forest	0.8
			Developed, High Intensity	1.0

Table 4.2: Established roughness regimes, z_0 boundaries, and assigned C-CAP land cover classes.

The five different roughness regimes were chosen to group areas with similar surface characteristics, with the broad classifications of regime A, water bodies, regime B, open land, regime C, roughly open, regime D, dense suburban, and regime E, high intensity/forested. More specifically, regime A contains all water bodies with $z_0 < 0.01$ m, which includes ocean, lakes, rivers as well as Estuarine and Palustrine Aquatic Beds. Regime B was named "open land" containing flat, open land cover types such as bare soils, rock, sand, and gravel with little or no vegetation. Little vegetation includes grassland, pasture/hay, and cultivated land. Proceeding to rougher terrain, regime C is dominated

by woody vegetation of less then five meters in height such as shrubs and young trees. In addition, "roughly open" regime C contains terrain with a mixture of some constructed materials and vegetation, which includes park, lawns, and sports fields. Terrain that is made up of substantial amounts of constructed surface mixed with vegetated surface or deciduous forests with trees greater than five meters belong to the "dense suburban" regime D. The roughest regime E was named "high intensity/-forested" and includes dense forests, heavily built-up urban areas or large constructed surfaces.

Beyond the roughness regimes established in Table 4.2, other approaches exist to classify the surface. Examples of this are those described in AS/NZS1170.2 [*AS/NZS 1170.2:2011*, 2011] and the American Society of Civil Engineers 7 [*ASCE 7*, 2003] standard. Table 4.3 matches exposure descriptions to z_0 values and exposure categories for each method.

Exposure description	z_0 - boundaries [m]			Exposure category		
	Thesis	ASCE 7	AS/NZS1170.2	Thesis	ASCE 7	AS/NZS1170.2
Open water, aquatic beds	< 0.01	< 0.01	0.002	A	D	1
Bare land, crops, pasture/hay	$0.01 \leq z_0 < 0.051$	$0.01 \leq z_0 < 0.15$	0.02	B	C	2
Developed open space, shrubs, flat terrain with a few obstacles	$0.051 \leq z_0 < 0.31$	$0.01 \leq z_0 < 0.15$	0.02	C	C/B	2
Forests, suburban terrain, single family houses	$0.31 \leq z_0 < 0.61$	$0.15 \leq z_0 < 0.7$	0.2	D	B	3
Evergreen forests, high-rise buildings, inner cities	$z0 > 0.61$	$0.15 \leq z_0 < 0.7$	2.0	E	B	4

Table 4.3: Comparison of established roughness regimes in Table 4.2 with ASCE 7 and AS/NZS1170.2 standards.

With respect to the differences in z_0 – boundaries and exposure categories, ASCE 7 uses B, C, and D regimes, with exposure B containing rough terrain and exposures C and D smoother terrains as opposed to roughness regimes established in this thesis. The range of AS/NZS1170.2 exposure categories varies from 1 to 4 with lower numbers indicating smoother terrain. The main difference between all three methods is the number of exposure categories. While ASCE 7 and AS/NZS1170.2 use four different categories, established roughness regimes in this thesis encompass five. Of note is that exposure descriptions for thesis roughness regimes B and C match only one category for ASCE 7 (i.e. C) and AS/NZS1170.2 (i.e. 2).

Using the roughness classes established in the thesis, the third step in the observational analyses involved the determination of preliminary roughness profiles upstream of all 129 tower locations within a 10 km radius. These preliminary roughness profiles contain step changes in roughness at 30 m resolution, based on the C-CAP land cover resolution. Undertaking this step allows an assessment of the C-CAP land cover dataset accuracy and whether further terrain quality control is required. Figure 4.1 shows a surrounding roughness profile in a direction of 90° for Tower 222A, deployed in Hurricane Bill (2015) about 3 km North-West of Palacios, Texas, USA.
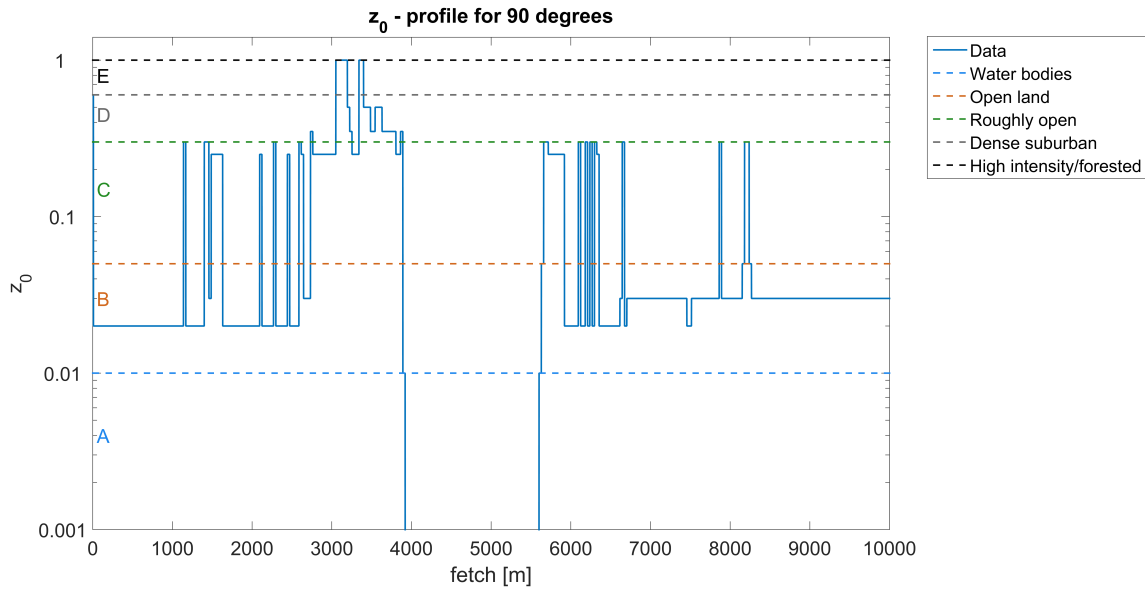
Figure 4.1: Plain z_0 profile over fetch: Tower 222A, 90° direction, deployed in Hurricane Bill (2015) about 3 km North-West of Palacios, Texas, USA.

It is shown that the tower is located in roughness regime D before transitioning to a patch of open land of 1129 m length. Considering the fact that roughness regime D includes residential buildings and dense forests with trees greater than five meters, it is unlikely that a tower would have been deployed in such a region. Hence, it is apparent that regime D was assigned incorrectly. This conclusion is further supported through historical areal imagery displayed in Figure 4.2.
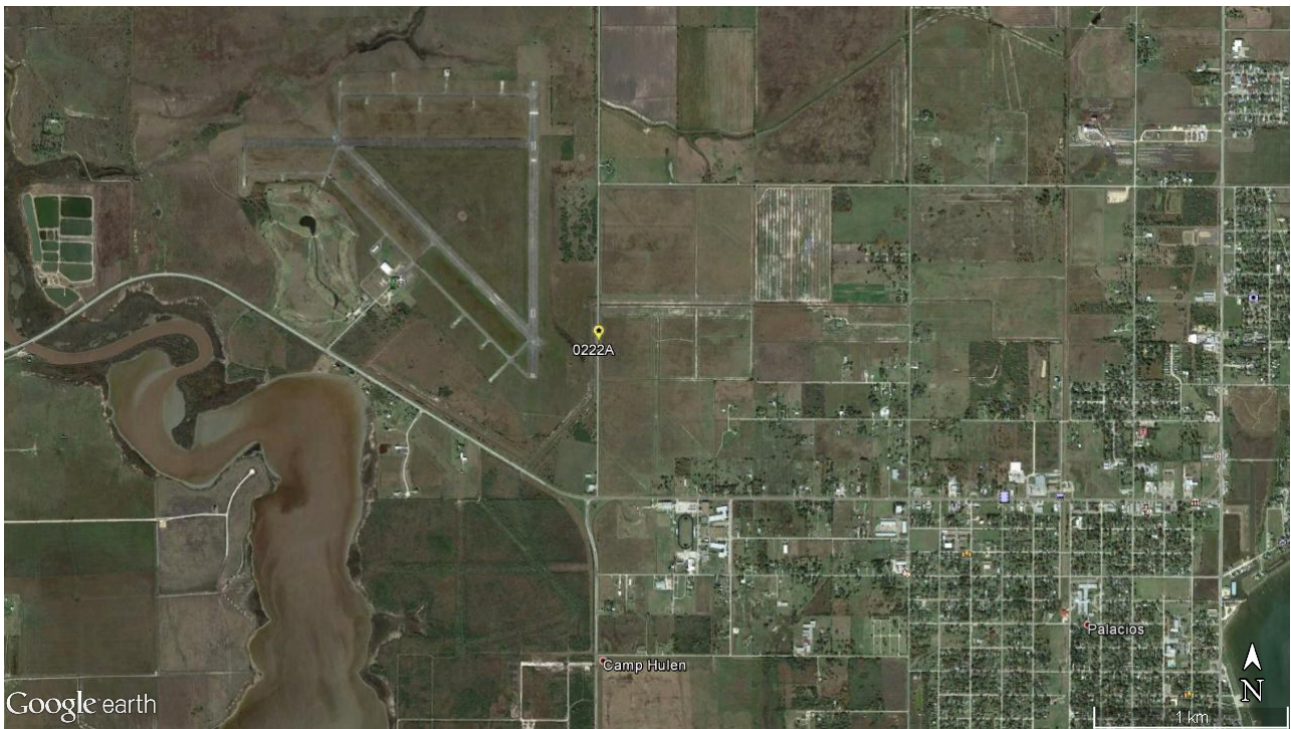
Figure 4.2: Location of Tower 222A deployed in Hurricane Bill (Google Earth Pro imagery with historical map from 11/2014)

Referring to Figure 4.2, Tower 222A is deployed about 300 m east of an airport runway and next to a street with mostly flat grassland surrounding the site. As a consequence, terrain surrounding the tower is more appropriately classified as open land (roughness regime B) instead. There are two reasons for such inconsistencies: First, streets in the C-CAP Land Cover Atlas belong to "Low Intensity Developed", which was assigned a z_0 of 0.35 m and therefore classified in dense suburban regime D. Second, the resolution of the C-CAP dataset is 30 m. Given many towers were deployed near roads, this resolution meant many towers were misclassified in this manner. To improve imprecise classifications and terrain fetch distances, further methods to improve land cover quality were explored.

A solution considered was to re-evaluate the assigned z_0 of the "Low Intensity Developed" land cover class. However, a review of *NOAA* [2010] reveals that constructed surface such as streets, roads, large sheds single family housing along with vegetation (trees and grasses) are all considered together within the "Low Intensity Developed" land cover typology. Assigning a smaller roughness value to this class would misclassify small buildings and trees into roughness regime C (roughly open), despite being the appropriate type for roads, carparks, etc. Consequently, the method of adjusting z_0 would have added more bias to the current classification because of the inherent groupings within the C-CAP atlas.

Another error arose in the C-CAP terrain classification system due to streets always being considered to be embedded in areas of trees or (small) buildings, according to the official *NOAA* [2010] documentation. In other words, streets surrounded by flat, open land are not considered any different than embedded in suburban terrain. This finding is contrary to previous studies which have suggested "no significant roughness differences appear to exist between various forms of such naturally-flattened

terrain types and artificial flat hard surfaces like tarmac or concrete" [*Wieringa*, 1993]. Consequently, streets embedded in open land should also be treated as being part of open land. In order to apply this individual treatment of terrain types, it was deemed necessary to quality-control and reassess all 129 tower sites. This reassessment will also improve resolution errors that were found to be present in fetch measurements.

4.2.1 Quality Control of Upstream Roughness Profiles

Following the example of Tower 222A deployed in Hurricane Bill (2015), land cover classification profiles were reviewed for all 129 towers. Considering deployment strategies in place for all programs, each tower is expected to only be located within either open land (B) or roughly open (C) terrains. This expectation contrasts the findings of *Giammanco et al.* [2016], who found a total of 503 10-minute data segments being measured in rough terrain (0.19 m $< z_0 < 0.5$ m). As such, to ensure that all towers are assigned accurate roughness profiles, initial C-CAP land cover classifications were thoroughly reviewed. During this investigation it was found that two towers were classified in regime A, 51 in regime B, 17 in regime C, 48 in regime D, and 11 in regime E. Consequently, at least 47% of the 129 towers were assigned to roughness regimes they are not expected to be located in. This finding was mainly attributed to towers being deployed close to streets, parking lots or airport runways, which are all part of C-CAP land cover classes assigned to roughness regime D. Another source of uncertainty was the resolution dependence previously discussed. Hence, towers 111A and 109A were both deployed close to water in Hurricane Isaac (2012) and Hurricane Sandy (2012), respectively, and were assigned to water bodies (regime A) by C-CAP.

In order to eliminate C-CAP errors, a manual assignment method using historical Google Earth areal imagery data taken close to the date of TC occurrence was developed. Areal imagery data was combined with the knowledge of all 129 geographical tower positions to document upstream terrain along the centreline of 10° bins, with the first three terrain changes identified and characterised. Information about the upstream terrain included assigning the roughness regime A, B, C, D, or E, and the regime fetch. Necessary distance and fetch measurements were made using the ruler tool in Google Earth. A practical example of how these measurements were undertaken is illustrated in Figure 4.3.
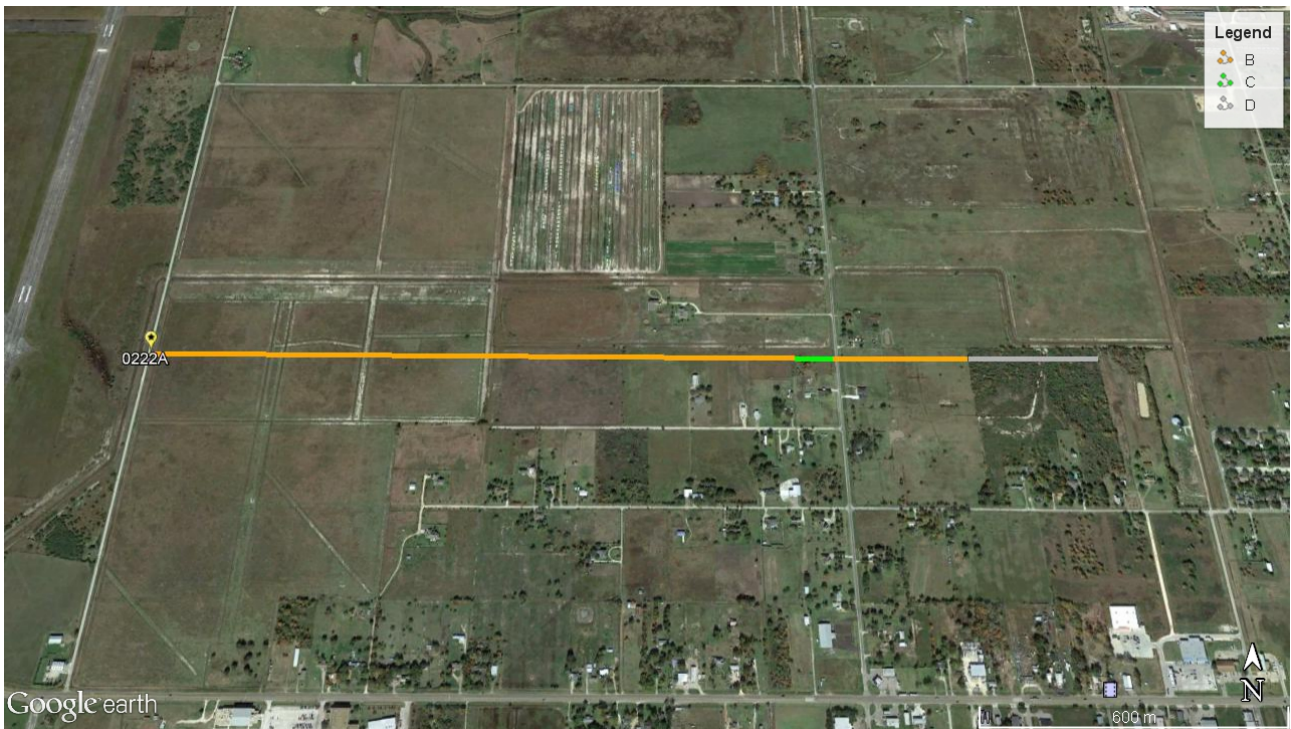
Figure 4.3: Upstream Terrain of Tower 222A deployed in Hurricane Bill (Google Earth Pro imagery with historical map from 11/2014)

Figure 4.3 denotes Tower 222A being deployed next to a street with open, flat land in the 90° cone, which was classified as regime B, open land (orange color). After a fetch of about 1500 m the underlying terrain changes to a 100 m patch of roughly open, including a few shrubs and single trees (green color). The terrain then transitions back to regime B featuring bare, flat land with a fetch of about 300 m (orange color). Finally, the terrain changes from open land to dense suburban with a 300 m fetch of a forest (grey color). To demonstrate the discrepancy between assigned roughness regimes using C-CAP and the quality-controlled manual approach, Table 4.4 shows a side-by-side comparison of roughness regimes determined for Tower 222A in Hurricane Bill (2015).

C-CAP Regime	C-CAP Fetch [m]	New Regime	New Fetch [m]
D	8	B	1504
B	1129	C	97
D	28	B	312
B	231	D	306

Table 4.4: Determined roughness regimes upstream of Tower 222A in Hurricane Bill (2015) using C-CAP and the quality-controlled manual approach.

Roughness regimes and fetches shown in Table 4.4 highlight the discrepancy when using an automated approach compared to a manual procedure. First, the underlying roughness regime of Tower 222A changed from D to B, and the fetch of B dramatically increased to about 1500 m. Within this distance, the C-CAP roughness regimes changed five times before a transition from roughly open terrain

(regime C) is evident (not shown). This example underpins the importance of using the quality-controlled manual approach to ensure roughness regimes and fetches are assigned correctly. This holds especially true in Australian regions, where existing land cover datasets exhibit much coarser resolutions. However, the entire assessment of fetches and roughness regimes for all 129 towers requires a range of assumptions, which are explained in the following section.

4.2.2   Assumptions and Known Limitations

In this study, a terrain change is defined as a step change in terrain following a fetch of at least 25 m. This fetch threshold was introduced, because the surface character of terrain may change very rapidly in nature. For some towers, three or more terrain changes would occur within the first 50 m. A further assumption is that the terrain and its surface characteristics are static. Due to strong wind speeds during TCs, the shape of vegetation may change with trees losing their leaves or uprooted bushes, which is almost impossible to account for. This possible change of the surface characteristics also manifests over water bodies. In fact, towers deployed in close proximity to rivers, lakes, and oceans are affected as water might be pushed towards the tower. If that occurs, the distance between tower and water may reduce, which is not being considered in the analysis, but is part of the discussion as a potential error source. A second effect of the uncertainty of the waterline due to high wind speeds is the development of high waves, which might have an increased roughness compared to a smooth water surface with $z_0 \approx 0.0005$ m (compare Table 4.2). However, it is assumed that a rougher water surface will not exceed $z_0 = 0.01$ m so the classification into regime A (water bodies) still holds true.

Along with the assumptions described above, the method of determining upstream roughness profiles based on Google Earth areal imagery has its limitations. Due to the choice of the small 10° cones, it is implicitly assumed that the peak gust wind speed for a particular 10-minute interval falls within 5° of the mean wind direction over the same interval. The 10° increments were primarily chosen because the surface terrain character can change rapidly along and also across the 10° wind direction cone. For simplicity it was decided that terrain along the centerline of a 10° wind direction cone represents the surface conditions for the entire cone. However, a roughness profile in a certain direction gives an indication of the terrain along the upwind direction, but not the horizontal extend across the wind direction cone. For example, turbulent parameters such as turbulence intensity and integral length scale may be modified differently given a small area of forest 500 m away from a tower compared to a large area of forest in the same distance. Another limitation when determining upstream roughness profiles occurred in cases where historical Google Earth areal imagery had poor image quality, which added uncertainty to the estimation of the vegetation height. Furthermore, determining appropriate terrain classification based on low resolution images was found to also be erroneous. Measurements taken to estimate the fetch of each terrain class was also prone to errors, as it remains unclear, where exactly the terrain change occurs. Most terrain changes occur in a continuous pattern rather than a step change. Therefore, distance measurements obtained from aerial imagery give a rough estimation of the fetch rather representing exact fetches. As a side effect, the error in fetch becomes bigger over longer distances. However, knowledge of all the aforementioned assumptions and limitations will

help to understand error sources and support the discussion of the observational analysis.

4.3   Aggregation of Events

As turbulent characteristics were obtained and upstream tower roughness profiles determined, the final step in the observational methodology involved the aggregation of events. This was done in several ways:

- Aggregation based on underlying terrain

Towers and corresponding turbulence characteristics were aggregated based on the updated underlying roughness regime at the site. A total of 118 towers were found located in open land and 11 towers in roughly open terrain. Observed 10-min segments were selected independent of any thresholds, upwind terrain or fetch requirements to study the behaviour of turbulence characteristics in open land and roughly open first.

- Aggregation based on underlying and upwind terrain

Towers and corresponding turbulent characteristics were matched when upstream roughness profiles were the same for 10°-wide wind direction cones. Moreover, upstream roughness profiles exhibiting single or multiple terrain changes were identified. To investigate the response of turbulent statistics to different upwind terrain, transitions from water bodies (A), roughly open (C), dense suburban (D), high intensity/forested (E) to open land (B) and water bodies (A), open land (B), dense suburban (D), high intensity/forested (E) to roughly open (C) were investigated. To be included in this aggregation, the upwind terrain z_{01} must exhibit a sufficient fetch x_1 to maximise the probability that turbulent characteristics are in equilibrium with the underlying surface before the flow transitions to z_0 surrounding the measurement site. The upwind fetch requirement x_1 is defined as approximately 100 times the measurement height z, based on previous research [e.g. *Wieringa*, 1993]. In particular, x_1 must exhibit a length of at least 200 m, 300 m, 500 m, and 1000 m at measurement heights of 2.25 m, 3.2 m, 5 m, and 10 m.

- Aggregation based on underlying terrain, upwind terrain, wind speed and distance bins

For each upwind terrain sub-class identified in the previous paragraph,, turbulence characteristics are further segregated into wind speed and distance bins. Wind speed bins of 5-10 m/s, 10-15 m/s, 15-20 m/s, and over 20 m/s were used at 2.25 m and 3.2 m. For 5 m and 10 m, additional wind speed bins of 20-25 m/s and over 25 m/s were introduced given measured wind speeds at these elevations were higher. Distance bins consist of 25 m increments from 25-100 m, 100 m increments from 100-2000 m, and 1000 m increments from 2000-10000 m. As distances greater than 10000 m to the first roughness change seldom occur, observational analysis will focus on transitions where $x \leq 10$ km. The analysis will include plots of turbulence characteristics over distance to the upwind terrain using aforementioned wind speed and distance bins to derive transition profiles.

4.4 Validation of the Method

The proposed analysis technique is tested against the independent analysis using the same 10 m measurements of Tower 1 in Hurricane Irene (1999) as presented in *Miller et al.* [2015] to determine whether the current approach could replicate their results. The authors utilised these measurements to investigate turbulence intensity and gust factor transitions during TC landfall when considering the distance between tower and roughness change, and change in upwind terrain. Tower 1 was deployed in a car park next to Melbourne Beach on the east coast of Florida. Here, three primary mean 30° wide wind direction bins of 350–20°, 10–40°, and 40–70° associated with the TC passage were identified. For each bin more than 20 10-min mean wind speed segments of > 10 m/s were available with flow transitioning from open water at different distances of 80 m, 110 m, and 220 m. Acknowledging many of the known limitations described in the previous section, *Miller et al.* [2015] also highlight existing uncertainties associated with the exact position of the waterline during TC passage compared to what is viewed in areal imagery. The authors chose the centerline of each 30° cone to be representative for the measured distance between Tower 1 and the waterline in the areal imagery.

In order to replicate results presented in their Fig. 10 and 11 of *Miller et al.* [2015], roughness regimes and distances from the tower to the roughness change were documented from 350-70° in 10° increments using the current methodology. Tower 1 was found to be in open land exposure (B) with each of the directions showing a transition from water bodies at different distances of 75 m, 100 m, and 200 m. Along- and across-wind turbulence intensities I_u and I_v and 3-sec gust factors G_u and G_v were then calculated and aggregated based on the surrounding and upwind terrain (current methodology), with results shown in Figure 4.4.
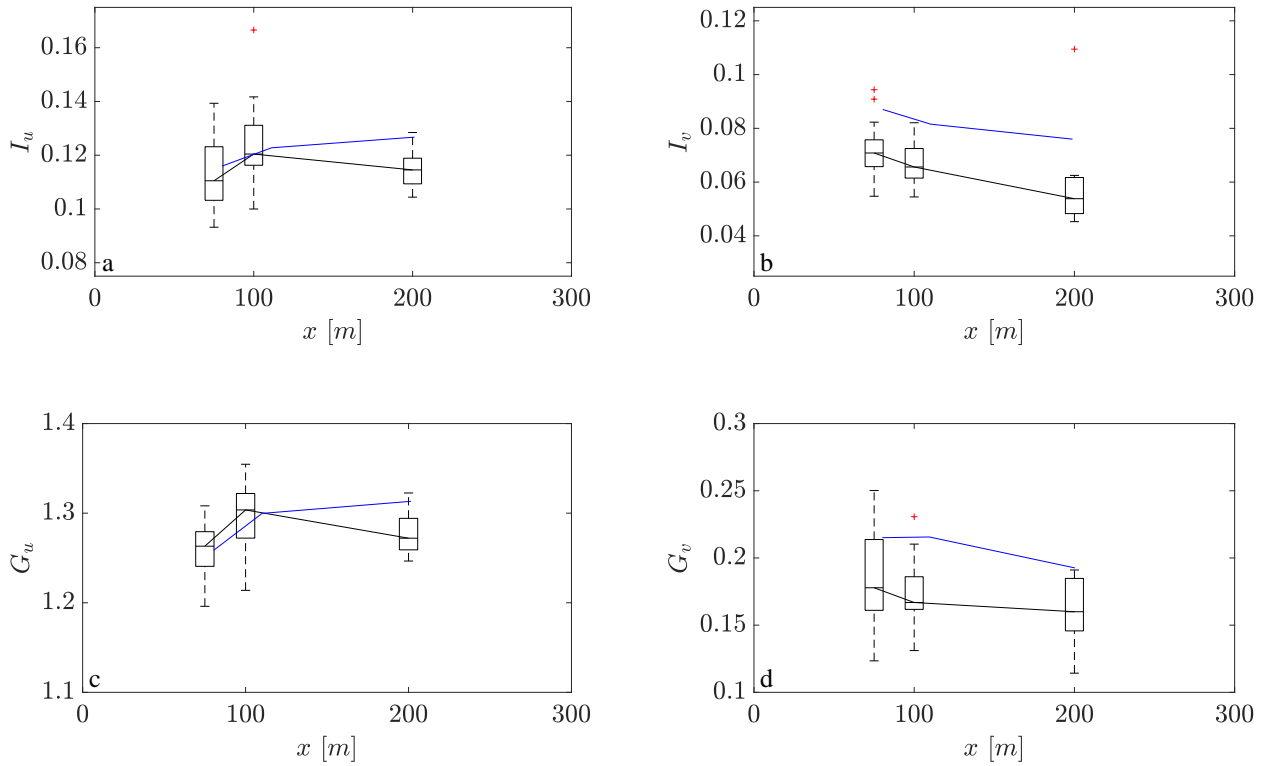
Figure 4.4: Transition of a) I_u, b) I_v, c) G_u , and d) G_v from water bodies to open land for Tower 1 in Hurricane Irene (1999). Black solid lines highlights median values and boxplots indicate variability using the current methodology. Blue solid lines denote mean values by *Miller et al.* [2015].

I_u, I_v, G_u, and G_v largely exhibit the same characteristics as observed by *Miller et al.* [2015]. Along-wind turbulence intensities and gust factors show an increase at $x = 100$ m before slightly decreasing with longer fetch distances. This is in good agreement with the results for the first two distances by *Miller et al.* [2015]. The 200 m results differ from the results of *Miller et al.* [2015], as the authors observed a greater variance in the 220 m distance bin compared to remaining distance bins. The greater variance likely led to higher I_u and G_u observed than those at lower distances. Observed across-wind turbulence intensities and gust factors in Figure 4.4 are smaller than in *Miller et al.* [2015], but I_v and G_v show the same decreasing trend in both studies. Minor discrepancies in the comparison of both analysis likely arise from processing the data. For example, *Miller et al.* [2015] used a 3-sec moving average to obtain gust factors from 10-min wind speeds, while block-averaged 3-sec gust factors were calculated in this thesis. *Miller et al.* [2015] discussed the influence of using block and moving averages with the latter being between 1.3-3.8% higher than block-averaged wind data. As such, the current methodology utilising block averages lead to lower gust factors and turbulence intensities than those observed by *Miller et al.* [2015]. As differences between the turbulence intensity and gust factor analysis are shown to be relatively small, the methodology described in previous sections is considered valid to be applied for further analysis in this thesis.

76

4.5 The Application of AS/NZS1170.2 (2011)

The calculation of AS/NZS1170.2 turbulence intensities is automated using conversions between information from Tables 2.3- 2.5. The conversions follow a simple three-step procedure, in which both the surface roughness z_0 at the measurement site and the upwind roughness z_{01} are translated into a terrain category (T_{Cat}) first using

$$T_{Cat} = log(z_0/2) + 4. \tag{4.2}$$

Eq. 4.2 follows a reformulation of Eq. 2.58 in Chapter 2.1.4.2. In the second step of the automation process, T_{Cat} values for terrain at the tower and upwind terrain are converted into $M_{z,cat}$ using values from Table 2.4. A linear relationship between T_{Cat} and $M_{z,cat}$ at multiple heights is found using

$$M_{z,cat} = \begin{cases} -0.08\,T_{Cat} + 1.07 & \text{for } z \leq 3m \\ -0.1073\,T_{Cat} + 1.1527 & \text{for } z = 5m \\ -0.1267\,T_{Cat} + 1.2373 & \text{for } z = 10m \end{cases} \tag{4.3}$$

The conversion to $M_{z,cat}$ is again required for z_0 and z_{01}, which leads to at least two different $M_{z,cat}$ values that have to be terrain-averaged using Eq. 2.59. In the final step of the automation process, terrain-average $M_{z,cat}$ values are translated into turbulence intensities using Table 2.5. Again, a relationship between $M_{z,cat}$ and I_u is established through the following equations, which are only valid within the range of T_{Cat} 1-4:

$$I_u(z) = \begin{cases} -29.593\,M_{z,cat}^4 + 113.4\,M_{z,cat}^3 - 159.64\,M_{z,cat}^2 + 97.34\,M_{z,cat} - 21.344 & \text{for } z \leq 3m \\ -85.521\,M_{z,cat}^4 + 310.53\,M_{z,cat}^3 - 418.84\,M_{z,cat}^2 + 248.04\,M_{z,cat} - 54.043 & \text{for } z = 5m \\ 37.307\,M_{z,cat}^4 - 134.97\,M_{z,cat}^3 + 182.59\,M_{z,cat}^2 - 110.14\,M_{z,cat} + 25.371 & \text{for } z = 10m \end{cases} \tag{4.4}$$

Chapter 5

Idealised Tropical Cyclone Modelling Methodology

This chapter addresses how research questions raised in Chapter 2.3.2 will be answered through numerical methods. The key method used to determine mean TCBL profiles over different land surface conditions is the Hybrid WRF Cyclone Model (HWCM) by *Bruyere et al.* [2016], which is a tool to numerically simulate idealised TCs in a real-world environment. To build the components of this method, a technical description of the WRF model is provided first.

5.1 The Weather Research and Forecasting Model

5.1.1 Overview

The Weather Research and Forecasting Model (WRF) is utilised to conduct idealised TC simulations in this thesis. Its development relies on a multi-agency effort and provides a flexible code that is portable on various computing platforms ranging from supercomputers to laptops [*Skamarock et al.*, 2008]. As indicated in Chapter 2.2.1, the WRF model exhibits two dynamical cores, Advanced Research WRF (WRF-ARW) and Nonhydrostatic Mesoscale Model (WRF-NMM), which are both Eulerian mass dynamical cores with terrain-following coordinates.

This study utilises WRF-ARW version 3.9 developed by the Mesoscale and Microscale Meteorology (MMM) Division at the National Center for Atmospheric Research (NCAR). WRF-ARW is fully compressible and non-hydrostatic and involves the following prognostic variables: Velocity components u and v in Cartesian coordinates, vertical velocity w, perturbation potential temperature, perturbation geopotential, and perturbation surface pressure of dry air [*Skamarock et al.*, 2008]. The horizontal grid is realised through an Arakawa C-grid staggering [*Arakawa and Lamb*, 1977], whereas u and v are normal to the respective faces of the grid cell and mass, thermodynamic, and scalar variables are fixed in its center [*Skamarock et al.*, 2008]. For real scenarios, initial and boundary conditions are provided through three-dimensional reanalyses datasets. For idealised simulations, one-,

two- and three-dimensional predefined cases are available. Options for lateral boundary conditions involve periodic, open, symmetric, nested, and specified choices. Physics options of the WRF-ARW model include various different schemes for microphysics, cumulus, surface, PBL parameterisation, and atmospheric radiation, which are addressed in Chapter 5.1.4.

Knowledge of all WRF-ARW features leads to six major arguments that support its use:

- The WRF model is a widely used and validated application to numerical TC modelling (more detail in Chapter 2.2).

- The WRF model has the ability to run in real, idealised and hybrid modes.

- The WRF model is configurable in various nesting options such as one-way and two-way nesting, and moving nest.

- The WRF model has the property to easily combine numerous physics packages for different weather phenomena.

- The WRF model includes the capacity to conserve mass and entropy.

- The WRF model is regularly maintained and updated.

5.1.2 Model Flow

The WRF-ARW model is composed of a preprocessing system and solver. The preprocessing system (WPS) is made up of three major programs, named geogrid, ungrib, and metgrid, which calculate and condition both terrestrial and meteorological input data. Figure 5.1 demonstrates data flow through WRF-ARW in the form of a flow chart.
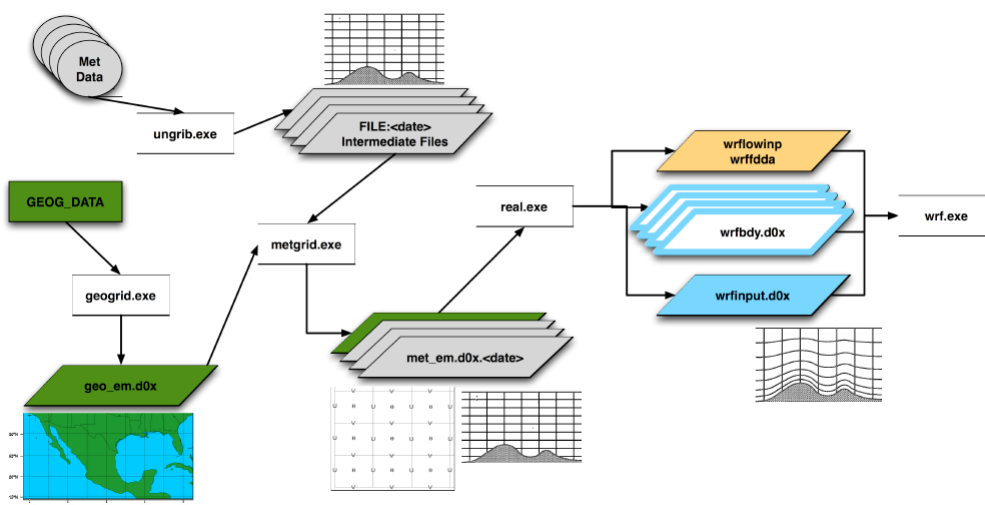
Figure 5.1: WRF-ARW program flow [*Dudhia*, 2016a]

The first step of the WPS involves the program *geogrid.exe*, which defines map projection, geographic location and dimension of domains and provides values for static (time-invariant) fields at each model grid point [*Skamarock et al.*, 2008]. This requires an external dataset with topography information (*GEOG_DATA*) that is used by *geogrid.exe* to compute latitude, longitude, Coriolis parameters, topography height, land use category, soil type for the entire domain (*geo_em.d0x*). Observational data, such as reanalyses data, are read by *ungrib.exe* and its meteorological fields are extracted from GRIB format and transformed into an *intermediate file* [*Skamarock et al.*, 2008]. If necessary, required fields are calculated from related ones, particularly temperature, pressure, and water vapour are used to compute the relative humidity. *Metgrid.exe* combines the results from the two previous steps and horizontally interpolates the atmospheric data onto the simulation domain(s) [*Skamarock et al.*, 2008]. Furthermore, it rotates the u and v wind components parallel to x- and y-axis, respectively. The result of the WPS, *met_em.d0x.<date>*, encompasses a three-dimensional snapshot of the atmosphere on the defined grid and selected time steps, which is an input for the ARW real-data processor called *real.exe*. This program is responsible for vertically interpolating the meteorological fields onto the model levels, generating initial and boundary conditions (*wrfbdy.d0x*), and creating a first guess field (*wrfinput.d0x*). Optionally, observational nudging (*wrffdda*) allows the model to keep simulations close to observations over the course of an integration [*Skamarock et al.*, 2008]. Using long simulations ($\approx$ 1 year), values for sea surface temperatures, vegetation fraction, albedo, and sea ice can be updated (*wrflowinp*), as WRF model physics do not predict these parameters. Finally, *wrf.exe* calculates the output from *real.exe* using initial and boundary conditions and physics set up over the entire domain for the desired time range.

In the case of an idealised simulation, WRF provides several predefined one-, two-, and three-dimensional domain setups such as baroclinic wave, squall line, and tropical cyclone, that replace the use of the entire WPS [*Wang et al.*, 2015].

- three-dimensional idealised cases
    - em_b_wave - baroclinic wave, 100 km
    - em_fire – surface fire, 50 m
    - em_heldsuarez – global case with polar filtering, 625 km
    - em_les – large eddy simulation, 100 m
    - em_quarter_ss - super cell, 2 km
    - em_tropical_cyclone – hurricane, 15 km
- two-dimensional idealised cases
    - em_grav2d_x – gravity current, 100 m
    - em_hill2d_x – flow over a hill, 2 km
    - em_seabreeze2d_x – water and land, 2 km, full physics
    - em_squall2d_x – squall line, 250 m

– em_squall2d_y – transpose of above problem

- one-dimensional idealised cases

  – em_scm_xy – single column model, 4 km, full physics

After selecting one of the above listed cases, output from *ideal.exe* is utilised by *wrf.exe*, which performs the desired simulation over a predefined time range.

The final method used to simulate idealised TCs during the landfall process will involve both real and idealised WRF model components, which has not been done in previous research. To adequately describe this real-idealised method (henceforth referred to as either hybrid method or HWCM), the model fundamentals are now discussed.

5.1.3 Governing Equations

The premise of an atmospheric model is to predict spatial fields of dynamic and thermodynamic parameters that describe the state of the atmosphere [*Ooyama*, 1990]. Therefore, the WRF-ARW model integrates compressible, nonhydrostatic Euler equations that are formulated in flux form with variables that have conservation properties [*Ooyama*, 1990; *Skamarock et al.*, 2008]. In general, the Euler equations are simplified Navier-Stokes equations that neglect the effects of the viscosity of the fluid and they describe how pressure, density, and velocity of a fluid are related. All equations are adjusted to the terrain-following mass vertical coordinate [*Laprise*, 1992],

$$\mu = p_{hs} - p_{ht} \tag{5.1}$$

where p_{hs} and p_{ht} denote the hydrostatic pressure along the surface and top boundary (see Figure 5.2), respectively [*Skamarock et al.*, 2008].
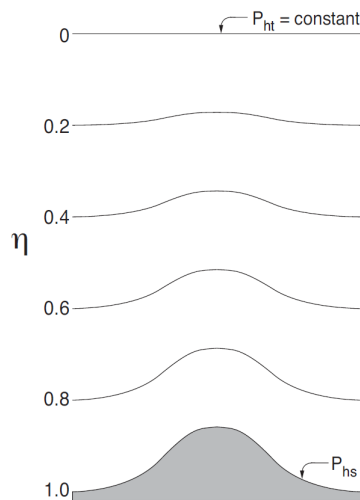
Figure 5.2: WRF-ARW terrain-following η coordinate [*Skamarock et al.*, 2008]

Hence, the terrain-following hydrostatic pressure vertical coordinate is introduced as

$$\eta = \frac{p_h - p_{ht}}{\mu} \qquad (5.2)$$

where p_h is the hydrostatic component of pressure. The terrain-following vertical coordinate η varies from 1 at the surface to 0 at the model top layer. Utilising the column mass μ the prognostic variables are

$$\boldsymbol{V} = \mu\boldsymbol{v} = (U, V, W) \text{ with } \boldsymbol{v} = (u, v, w), \ \Theta = \mu\theta \qquad (5.3)$$

with the three dimensional coupled vector velocity $\boldsymbol{V}$ and its two coupled horizontal and vertical velocities U, V, and W, respectively [*Skamarock et al.*, 2008]. Similarly, the three dimensional vector velocity $\boldsymbol{v}$ is given with its components u, v, and w, while Θ denotes the coupled potential temperature and θ the potential temperature. The coupled definitions refer to the expansion with the column mass μ. The governing equations within the ARW solver also encompass the non-conserved variables geopotential $\phi = gz$, pressure p, and the inversed density $\alpha = 1/\rho$.

With the parameters described above, the Euler equations in flux formulation can be expressed through Eq. 5.4 - 5.9

$$\partial_t U + (\nabla \cdot \boldsymbol{V}u) - \partial_x(p\phi_\eta) + \partial_\eta(p\phi_x) = F_U \qquad (5.4)$$
$$\partial_t V + (\nabla \cdot \boldsymbol{V}v) - \partial_y(p\phi_\eta) + \partial_\eta(p\phi_y) = F_V \qquad (5.5)$$
$$\partial_t W + (\nabla \cdot \boldsymbol{V}w) - g(\partial_\eta p - \mu) = F_W \qquad (5.6)$$
$$\partial_t \Theta + (\nabla \cdot \boldsymbol{V}\theta) = F_\Theta \qquad (5.7)$$
$$\partial_t \mu + (\nabla \cdot \boldsymbol{V}) = 0 \qquad (5.8)$$
$$\partial_t \phi + \mu^{-1}[(\boldsymbol{V} \cdot \nabla\phi) - gW] = 0 \qquad (5.9)$$

where Eq. 5.4 - 5.6 describe the momentum equations, Eq. 5.7 conservation equation for the potential temperature, Eq. 5.8 denotes the mass conservation, and Eq. 5.9 the geopotential equation [*Skamarock et al.*, 2008]. The diagnostic equation for the inverse density (Eq. 5.10) and the equation of state (Eq. 5.11) are:

$$\partial_\eta \phi = -\alpha\mu \qquad (5.10)$$
$$p = p_0(R_d\theta/p_0\alpha)^{c_p/c_v} \qquad (5.11)$$

The ratio c_p/c_v= 1.4 is the heat capacities for dry air, the gas constant R_d for dry air, and the reference

pressure p_0 of 1000 hPa complete the description of a dry atmosphere. Eq. 5.4 - 5.8 are written in conservative form [*Skamarock et al.*, 2008].

Building on Eq. 5.4 - 5.11, *Skamarock et al.* [2008] expand these equations for more sophisticated and complicated model applications. Hence, the authors first include moisture, secondly incorporate map projections, Coriolis and curvature terms, and finally a perturbation form of the governing equations. As the atmosphere is not considered dry, moisture has to be included in the governing equations. For simplicity, *Skamarock et al.* [2008] retain the coupling of dry air mass to the prognostic variables and the conversation equation for dry air. Combined with the dry air mass and mixing ratios of dry air for water vapor, cloud, rain, and ice, *Skamarock et al.* [2008] derive the moist Euler equations. Furthermore, the authors incorporate the four supported sphere projections, Lambert conformal, polar stereographic, Mercator, and latitude-longitude projections [*Haltiner and Williams*, 1980], as well as Coriolis and curvature terms. To adjust the governing equations, *Skamarock et al.* [2008] introduced map scale factors m_x and m_y that describe the ratio of the distance in computational space $(\Delta x, \Delta y)$ to the corresponding distance on the earth's surface

$$(m_x, m_y) = \frac{(\Delta x, \Delta y)}{\text{distance on the earth}}. \tag{5.12}$$

Along with the last modification of Eq. 5.4 - 5.11, *Skamarock et al.* [2008] reduce truncation errors and machine rounding errors in the horizontal and vertical pressure gradient, respectively. Therefore, the authors consider defining new variables as perturbations from a hydrostatically-balanced reference state and reference state variables (pressure $\overline{p}$, geopotential $\overline{\phi}$, inverse density of dry air $\overline{\alpha}_d$, dry hydrostatic pressure difference between surface and top of the model $\overline{\mu}_d$ marked with overbars) that only depend on the height $\overline{z}$ and satisfy the governing equations for an atmosphere at rest, particularly

$$p = \overline{p}(\overline{z}) + p' \tag{5.13}$$

$$\phi = \overline{\phi}(\overline{z}) + \phi' \tag{5.14}$$

$$\alpha = \overline{\alpha}_d(\overline{z}) + \alpha'_d \tag{5.15}$$

$$\mu_d = \overline{\mu}_d(x, y) + \mu'_d \tag{5.16}$$

where the perturbation from the reference state of pressure, geopotential, inverse density of dry air, and dry hydrostatic pressure difference between surface and top of the model are denoted by an apostrophe. Finally, the governing equations including moisture, map projections, and perturbation terms, can be expressed as

$$F_U = \partial_t U + m_x[\partial_x(Uu) + \partial_y(Vu)] + \partial_\eta(\Omega u)$$
$$+(m_x/m_y)(\alpha/\alpha_d)[\mu_d(\partial_x\phi' + \alpha_d\partial_x p' + \alpha'_d\partial_x\overline{p} + \partial_x\phi(\partial_\eta p' - \mu'_d)] \quad (5.17)$$
$$F_V = \partial_t V + m_y[\partial_x(Uv) + \partial_y(Vv) + (m_x/m_y)\partial_\eta(\Omega v)$$
$$+(m_x/m_y)(\alpha/\alpha_d)[\mu_d(\partial_x\phi' + \alpha_d\partial_x p' + \alpha'_d\partial_x\overline{p} + \partial_x\phi(\partial_\eta p' - \mu'_d)] \quad (5.18)$$
$$F_W = \partial_t W + (m_x m_y/m_y)[\partial_x(Vw) + \partial_y(Vw)]$$
$$+\partial_\eta(\Omega w) - m_y^{-1} g(\alpha/\alpha_d)[\partial_\eta p' - \overline{\mu}_d(q_v + q_c + q_r)] + m_y^{-1}\mu'_d g \quad (5.19)$$

with Ω as coupled coordinate velocity and g as gravity acceleration within the momentum equations (Eq. 5.17 - 5.19). Mass conservation (Eq. 5.20), geopotential equation (Eq. 5.21), potential temperature relation (Eq. 5.22), and coupled moisture (Eq. 5.23) become

$$\partial_t\mu'_d + m_x m_y[\partial_x U + \partial_y V] + m_y\partial_\eta\Omega = 0 \quad (5.20)$$
$$\partial_t\phi' + \mu_d^{-1}[m_x m_y(U\partial_x\phi + V\partial_y\phi) + m_y\Omega\partial_\eta\phi - m_y gW] = 0 \quad (5.21)$$
$$\partial_t\Theta + m_x m_y[\partial_x(U\theta) + \partial_y(V\theta)] + m_y\partial_\eta(\Omega\theta) = F_\Theta \quad (5.22)$$
$$\partial_t Q_m + m_x m_y[\partial_x(Uq_m) + \partial_y(Vq_m)] + m_y\partial_\eta(\Omega q_m) = F_{Q_m}. \quad (5.23)$$

where Θ again denotes the coupled potential temperature, θ the potential temperature, Q_m the generic coupled moisture variable, and q_m the generic mixing ratios for moisture [*Skamarock et al.*, 2008]. The hydrostatic relation (Eq. 5.24) is expressed as

$$\partial_\eta\phi' = -\overline{\mu}_d\alpha'_d - \alpha_d\mu'_d. \quad (5.24)$$

Along with the equation of state $p = p_0(R_d\theta_m/p_0\alpha_d)^{c_p/c_v}$, Eq. 5.17 - 5.23 are solved within WRF-ARW [*Skamarock et al.*, 2008]. The forcing terms in these equations (denoted with F) incorporate Coriolis terms, mixing terms, and physics parameterisations, which will be described in the following section.

5.1.4 Physical Parameterisation Schemes

The result of a numerical simulation within WRF-ARW is largely dependent on the chosen physics schemes [*Skamarock et al.*, 2008]. These parameterisations are separated into cumulus, microphysics, PBL, land-surface, and radiation schemes. In particular, they describe how clouds, water vapor, convective processes, and the transfer of moisture, heat, and momentum between surface and atmosphere are resolved in the model.

Incorporating a WRF-ARW physics combination to simulate idealised or replicate real TC path, intensity and size, is still a modelling challenge [e.g. *Hill and Lackmann*, 2009; *Nolan et al.*, 2009; *Osuri et al.*, 2012], because cumulus convection, surface fluxes of heat, moisture, momentum, vertical mixing in the TCBL, radiative heating and cooling all play important roles in TC development [*Anthes*, 1982; *Raju et al.*, 2011]. In WRF-ARW physics parameterisations are coupled, as schematically demonstrated in Figure 5.3, and described in more detail throughout this section.
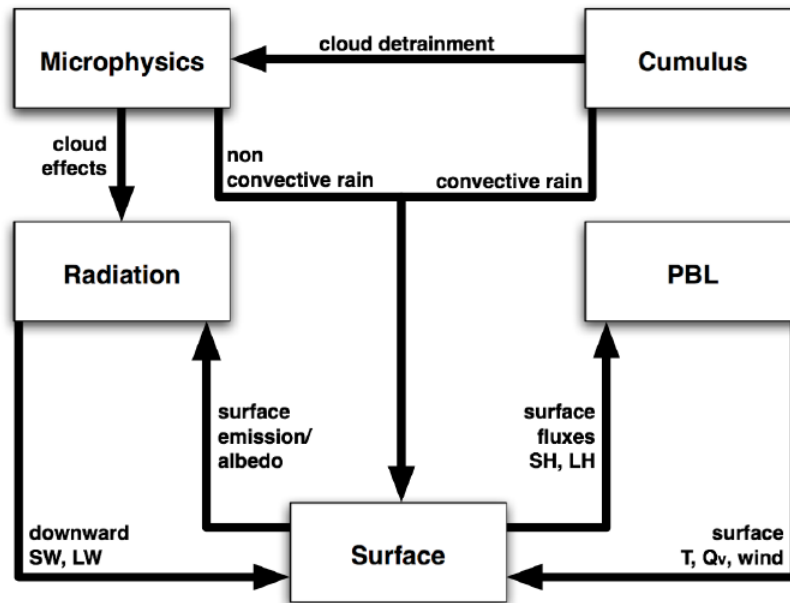
Figure 5.3: Direct interactions of physics paramaterisations within WRF-ARW [*Dudhia*, 2016b]

5.1.4.1   Cumulus Schemes

Illustrated in Figure 5.4, cumulus (CU) parameterisation schemes in WRF-ARW resolve thermodynamic and dynamic processes of moist convection occurring at sub-grid scales [e.g. *Ooyama*, 1971; *Arakawa and Schubert*, 1974; *Kain and Fritsch*, 1990].

Illustration of Cumulus Processes
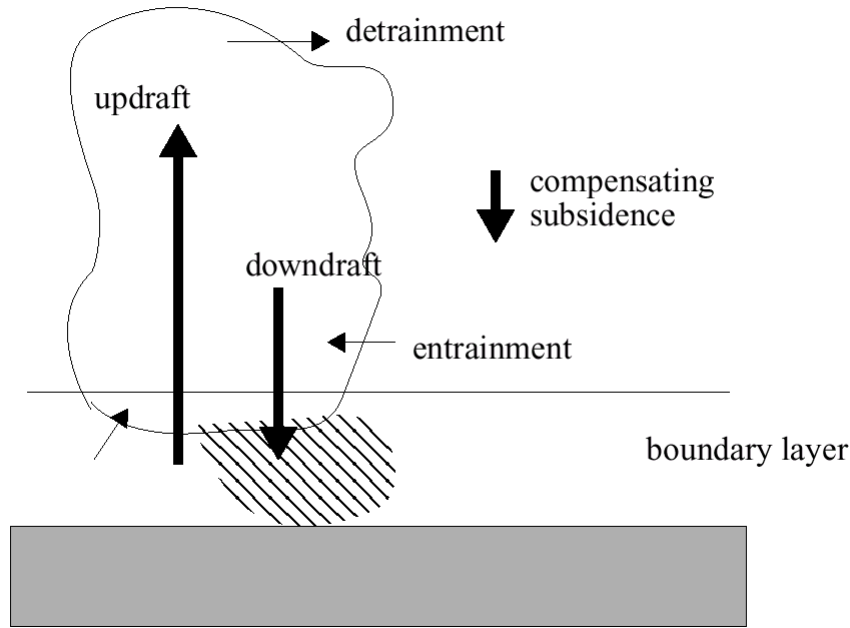
Figure 5.4: Illustration of the main processes modelled by the cumulus parameterisations schemes in WRF-ARW [*Dudhia*, 2016b].

The process of convection is responsible for redistributing heat and moisture vertically through up- and downdrafts. Ambient air is cycled in and out into the convective cloud through entrainment and detrainment, respectively [*Bretherton*, 1997]. Convection occurs in many different shapes, sizes, and durations, e.g. isolated thunderstorms, organised mesoscale systems, and TCs. These phenomena produce feedback that influences large-scale flow patterns through, for example, the ability of an organised convective system to alter upper-level winds [e.g. *Parker and Johnson*, 2000; *Houze*, 2004].

In general, CU schemes have to account for deep and shallow convection, whereas more subcategories like convective and stratiform are possible [*Dudhia*, 2016b]. The parameterisation of convection is essential for horizontal grid spacing greater than 10 km [*Liu et al.*, 2001], while there is still no consent for the usage of a CU scheme for finer resolutions. Summarised by *Stensrud* [2012], a cumulus parameterisation scheme determines the activation of convection through a specified trigger function, the intensity through closure assumptions and the vertical distribution through a specified profile or cloud model [*Stensrud*, 2012]. Using the Kain-Fritsch (KF) CU scheme [*Kain and Fritsch*, 1990, 1993; *Kain*, 2004], as an example, the basic functionality shall be explained here. In WRF-ARW, the KF CU parameterisation is the default CU scheme.

The trigger function within the KF scheme mixes adjacent surface layers until a depth of at least 60 hPa is reached to identify potential source layers for convective clouds [*Kain*, 2004]. If the temperature of a parcel of such a mixed layer is warmer than the environmental pressure at the lifting condensation level (LCL), the parcel's vertical velocity is computed at each model level including entrainment, detrainment and water loading [*Kain*, 2004]. Then convection is activated until 90% of the convective available potential energy (CAPE) is removed (closure assumption) if the vertical velocity is positive over a specified minimum cloud depth of 3-4 km [*Kain*, 2004]. Deep convection

is not favoured unless CAPE is greater than zero. Depending on the utilised scheme, some are tied to different trigger functions and closure assumptions.

5.1.4.2 Microphysics Schemes

Microphysics (MP) paramaterisations resolve cloud particles and precipitation drops of liquid or solid phase. Basically, they emulate cloud and precipitation processes that remove atmospheric moisture from the air, as demonstrated in Figure 5.5. Microphysics schemes have to account for latent heat release and absorption from condensation, evaporation, deposition, sublimation, freezing, and melting for particle types like cloud water, rain drops, ice crystals, snow, and graupel [*Dudhia*, 2016b]. Figure 5.5 gives an overview of the aforementioned hydrometeors and the processes between them. Within TCs most of these hydrometeors appear at different height levels where the bulk of the water content is close to the eye and in the spiral rainbands [*Holland*, 1987; *McFarquhar et al.*, 2006].
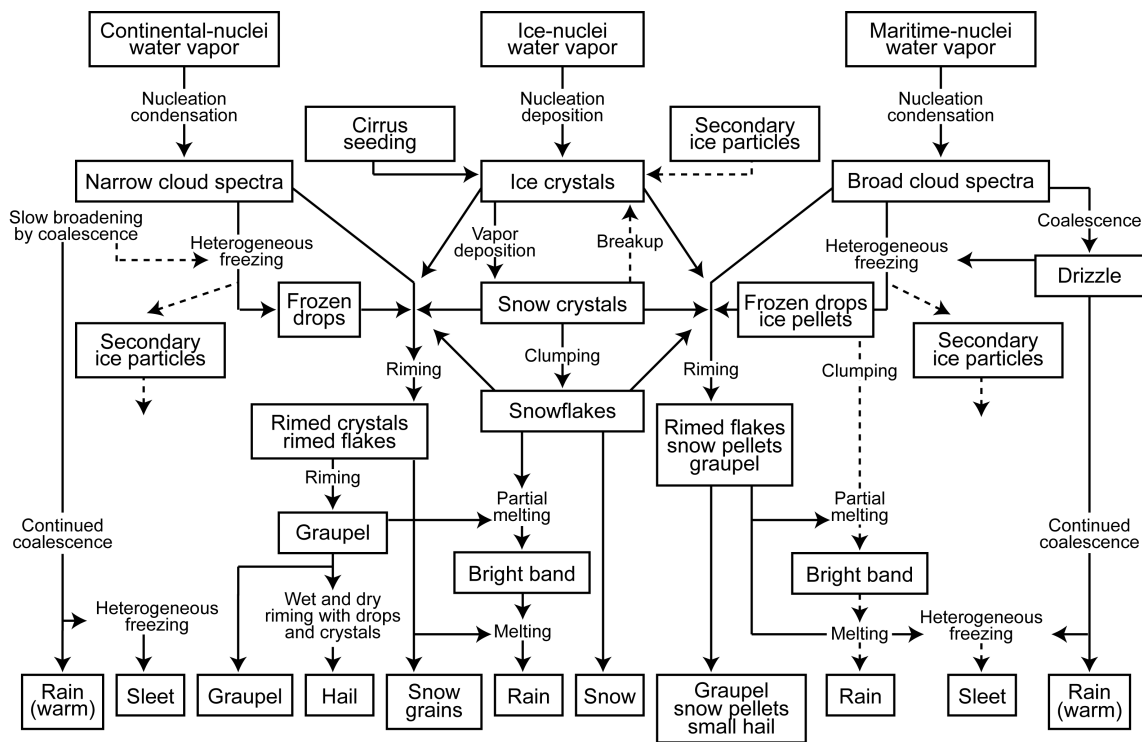
Figure 5.5: Microphysics Parameterisation: Major types of hydrometeors and the physical processes altering their shape [*Braham and Squires*, 1974]

The parameterisation of such particles and processes can broadly be categorised into two types: bin and bulk cloud microphysics algorithms [*Morrison*, 2010]. Bin-based schemes incorporate the droplets size distribution divided into bins [e.g. *Kogan*, 1991; *Milbrandt et al.*, 2008]. Bulk algorithm schemes assume the size distribution to follow a functional form. This type is adopted by most WRF-ARW schemes [*Milbrandt et al.*, 2008]. Within the bulk microphysics, single-moment, double-moment, and triple-moment schemes exist. Single-moment parameterisations exhibit one prediction equation for mixing ratios of hydrometeors [*Lin et al.*, 1983; *Hong et al.*, 2004], double-moment schemes add a prediction for the number of concentrations of hydrometeors [*Ferrier*, 1994; *Morrison et al.*, 2005], and triple-moment schemes further predict the reflectivity [*Szyrmer et al.*, 2005].

5.1.4.3 PBL and Surface Schemes

Planetary boundary layer (PBL) schemes parameterise the vertical diffusion and the fluxes of heat, moisture, and momentum up to vertical extend of the PBL. Therefore, PBL schemes process friction stress, land-surface and water-surface heat and moisture fluxes through surface layer and land surface schemes [*Dudhia*, 2016b]. In particular, surface layer schemes calculate friction velocities and exchange coefficients that enable the calculation of surface heat and moisture fluxes by land-surface models [*Trier et al.*, 2011; *Hong*, 2015]. Over water surfaces, fluxes are computed within the scheme itself, without using a land-surface model [*Hong*, 2015]. As a result, the computed fluxes within the surface models provide a lower boundary condition for the vertical transport realised in the PBL parameterisation. Figure 5.6 graphically summarizes the main processes that are modelled using the PBL and surface layer schemes.
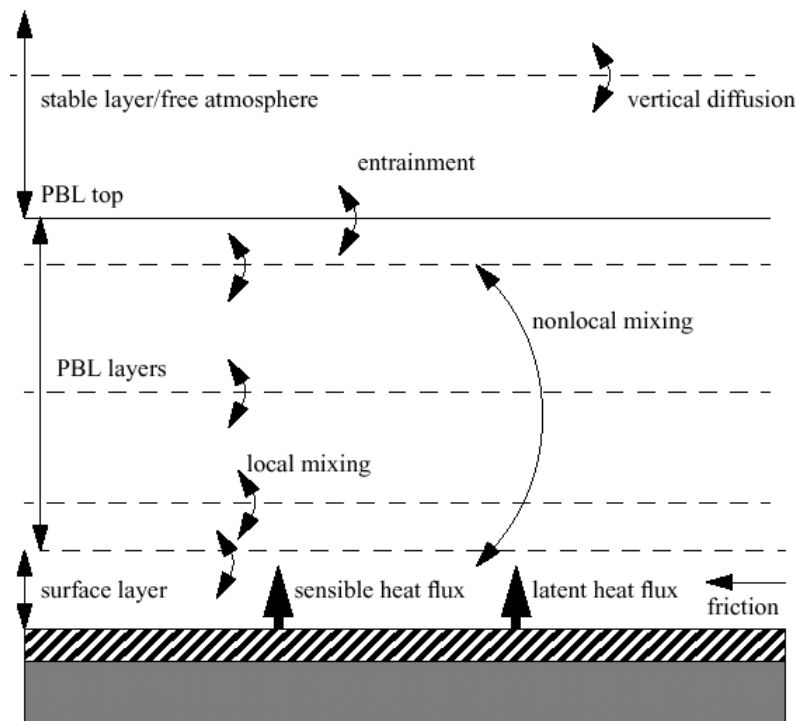
Figure 5.6: Illustration of the main processes modelled by the PBL and surface layer parameterisations schemes in WRF-ARW [*Dudhia*, 2016b].

The theoretical foundation for a PBL scheme to parameterise the processes shown above is composed of two major components: the order of turbulence closure and whether a local or nonlocal mixing approach is employed [*Cohen et al.*, 2015]. For the order of turbulence closure, the variables of the motion equations are decomposed into mean and perturbation components, where the latter ones are related to turbulent fluctuations or deviations from the atmospheric state. Equations that incorporate turbulence modelling contain more unknown terms than known terms with the unknown expressions being one order above the maximum among the other terms [*Cohen et al.*, 2015]. Within a PBL scheme, the unknown term moment is characterised as n + 1 relative to the lower-moment ones (n-th order turbulence closure). Following the example of *Cohen et al.* [2015], a 1.5-order closure scheme would predict second order TKE through the diagnoses of second-order moments for variables like

potential temperature and mixing ratio. The second important difference between the PBL parameterisations manifests through the calculation of the depth over which the variables are able to affect a given point [*Cohen et al.*, 2015]. In local closure parameterisations, only directly adjacent layers are taken into account, whereas non-local closures include multiple vertical levels to determine variables at a certain point [*Cohen et al.*, 2015].

At earlier stages of the PhD, the quality of WRF along with the aforementioned parameterisation schemes were tested extensively. Appendix B provides data and methods used to examine the choice of parameterisations on TC track and intensity behaviour through the reconstruction of TC Ita (2014). As a consequence, all idealised TC simulations introduced below were generated with the modified Tiedtke CU scheme, WSM-6 MP physics, and the YSU PBL scheme [*Hong et al.*, 2006]. The modified Tiedtke CU scheme was the preferred choice over the KF CU scheme which is suggested in the well-tested "Tropical Physics Suite"[1] in WRF version 3.9.

5.2 Hybrid WRF Cyclone Model Configuration

The major aim of this component of the thesis is to investigate TCBL profiles over different types of terrain (i.e. different surface roughness) throughout and prior to TC landfall. To do this, the Hybrid WRF Cyclone Model (HWCM) conceptualised by *Bruyere et al.* [2016] is used to generate TCBL profiles from idealised TC simulations. The HWCM is unique as it incorporates both real and idealised WRF-ARW components. Moreover, this hybrid approach sets an idealised TC into a real-world environment including β-drift and Coriolis terms, which are usually neglected in idealised TC studies [e.g. *Hill and Lackmann*, 2009; *Wong and Chan*, 2007]. Two major steps are required to successfully conduct the hybrid simulation:

1. Spin up of an idealised TC (idealised component)

2. Place the generated TC into a real-world environment (real component)

The following subsections will explicitly explore both idealised and real components in order to shed light on how idealised TC simulations are conducted and subsequent TCBL profiles are generated.

5.2.1 Idealised Component

The idealised component of the HWCM involves spinning up an idealised TC over an open water surface that has the ability to sustain in a favorable environment. To do this, the first step requires to compile the WRF model in the three-dimensional em_tropical_cyclone case. Before executing the compilation, predefined TC properties by *Rotunno and Emanuel* [1987] were examined and modified

---

[1]http://www2.mmm.ucar.edu/wrf/users/wrfv3.9/tropical_suite.html

to create a severe TC, that was able to sustain and develop in a real-world environment. These pre-defined TC parameters, listed in Table 5.1, include the outer radius r_0, the radius of maximum winds r_{max}, the value of maximum winds v_{max}, the depth of the vortex z_{dd}, the Coriolis parameter f, and the sea-surface temperature sst. These parameters mark the initial state of the vortex and will evolve throughout the spin-up process. The storm dimensions and characteristics are based on TC Debbie (2017), which made landfall as a Category 4 Severe TC at the Whitsunday Coast in Queensland, Australia. TC spin up initial parameters were set up as shown in Table 5.1.

Parameter	RE87 Value	New Value	Description (unit)
r_0	412500	500000	outer radius (m)
r_{max}	82500	65000	approximate radius of max winds (m)
v_{max}	15.0	15.0	approximate value of max wind speed (m/s)
z_{dd}	20000	20000	depth of vortex (m)
f	5.0×10^{-5}	-3.76×10^{-5}	Coriolis parameter (1/s)
sst	28	30	sea-surface temperature (Celsius)

Table 5.1: Idealised TC spin-up default [*Rotunno and Emanuel*, 1987] and adjusted parameters.

The challenge of parameter adjustment was to generate a Southern Hemisphere storm that has the ability to further develop in a TC-favorable environment for multiple days before making landfall. This holds particularly true during the first couple of timesteps within the simulation, when the generated TC is placed into a real-world environment. While the real-world environment exhibits favorable TC conditions, it will not include a TC as default. Therefore, the WRF model has to balance the sudden occurrence of a spun-up TC in the early stages of the simulation so the TC is particularly designed to largely keep its properties during this time. This is the reason a more intense TC is created than the basic control run TC in *Rotunno and Emanuel* [1987]. In particular, r_0 is increased to 500 km and r_{max} is reduced to 65 km. To account for a Southern Hemisphere TC at 15°, the Coriolis parameter was assigned negative. Of further note is the SST increase to 30°C to supply enough energy for the TC to sustain its strength before landfall. To drive the dynamic and thermodynamic properties of the storm in the horizontal and vertical direction, an atmospheric background sounding supportive of TC intensification was required during spin up. Ideally, the atmospheric sounding should have high moisture throughout all vertical levels as well as low wind shear $\leq$ 10 m/s [e.g. *Finocchio et al.*, 2016]. However, winds are set to zero in the idealised run to prevent the TC from moving. Figure 5.7 shows the atmospheric sounding used in this thesis that is initially based on a 30-year climatological average of Willis Island [*Črnivec and Smith*, 2017], a small coral island about 500 km offshore of Northeast Queensland, Australia. The vertical moisture profile was increased so that the relative humidity rH = 90% at the lowest level and rH = 75% at 550 hPa. The surrounding atmospheric pressure of 1005.6 hPa in the 30-year Willis Island sounding represents a typical pressure found in the immediate vicinity of a TC [*Holland*, 1997].
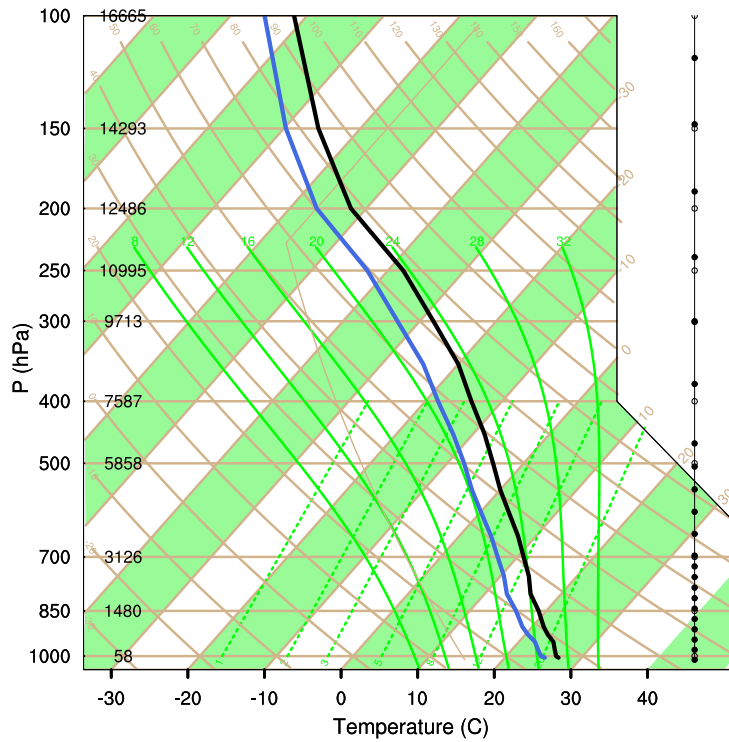
Figure 5.7: Atmospheric background sounding with zero winds to spin-up an idealised TC. Black and blue solid lines represent temperature and dewpoint, respectively.

The TC is spun up on three domains of 2160 grid points each using 18, 6, and 2 km horizontal resolution and 50 vertical levels. During the five-day TC spin-up process, initial parameters listed in Table 5.1 will evolve. Figure 5.8 contains a time series of how minimum central pressure and maximum wind speed v_{max} change throughout TC spin-up.
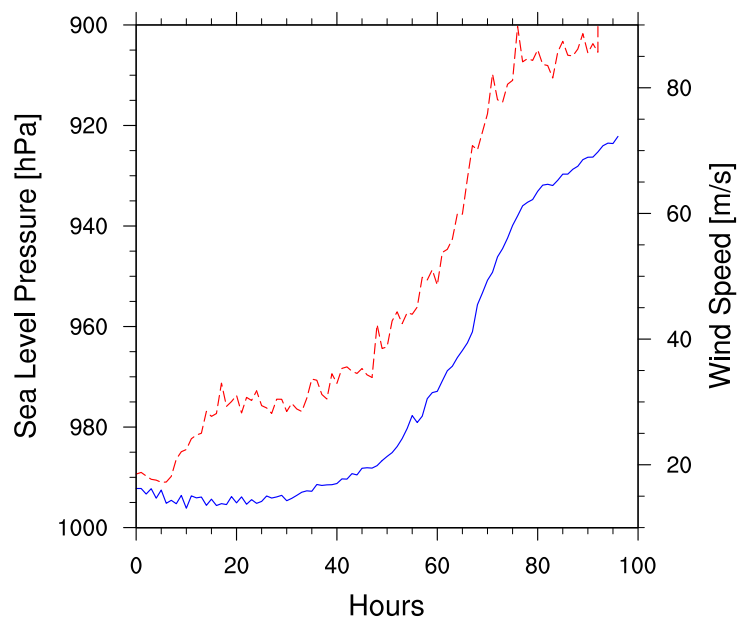
Figure 5.8: Minimum central pressure (blue solid line) and maximum wind speed v_{max} (red dashed line) during TC spin up at 6 km horizontal resolution.

The TC spin-up simulation runs for 96 hours in total with minimum central pressure and v_{max} rapidly increasing between 50 and 70 hours into the simulation. The time and rate of v_{max} intensification aligns well with experiment D in *Rotunno and Emanuel* [1987], where the authors decreased r_{max} by 50% but for a smaller vortex and lower SST. After 70 hours into TC spin up the intensification rate of both parameters slows down and shows a more gradual increase until the end of the simulation. To allow the TC to further develop within a real-world environment, the TC at a timestep of 78 hours is extracted for further analysis. At this time the generated TC is found to exhibit all requirements for a major TC. The idealised storm is well-organised with $v_{max} = 85$ m/s, $r_0 \approx 300$ km, $r_{max} \approx 35$ km and a minimum sea level pressure of 935.3 hPa, as calculated on the 6 km horizontal resolution grid. Captured TC properties at this timestep are inserted into the real-world environment, which is further explained in the following subsection.

5.2.2 Real Component

The real component of the HWCM provides initial and boundary conditions for the hybrid simulations to be conducted. The general procedure is outlined below and explained in more detail in the text that follows.

1. Setup domain and nests

2. Generate prerequisite atmospheric conditions

3. Replace prerequisite atmospheric conditions with favorable TC environment

4. Replace existing land-water distribution

5. Insert idealised TC at desired location

More specifically, the WRF preprocessing tools geogrid, ungrib, and metgrid (Chapter 5.1.2) were run first to set up a triply nested domain of 10800 km x 10800 km, 4800 km x 3000 km, and 1200 km x 1200 km with resolutions of 18, 6, and 2 km, respectively. To fill each grid point with information about atmospheric conditions through ungrib and metgrid, one timestep of NCEP Re-analysis (Appendix B.1.2.1) data for the 25th March 2017 00 UTC was chosen. The choice of date and time had no particular significance, because meteorological values from NCEP Reanalysis are replaced with atmospheric conditions at each grid point from the adapted Willis Island sounding in Figure 5.7. The replacement of atmospheric conditions is crucial to ensure a conducive environment in which the TC can persist and develop. In addition, an easterly wind regime with wind speeds of 10 kts (5.14 m/s) from 90° is set on all vertical levels to push the TC towards land and to account for the Coriolis force making the TC drift southwest. Various vertical wind speed profiles were tested with vertical wind shear values up to 10 m/s. It was found that the inclusion of such vertical wind profiles added too much complexity to the simulated TCs and attempts to fully control the storm prior to landfall failed. Therefore, the conceptualised easterly wind regime was held as simple as possible.

After initially defining favorable TC environment at each grid point, the domain undergoes further processing. This involves setting the land-water distribution and the land cover information. Land covers about 40% of the second nest, d02, whereas the inserted storm domain d03 was placed about 1300 km off the coastline to ensure enough time for the TC to stabilise before translating onto land. The spun-up TC is positioned at the center of d03. Figure 5.9 shows the land-water distribution and the setup of all nests.
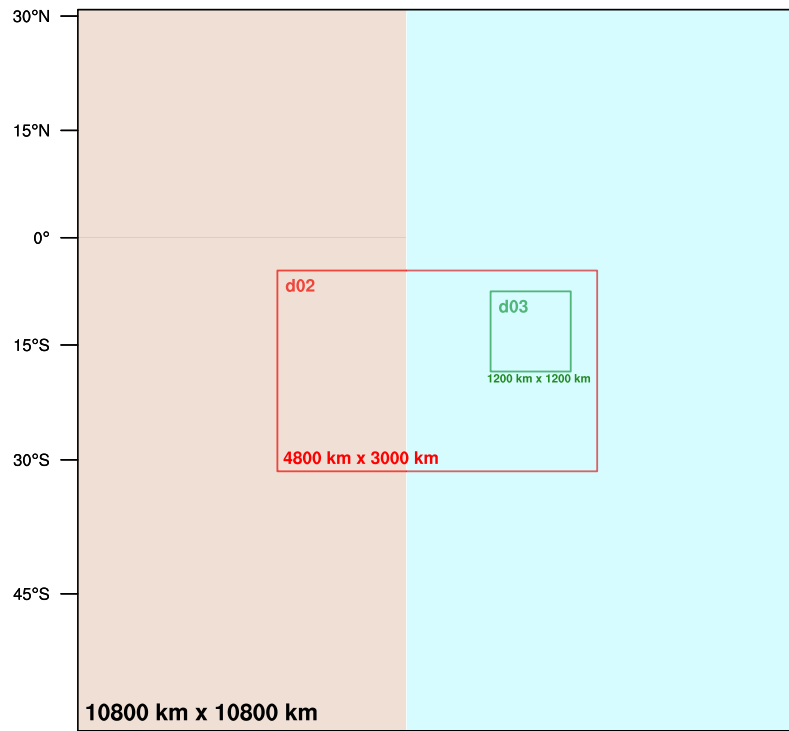
Figure 5.9: Domain setup and land-water distribution for TC simulations.

Various sensitivity tests were run to arrive at this domain setup. In these sensitivity runs two to four domains of different sizes, resolutions and positions were tested. The purpose was to obtain an appropriate domain setup that is computationally effective and satisfies all requirements to successfully conduct idealised TC simulations. Therefore, a total of three domains was found to be most suitable. Of note is the large outer domain size, which was chosen to avoid boundary effects that would influence TC track and intensity.

For the purpose of investigating the TCBL response to different land surface conditions at landfall, the surface roughness z_0 is changed for each experiment. The WRF model generally uses the MODIS-based land use classification values outlined in Table 5.2.

Land Use Category	Land Use Description	WRF surface roughness [m]
1	Evergreen Needleleaf Forest	0.50
2	Evergreen Broadleaf Forest	0.50
3	Deciduous Needleleaf Forest	0.50
4	Deciduous Broadleaf Forest	0.50
5	Mixed Forests	0.50
6	Closed Shrublands	0.05
7	Open Shrublands	0.06
8	Woody Savannas	0.05
9	Savannas	0.15
10	Grasslands	0.12
11	Permanent Wetlands	0.30
12	Croplands	0.15
13	Urban and Built-Up	0.80
14	Cropland/Natural Vegetation Mosaic	0.14
15	Snow and Ice	0.01
16	Barren or Sparsely Vegetated	0.10
17	Water	0.001
18	Wooded Tundra	0.30
19	Mixed Tundra	0.15
20	Barren Tundra	0.10

Table 5.2: IGBP-Modified MODIS 20-category Land Use Categories in WRF-ARW (Table 2 in http://www2.mmm.ucar.edu/wrf/users/docs/user_guide_V3/users_guide_chap3.htm) with z_0 values given in LANDUSE.TBL (https://github.com/yyr/wrf/blob/master/run/LANDUSE.TBL)

To avoid an unduly large number of possible simulations, four different land use categories are chosen from Table 5.2 to represent roughness regimes B-E established in Chapter 4. The base simulation was modified through a parametric set of tests listed in Table 5.3. The base run (open land, B) includes flat terrain and low roughness of $z_0 = 0.01$ m. Subsequent simulations are conducted on rougher terrain (regime C to E) over the entire land area as shown in Table 5.3. All simulations were ran for five days (120 hours) in total on NCAR's supercomputer Cheyenne.

	Regime	Land cover type	z_0 [m]
Base	B	Barren or Sparsely Vegetated	0.01
	C	Savannahs	0.15
	D	Mixed Forests	0.50
	E	Urban and Built-Up	0.80

Table 5.3: Numerical simulations with adjusted surface roughness

Chapter 6

Turbulence Variation with Terrain in Landfalling Tropical Cyclones

This chapter addresses the research questions raised in Chapter 2.3.1 through a detailed analysis of all observational data introduced in Chapter 3 using the techniques discussed in Chapter 4.

A better understanding of near-surface turbulence characteristics in cyclone-prone regions is important to allow forecasters and engineers to accurately predict TC wind speeds and to design buildings so they can withstand strong winds. These turbulence characteristics are modified by surface roughness elements such as bushes, trees, and houses upwind of a given location, as indicated by previous research [e.g. *Miller et al.*, 2015]. The present analysis builds on this research and explores in detail how near-surface turbulence characteristics transition from one roughness regime to another at elevations of 2.25 m (StickNet), 3.2 m (SWIRLnet), 5 m and 10 m (FCMP).

6.1   Analysis based on Terrain Conditions at the Tower Site

It is common during TC field deployments to site weather towers in largely smooth, flat terrain with few obstacles in the immediate vicinity (i.e. < 50 m). This is true for the campaigns discussed in the observational methods Chapter 4.2.1. A total of 129 towers were deployed in three different campaigns during 11 TCs between 2004 and 2017, with 118 towers sited in open land (roughness regime B) and 11 towers in roughly open (roughness regime C). Table 6.1 gives a detailed overview of the total number of towers and 10-min segments used for each roughness regime (see also Table 4.1).

| | open land B | | roughly open C | |
Height [m]	Tower	10-min segments	Tower	10-min segments
2.25	94	18830	5	1083
3.2	6	2968	-	-
5	17*	1500	6	368
10	18	1631	6	365
Total	**118**	**24929**	**11**	**1816**

Table 6.1: Summary of Table 4.1 with number of 10-min segments for open land and roughly exposure. Measurements at 5 m and 10 m elevation originate from the same tower and therefore count as one tower. *Wind measurements at 5 m from T0 during Hurricane Francis (2004) were faulty and therefore not included in the analysis.

The first step in the observational analysis is to calculate the turbulence statistics from all 129 towers located within open land and roughly open exposure. Of note is that all turbulence characteristics were aggregated irrespective of the upwind terrain z_{01} or the distance x between tower and first roughness change. Figures 6.1-6.2 display open land along- (Fig. 6.1) and across- (Fig. 6.2) 10-minute mean wind components of the turbulence intensity I_u and I_v, 3-second gust factor G_{u3} and G_{v3}, peak factor g_{u3} and g_{v3}, skewness γ_{su} and γ_{sv}, kurtosis γ_{ku} and γ_{kv}, and integral length scale L_u and L_v, respectively, at 2.25 m elevation, displayed as grey circles. The number following I_u (i.e. $I_{u,2.25}$) and all other variables is the measurement elevation. Shaded regions in these plots denote the area between the 25th and 75th percentile with the median curve (red solid line) in the middle. In all subsequent plots, median values are chosen over mean values as extreme values were found not to affect the median as much as the mean. Figures 6.3-6.4 show the same data for roughly open towers. Observational analysis in these figures and all subsequent plots is based on a 10-min wind speed mean and a 3-sec gust average time.
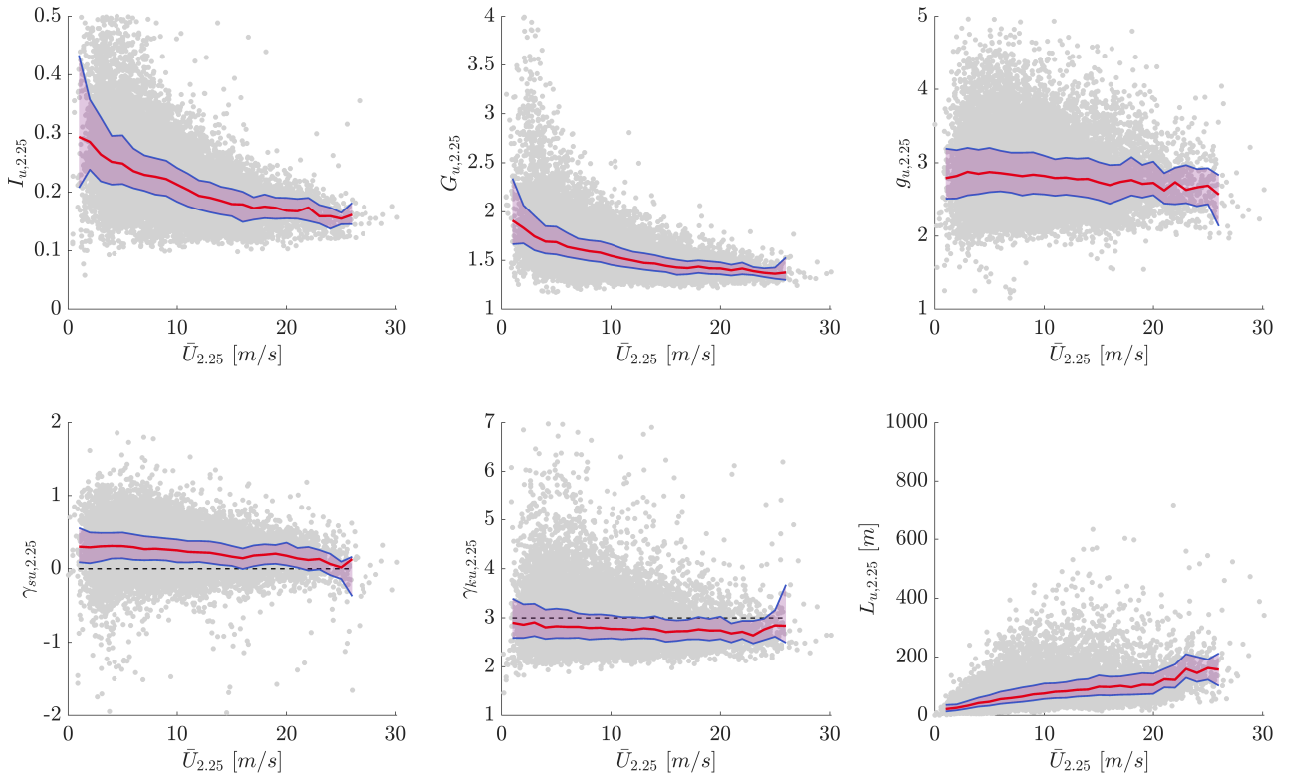
Figure 6.1: Along-wind component of turbulent characteristics in open land at 2.25 m measurement height. Grey circles show data for each analysed 10-minute segment with the 1 m/s binned median and area between 25th and 75th percentile presented by the red solid line and the shaded region, respectively. Black-dashed lines on γ_{su} and γ_{ku} plots represent the value for a normal distribution.
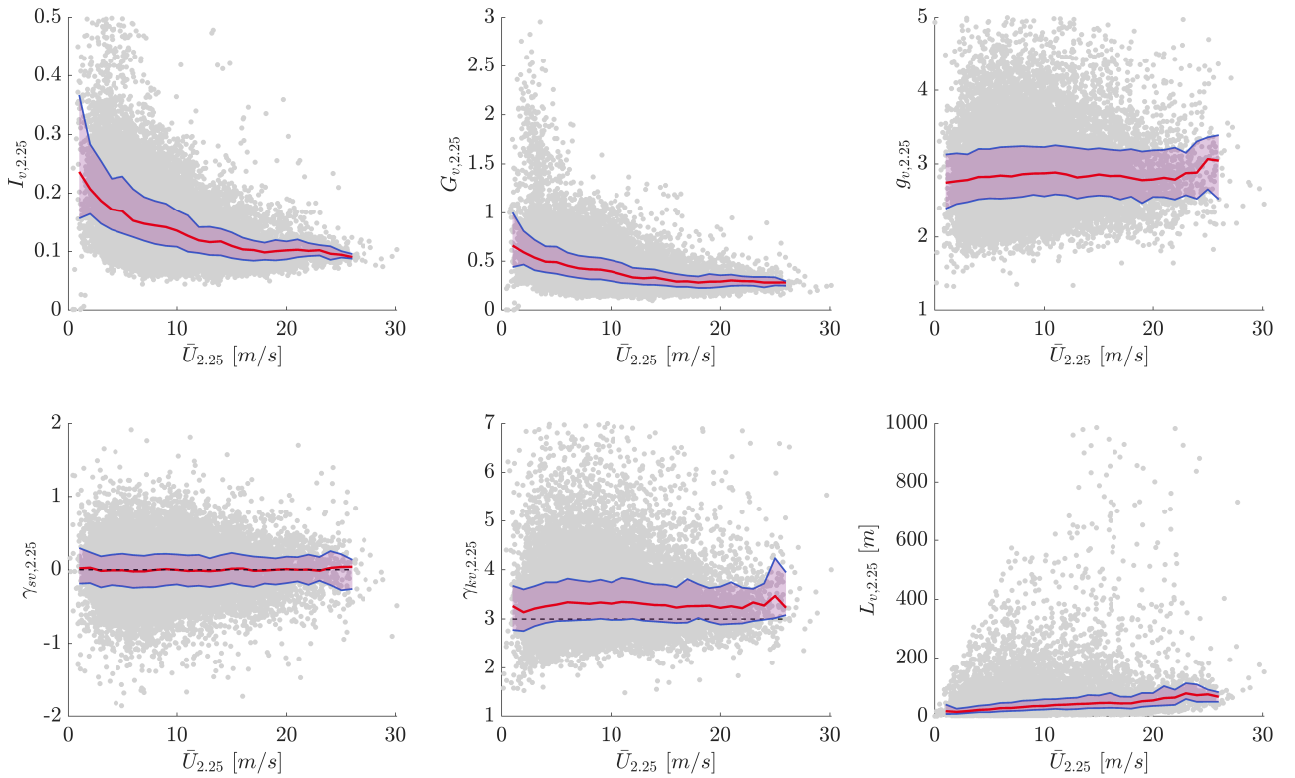
Figure 6.2: Across-wind component of turbulent characteristics in open land at 2.25 m measurement height. Grey circles show data for each analysed 10-minute segment with the 1 m/s binned median and area between 25th and 75th percentile presented by the red solid line and the shaded region, respectively. Black-dashed lines on γ_{sv} and γ_{kv} plots represent the value for a normal distribution.
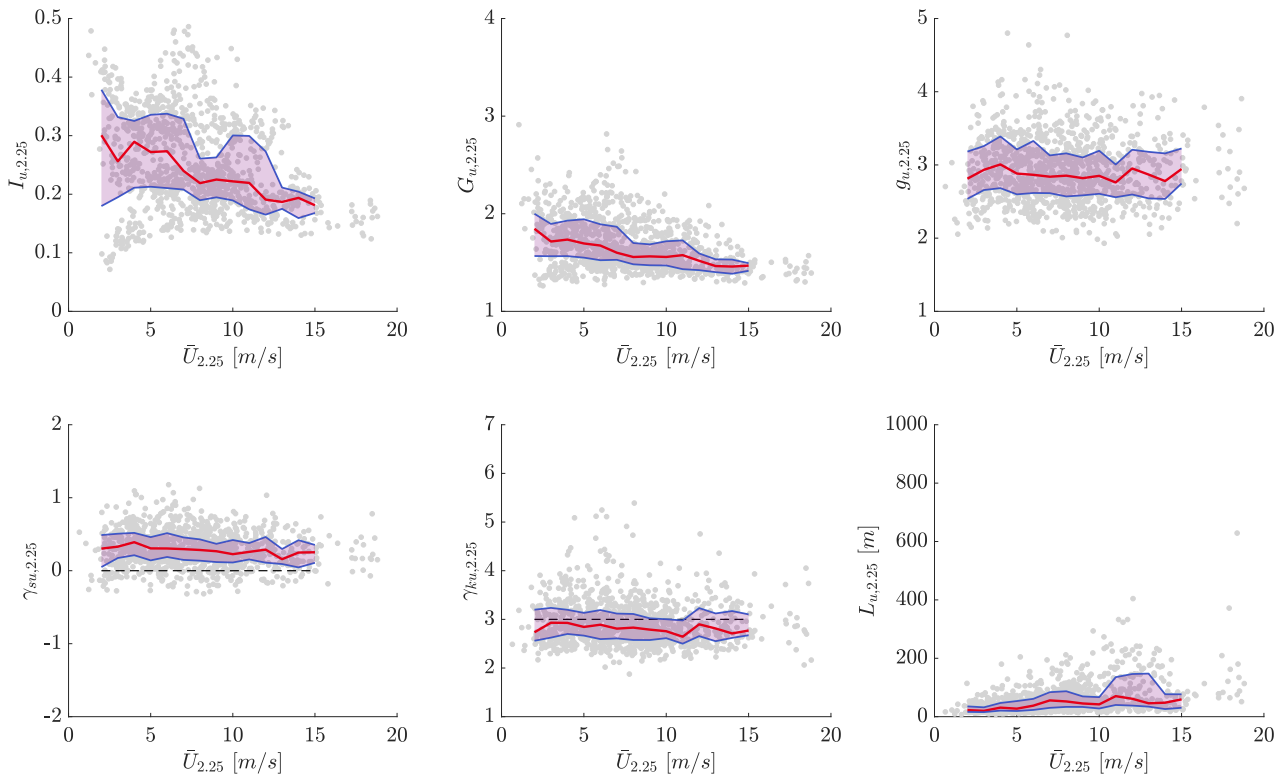
Figure 6.3: Along-wind component of turbulent characteristics in roughly open at 2.25 m measurement height. Grey circles show data for each analysed 10-minute segment with the 1 m/s binned median and area between 25th and 75th percentile presented by the red solid line and the shaded region, respectively. Black-dashed lines on γ_{su} and γ_{ku} plots represent the value for a normal distribution.
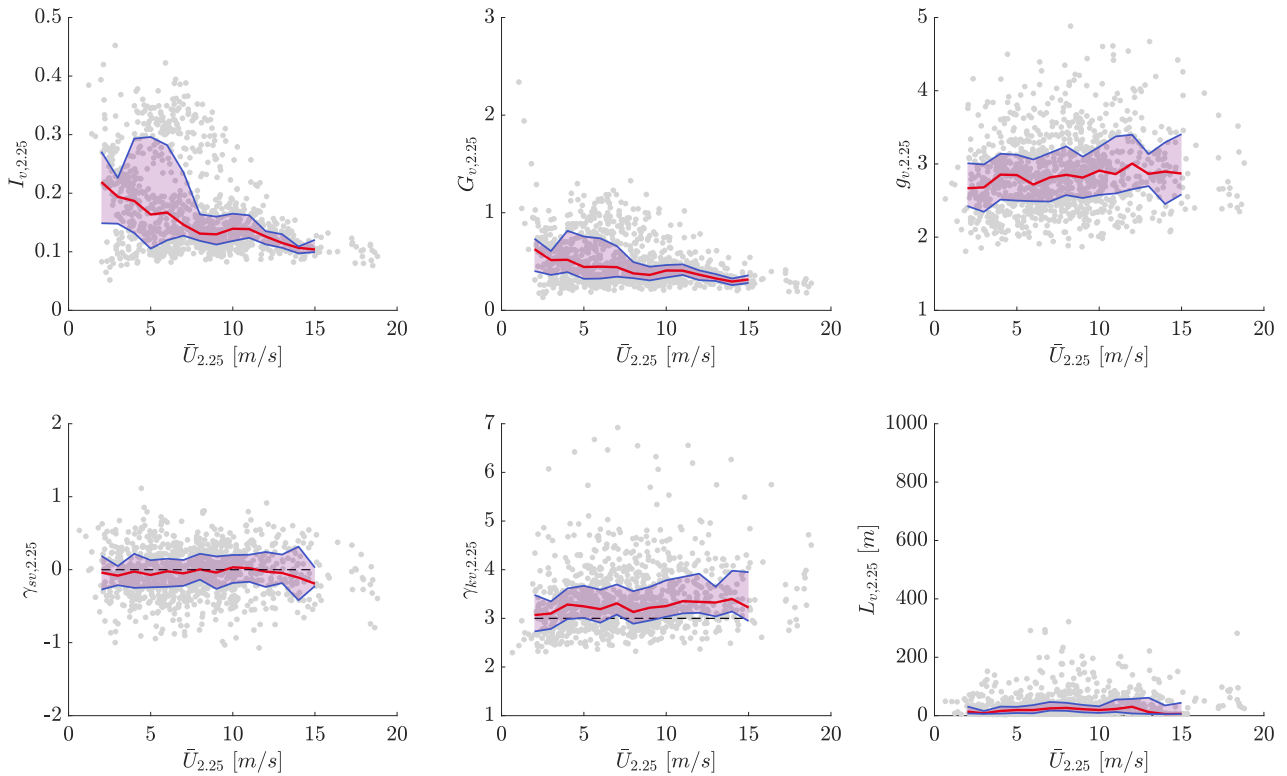
Figure 6.4: Across-wind component of turbulent characteristics in roughly open at 2.25 m measurement height. Grey circles show data for each analysed 10-minute segment with the 1 m/s binned median and area between 25th and 75th percentile presented by the red solid line and the shaded region, respectively. Black-dashed lines on γ_{sv} and γ_{kv} plots represent the value for a normal distribution.

In Figures 6.1-6.4 both turbulent along- and across-wind components exhibit significant scattering around the median trends shown. This scattering is evident for all turbulent characteristics, roughness regimes, and measured elevations of 3.2 m (Figures A.1, A.2), 5 m (Figures A.3-A.6) and 10 m (Figures A.7-A.10). However, disparities generally become smaller with increasing $\bar{U}$, which is highlighted by narrower shaded areas between 75th and 25th percentiles (blue solid lines) and a levelling off of the median (red solid line) at about 20 m/s. More specifically, a decreasing trend of I_u, I_v, G_u, and G_v with increasing mean wind speed $\bar{U}$ is evident throughout all elevations. *Miller et al.* [2015] and *Giammanco et al.* [2016] found similar trends in their analysis. With regards to the two wind distribution characteristics γ_{su} and γ_{ku}, a positively skewed, light-tailed distribution was found for the along wind component. This positively skewed wind distribution appears to tend towards a normal distribution (black, dashed line) as wind speeds go beyond 20 m/s. This observation was also found in *Balderrama et al.* [2012]. In contrast, across wind γ_{sv} and γ_{kv} show characteristics of a normal and heavy-tailed distribution, respectively, which is evident irrespective of the tower location (open land or roughly open). Integral length scales L_u and L_v both increase with higher wind speeds, with L_u constantly being approximately 100% higher than L_v.

The decreasing trend in I_u, I_v, G_u, and G_v with $\bar{U}$ and the positively skewed wind distribution for along wind speeds were found throughout all heights. Exemplifying this, Figure 6.5 denotes the decreasing trend of median I_u and I_v values with increasing $\bar{U}$ at all elevations for open land (a and b) and roughly open sites (c and d).
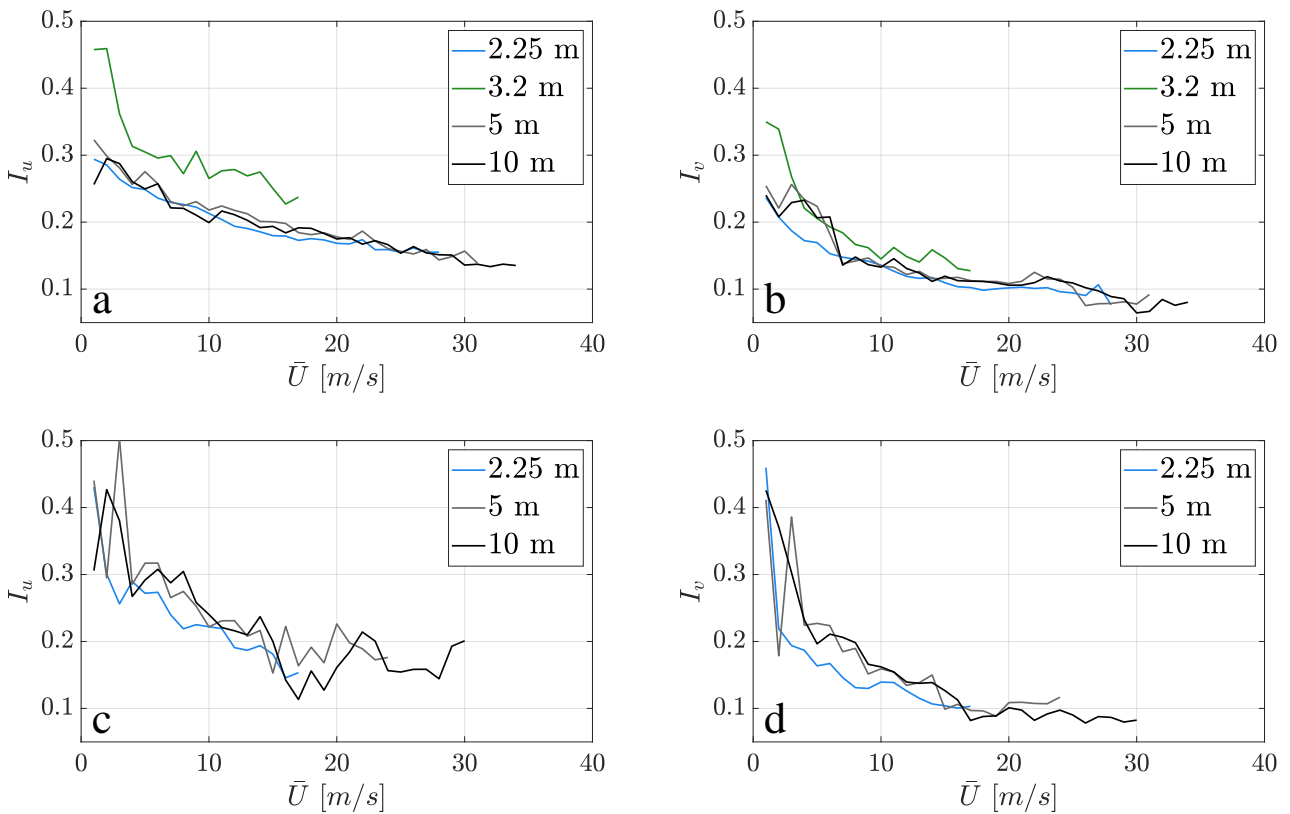
Figure 6.5: Variation of a) I_u and b) I_v medians in open land, and c) I_u and d) I_v medians in roughly open terrain at elevations of 2.25 m, 3.2 m, 5 m, and 10 m.

Figure 6.5 shows the same decreasing trend for median I_u and I_v curves over open land and roughly

open terrain, which continues beyond $\bar{U} > 25$ m/s (where data is available) except for I_{u10}. There are little differences between elevations of 2.25 m and 5 m with mean ratios of $I_{u,2.25}/I_{u,5} = 0.94$ and $I_{v,2.25}/I_{v,5} = 0.88$, between 2.25 m and 10 m with $I_{u,2.25}/I_{u,10} = 0.98$ and $I_{v,2.25}/I_{v,10} = 0.90$, and between 5 m and 10 m with $I_{u,5}/I_{u,10} = 1.03$ and $I_{v,5}/I_{v,10} = 1.01$ for towers sited over open land. For towers in roughly open terrain, mean ratios between elevations of 2.25 m and 5 m are $I_{u,2}/I_{u,5} = 0.77$ and $I_{v,2}/I_{v,5} = 0.65$, between 2.25 m and 10 m $I_{u,2.25}/I_{u,10} = 0.81$ and $I_{v,2.25}/I_{v,10} = 0.63$, and between 5 m and 10 m $I_{u,5}/I_{u,10} = 1.03$ and $I_{v,5}/I_{v,10} = 0.94$. These ratios between elevations are found to be around 19% and 35% smaller than those calculated through Eq. 2.22 for open land and roughly open towers, respectively. This suggests that the turbulence intensity equation (Eq. 2.22) overestimates the analysed TC near-surface wind data below 10 m elevation, when assuming $\sigma_u \approx 2.5u_*$. With respect to the relationship between I_u and I_v over open land and roughly open, mean ratios are 0.68 and 0.67, respectively. This is less than the ratio of 0.88 suggested by *Holmes* [2015] for synoptic wind records. Of note in Figure 6.5a and b is the 26-28% higher I_u and I_v median (green lines) at 3.2 m. There are two possible reasons these differences may exist. First, 3.2 m data is composed of wind records from only six towers, all of which were deployed during in TC Debbie (2017). Second, while these six towers were all deployed in open land exposure, the majority were within 150 m of suburban terrain. As such, most of these records are transitioning from considerably rougher surfaces (therefore higher I) and are not expected to yet be representative of the underlying terrain. This is explored further in section 6.2. Differences in ratios at different elevations likely arise because upstream terrain type and distance between the deployed tower and roughness changes are not considered in Figure 6.5 yet. For towers located in roughly open terrain (Figure 6.5c and d), up to 20% higher I_u and I_v than in open terrain are evident at measurement elevations of 5 m and 10 m. At 2.25 m, surprisingly I_u and I_v values are within 5% of the open land values. A possible reason for this is that 56% towers with wind measurements at 2.25 m deployed in roughly open terrain were within 200 m of the nearest terrain change. As such, the distance to the upwind terrain may be too short for the turbulent flow to adjust adequately to the new surface. Consequently, this highlights the importance of examining the upwind terrain and how it modifies measured turbulence at the measurement site.

The analysis of G_u and G_v medians (Figure A.11) revealed the same gradual decrease with increasing $\bar{U}$ at all measurement heights and roughness regimes. Similar to the I_u and I_v analysis, open land G_u and G_v medians at 3.2 m exhibit higher values than gust factors at remaining elevations. G_u and G_v medians vary between 1.58-2.39 and 0.39-0.98 at 3.2 m for open land towers, whereas along- and across-wind gust factors at 2.25 m, 5 m, and 10 m are in a range between 1.31-1.91 and 0.18-0.67, respectively. Along- and across-wind gust factor medians for roughly open towers show up to 21% higher values for wind speeds below 10 m/s at 5 m and 10 m measurement heights and minor variations at 2.25 m. G_u and G_v medians in roughly open terrain exhibit values between 1.28-2.41 and 0.20-1.01. Obtained along- and across-wind gust factors when $\bar{U} = 15$-20 m/s align well with gust factors of around 1.5 in open land and 1.8 in roughly open identified by previous research [*Schroeder and Smith*, 2003; *Paulsen and Schroeder*, 2005; *Schroeder et al.*, 2009; *Miller et al.*, 2015; *Giammanco et al.*, 2016].

Calculated median peak factors g_u and g_v (Figure A.12) vary within a range of 2.53-3.06 for open land

towers, while median peak factors in roughly open terrain display variations of 2.50-3.12. No clear trend in g_u and g_v with wind speed is observed for any height in open land or roughly open terrain except for a marginal decreasing trend in g_u values in roughness regime C. Wind distribution characteristics skewness (Figure A.13) and kurtosis (Figure A.14) show a positively skewed and platykurtic behaviour at all heights for both γ_{su} and γ_{ku} in open land and roughly open, which was also found by *Balderrama et al.* [2012]. There is a clear trend towards a skewness of zero as wind speed increases. In fact, by 30 m/s and 20 m/s the distribution appears to be effectively Gaussian in open land and roughly open, respectively. Lateral components γ_{sv} and γ_{kv} exhibit a normal and leptokurtic behaviour, whereas γ_{sv} at 5 m and 10 m tends to become positively skewed for $\bar{U} \geq 10$ m/s. The analysis of integral length scales (Figure A.15) reveals increasing L_u and L_v medians for all heights and roughness regimes with wind speed. At 10 m elevation, length scales appear to be the highest with up to 224 m. Conceptually, L_u and L_v at 3.2 m are lower than length scales at 2.25 m. However, given the larger values of I_u and I_v shown in 6.5, this result is expected. Median values of L_u and L_v in open land increase until $\bar{U} = 20$-30 m/s with values levelling off beyond these wind speeds, while median values of L_u and L_v in roughly open increase until $\bar{U} = 10$-20 m/s and remain constant after that. Considering where data stabilises, both L_u and L_v medians in open land are about 50 m greater than those in roughly open. This aligns well with the conceptual understanding that the higher the roughness, the more gusts are broken up and the shorter the length scales.

The above analysis indicates that turbulence characteristics approach wind speed independence as $\bar{U}$ increases. Based on the observations discussed, this wind speed may be between 20-30 m/s, but appears to be dependent on the roughness regime (i.e. rougher terrain seems to reach equilibrium at lower speeds). However, obtaining a particular wind speed value where turbulent characteristics do not change is quite challenging. The determination of such a wind speed value, however, is important for the engineering community, who must design buildings for high wind speeds.

The role of the mean wind speed needs to be explored further, because Figure 6.5 and the discussion below indicate that different upwind conditions may influence I_u and I_v median curves over open land and roughly open terrain. In order to initially explore the role of upwind fetch further, I_u median values are compared for data binned using various distances x between the measurement tower and the first upwind roughness change. The aim of this is to exclude variability that may result from short x. These distances are chosen according to previous research [e.g. *Wieringa*, 1993], who suggested that $100z$ is sufficient to reach equilibrium. Figures 6.6 and 6.7 show these data for minimum x thresholds ranging from zero up to 1 km for all towers located in open land and roughly open, respectively. A bar graph showing the number of observations was also added to quantitatively show how many observations went into each 1 m/s bin. This allows some measure of confidence to be drawn from the results.
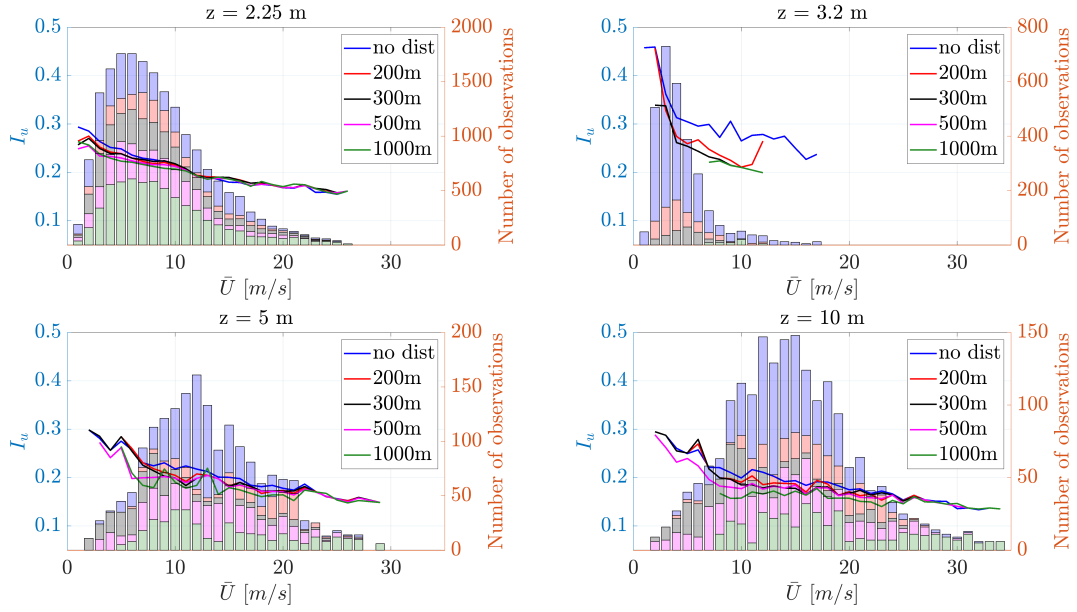
Figure 6.6: Median I_u curves for $x >$ of 200 m, 300 m, 500 m, and 1 km to the first roughness change against $\bar{U}$ along with number of 10-min observations for each 1 m/s bin at 2.25 m, 3.2 m, 5 m, and 10 m for all towers located in open land.
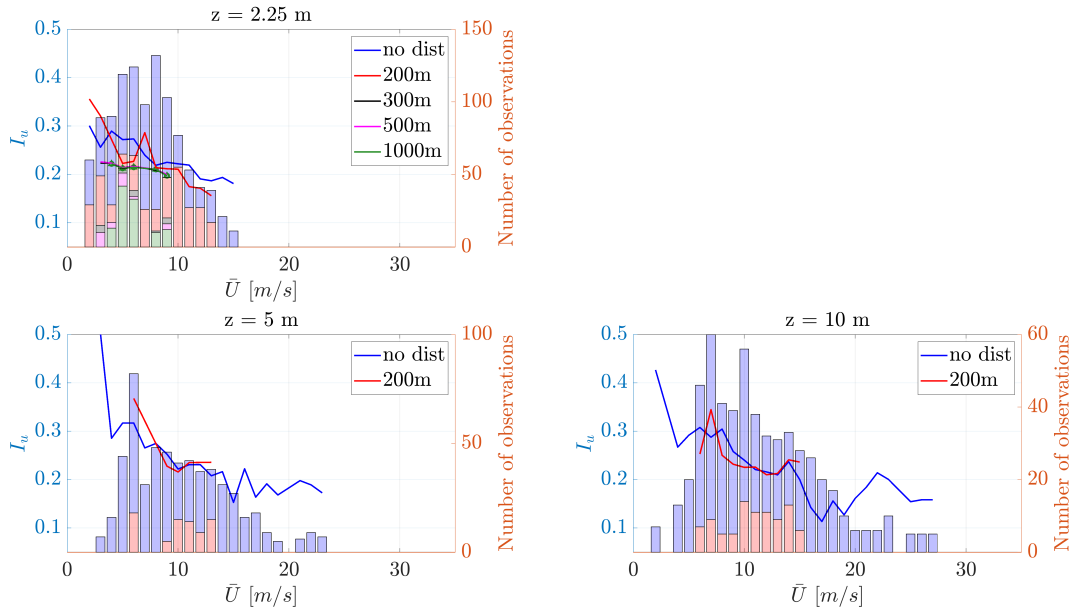
Figure 6.7: Median I_u curves for $x >$ of 200 m, 300 m, 500 m, and 1 km to the first roughness change against $\bar{U}$ along with number of 10-min observations for each 1 m/s bin at 2.25 m, 3.2 m, 5 m, and 10 m for all towers located in roughly open.

Comparing the curves at $z = 2.25$ m in Figure 6.6, about 15% higher I_u is evident for wind speeds up to 10 m/s when there is no restriction on x. For wind speeds beyond 10 m/s, no significant difference exists between the median curves. It seems that the 200 m threshold is reasonable for this height given the lack of difference with other threshold distance values. Considering this, and the preceding discussion, I_u curves seem to become independent of wind speeds of about 25 m/s. To identify a particular wind speed, the number of 10-min observations are taken into consideration. Overall,

91 10-minute I_u samples belong to the 20 m/s bin, whereas the number of observations drops to 30 for the 25 m/s bin for a distance of at least 500 m between tower and roughness change. Although the median turbulence intensity drops from 16.9% at 20 m/s to 15.7% at 25 m/s, the number of observations was approximately three times higher for the 20 m/s bin. There is less confidence in values for higher wind speed bins. Hence, it is assumed that I_u levels off at 16.9% at 2.25 m for wind speeds of 20 m/s (although not fully converged) and above considering all possible transitions from upwind terrain, e.g. water bodies to open land or dense suburban to open land. Figure 6.7 shows that significantly less data were available to describe transitions to roughly open terrain at 2.25 m with $x > 500$ m. These data are also at significantly lower wind speeds than for open terrain, with $\bar{U}$ only reaching up to 14 m/s. This makes it difficult to estimate wind independent I_u at this height in roughly open terrain. At 3.2 m measurement height, it was found that only 50 10-min segments are available to calculate curves for $x \geq 1000$ m for open land exposure. Since wind speed observations at 3.2 m are well below 20 m/s it is difficult to determine when turbulence intensities become independent of wind speed. Considering I_u values at the lowest elevation level off at $\bar{U} > 20$ m/s, it is hypothesised that similar wind speeds would be required to reach independence at 3.2 m. However, the observation that increasing the x threshold leads to lower I_u values is more distinctly than for 2.25 m. This explains the higher I_u values at 3.2 m in Figure 6.6, because removing values close to a terrain change shows I_u values that a very similar to those at 2.25 m. At 5 m and 10 m measurement height, I_u values are 15.6% and 15.8% when they become wind speed independent at around 25 m/s for distances x of at least 500 m, based on 13 and 11 10-minute samples, respectively. The small number of observations can be explained due to the lower number of towers being taken out for deployment in the FCMP campaign (see Table 6.1). For I_u-transitions to roughly open terrain, no definitive wind speed independence could be empirically identified at 5 m and 10 m due to limited 10-segments available (Figure 6.7). However, results indicate that wind speeds need to be generally greater than 25 m/s at all heights for I_u to be independent of $\bar{U}$. Moreover, median I_u values follow a similar trend for all x thresholds. The x threshold did not appear to influence the median results significantly (except for 3.2m). It is hypothesised that this occurs because of a mix of rough and smooth z_{01} values, which might tend to cancel each other out.

6.2 Single Terrain Transition Analysis

Within Chapter 6.1, all towers located within open land and roughly open were examined first irrespective of the upwind terrain. However, a considerable body of evidence [e.g. *Wieringa*, 1993; *Miller et al.*, 2015; *Giammanco et al.*, 2016] suggest the nature of upwind terrain modifies turbulence characteristics after the roughness change. Available observations are used to explore how turbulence transitions from one regime to another, and assess whether the magnitude of surface roughness influences how this transition occurs.

In order to incorporate upwind surface conditions, the upwind surface roughness z_{01} and the length of the upwind terrain, referred to as fetch x_1, are included. According to previous literature x_1 must

be at least 100 times the measurement height [e.g. *Wieringa*, 1993] for turbulent statistics to be in equilibrium with the underlying terrain. This will be tested here. Thus, in the first instance it is assumed that this relationship holds true. The initial choice of x_1 thresholds are therefore 200 m, 300 m, 500 m, and 1000 m for 2.25 m, 3.2 m, 5 m, and 10 m measurement height, respectively. Table 6.2 summarises the number of observations that meet this threshold for each height and transition category where $\bar{U} > 5$ m/s. For transitions from water bodies (A) to open land (B), the nomenclature *BA* will be used. The same applies for transitions from roughly open (C), dense suburban (D), and high intensity/forested (E) to open land (B), termed *BC*, *BD*, and *BE*. Transitions to roughly open (C) terrain are similarly termed as CA, CB, CD, and CE.

	2.25 m	3.2 m	5 m	10 m	Total
BA	2588	3	19	-	2610
BC	2312	57	183	52	2604
BD	1303	421	173	53	1950
BE	824	-	54	38	916
CA	74	-	68	49	191
CB	296	-	4	1	301
CD	71	-	12	-	83
CE	-	-	-	-	-

Table 6.2: Number of 10 min observations for transitions from water bodies (BA), roughly open (BC), dense suburban (BD), and high intensity/forested (BE) to open land, and water bodies (CA), open land (CB), dense suburban (CD), and high intensity/forested (CE) to roughly open at 2.25 m, 3.2 m, 5 m, and 10 m with upwind terrain length x_1 restrictions of 200 m, 300 m, 500 m, and 1000 m, respectively.

The greatest number of 10 min observations are available for transitions from water bodies and roughly open to open land (transition BA and BC, respectively). The transition from dense suburban to open land exhibits the third most 10-min segments (1950). Transitions from water bodies to open land are predominantly present at 2.25 m (2588 10 min segments), because various StickNet were deployed close to the ocean. A total of 916 10 min observations originate from the vicinity of high intensity/forested terrain transitioning to open land predominantly measured at 2.25 m. In contrast, no data was measured by SWIRLnet towers for transitions from high intensity/forested and roughly open surfaces and just three 10-minute means were measured at marine exposure. Less data is available for towers deployed in roughly open terrain, as only 11 towers recorded wind speeds and direction in an roughly open environment.

6.2.1 Transition from smooth-to-rough and rough-to-smooth

Upstream terrain properties can be classified as either smooth or rough, relative to the immediate terrain at the measurement site. Hence, the next step in the analysis sheds light on how broadly classified smooth and rough upwind terrain change the near-surface turbulent structure in landfalling

TCs. With respect to available transitions listed in Table 6.2, smooth-to-rough transitions contain changes in terrain from A to B, A to C, and B to C. Rough-to-smooth transitions occur when surface properties change from C to B, D to B, E to B, D to C, and E to C. Figure 6.8 shows the variation of turbulent statistics with $\bar{U}$. The 25th to 75th percentile range at 2.25 m height including all open land towers with smooth-to-rough (blue-shaded area) and rough-to-smooth (green-shaded area) transitions is shown for wind speeds ≥ 5 m/s, where $x_1 > 200$ m.
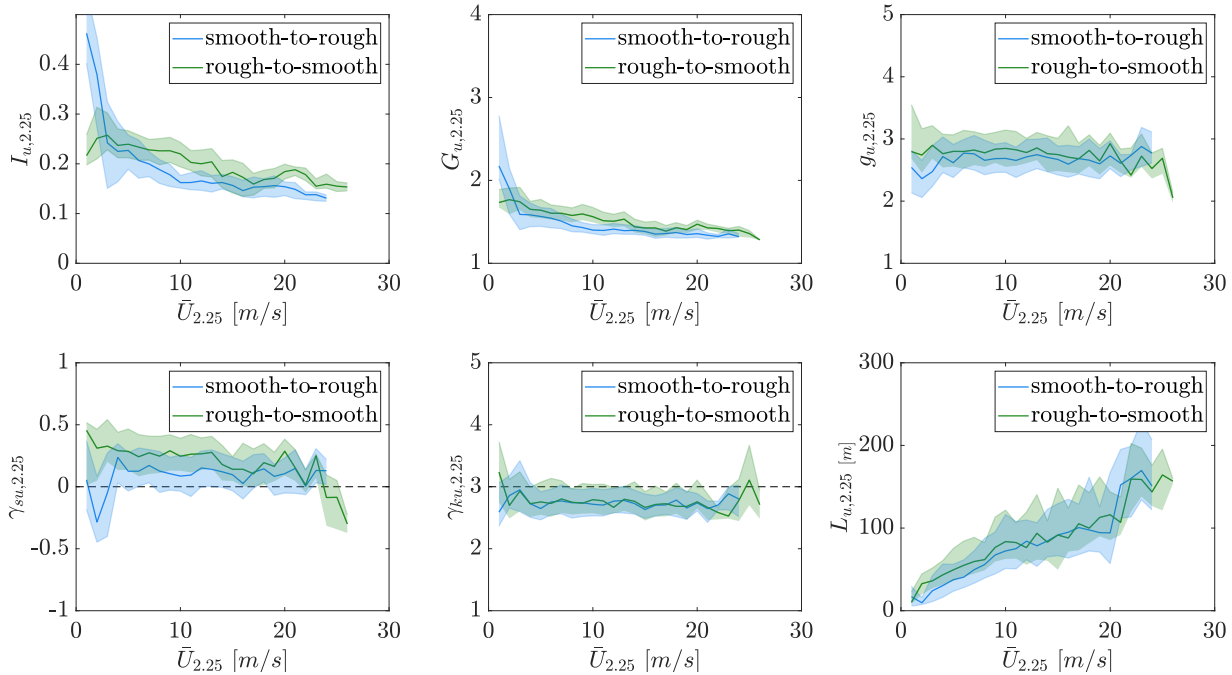
Figure 6.8: Smooth-to-rough (blue-shaded area) and rough-to-smooth (green-shaded area) transitions of along-wind turbulence statistics in open land at 2.25 m.

Figure 6.8 generally shows higher turbulence statistics values for rough-to-smooth transitions than smooth-to-rough transitions, when inspecting I_u, G_u, and g_u variables. Similar observations are made at 2.25 m when transitioning to roughly open (Figure A.18), while 5 m and 10 m plots (Figures A.16-A.20) show very little difference between the smooth-to-rough and rough-to-smooth curves. This may suggest that the x threshold for 2.25 m is too short, but reasonable for 5 m and 10 m. Results also indicate that smooth-to-rough transitions reach $\bar{U}$ independence at lower wind speeds than rough-to-smooth transitions. However, at wind speeds $\bar{U} > 15$-20 m/s, smooth-to-rough and rough-to-smooth plots do generally appear to collapse onto each other. This collapse suggests the threshold choice is reasonable for these higher wind speeds, but it is evident that turbulence characteristics of the upwind terrain still remain at lower wind speeds. The skewness for rough-to-smooth transitions shows a downward trend while γ_{su} for smooth-to-rough transitions exhibits a flat trend. Due to limited data available at remaining heights and over roughly open terrain it is difficult to infer a trend for many of the turbulence statistics. The following sections will provide more detail on these single terrain transitions considering each of the turbulence statistics individually.

6.2.2 Turbulence Intensity Transitions

As indicated in the previous section, the upwind terrain of each tower is important when examining the transition from one surface to another. In this section, the smooth-to-rough and rough-to-smooth analysis is further broken down to the individual upwind roughness regimes, which in the case of a tower being deployed in open land is either water bodies, roughly open, dense suburban or high intensity/forested. Table 6.2 shows the number of observations available for each transition and height with upwind terrain fetch x_1 greater than the specified threshold. During this transition, the role of the distance x is investigated with a particular focus on determining where equilibrium conditions occur. It is hypothesised that turbulent statistics will reach equilibrium with the underlying surface at different distances x depending on the upwind surface roughness z_{01} and the measurement height z. In addition, turbulent statistics might show a different behaviour at different wind speeds. Therefore, the following analysis breaks the measured wind speed at 2.25 m and 3.2 m up into $\bar{U}$ = 5-10 m/s, 10-15 m/s, 15-20 m/s, and over 20 m/s bins. At 5 m and 10 m elevations, wind speed bins of 20-25 m/s and $\bar{U} > 25$ m/s were also used because of the occurrence of higher wind speeds at these elevations, as shown in Figures A.3 and A.7.

The analysis of different upwind terrain starts with an investigation of the along- and across-wind turbulence intensity transition from available upwind terrain with the restriction $x_1 \geq 100 \cdot z$. Figures 6.9 and 6.10 show the transition of I_u and I_v from water bodies (A), roughly open (C), dense suburban (D), and high intensity/forested of at least 200 m to open land at 2.25 m. The solid line in each plot represents the median curve with shaded regions visualising the 25th to 75th percentile range.
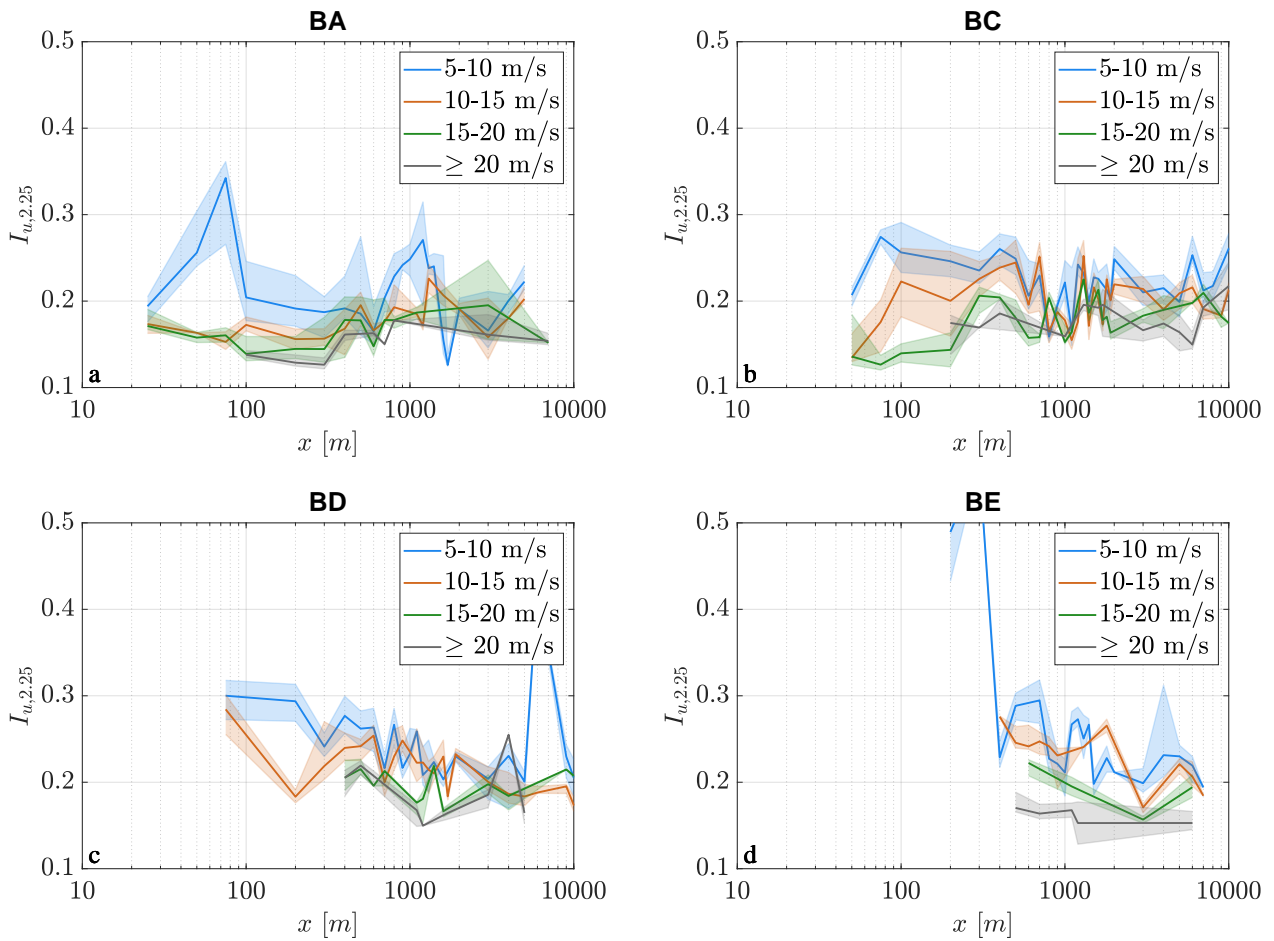
Figure 6.9: I_u transition from a) water bodies (BA), b) roughly open (BC), c) dense suburban (BD), and d) high intensity/forested (BE) to open land at 2.25 m for 5-10 m/s, 10-15 m/s, 15-20 m/s, and over 20 m/s wind speed bins. Medians and the area between 25th and 75th percentile are represented by solid lines and shaded regions, respectively.
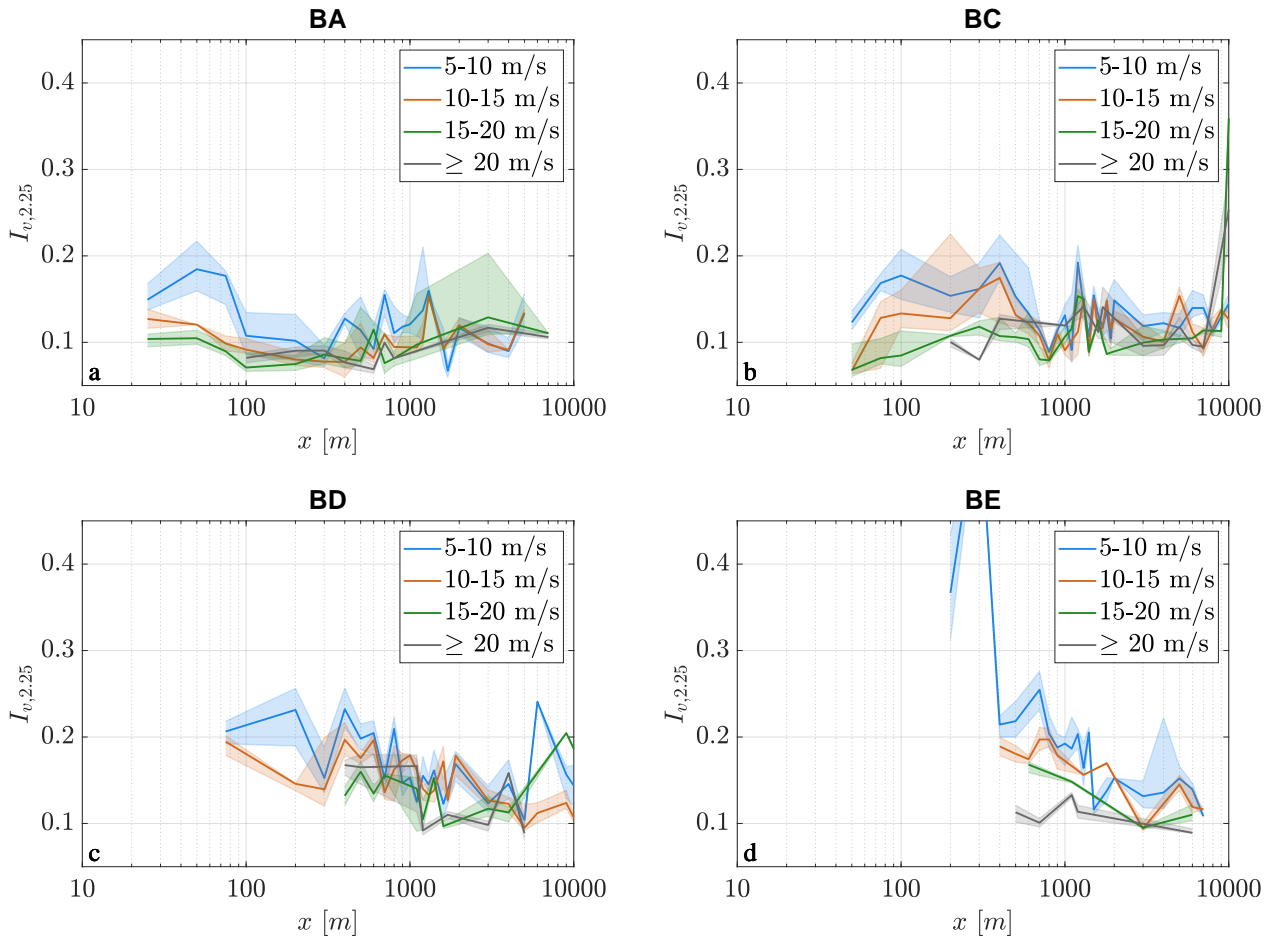
Figure 6.10: I_v transition from a) water bodies (BA), b) roughly open (BC), c) dense suburban (BD), and d) high intensity/forested (BE) to open land at 2.25 m for 5-10 m/s, 10-15 m/s, 15-20 m/s, and over 20 m/s wind speed bins. Medians and the area between 25th and 75th percentile are represented by solid lines and shaded regions, respectively.

The I_u transition from water bodies to open land exhibits a small uptrend to higher turbulence intensity values. This is more evident for wind speed bins ≥ 10 m/s, whereas high fluctuations for $x \leq 100$ m and $x \approx 1000$ m cause no visible trend for the 5-10 m/s data. The transition to higher I_u values is expected given the fact that open land exhibits a rougher surface than water bodies, as shown in Table 4.2. Across all x, lower I_u values are observed for higher wind speed bins. However, these differences seem to get smaller for $x > 2$ km, which also holds true for other transitions from C, D, and E at 2.25 m. While transitions from rougher terrain in Figure 6.9b, c, and d to open land exhibit higher I_u values at small x, along-wind turbulence intensities decrease with increasing x up until approximately 1000-2000 m. Beyond 2000 m, I_u values only show little fluctuations, suggesting that equilibrium may be reached. Along-wind turbulence intensities reach equilibrium with uniform terrain of about 2000 m independent of the upwind terrain at 2.25 m for transitions to open land. Although I_u is dependent on the wind speed, the transition to equilibrium appears to occur at approximately the same distance for all wind speed bins. Properties of I_u transitions are also observed during the analysis of I_v, despite lateral component of the turbulence intensity being around 43% smaller than I_u, independent of the distance from the tower to the first change in roughness x.

Due to the lack of data for $x > 2000$ m and wind speed bins at the remaining measurement heights, it

becomes difficult to fully characterise the turbulence transition or obtain a distance x, where equilibrium conditions are satisfied. Despite this, results indicate that I_u will likely have reached equilibrium by $x = 2000$ m for higher measurement elevations.

Because there is a similar decreasing trend in I_u when viewed against $\bar{U}$, it is proposed that each $\bar{U}$ bin can be normalised by the ratio of their high velocity value (generally taken as I_u at the greatest two x available, i.e. equilibrium) divided by the same value for the $\bar{U} > 20$ m/s binned data at 2.25 m, and $\bar{U} > 25$ m/s at 5 m and 10 m. Wind speeds at those heights are chosen as these thresholds are approximately where I_u starts levelling off. This approach of collapsing I_u down to $I_{u,eq}$ is beneficial in the sense that it allows the inclusion of data at lower wind speeds. In essence, data at lower wind speeds were found to provide information about how turbulence transitions, therefore these data are included for further analysis. This helps to fill in regions where high wind speed data is unavailable. For measurements at 3.2 m, observed $\bar{U}$ are well below 20 m/s, and therefore data is normalised by $\bar{U} > 15$ m/s. Figures 6.11- 6.14 show the collapsed along-wind turbulence intensities at 2.25 m, 3.2 m, 5 m, and 10 m for the same upwind terrain classes displayed in Figure 6.9.
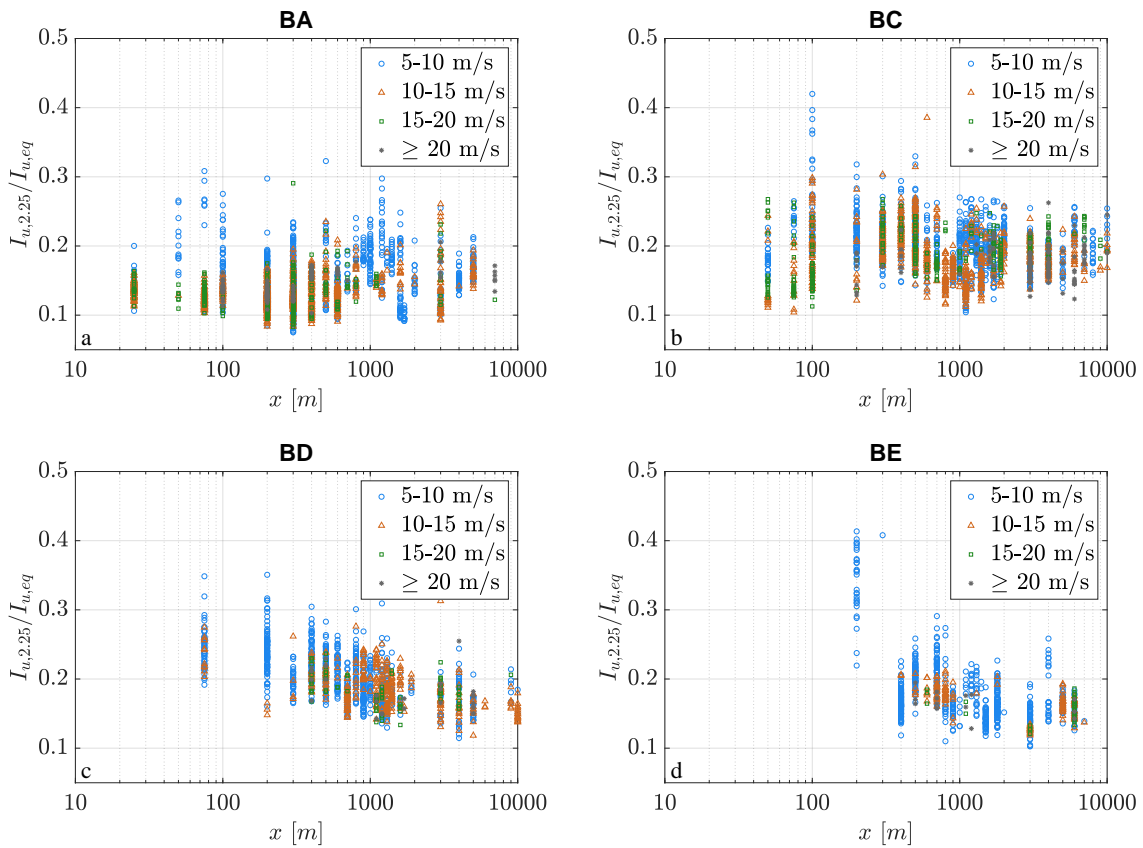
Figure 6.11: I_u transition from a) water bodies (BA), b) roughly open (BC), c) dense suburban (BD), and d) high intensity/forested (BE) to open land normalised by $I_{u,eq}$ at 2.25 m elevation.
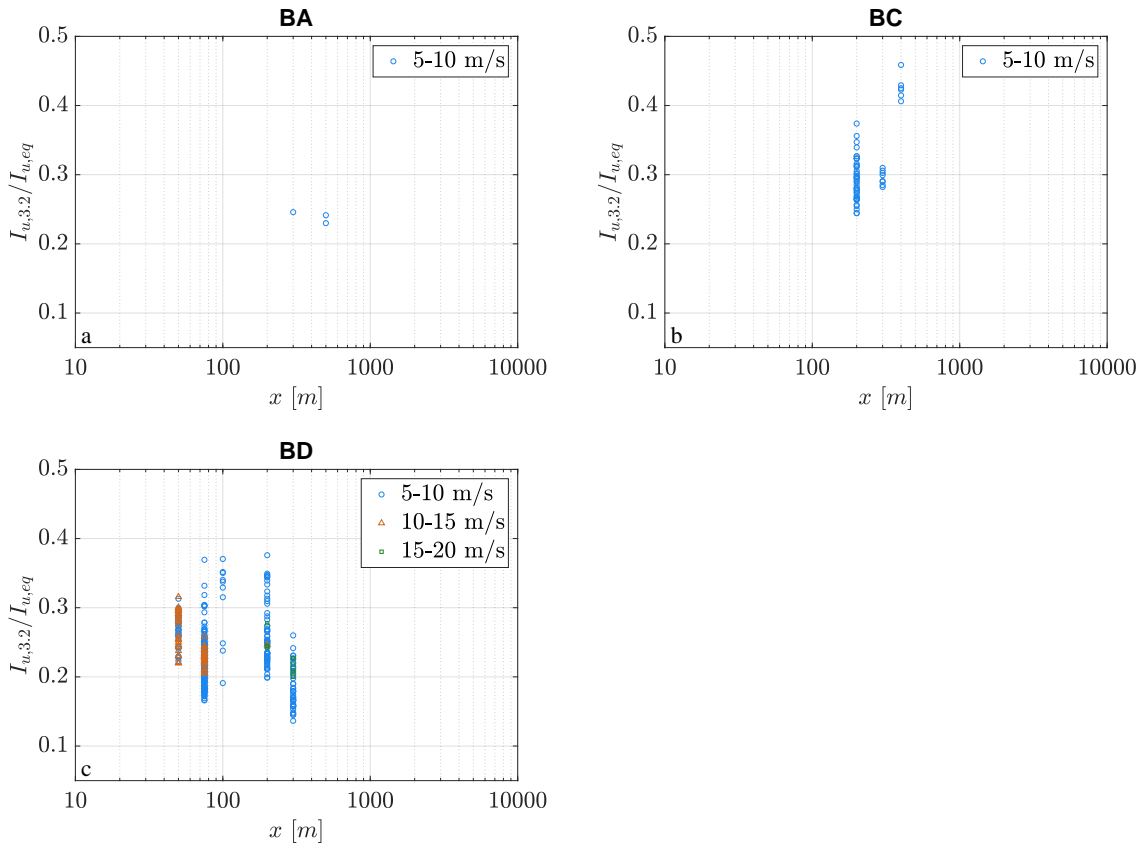
Figure 6.12: I_u transition from a) water bodies (BA), b) roughly open (BC), and c) dense suburban (BD) to open land normalised by $I_{u,eq}$ at 3.2 m elevation.
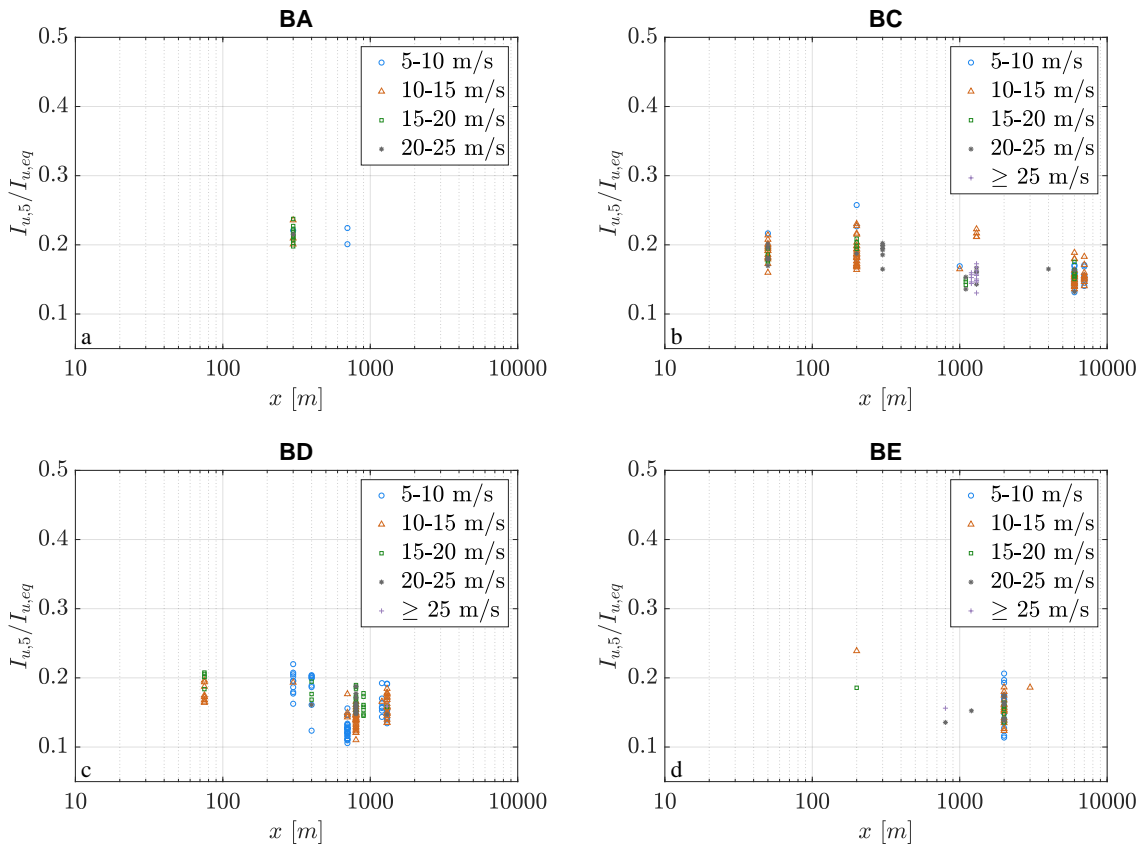
Figure 6.13: I_u transition from a) water bodies (BA), b) roughly open (BC), c) dense suburban (BD), and d) high intensity/forested (BE) to open land normalised by $I_{u,eq}$ at 5 m elevation.
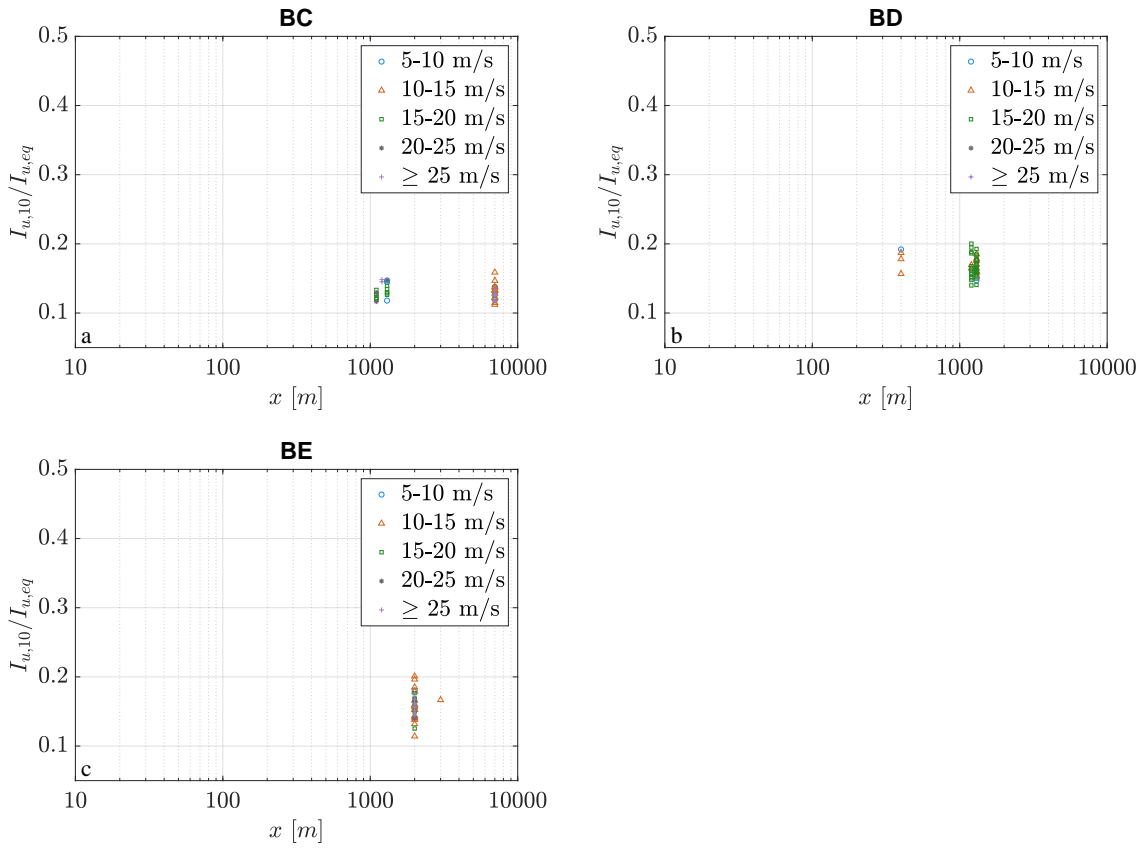
Figure 6.14: I_u transition from a) roughly open (BC), b) dense suburban (BD), and c) high intensity/forested (BE) to open land normalised by $I_{u,eq}$ at 10 m elevation.

At higher elevations, 10-min segments become sparse due to the higher restriction on the length of the upwind terrain so it becomes difficult to infer x where equilibrium is reached. However, transitions from roughly open to open land (BC) at 5 m height also seem to suggest that equilibrium conditions are reached around 1500-2000 m. Data availability also becomes an issue when assessing transitions to roughly open terrain. Since 11 towers could be considered for analysis, only a few wind speed and distance bins are available for analysis.

To better quantify the transition profiles for each height and upwind roughness, an attempt was made to develop a simple transition model that predicts how turbulence intensities progress from z_{01} to z_0 for a specific height z.

6.2.2.1 Development of a Terrain Transition Model

An attempt to develop an empirical turbulence intensity transition model is proposed in this subsection. Research results are integrated into the development of what is referred to as the transition model hereafter. Analysis outcomes at $z = 2.25$ m are primarily used for developing the model equations because they provide the most data at a variety of x for almost all transitions to open land. The transition model will also be used to empirically estimate equilibrium conditions for terrain regimes A, D, and E, at all measurement heights.

The first step in the development of the transition model is to find an equation that fits the distributions observed in Figure 6.11. Here, different equation types were tested including power, linear, logarithmic, polynomial and exponential functions. The exponential approach proved to deliver most accurate results. More specifically, the exponential function

$$I_u = \alpha \cdot exp\left[-x/\beta\right] + \gamma \tag{6.1}$$

is used to describe the transition from terrain with surface roughness z_{01} to a terrain with surface roughness z_0. In Eq. 6.1, α describes the difference in equilibrium turbulence intensities between surfaces of z_{01} and z_0, β is a roughness-dependant transition length constant, and γ the turbulence intensity associated with z_0. The best fit of Eq. 6.1 to the data was achieved through the curve fitting tool in Matlab using the method of linear least squares. To drive the curve fitting tool, initial values for α, β, and γ were required, whereas none of these variables have fixed ranges during the fitting. The best fit is based on normalised $I_u/I_{u,eq}$ data so the transition model is designed to be used at high wind speeds. Once determined, estimates of α, β, and γ enable the transition model to be applied for any desired combination of z_0, z_{01}, z, and x. In an earlier attempt, a power law was implemented into the model equation (after the term in brackets) that would allow the rate of transition rather than just the location to also change. The data, however, could not be fit with any degree of confidence using this equation so the simpler version given in Eq. 6.1 was implemented. Figure 6.15 shows Eq. 6.1 fitted to the I_u transition data measured at 2.25 m from the four different terrain regimes A, C, D, and E to open land, normalised by $I_{u,eq}$.
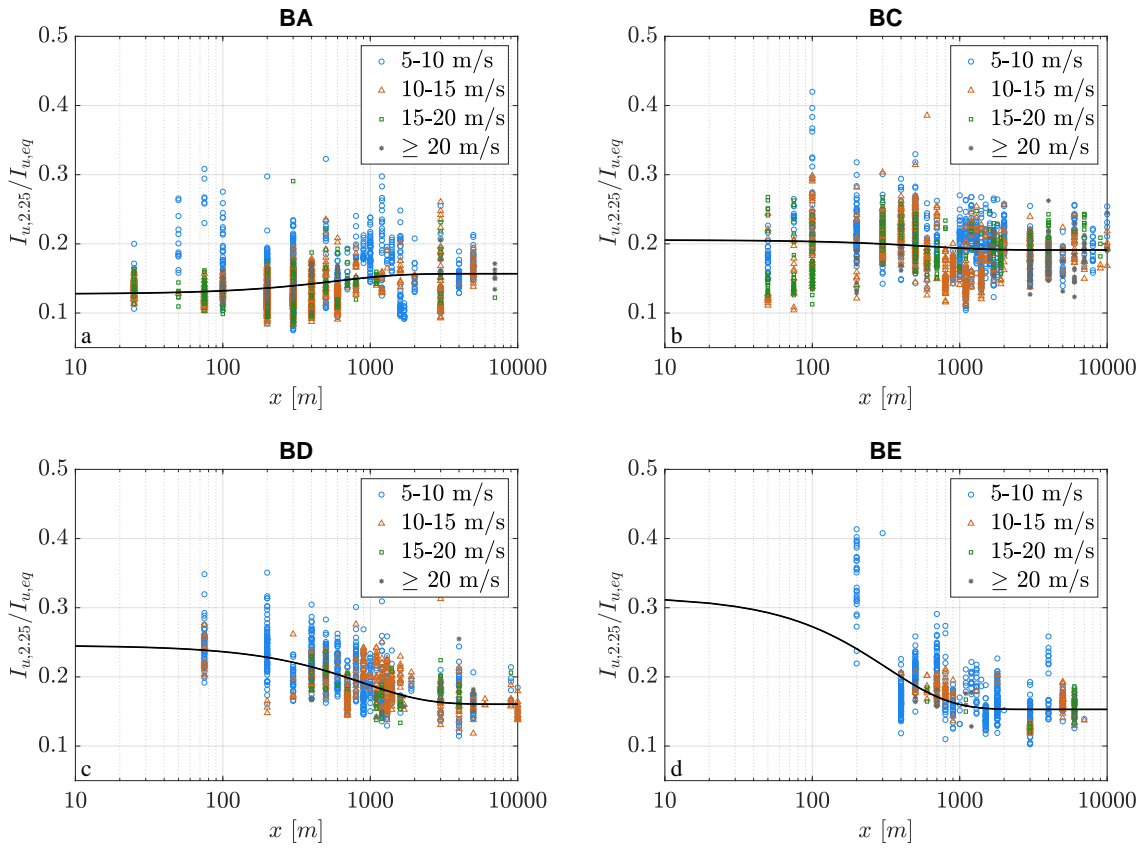
Figure 6.15: I_u transition from a) water bodies (BA), b) roughly open (BC), c) dense suburban (BD), and d) high intensity/forested (BE) to open land normalised by $I_{u,eq}$ with modelled fit (black line).

The fitted curves (black lines in Figure 6.15) show an increase of I_u for water bodies to open land (Figure 6.15a), and a decrease with x for rougher upwind terrain as identified in the previous section. These transition profiles were fit for all heights and upwind surfaces. Of importance are the results for α, β, and γ at each height, which are summarised in Table 6.3 including the 95% confidence intervals (Lower and Upper signify the lower and upper bounds of this interval).

	α			β [m]			γ
	Result	Lower	Upper	Result	Lower	Upper	Result
BA - 2.25 m	-0.034	-0.038	-0.030	465.8	336.5	577.2	0.1568
BC - 2.25 m	0.029	0.023	0.036	406.7	267.7	545.6	0.1911
BC - 3.2 m	0.244	-0.017	0.504	80.2	34.4	426.0	0.2617
BC - 5 m	0.037	0.030	0.045	659.2	255.1	1063.0	0.1577
BC - 10 m	0.030	0.023	0.034	435.7	102.8	768.7	0.1471
BD - 2.25 m	0.085	0.080	0.090	880.5	790.2	970.9	0.1605
BD - 3.2 m	0.063	0.046	0.080	149.9	79.1	220.7	0.2224
BD - 5 m	0.041	0.022	0.060	196.9	51.3	341.9	0.1584
BD - 10 m	0.020	0.003	0.037	243.7	-233.5	720.9	0.1577
BE - 2.25 m	0.164	0.135	0.192	320.2	273.0	367.4	0.1530
BE - 5 m	0.246	-207.6	208.1	76.2	-3.9×10^4	3.9×10^4	0.1646

Table 6.3: Results, lower, and upper 95%-confidence intervals when fitting the model to the observations at 2.25 m, 5 m, and 10 m.

Results in Table 6.3 show that α values become greater with rougher upwind terrain as expected given higher turbulence intensities associated with increasing z_{01}. Within 95%-confidence intervals the bulk of β values range from about 50 to 1000. This implies that the transition from z_{01} to z_0 occurs over a similar distance, independent of z. Here, β has a physical meaning. It represents the location (x), where I_u has transitioned 2/3 of the way from initial to final value. It is an important part of the model as controls whether the different transitions occur at shorter or longer distances from the change in surface roughness. Of note is that upper and lower bounds become very large when limited observed data was available. This is evident for transition BE at 5 m height. To determine β, results from Table 6.3 were plotted against mean values for each roughness regime, which leads to the following expression for β:

$$\beta = 448.08 \cdot exp\left[-0.434\, z_{01}\right] \tag{6.2}$$

Displayed γ values are, in essence, empirical estimates of the expected along-wind turbulence intensities of open land tower sites. These tend to become smaller with z except at 3.2 m, where exceptionally high turbulence characteristics were observed throughout TC Debbie (2017) deployment. This is because no high wind speed data (i.e. $\bar{U} > 20$ m/s) are available from TC Debbie (2017) records to normalise the I_u values by. To express model parameters α and γ with z, z_0, z_{01}, x, estimated γ values at each z were averaged over all z_{01} for open land. This is reasonable as γ values at a given height should theoretically be the same irrespective of where the flow is transitioning from. Apart

from transition BC (roughly open to open land), at 2.25 m 0.1568 (BA), 0.1605 (BD), and 0.1530 (BE) confirm that turbulence intensities of similar magnitude are found when a transition to open land occurs. Taking these values into consideration, the average γ at 2.25 m is 0.1653. The same procedure is applied to 3.2 m, 5 m and 10 m measurement heights, as shown in Table 6.4.

z	mean γ
2.25 m	0.1653
3.2 m	0.2420
5 m	0.1602
10 m	0.1521

Table 6.4: Open land terrain-averaged γ at 2.25 m, 3.2 m, 5 m, and 10 m.

In practise, Table 6.4 represents the expected γ in open land at high wind speeds (i.e. $\bar{U} > 20$ m/s). Reasonably consistent values are found at each level, with $< 10\%$ difference noted between 2.25 m and 10 m values (excluding 3.2 m). Given the noted high values at 3.2 m, an interpolated γ value of 0.1635 will be used for further model development.

In addition to estimating I_u for the terrain that flow is transitioning to - open land (B) in this case - values of α and γ shown in Tables 6.3 and 6.4, respectively, also allow the expected I_u for each upwind terrain to be simply estimated through $\gamma + \alpha$. Resulting expected I_u values for each terrain type are shown in Table 6.5 and in Figure 6.16 along with 95% confidence intervals. Lower and upper confidence intervals of I_u are determined by the summation of lower and upper α with γ. The theoretical estimates of I_u (Eq. 2.22) are also plotted (dashed lines).

z	A	B	C	D	E
2.25 m	0.1313	0.1653	0.1947	0.2503	0.3288
3.2 m		**0.1635**		0.2270	
5 m		0.1602	0.1950	0.2189	0.4104
10 m		0.1521	0.1774	0.1770	

Table 6.5: Terrain-averaged γ at 2.25 m, 3.2 m, 5 m, and 10 m for all upwind roughness regimes. Bold value is interpolated.
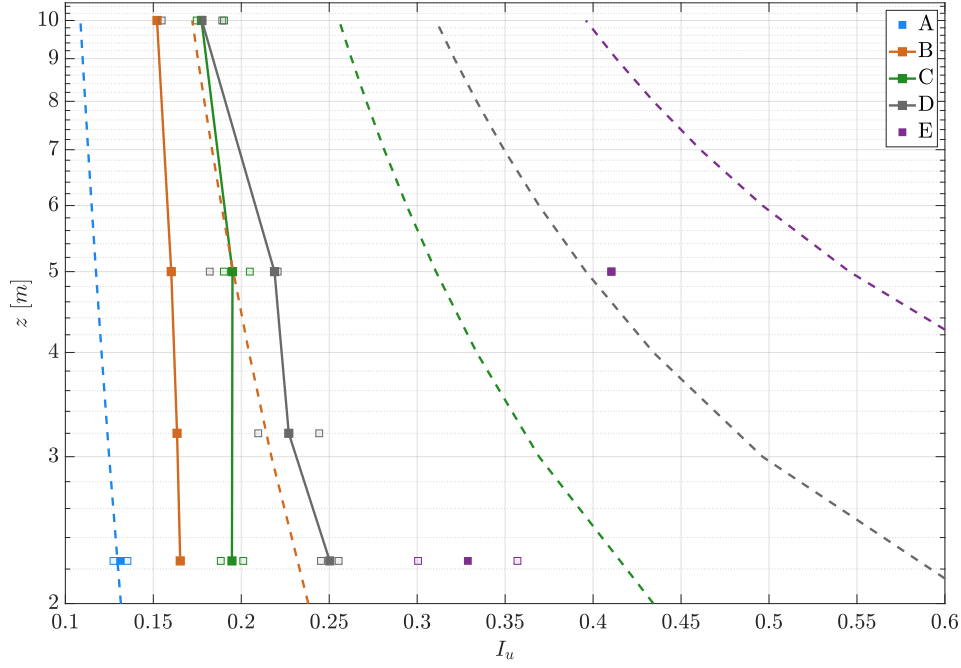
Figure 6.16: Vertical change of I_u for all roughness regimes (Solid marker and lines). Lower and upper 95% confidence intervals are marked transparent. Dashed lines represent I_u values using Eq. 2.22.

It is evident from Figure 6.16 that measured turbulence intensities generally do not follow Eq. 2.22 using observed data in a TC environment. In order to correct these discrepancies within the model, an empirical power equation based on the turbulence intensity at 10 m height is introduced using

$$\gamma = I_u(10m) \left(\frac{z}{10}\right)^{-\mu} \tag{6.3}$$

where μ is z_0-dependent and ranges from 0.05 for smooth surfaces to 0.22 for rough surfaces. This parameter is mathematically defined by $\mu = 0.2123 \, z_0 + 0.0512$. Turbulence intensity values at 10 m ($I_u(10m)$) for B and C roughness regimes are obtained from Table 6.5. $I_u(10m)$ values for roughness regimes A, D, E (little confidence or no data available for $x_1 = 100z$) are either estimated based on observed I_u for all x_1 available or observed I_u in the literature. More specifically, it is assumed that in roughness regime A $I_u(10m) = 0.12$ [e.g. *Yu and Gan Chowdhury*, 2009; *Miller et al.*, 2015], in roughness regime D $I_u(10m) = 0.21$, and in roughness regime E $I_u(10m) = 0.25$. However, it is noted that these values for $I_u(10m)$ represent approximations rather than exact values. The empirically developed Eq. 6.3 is then applied to vertical γ profiles in Fig. 6.16. Figure 6.17 shows the modified I_u profiles for each roughness regime for the lowest 10 m of the TCBL.
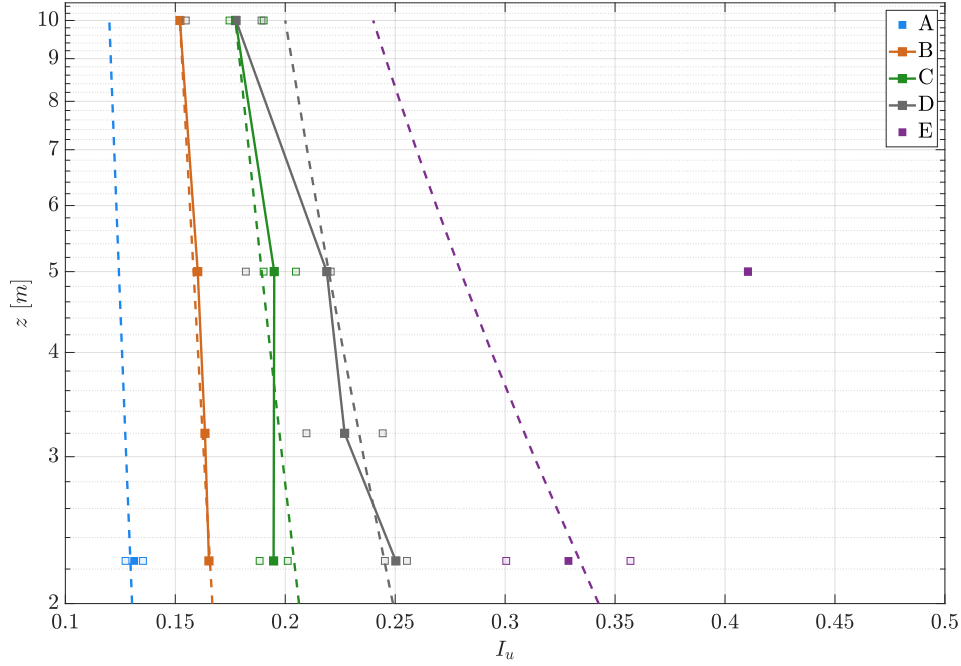
Figure 6.17: Vertical I_u profiles (dashed lines) using Eq. 6.3 with observed γ for all roughness regimes (where data was available). Lower and upper 95% confidence intervals are marked transparent.

The application of Eq. 6.3 shows reasonable approximation for vertical profiles observed in the lowest 10 m of the TCBL. Vertical γ profiles in all roughness regimes follow the observed data within the confidence intervals. The calculation of α directly follows the determination of γ for both z and z_0. It holds that

$$\alpha = \gamma_1 - \gamma \tag{6.4}$$

where γ_1 represents turbulence intensities of the upwind terrain.

To test the validity of the proposed transition model, Eq. 6.1 was used to calculate along-wind turbulence intensities at all heights and terrain transitions. Figures 6.18-6.21 contain mean transition profiles estimated at all measurement heights. Figure 6.18 compares model estimates at $z = 2.25$ m for transitions from each roughness regime to open land with the transition data used to derive it. Figures 6.19-6.21 make the same comparisons at $z = 3.2$ m, 5 m, and 10 m, respectively. Figures 6.22-6.24 then compare model estimates with observed data for transitions to roughly open terrain (C). Significantly less observational data exist for these cases, but qualitative comparisons are still instructive.
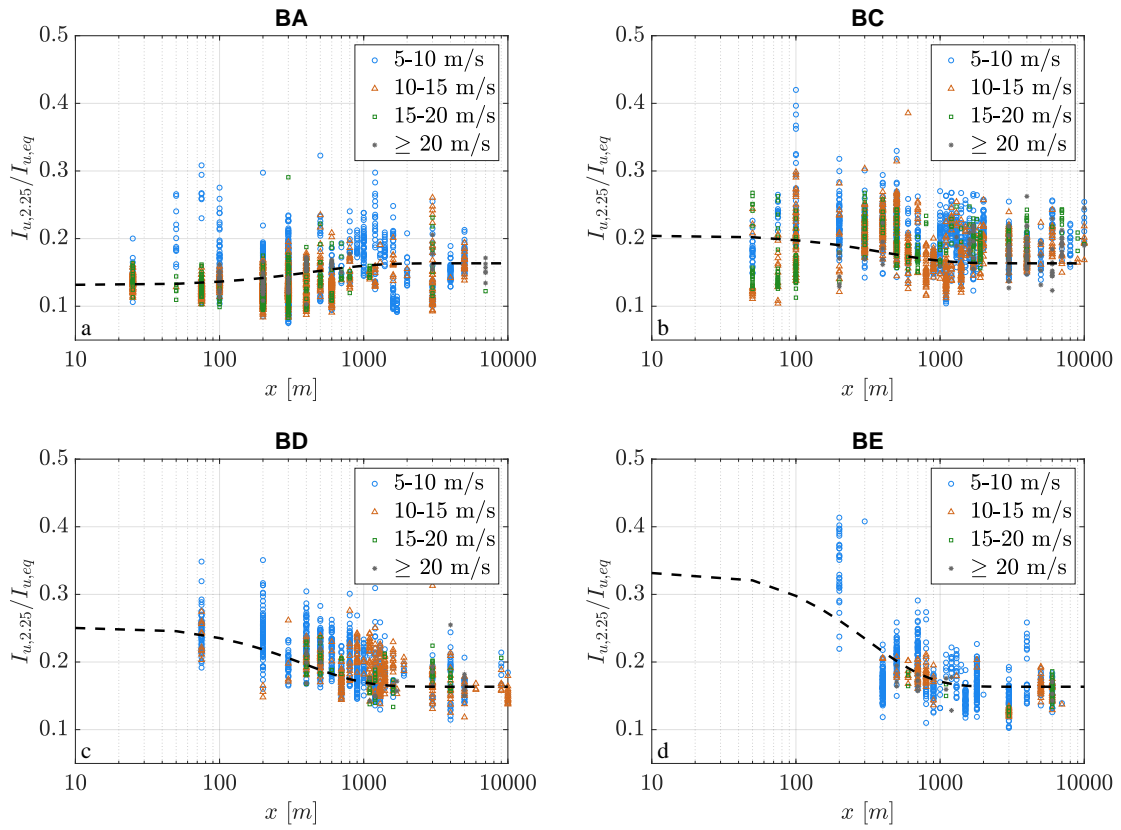
Figure 6.18: I_u transition from a) water bodies (BA), b) roughly open (BC), c) dense suburban (BD), and d) high intensity/forested (BE) to open land normalised by $I_{u,eq}$ at 2.25 m. The modelled transition is displayed as black dashed line.
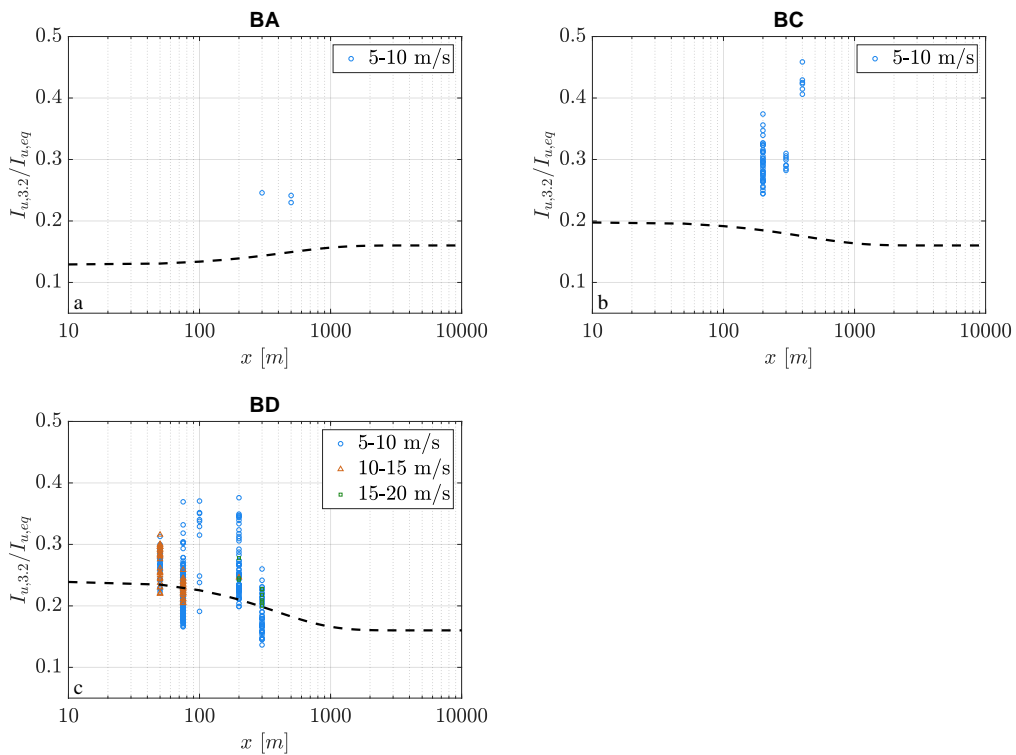
Figure 6.19: I_u transition from a) water bodies (BA), b) roughly open (BC), and c) dense suburban (BD) to open land normalised by $I_{u,eq}$ at 3.2 m. The modelled transition is displayed as black dashed line.
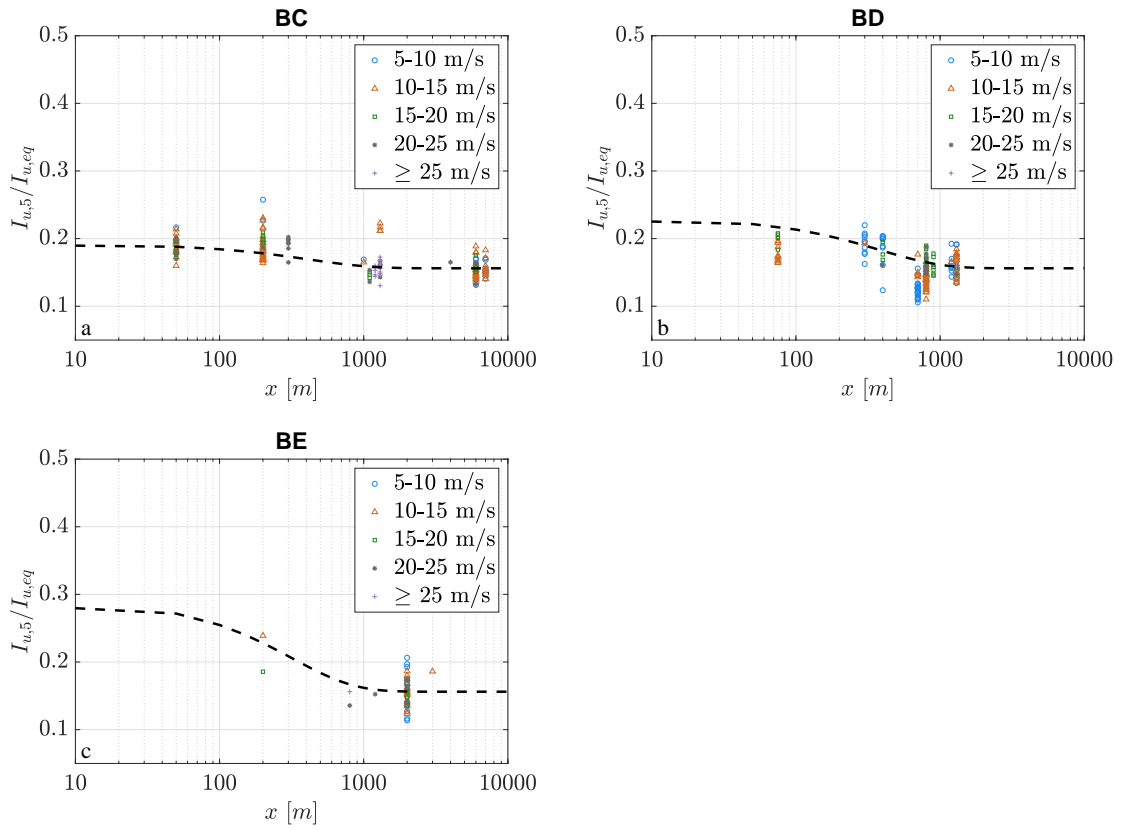
Figure 6.20: I_u transition from a) roughly open (BC), b) dense suburban (BD), and c) high intensity/forested (BE) to open land normalised by $I_{u,eq}$ at 5 m. The modelled transition is displayed as black dashed line.
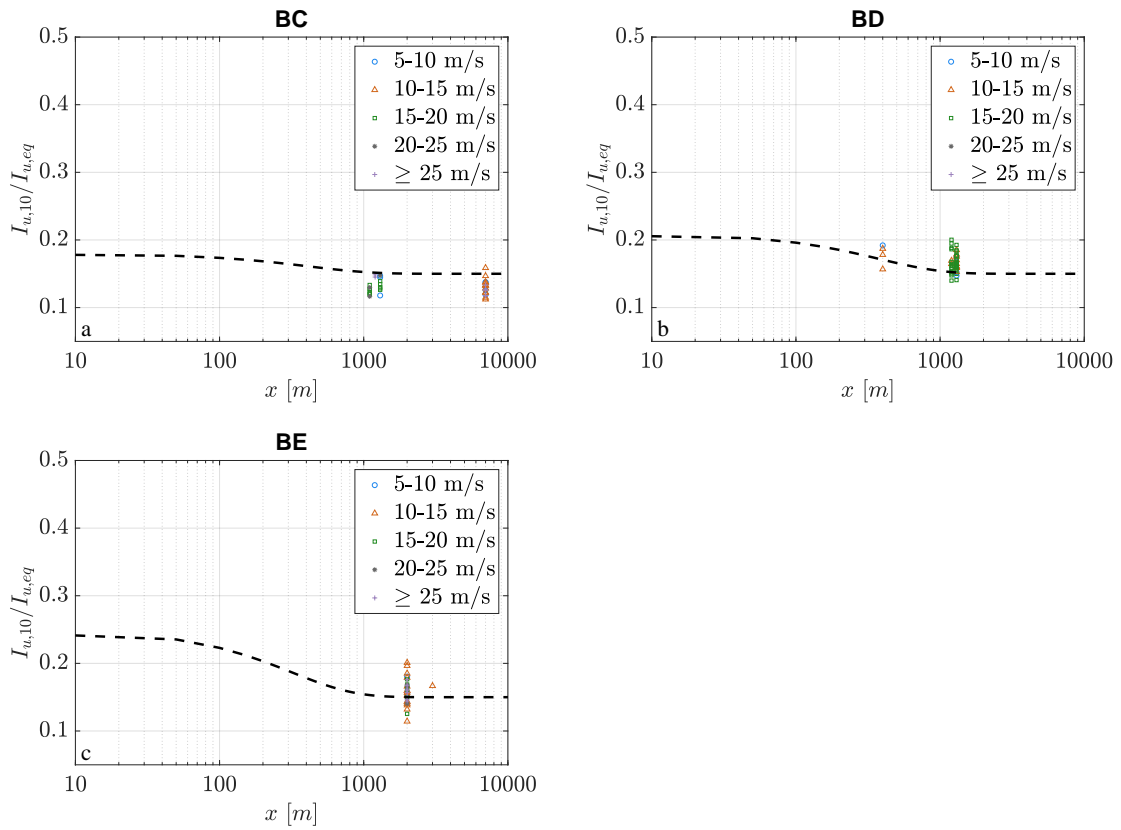
Figure 6.21: I_u transition from a) roughly open (BC), b) dense suburban (BD), and c) high intensity/forested (BE) to open land normalised by $I_{u,eq}$ at 10 m. The modelled transition is displayed as black dashed line.
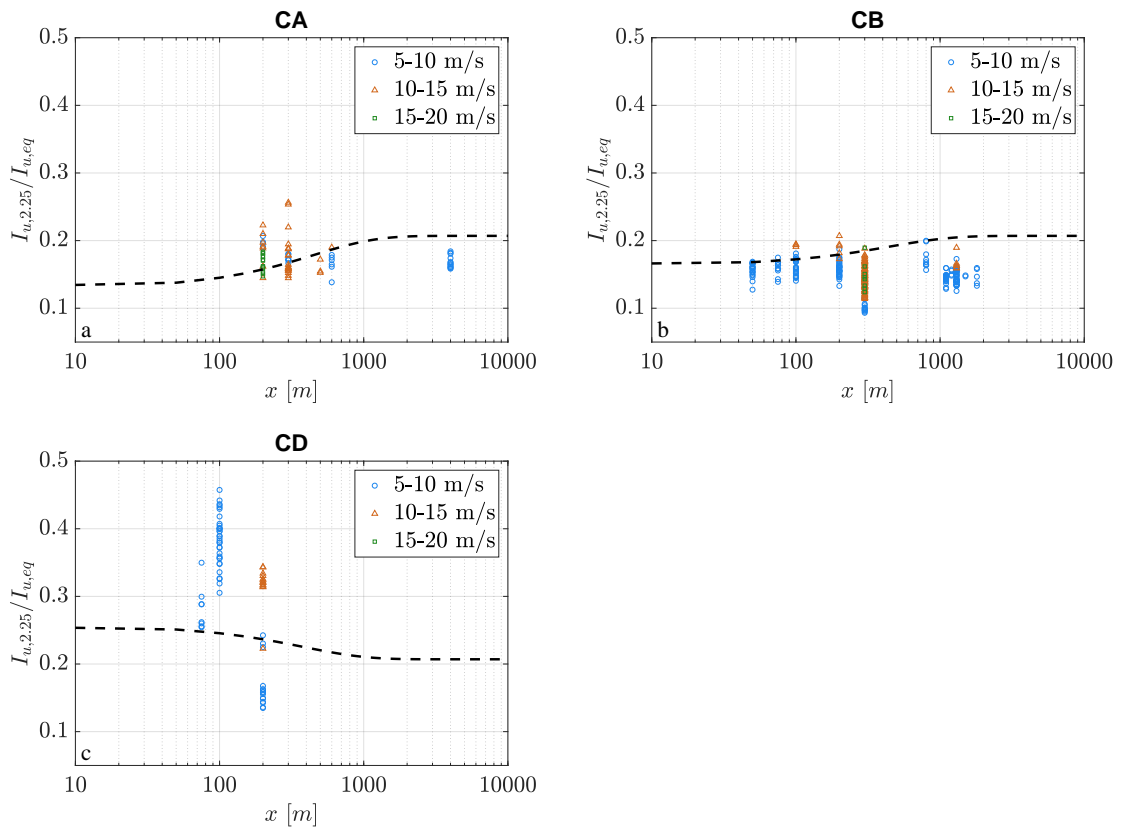
Figure 6.22: I_u transition from a) water bodies (CA), b) open land (CB), and c) dense suburban (CD) to roughly open normalised by $I_{u,eq}$ at 2.25 m. The modelled transition is displayed as black dashed line.
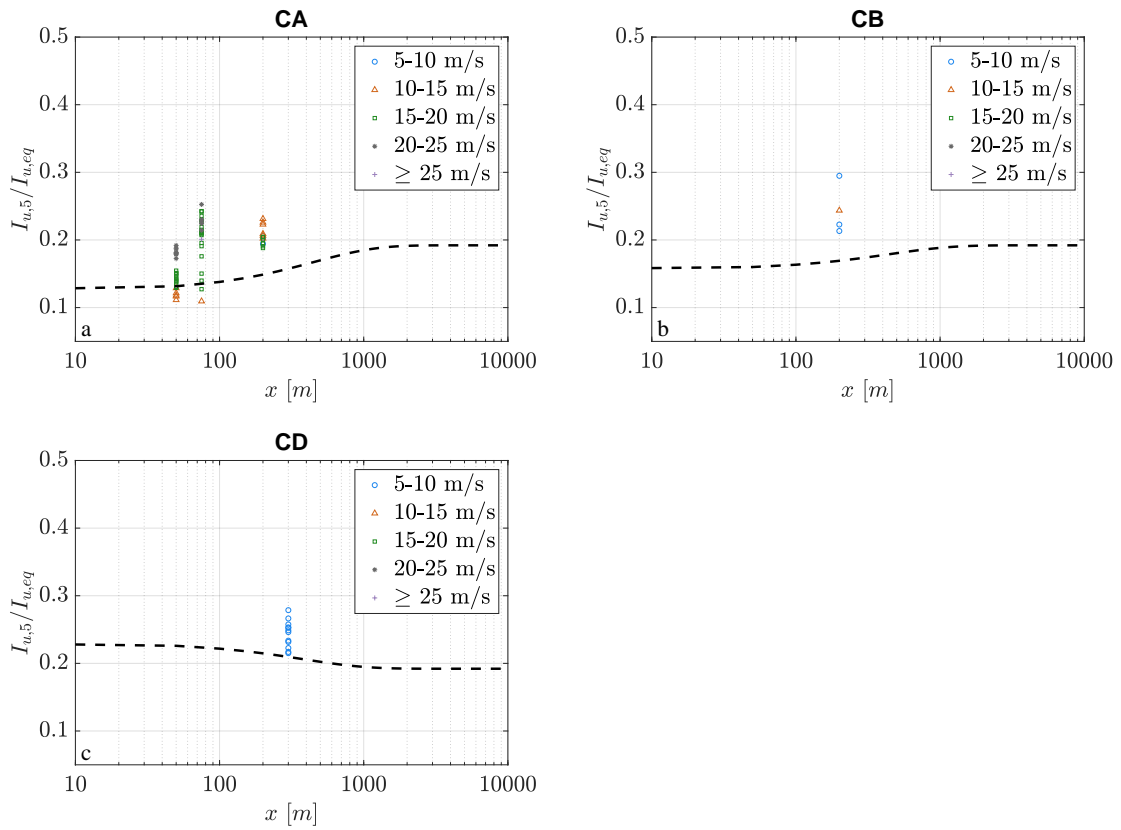
Figure 6.23: I_u transition from a) water bodies (CA), b) open land (CB), and c) dense suburban (CD) to roughly open normalised by $I_{u,eq}$ at 5 m. The modelled transition is displayed as black dashed line.
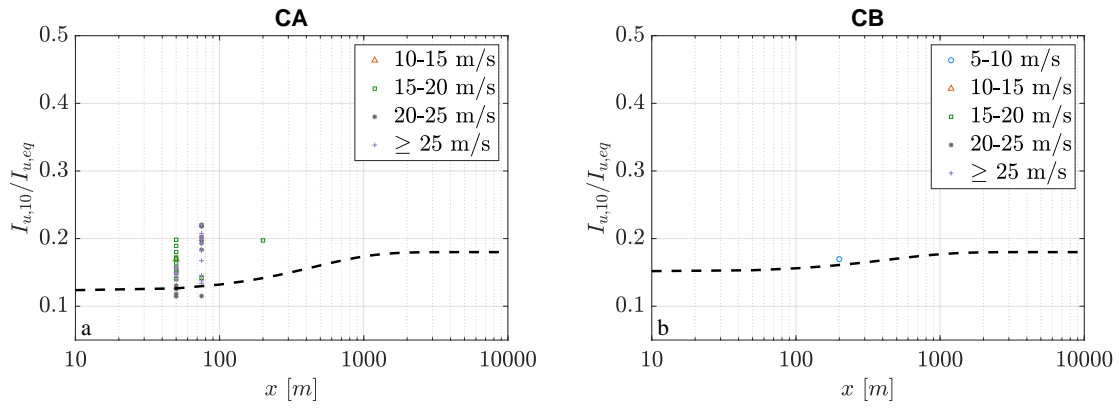
Figure 6.24: I_u transition from a) water bodies (CA) and b) open land (CB) to roughly open normalised by $I_{u,eq}$ at 10 m. The modelled transition is displayed as black dashed line.

Modelled transition profiles are generally in good agreement with observed data over open land. However, transitions BC at 2.25 m and 3.2 m, and BA and BD at 3.2 m show lower along-wind turbulence intensities than observed I_u. Calculated transitions at 5 m and 10 m also exhibit a close agreement at distances, where observations are available. However, the modelled transition from roughly open to open land (BC) in Figure 6.21a exhibits about 10% higher along-wind turbulence intensities. Transition to roughly open terrain show that observed I_u values in Figures 6.22-6.24 do not exhibit a trend towards higher or lower along-wind turbulence intensities. This can, in part, be attributed to the scarcity of data. As such, modelled transitions calculated over roughly open terrain exhibit greater deviations for all upwind terrain and at all heights, where observations are available.

6.2.2.2 Comparison with existing Engineering Transition Models

In the previous section, the empirical transition model was shown to deliver adequate I_u estimates for transitions from different upwind terrain to open land in a TC environment. In contrast, traditional engineering models used to determine transitions, such as AS/NZS1170.2 [*AS/NZS 1170.2:2011*, 2011] and ESDU [*ESDU*, 1982, 1983], were originally developed based on large-scale synoptic ABL winds. To determine whether these models are appropriate for estimating I_u transitions in a TC environment, they are here compared with estimates from the current empirical transition model. Figures 6.25 and 6.26 show the I_u transition to open land and roughly open, respectively, calculated for ESDU, AS/NZS1170.2, and the transition model at all heights and upwind terrain using mean z_0 values from established roughness regimes in Table 4.2.
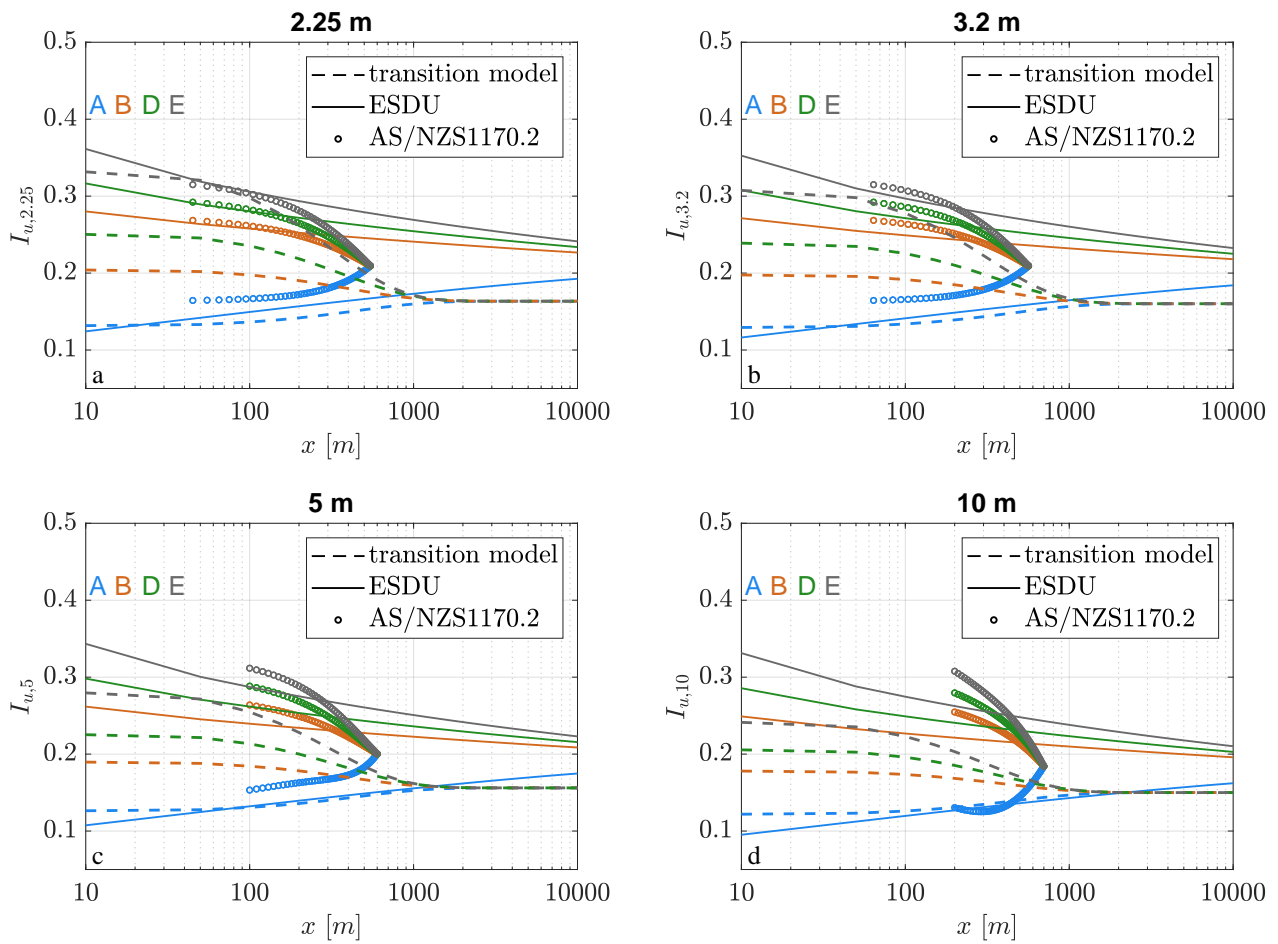
Figure 6.25: Modelled I_u transition from water bodies (A), roughly open (C), dense suburban (D), and high intensity/forested (E) to open land at a) 2.25 m, b) 3.2 m, c) 5 m, and d) 10 m using transition model (dashed), ESDU model (solid lines), and AS/NZS1170.2 (circles).
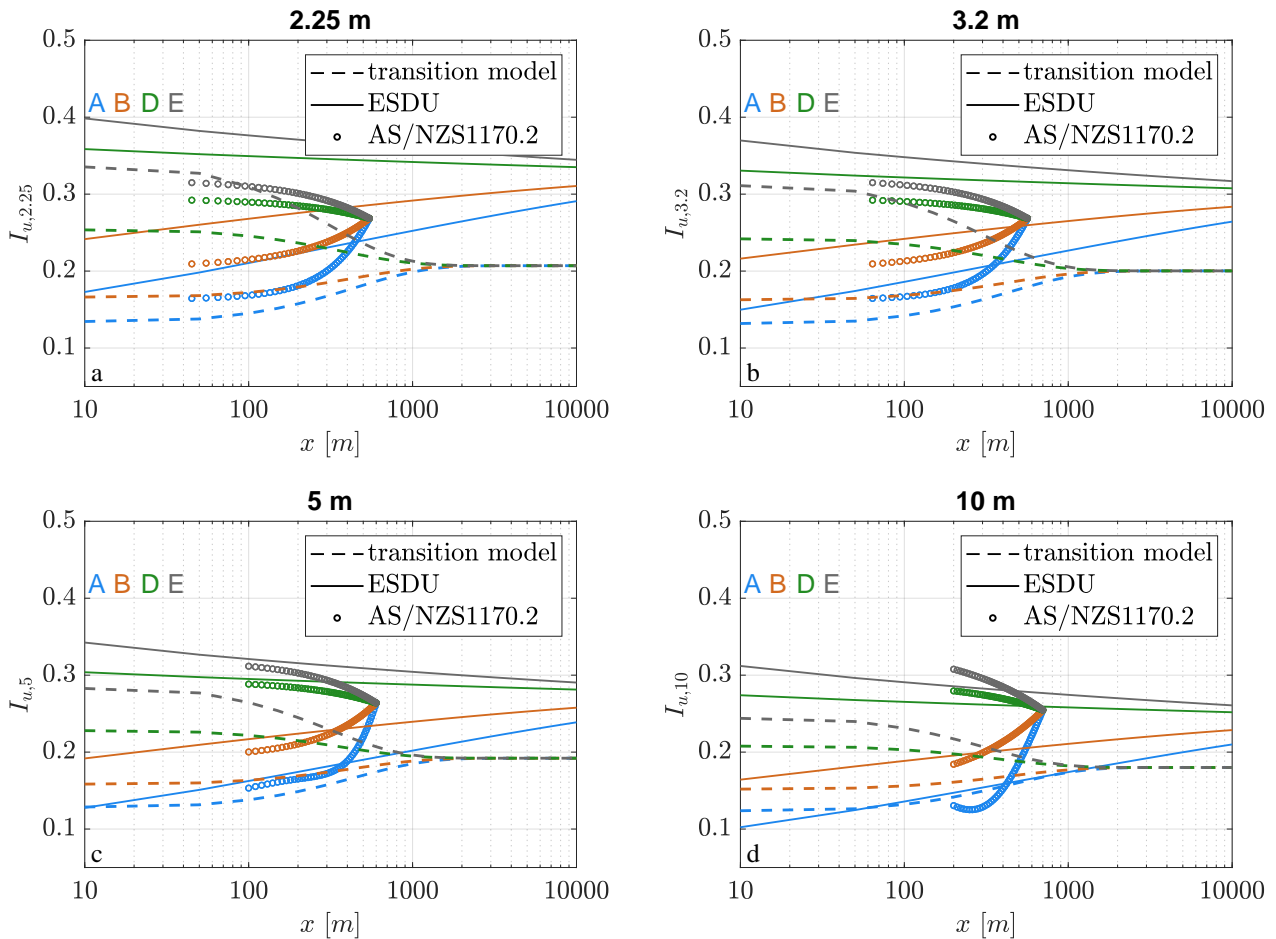
Figure 6.26: Modelled I_u transition from water bodies (A), open land (B), dense suburban (D), and high intensity/forested (E) to roughly open at a) 2.25 m, b) 3.2 m, c) 5 m, and d) 10 m using transition model (dashed), ESDU model (solid lines), and AS/NZS1170.2 (circles).

Modelled I_u transitions show that engineering approaches generally overestimate turbulence intensities when compared with TC observations. Independent of the upwind terrain, both ESDU and AS/NZS1170.2 models exhibit higher I_u at equilibrium conditions and also throughout the transition region. However, with increasing height, the difference between both engineering models and the proposed empirical model reduces. Inspecting the transition region, the ESDU model shows a steady transition of I_u over the full 10 m to 10000 m region, while both the empirical model and AS/NZS1170.2 profiles are characterised by an exponential and a more rapid transition, respectively. Furthermore, the AS/NZS1170.2 transition model is limited to occur over a 500 m region downstream of the lag distance that increases with z. Consequently, the AS/NZS1170.2 model assumes equilibrium with either upwind or local site conditions by approximately $x = 550$ m ($z = 2.25$ m) - 700 m ($z = 10$ m) downwind of the change in terrain. The proposed transition model is shown to be lower than the other two because of an overestimation in both ESDU and AS/NZS1170.2 models of the equilibrium I_u values for a given z_0. In particular, the transition model details the crucial part of the turbulence transition from a different upwind surface to z_0 that occurs largely between 100 m and 1000 m. The ESDU curves exhibit a small overlap with the transition model channel over long distances for smoother surfaces and over short x at 2.25 m for high intensity/forested terrain. With increasing measurement height, transition model results and ESDU output are in close agreement

for transitions from water surfaces (A) to open land (B), whereas differences in transition profiles become bigger for rougher upwind terrain. The AS/NZS1170.2 model seems to transition between ESDU and transition model as turbulence intensities are of similar magnitude with those modelled by the ESDU model for short x over open land surfaces. With increasing distance, AS/NZS1170.2 I_u values get closer to those calculated by the transition model. The overestimation of I_u values by ESDU and AS/NZS1170.2 models becomes greater over roughly open surfaces (Figure 6.26), particularly at lower elevations. In conclusion, the AS/NZS1170.2 model might be applicable to estimate turbulence intensities for $x \leq 400$ m distance in a TC environment when flow transitions from water surfaces onto land. The ESDU model is suitable for estimating I_u values that transition from water surfaces to open land, and at 5 m and 10 m elevations when flow transitions from water bodies to roughly open terrain.

6.2.3 Gust and Peak Factor Transitions

This subsection will explore how along- and across-wind gust and peak factors at 2.25 m, 3.2 m, 5 m, and 10 m evolve following transitions from different upwind terrain in a cyclonic environment. As with turbulence intensities, gust and peak factors were obtained using a non-overlapping 3-sec gust averaging time block within a 10-min mean wind speed (see Chapter 2.1.3.2). Previous analysis in this chapter showed lower G_u and G_v values with increasing $\bar{U}$. Figures 6.27 and 6.28 show the variation of G_u and G_v with x for available upwind terrain at 2.25 m using wind speed bins of 5-10 m/s, 10-15 m/s, 15-20 m/s, and over 20 m/s.
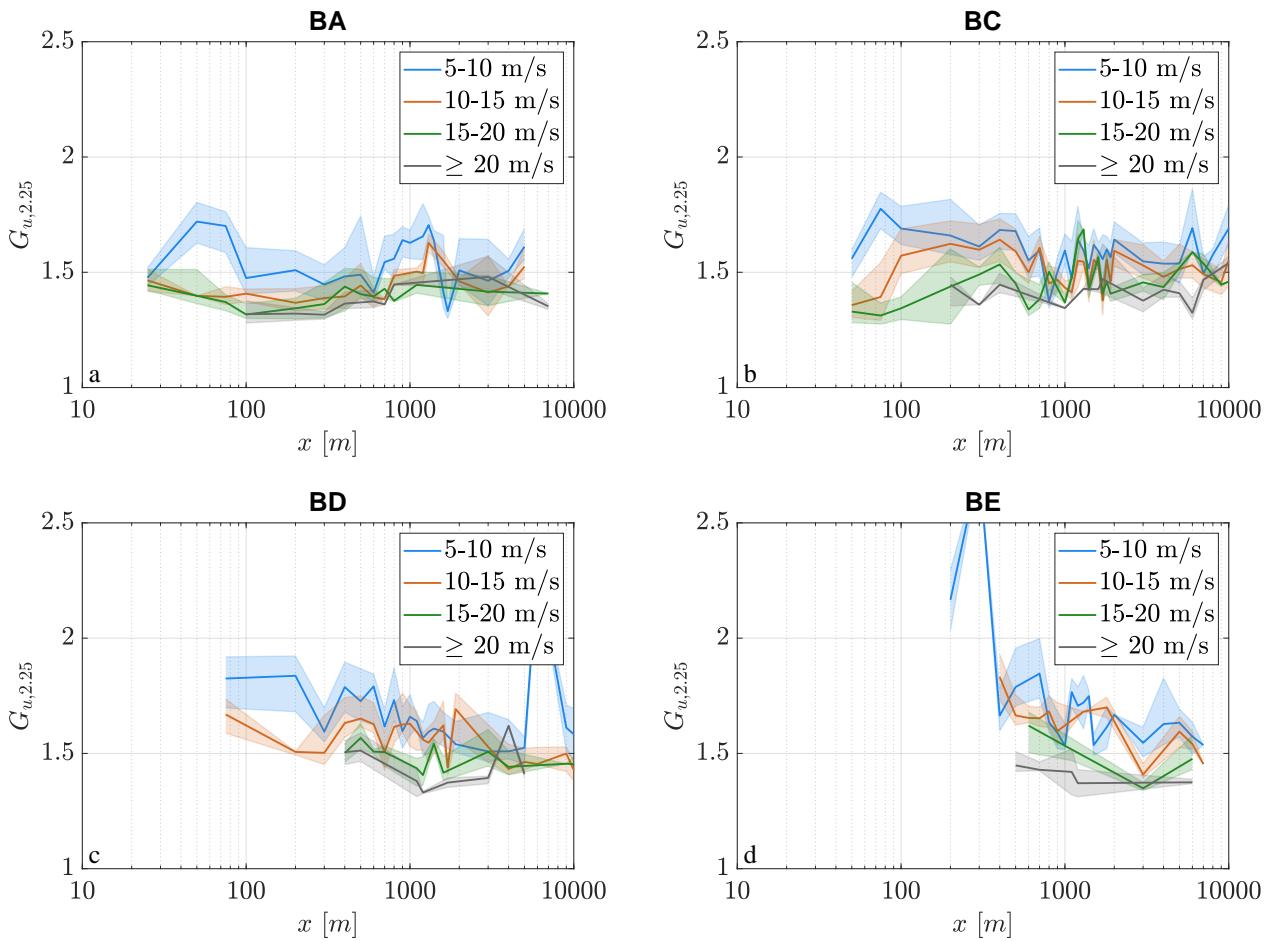
Figure 6.27: G_u transition from a) water bodies (BA), b) roughly open (BC), c) dense suburban (BD), and d) high intensity/forested (BE) to open land at 2.25 m for 5-10 m/s, 10-15 m/s, 15-20 m/s, and over 20 m/s wind speed bins. Medians and the area between 25th and 75th percentile are represented by solid lines and shaded regions, respectively.
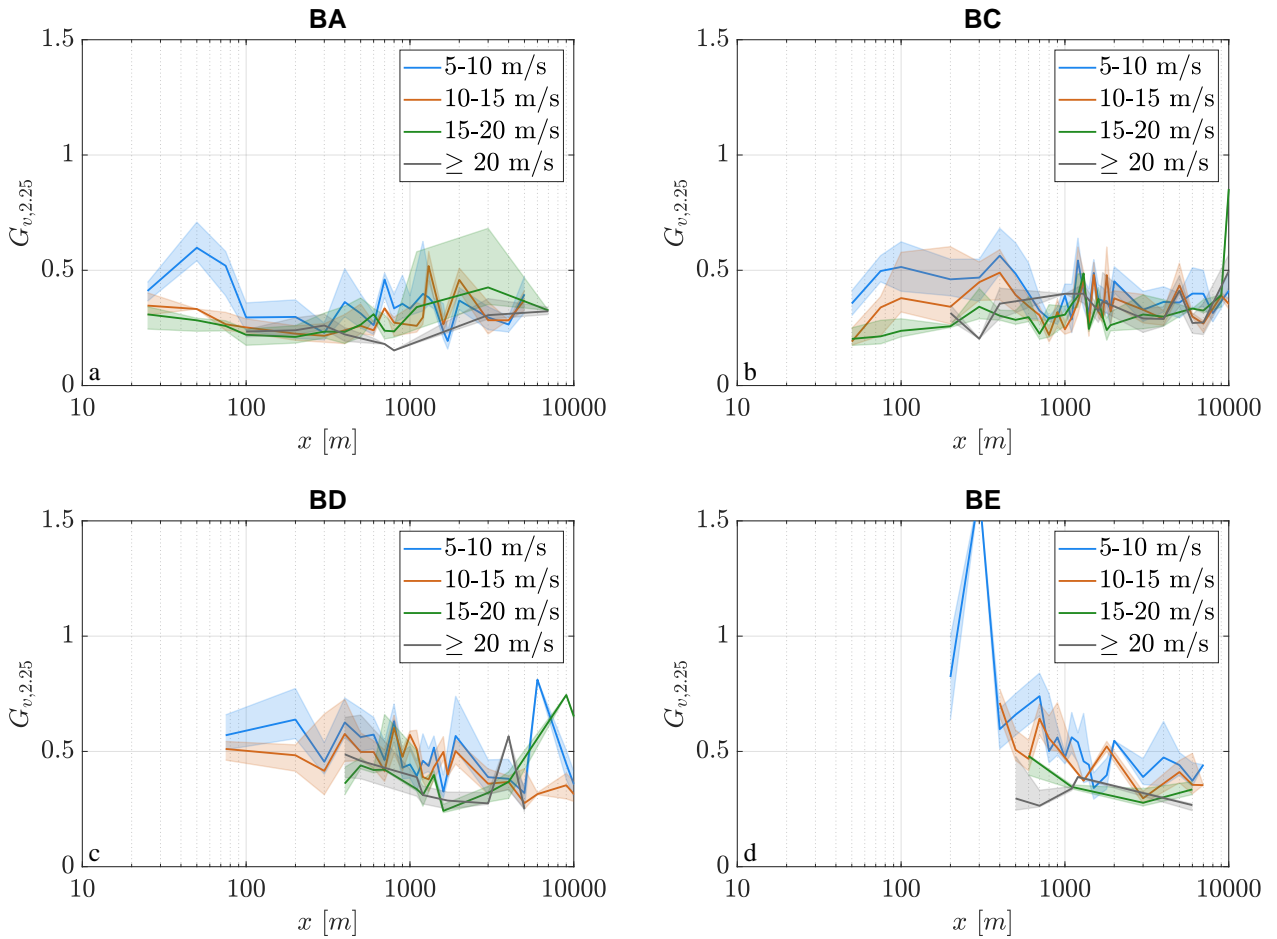
Figure 6.28: G_v transition from a) water bodies (BA), b) roughly open (BC), c) dense suburban (BD), and d) high intensity/forested (BE) to open land at 2.25 m for 5-10 m/s, 10-15 m/s, 15-20 m/s, and over 20 m/s wind speed bins. Medians and the area between 25th and 75th percentile are represented by solid lines and shaded regions, respectively.

Both Figures 6.27 and 6.28 show that lower along- and across-wind gust factors are associated with higher wind speeds as highlighted in the previous analysis of I_u and I_v. Moreover, median G_u and G_v exhibit similar trends with respect to x within each wind speed bin for all transitions to open land, which was also evident for along- and across-wind turbulence intensities. Considering the relationship of turbulence intensity and gust factor through Eq. 2.25 (Chapter 2.1.3.2), the trend of I and G towards higher (lower) values for rougher (smoother) upwind terrain with increasing x is reasonable, assuming g does not change. G_u and G_v values largely vary between 1.32 and 1.64, and 0.23 and 0.46, respectively, for water bodies to open land transitions (BA) considering all heights and wind speed bins with rougher upwind terrain, while G_u and G_v for rougher upwind terrain can exceed values of 2 and 1. More specifically, rougher upwind terrain leads to an increase of G_u largely for wind speeds below 20 m/s. Median along-wind gust factors for 5-10 m/s vary from 1.47 for BA to 2.17 for BE when the roughness change is at a distance of 100 m from the measurement site at 2.25 m. At higher x the increase in G_u is less pronounced and in some cases, G_u values are of similar magnitude for the different terrain transitions. This is also observed for towers deployed in roughly open terrain. At short distances to the roughness change, G_u in roughly open terrain tend to be higher than those over open land, however, with increasing measurement height z and x along-wind gust

factors become of similar magnitude. G_v values generally stay below 1 and are in accordance with along-wind gust factor results. However, this is not the case for BE transitions at $x = 200$ m, where G_v exceeds 1. The spike also appears in across-wind turbulence intensities in Figure 6.10 d), which is caused by a lack of data for transitions from high intensity/forested (E) to open land (B) at $x = 200$ m. All results are summarised using median gust factors at distances x of 100 m, 500 m, and 2000 m to cover multiple points along the transition. Tables 6.6 and 6.7 show the variation of along- and across-wind gust factors for several x at all measurement heights, respectively.

	wind bin [m/s]	100m				500m				2000m			
		2.25	3.2	5	10	2.25	3.2	5	10	2.25	3.2	5	10
BA	5-10	1.47	-	-	-	1.49	1.64	1.58	-	1.51	-	-	-
	>20	1.32	-	-	-	1.37	-	1.47	-	1.48	-	-	-
BC	5-10	1.69	1.81	1.73	-	1.68	2.14	-	-	1.64	-	-	1.48
	>20	1.45	-	1.56	-	1.45	-	1.53	-	1.47	-	1.42	1.55
BD	5-10	1.82	2.21	-	-	1.79	1.73	1.87	1.67	1.67	-	-	1.42
	>20	-	-	-	-	1.51	-	1.87	-	1.37	-	1.38	-
BE	5-10	2.17	-	-	-	1.73	-	-	-	1.54	-	1.44	1.41
	>20	-	-	-	-	1.45	-	-	-	1.37	-	1.51	1.38
CA	5-10	1.65	-	1.61	-	1.59	-	-	-	-	-	-	-
	>20	-	-	1.47	1.51	-	-	-	-	-	-	-	-
CB	5-10	1.56	-	1.54	1.39	1.47	-	-	-	1.67	-	-	-
	>20	-	-	-	-	-	-	-	-	-	-	-	-
CD	5-10	2.18	-	-	-	-	-	2.09	-	-	-	-	-
	>20	-	-	-	-	-	-	-	-	-	-	-	-

Table 6.6: Median G_u values for $x = 100$ m, 500 m, and 2000 m bins categorised into 5-10 m/s and over 20 m/s wind speed bins at 2.25 m, 3.2 m, 5 m and 10 m measurement height considering upstream terrain.

	wind bin [m/s]	100m				500m				2000m			
		2.25	3.2	5	10	2.25	3.2	5	10	2.25	3.2	5	10
BA	5-10	0.30	-	-	-	0.31	0.46	0.44	-	0.37	-	-	-
	>20	0.23	-	-	-	0.22	-	0.34	-	0.30	-	-	-
BC	5-10	0.51	0.59	0.33	-	0.49	0.87	-	-	0.45	-	-	0.39
	>20	0.31	-	0.40	-	0.36	-	0.44	-	0.36	-	0.23	0.32
BD	5-10	0.57	0.94	-	-	0.56	0.52	0.43	0.31	0.57	-	-	0.34
	>20	-	-	-	-	0.46	-	0.33	-	0.29	-	0.42	-
BE	5-10	0.82	-	-	-	0.66	-	-	-	0.55	-	0.23	0.31
	>20	-	-	-	-	0.30	-	-	-	0.39	-	0.19	0.50
CA	5-10	0.32	-	0.41	-	0.32	-	-	-	-	-	-	-
	>20	-	-	0.28	0.26	-	-	-	-	-	-	-	-
CB	5-10	0.35	-	0.37	0.43	0.36	-	-	-	0.40	-	-	-
	>20	-	-	-	-	-	-	-	-	-	-	-	-
CD	5-10	0.95	-	-	-	-	-	0.76	-	-	-	-	-
	>20	-	-	-	-	-	-	-	-	-	-	-	-

Table 6.7: Median G_v values for $x = 100$ m, 500 m, and 2000 m bins categorised into 5-10 m/s and over 20 m/s wind speed bins at 2.25 m, 3.2 m, 5 m and 10 m measurement height considering upstream terrain.

Results above align with the findings of previous research by *Miller et al.* [2015] who found upstream terrain to impact gust factors. Lower gust factors with greater x during the present analysis confirm results by these authors. In addition, *Giammanco et al.* [2016] found mean gust factors to stay below 2.00 for open land exposure, which is also shown in present gust factor analysis. Similar to the analysis of equilibrium values for I_u in Table 6.5, resulting observed G_u and G_v over open land (B) and roughly open (C) at 2.25 m, 5 m, and 10 m are presented in Table 6.8. Here, equilibrium G_u and G_v values are determined by averaging median values at available $x > 2000$ m with flow transitioning to either open land (B) or roughly open (C) in Tables 6.6 and 6.7.

	G_u		G_v	
z	B	C	B	C
2.25 m	1.506	1.670	0.410	0.400
5 m	1.438	-	0.267	-
10 m	1.448	-	0.372	-

Table 6.8: Equilibrium values of G_u and G_v at 2.25 m, 5 m, and 10 m for transitions to open land (B) and roughly open (C).

Observed 10-min segments from 129 towers were also used to investigate how 3-sec along- and across wind peak factors g_u and g_v change with upwind terrain, measurement height, and wind speed

magnitude. *Yu and Gan Chowdhury* [2009] found lower peak factors over water than over land and in general increasing g for higher z_0. *Balderrama et al.* [2012] noted a peak factor decrease evident for increasing wind speeds in open exposure if gust averaging times are at least 3-sec. The present analysis shown in Figures 6.29 and 6.30, and Tables 6.9 and 6.10 reveals peak factors to exhibit no dependency on x, z_{01}, or $\bar{U}$. The independence of the wind speed (see also g_u in Figure 6.1) in particular contradicts the findings by *Balderrama et al.* [2012]. Median along-wind peak factors range from 2.23 to 3.39, while g_v vary between 2.23 and 3.49. Equilibrium values of g_u and g_v at 2.25 m, 5 m, and 10 m for transitions to open land (C) and roughly open (C) are presented in Table 6.11. Results show little variance of g_u over open land (B) with z, whereas g_v over the same terrain appears to be up to 12% greater.
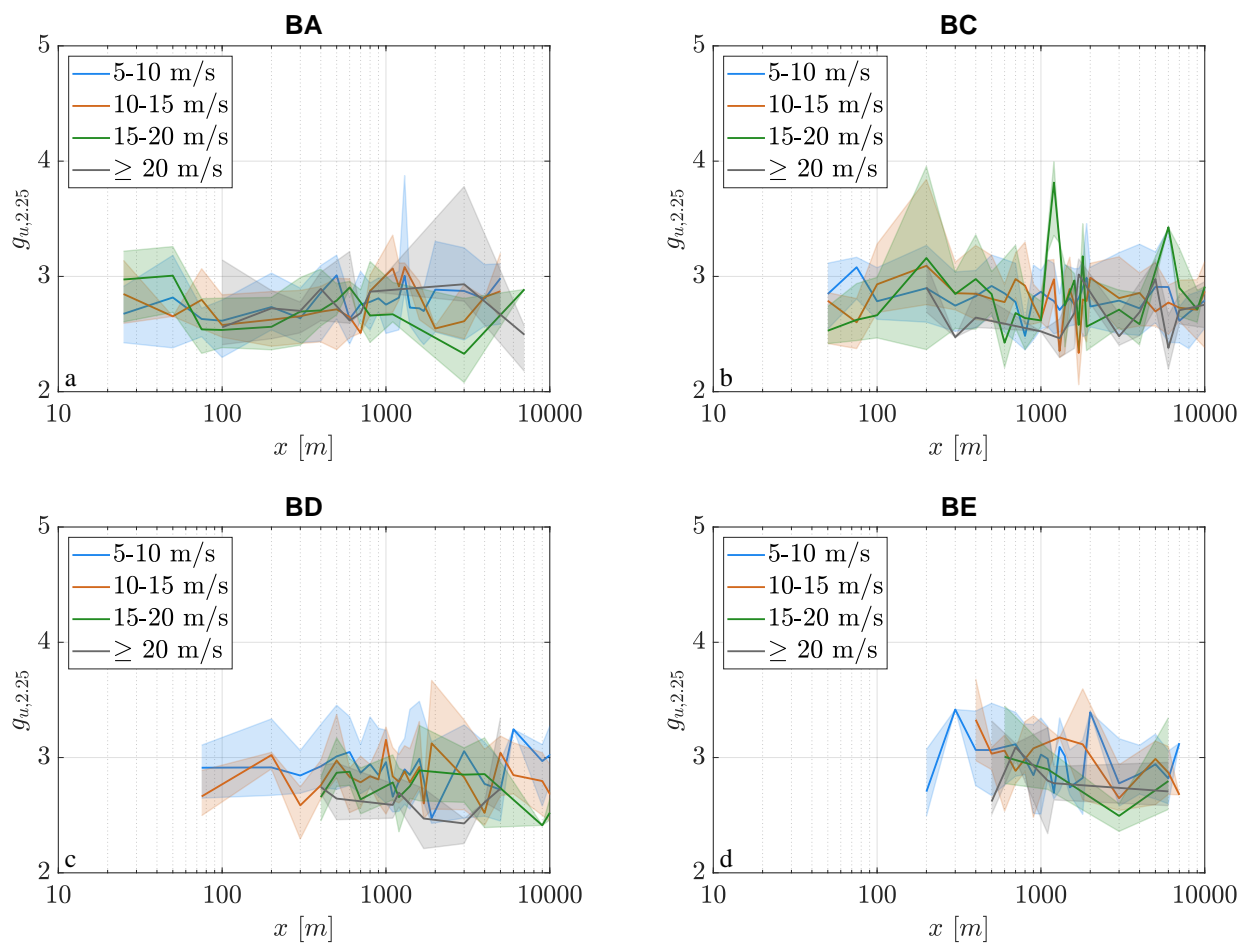
Figure 6.29: g_u transition from a) water bodies (BA), b) roughly open (BC), c) dense suburban (BD), and d) high intensity/forested (BE) to open land at 2.25 m for 5-10 m/s, 10-15 m/s, 15-20 m/s, and over 20 m/s wind speed bins. Medians and the area between 25th and 75th percentile are represented by solid lines and shaded regions, respectively.
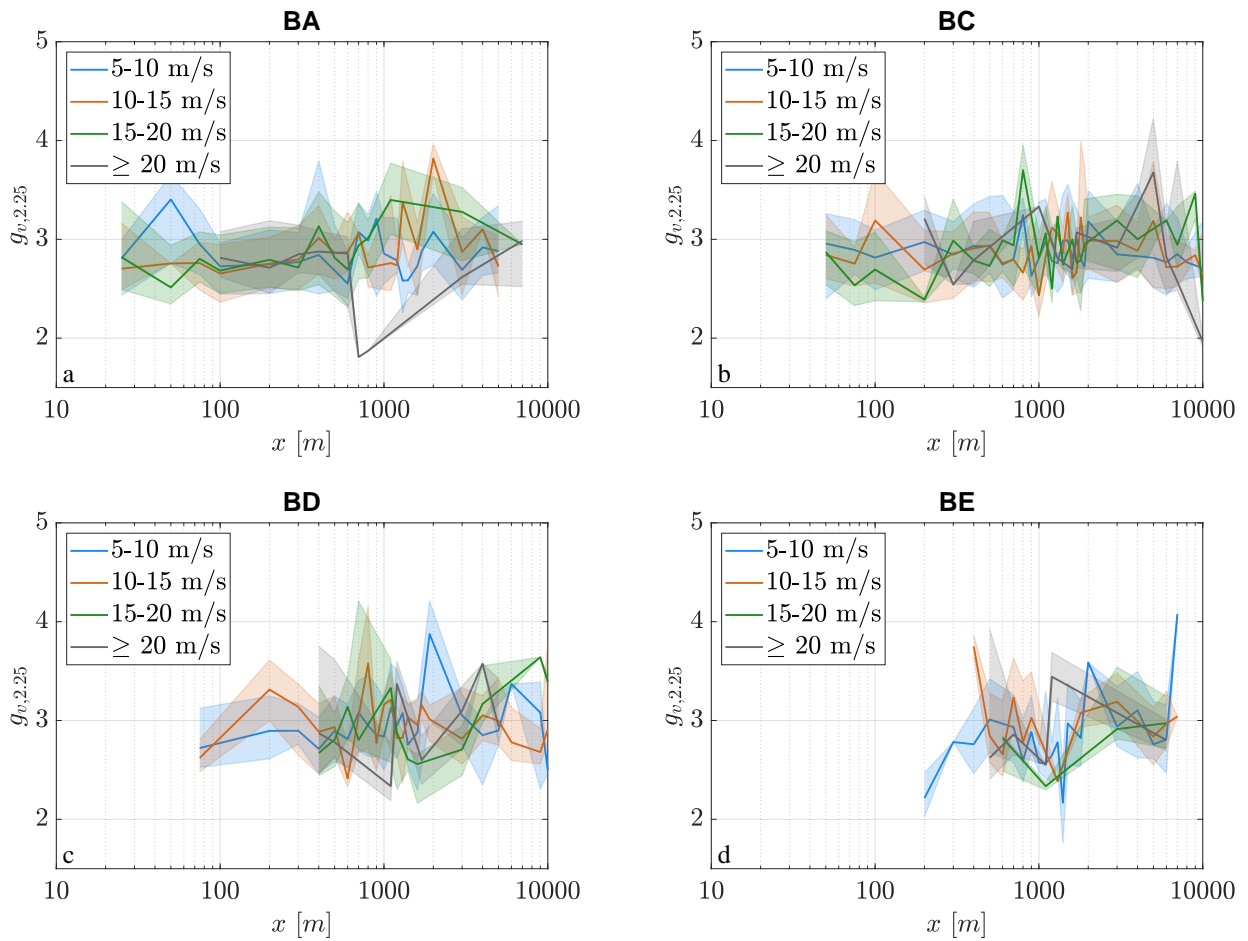
Figure 6.30: g_v transition from a) water bodies (BA), b) roughly open (BC), c) dense suburban (BD), and d) high intensity/forested (BE) to open land at 2.25 m for 5-10 m/s, 10-15 m/s, 15-20 m/s, and over 20 m/s wind speed bins. Medians and the area between 25th and 75th percentile are represented by solid lines and shaded regions, respectively.

	wind bin [m/s]	100m 2.25	3.2	5	10	500m 2.25	3.2	5	10	2000m 2.25	3.2	5	10
BA	5-10	2.61	-	-	-	3.01	2.88	2.92	-	2.89	-	-	-
	>20	2.56	-	-	-	2.62	-	2.41	-	2.87	-	-	-
BC	5-10	2.78	3.07	2.57	-	2.92	3.16	-	-	2.74	-	-	2.97
	>20	2.90	-	2.63	-	2.64	-	2.81	-	3.02	-	2.84	3.38
BD	5-10	2.91	2.86	-	-	3.01	2.95	3.09	3.49	2.47	-	-	2.70
	>20	-	-	-	-	2.64	-	2.53	-	2.59	-	2.66	-
BE	5-10	2.70	-	-	-	3.07	-	-	-	3.39	-	2.84	2.60
	>20	-	-	-	-	2.62	-	-	-	2.80	-	3.32	2.58
CA	5-10	2.77	-	2.68	-	2.86	-	-	-	-	-	-	-
	>20	-	-	2.35	2.64	-	-	-	-	-	-	-	-
CB	5-10	2.78	-	2.23	2.23	2.66	-	-	-	3.33	-	-	-
	>20	-	-	-	-	-	-	-	-	-	-	-	-
CD	5-10	3.14	-	-	-	-	-	2.96	-	-	-	-	-
	>20	-	-	-	-	-	-	-	-	-	-	-	-

Table 6.9: Median g_u values for $x = 100$ m, 500 m, and 2000 m bins categorised into 5-10 m/s and over 20 m/s wind speed bins at 2.25 m, 3.2 m, 5 m and 10 m measurement height considering upstream terrain.

	wind bin [m/s]	100m 2.25	3.2	5	10	500m 2.25	3.2	5	10	2000m 2.25	3.2	5	10
BA	5-10	2.73	-	-	-	2.68	3.26	3.02	-	3.08	-	-	-
	>20	2.81	-	-	-	2.86	-	2.80	-	2.62	-	-	-
BC	5-10	2.82	2.97	2.69	-	2.93	3.19	-	-	3.18	-	-	2.93
	>20	3.21	-	2.65	-	2.79	-	3.14	-	3.07	-	2.81	2.75
BD	5-10	2.72	2.79	-	-	2.89	2.76	2.48	2.47	3.87	-	-	2.53
	>20	-	-	-	-	2.79	-	2.23	-	2.60	-	3.37	-
BE	5-10	2.21	-	-	-	3.01	-	-	-	3.59	-	2.65	3.32
	>20	-	-	-	-	2.62	-	-	-	3.44	-	1.87	3.85
CA	5-10	2.68	-	3.06	-	2.94	-	-	-	-	-	-	-
	>20	-	-	2.81	3.08	-	-	-	-	-	-	-	-
CB	5-10	2.84	-	2.60	2.61	2.83	-	-	-	2.84	-	-	-
	>20	-	-	-	-	-	-	-	-	-	-	-	-
CD	5-10	2.72	-	-	-	-	-	2.37	-	-	-	-	-
	>20	-	-	-	-	-	-	-	-	-	-	-	-

Table 6.10: Median g_v values for $x = 100$ m, 500 m, and 2000 m bins categorised into 5-10 m/s and over 20 m/s wind speed bins at 2.25 m, 3.2 m, 5 m and 10 m measurement height considering upstream terrain.

	g_u		g_v	
z	B	C	B	C
2.25 m	2.846	3.330	3.181	2.840
5 m	2.915	-	2.675	-
10 m	2.846	-	3.076	-

Table 6.11: Equilibrium values of g_u and g_v at 2.25 m, 5 m, and 10 m for transitions to open land (B) and roughly open (C).

6.2.4   Skewness and Kurtosis Transitions

Along- and across-wind components of skewness γ_{su}, γ_{sv} and kurtosis γ_{ku}, γ_{kv} are used to characterise the behaviour of the TC near-surface wind field distribution in this thesis. Analysis of $\gamma_{su}, \gamma_{sv}, \gamma_{ku}, \gamma_{kv}$ in a TC environment has been rare, however, *Balderrama et al.* [2012] noted an increase of skewness and kurtosis with I_u. The authors found a positively skewed and platykurtic TC wind distribution to be evident for wind speeds over 20 m/s at 10 m height. Due to the increase with I_u, the authors conclude that skewness exhibits some dependence on the upwind terrain roughness. This was confirmed by *Fernández-Cabán and Masters* [2017], who demonstrated that skewness values increased with surface roughness for all wind speeds. The authors further note that the kurtosis shows no significant change with surface roughness at 10 m, but a slight increase at 5 m. The present analysis also confirms a positively skewed distribution with higher γ_{su} values that tend to exhibit higher values when rougher upwind terrain is present for all wind speed bins. Results further indicate that γ_{su} appears to transition in a similar fashion to I_u with equilibrium being reached at $x \approx 2000$ m. Median γ_{su} equilibrium values are 0.304, 0.343, and 0.344 at 2.25 m, 5 m, and 10 m for transitions to open land (Table 6.14), whereas 25th and 75th percentiles shown in Figure 6.31 barely exceed 0.5. These results align with research findings by *Balderrama et al.* [2012] and *Fernández-Cabán and Masters* [2017], although the latter study found a mean $\gamma_{su} = 0.49$ at 5 m. This value, however, is in close agreement with the equilibrium value of $\gamma_{su} = 0.46$ at 5 m for transitions to roughly open terrain. Across-wind skewness values shown in Figure 6.32 and Table 6.13 show signs of a normal distribution because values fluctuate around zero independent of $\bar{U}$, z, z_0, z_{01}, and x. That is expected as it is conceptually difficult to explain why any directional bias may exist.

Figure 6.31: γ_{su} transition from a) water bodies (BA), b) roughly open (BC), c) dense suburban (BD), and d) high intensity/forested (BE) to open land at 2.25 m for 5-10 m/s, 10-15 m/s, 15-20 m/s, and over 20 m/s wind speed bins. Medians and the area between 25th and 75th percentile are represented by solid lines and shaded regions, respectively.

Figure 6.32: γ_{sv} transition from a) water bodies (BA), b) roughly open (BC), c) dense suburban (BD), and d) high intensity/forested (BE) to open land at 2.25 m for 5-10 m/s, 10-15 m/s, 15-20 m/s, and over 20 m/s wind speed bins. Medians and the area between 25th and 75th percentile are represented by solid lines and shaded regions, respectively.

	wind	**100m**				**500m**				**2000m**			
	bin [m/s]	2.25	3.2	5	10	2.25	3.2	5	10	2.25	3.2	5	10
BA	5-10	-0.02	-	-	-	0.23	0.42	0.08	-	0.32	-	-	-
	>20	0.02	-	-	-	0.16	-	0.14	-	0.51	-	-	-
BC	5-10	0.30	0.42	0.16	-	0.32	0.53	-	-	0.29	-	-	0.19
	>20	0.08	-	0.21	-	0.24	-	0.19	-	0.29	-	0.08	0.62
BD	5-10	0.26	0.26	-	-	0.37	0.31	0.49	0.79	0.30	-	-	0.24
	>20	-	-	-	-	0.20	-	0.02	-	0.09	-	0.36	-
BE	5-10	0.14	-	-	-	0.38	-	-	-	0.59	-	0.33	0.40
	>20	-	-	-	-	0.29	-	-	-	-0.04	-	0.60	0.27
CA	5-10	0.26	-	0.14	-	0.16	-	-	-	-	-	-	-
	>20	-	-	-0.01	-0.02	-	-	-	-	-	-	-	-
CB	5-10	0.17	-	0.27	0.10	0.41	-	-	-	0.46	-	-	-
	>20	-	-	-	-	-	-	-	-	-	-	-	-
CD	5-10	0.47	-	-	-	-	-	0.33	-	-	-	-	-
	>20	-	-	-	-	-	-	-	-	-	-	-	-

Table 6.12: Median γ_{su} values for $x = 100$ m, 500 m, and 2000 m bins categorised into 5-10 m/s and over 20 m/s wind speed bins at 2.25 m, 3.2 m, 5 m and 10 m measurement height considering upstream terrain.

	wind	**100m**				**500m**				**2000m**			
	bin [m/s]	2.25	3.2	5	10	2.25	3.2	5	10	2.25	3.2	5	10
BA	5-10	-0.02	-	-	-	-0.05	0.04	0.25	-	0.09	-	-	-
	>20	0.01	-	-	-	0.17	-	0.43	-	0.03	-	-	-
BC	5-10	-0.04	0.12	-0.34	-	0.04	0.24	-	-	0.03	-	-	0.02
	>20	-0.01	-	0.06	-	0.12	-	-0.03	-	-0.02	-	0.07	0.15
BD	5-10	-0.05	0.08	-	-	0.01	0.01	-0.28	-0.09	0.64	-	-	0.28
	>20	-	-	-	-	0.04	-	-0.71	-	-0.18	-	0.91	-
BE	5-10	-0.63	-	-	-	0.05	-	-	-	-0.15	-	-0.16	0.14
	>20	-	-	-	-	-0.03	-	-	-	0.14	-	-0.85	0.81
CA	5-10	-0.19	-	0.12	-	-0.05	-	-	-	-	-	-	-
	>20	-	-	0.16	0.16	-	-	-	-	-	-	-	-
CB	5-10	0.08	-	0.05	0.39	0.03	-	-	-	0.08	-	-	-
	>20	-	-	-	-	-	-	-	-	-	-	-	-
CD	5-10	-0.08	-	-	-	-	-	-0.32	-	-	-	-	-
	>20	-	-	-	-	-	-	-	-	-	-	-	-

Table 6.13: Median γ_{sv} values for $x = 100$ m, 500 m, and 2000 m bins categorised into 5-10 m/s and over 20 m/s wind speed bins at 2.25 m, 3.2 m, 5 m and 10 m measurement height considering upstream terrain.

	γ_{su}		γ_{sv}	
z	B	C	B	C
2.25 m	0.304	0.460	0.090	0.08
5 m	0.343	-	-0.008	-
10 m	0.344	-	0.148	-

Table 6.14: Equilibrium values of γ_{su} and γ_{sv} at 2.25 m, 5 m, and 10 m for transitions to open land (B) and roughly open (C).

In general, the along-wind kurtosis analysis shown in Figure 6.33 and Table 6.15 reveals values below 3, which represents a platykurtic wind distribution. This behaviour was observed for all $\bar{U}$, z, z_0, z_{01}, and x. More specifically, observed γ_{ku} values at lower elevations were up to 14% lower for $\bar{U}$ greater than 20 m/s compared to 5-10 m/s. In contrast, γ_{ku} at higher elevations tend to be up to 15% higher for $\bar{U}$ greater than 20 m/s compared to 5-10 m/s. However, results indicate that these differences were independent of the upwind roughness and distance to the roughness change. That is, no clear transition region was observed in any of analysed data for any combination of z_0, z_{01}, or z. This result is also confirmed by *Balderrama et al.* [2012] and *Fernández-Cabán and Masters* [2017], who independently found that the kurtosis does not change significantly for different terrain exposures and elevations. Equilibrium values in Table 6.17 also align with these two studies with γ_{ku} = 3.00, 2.99. and 2.86 at 2.25 m, 5 m, and 10 m, respectively. Across-wind kurtosis analysis displayed in Figure 6.34 and Table 6.16 exhibits a greater γ_{kv} variation with values generally above 3 representing a leptokurtic distribution. This follows the behaviour of the across-wind component with high fluctuations around zero where greater standard deviations are more likely. Results in Table 6.16 indicate slightly higher γ_{kv} with rougher upwind terrain independent of $\bar{U}$, z, z_0, and x.

Figure 6.33: γ_{ku} transition from a) water bodies (BA), b) roughly open (BC), c) dense suburban (BD), and d) high intensity/forested (BE) to open land at 2.25 m for 5-10 m/s, 10-15 m/s, 15-20 m/s, and over 20 m/s wind speed bins. Medians and the area between 25th and 75th percentile are represented by solid lines and shaded regions, respectively.

Figure 6.34: γ_{kv} transition from a) water bodies (BA), b) roughly open (BC), c) dense suburban (BD), and d) high intensity/forested (BE) to open land at 2.25 m for 5-10 m/s, 10-15 m/s, 15-20 m/s, and over 20 m/s wind speed bins. Medians and the area between 25th and 75th percentile are represented by solid lines and shaded regions, respectively.

	wind	100m				500m				2000m			
	bin [m/s]	2.25	3.2	5	10	2.25	3.2	5	10	2.25	3.2	5	10
BA	5-10	2.85	-	-	-	2.89	2.80	2.69	-	2.80	-	-	-
	>20	2.70	-	-	-	2.73	-	2.48	-	3.19	-	-	-
BC	5-10	2.86	3.01	2.68	-	2.91	3.04	-	-	2.72	-	-	2.72
	>20	2.93	-	2.77	-	2.67	-	2.74	-	2.99	-	3.07	3.80
BD	5-10	2.92	3.03	-	-	2.99	2.82	2.97	3.46	2.61	-	-	2.56
	>20	-	-	-	-	2.57	-	2.72	-	2.69	-	2.74	-
BE	5-10	2.97	-	-	-	3.02	-	-	-	3.78	-	2.80	2.63
	>20	-	-	-	-	2.71	-	-	-	3.24	-	3.36	2.60
CA	5-10	2.79	-	2.47	-	2.80	-	-	-	-	-	-	-
	>20	-	-	2.84	2.74	-	-	-	-	-	-	-	-
CB	5-10	2.77	-	2.57	2.39	2.86	-	-	-	2.93	-	-	-
	>20	-	-	-	-	-	-	-	-	-	-	-	-
CD	5-10	3.07	-	-	-	-	-	2.93	-	-	-	-	-
	>20	-	-	-	-	-	-	-	-	-	-	-	-

Table 6.15: Median γ_{ku} values for $x = 100$ m, 500 m, and 2000 m bins categorised into 5-10 m/s and over 20 m/s wind speed bins at 2.25 m, 3.2 m, 5 m and 10 m measurement height considering upstream terrain.

	wind	100m				500m				2000m			
	bin [m/s]	2.25	3.2	5	10	2.25	3.2	5	10	2.25	3.2	5	10
BA	5-10	3.18	-	-	-	3.19	3.50	3.12	-	3.57	-	-	-
	>20	3.03	-	-	-	3.07	-	3.20	-	3.04	-	-	-
BC	5-10	3.19	3.42	3.33	-	3.37	4.30	-	-	3.38	-	-	3.00
	>20	3.68	-	3.37	-	2.83	-	3.81	-	3.15	-	3.07	2.89
BD	5-10	3.07	2.90	-	-	3.44	3.08	3.17	2.65	4.31	-	-	2.97
	>20	-	-	-	-	3.48	-	4.23	-	3.01	-	3.10	-
BE	5-10	3.46	-	-	-	3.56	-	-	-	3.88	-	3.15	3.81
	>20	-	-	-	-	3.42	-	-	-	3.35	-	4.24	4.36
CA	5-10	3.20	-	3.26	-	3.16	-	-	-	-	-	-	-
	>20	-	-	3.15	3.34	-	-	-	-	-	-	-	-
CB	5-10	2.91	-	2.75	2.39	3.28	-	-	-	3.13	-	-	-
	>20	-	-	-	-	-	-	-	-	-	-	-	-
CD	5-10	3.42	-	-	-	-	-	3.21	-	-	-	-	-
	>20	-	-	-	-	-	-	-	-	-	-	-	-

Table 6.16: Median γ_{kv} values for $x = 100$ m, 500 m, and 2000 m bins categorised into 5-10 m/s and over 20 m/s wind speed bins at 2.25 m, 3.2 m, 5 m and 10 m measurement height considering upstream terrain.

	γ_{ku}		γ_{kv}	
z	B	C	B	C
2.25 m	3.003	2.93	3.461	3.130
5 m	2.993	-	3.390	-
10 m	2.862	-	3.406	-

Table 6.17: Equilibrium values of γ_{ku} and γ_{kv} at 2.25 m, 5 m, and 10 m for transitions to open land (B) and roughly open (C).

6.2.5 Integral Length Scale Transitions

To conclude the analysis of near-surface turbulent characteristics in landfalling TCs, along- and across-wind integral length scales L_u and L_v and their behaviour with changing upwind terrain are described in more detail in this subsection. Similar to previous analysis, L_u and L_v were determined for each 10-min segment available according to Eq. 2.38. Analysis of L_u and L_v in Figures 6.35 and 6.36 and Tables 6.18 and 6.18 tend to exhibit greater along- and across-wind integral length scales with $\bar{U}$ (see also Figure 6.1), which is evident throughout the lower TCBL where measurements are available. While maximum L_u values reach up to 1200 m, which was also found by *Masters et al.* [2010], length scales do not appear to exhibit a dependency on z_0, z_{01}, and x at 2.25 m. However, L_u and L_v appear to become slightly smaller with greater z_{01} but $x < 200$ m at 5 m and 10 m elevations. This aligns with findings by *Yu and Gan Chowdhury* [2009], who suggest L_u over water to be larger than over land. Moreover, equilibrium L_u and L_v values are observed to be of higher magnitude with z as shown in Table 6.20 and as identified in earlier research by *Kolmogorov* [1941].
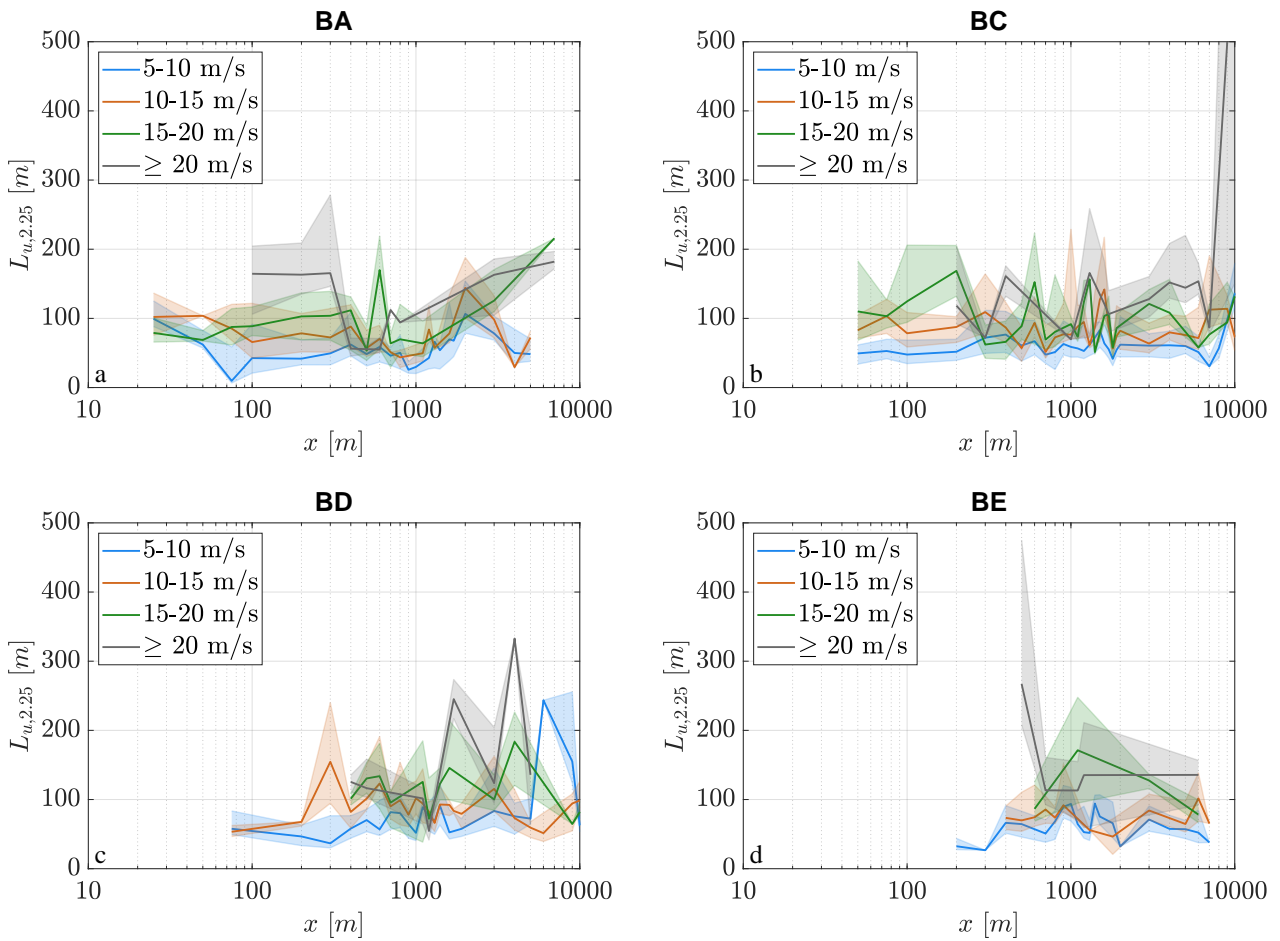
Figure 6.35: L_u transition from a) water bodies (BA), b) roughly open (BC), c) dense suburban (BD), and d) high intensity/forested (BE) to open land at 2.25 m for 5-10 m/s, 10-15 m/s, 15-20 m/s, and over 20 m/s wind speed bins. Medians and the area between 25th and 75th percentile are represented by solid lines and shaded regions, respectively.
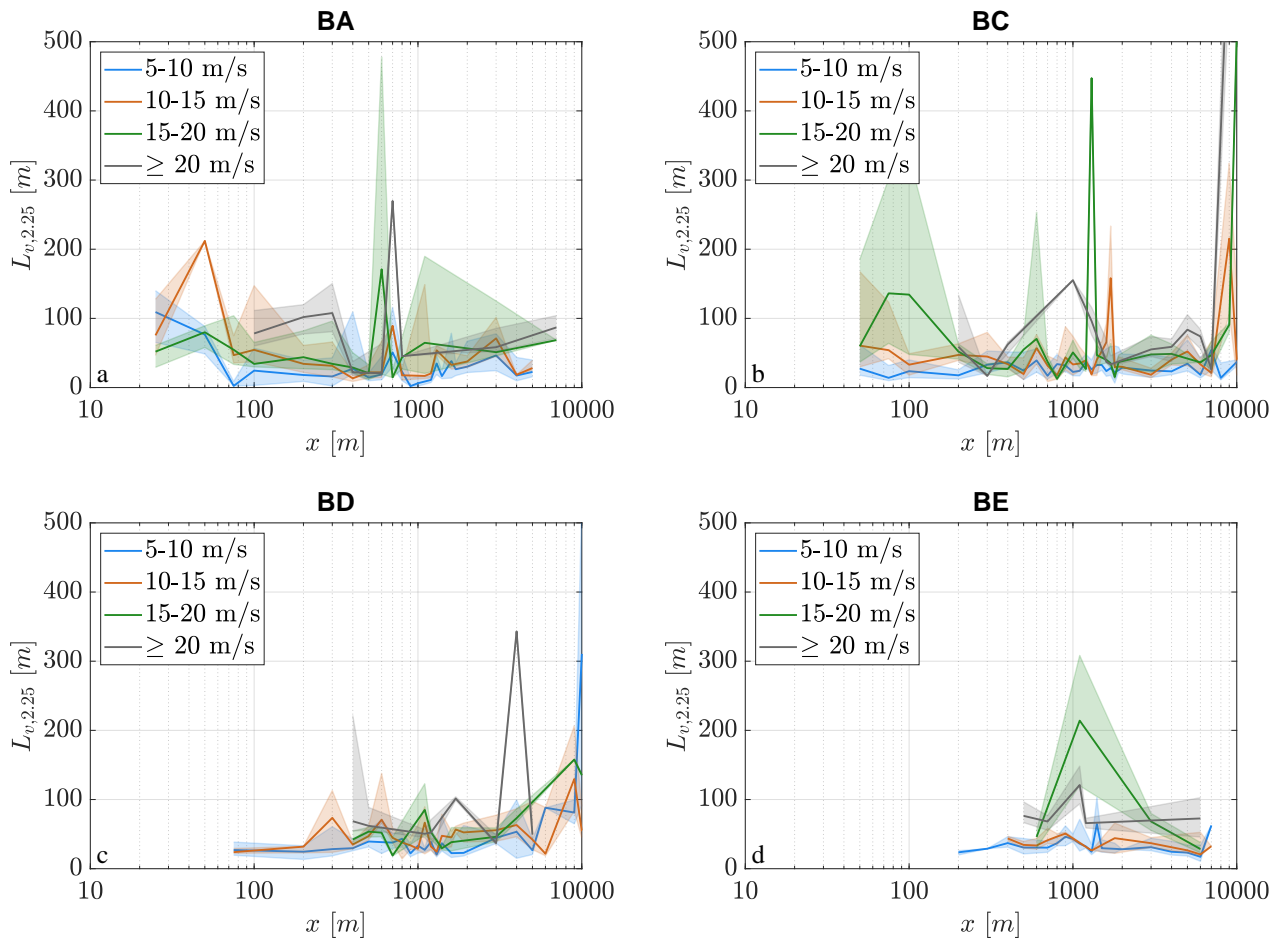
Figure 6.36: L_v transition from a) water bodies (BA), b) roughly open (BC), c) dense suburban (BD), and d) high intensity/forested (BE) to open land at 2.25 m for 5-10 m/s, 10-15 m/s, 15-20 m/s, and over 20 m/s wind speed bins. Medians and the area between 25th and 75th percentile are represented by solid lines and shaded regions, respectively.

	wind	100m				500m				2000m			
	bin [m/s]	2.25	3.2	5	10	2.25	3.2	5	10	2.25	3.2	5	10
BA	5-10	42.6	-	-	-	48.4	33.4	38.3	-	106.6	-	-	-
	>20	164.5	-	-	-	56.2	-	144.8	-	163.0	-	-	-
BC	5-10	47.7	44.1	119.5	-	60.7	24.0	-	-	62.0	-	-	147.7
	>20	118.4	-	122.9	-	161.1	-	167.7	-	106.2	-	160.7	186.2
BD	5-10	57.7	23.2	-	-	70.3	46.2	84.6	167.6	57.7	-	-	59.6
	>20	-	-	-	-	116.4	-	89.9	-	245.2	-	121.6	-
BE	5-10	32.5	-	-	-	64.5	-	-	-	32.2	-	168.4	179.3
	>20	-	-	-	-	267.2	-	-	-	135.3	-	164.4	153.4
CA	5-10	56.5	-	43.0	-	33.0	-	-	-	-	-	-	-
	>20	-	-	73.0	107.4	-	-	-	-	-	-	-	-
CB	5-10	40.5	-	78.4	110.2	93.7	-	-	-	45.7	-	-	-
	>20	-	-	-	-	-	-	-	-	-	-	-	-
CD	5-10	40.5	-	-	-	-	-	35.4	-	-	-	-	-
	>20	-	-	-	-	-	-	-	-	-	-	-	-

Table 6.18: Median L_u values for $x = 100$ m, 500 m, and 2000 m bins categorised into 5-10 m/s and over 20 m/s wind speed bins at 2.25 m, 3.2 m, 5 m and 10 m measurement height considering upstream terrain.

	wind	100m				500m				2000m			
	bin [m/s]	2.25	3.2	5	10	2.25	3.2	5	10	2.25	3.2	5	10
BA	5-10	24.5	-	-	-	14.5	40.0	71.4	-	30.2	-	-	-
	>20	78.2	-	-	-	22.0	-	280.9	-	58.3	-	-	-
BC	5-10	23.7	13.3	302.9	-	24.5	17.2	-	-	28.9	-	-	64.6
	>20	59.0	-	103.1	-	62.2	-	88.9	-	33.5	-	105.8	73.9
BD	5-10	27.0	10.1	-	-	39.3	19.4	75.8	31.2	22.8	-	-	129.1
	>20	-	-	-	-	62.0	-	75.1	-	101.5	-	84.7	-
BE	5-10	23.7	-	-	-	24.5	-	-	-	28.9	-	56.7	81.8
	>20	-	-	-	-	76.4	-	-	-	65.9	-	104.3	217.6
CA	5-10	15.3	-	19.5	-	11.5	-	-	-	-	-	-	-
	>20	-	-	59.5	75.8	-	-	-	-	-	-	-	-
CB	5-10	41.4	-	138.8	535.3	70.1	-	-	-	13.7	-	-	-
	>20	-	-	-	-	-	-	-	-	-	-	-	-
CD	5-10	18.4	-	-	-	-	-	22.9	-	-	-	-	-
	>20	-	-	-	-	-	-	-	-	-	-	-	-

Table 6.19: Median L_v values for $x = 100$ m, 500 m, and 2000 m bins categorised into 5-10 m/s and over 20 m/s wind speed bins at 2.25 m, 3.2 m, 5 m and 10 m measurement height considering upstream terrain.

	L_u [m]		L_v [m]	
z	B	C	B	C
2.25 m	113.5	45.7	46.25	13.7
5 m	153.8	-	87.88	-
10 m	145.2	-	113.4	-

Table 6.20: Equilibrium values of L_u and L_v at 2.25 m, 5 m, and 10 m for transitions to open land (B) and roughly open (C).

6.3 Multiple Terrain Transition Analysis

Previous analysis has solely focused on single terrain changes and how they affect turbulence characteristics. As the Earth's surface conditions often exhibit multiple changes from one terrain to another, it is important to explore the effect of multiple terrain changes on measured wind records. For the majority of the 10° wind cones 129 analysed towers in this thesis, the flow transitioned at least four times over relatively short distances. This leads to many existing combinations of upwind terrain with little data available for common combinations. As an initial investigation into how multiple terrain changes influence turbulence, it is investigated how the ESDU procedure performs, which may allow to infer information on the modification of the flow.

Similar to the investigation of single terrain transitions, multiple upstream terrain properties can be classified as either smooth or rough with respect to the underlying terrain at the measurement site. In addition, as observations are scarce for specific combinations of multiple upwind terrain changes, a classification into smooth or rough upstream terrain groups data together. With respect to available transitions, smooth-to-rough transitions contain changes from A to B to C while rough-to-smooth transitions occur when surface properties change from D to C to B. Figure 6.37 shows a comparison between measured I_u medians, 25th and 75th percentiles against modelled along-wind turbulence intensities using the ESDU multiple terrain change model. This is shown for 2.25 m, 5 m, and 10 m elevations. Figure 6.38 shows the same but for smooth-to-rough transitions. In both figures, no restrictions on upwind fetches x_1 and x_2 are imposed.

For both smooth-to-rough and rough-to-smooth transitions, the ESDU model overpredicts along-wind turbulence intensities below 0.25 irrespective of the wind speed and measurement height. Moreover, the ESDU model tends to underestimate $I_u > 0.25$ for $\bar{U} < 15$ m/s. Consequently, the underlying terrain at the site does not seem to have an impact on modelled ESDU I_u values.
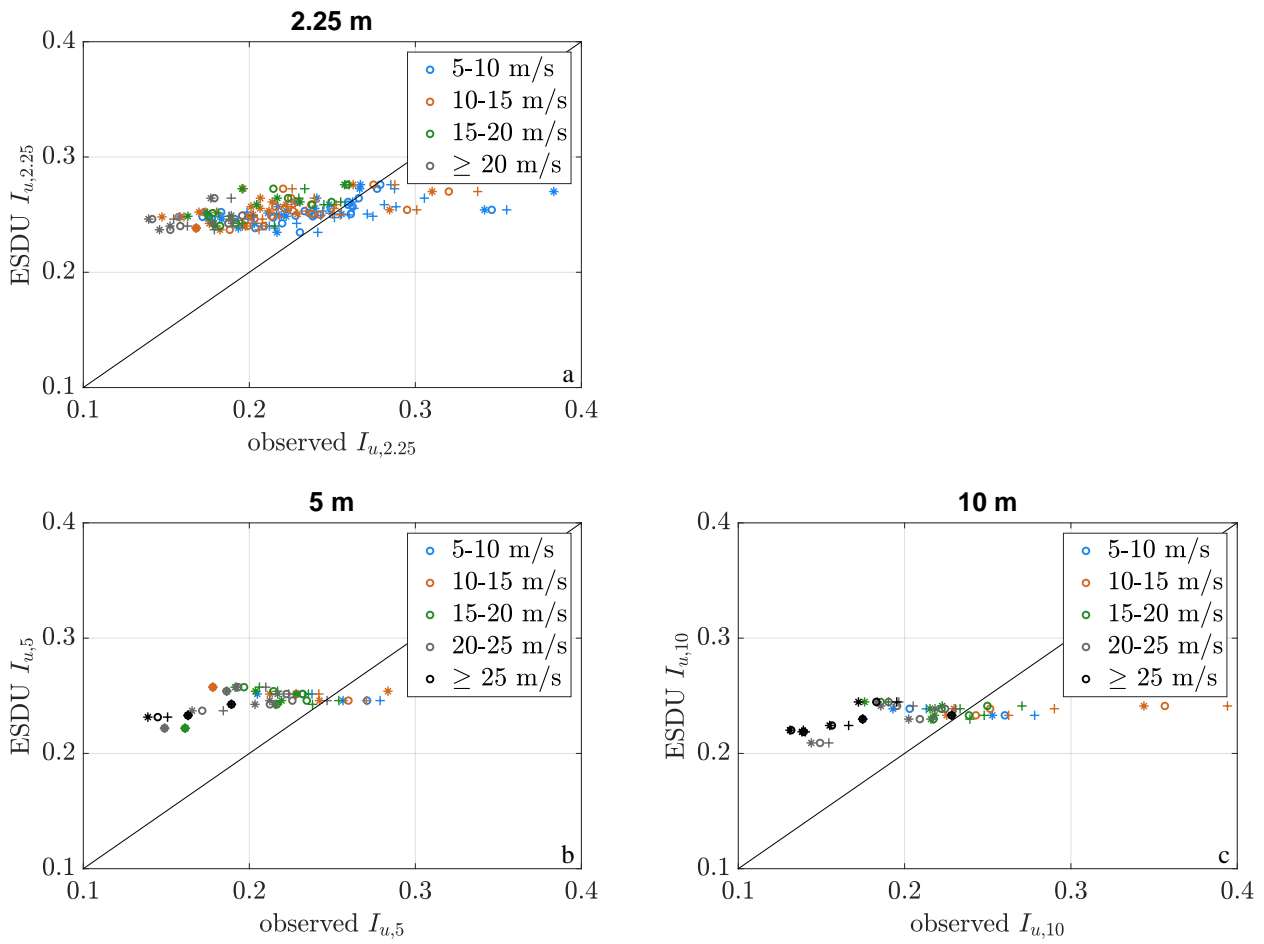
Figure 6.37: Rough-to-smooth transition: Observed I_u medians (circles), 25th and 75th percentiles (plus and stars) against and ESDU model I_u values for 5-10 m/s, 10-15 m/s, 15-20 m/s, and over 20 m/s wind speed bins at a) 2.25 m, b) 5 m, and c) 10 m height.
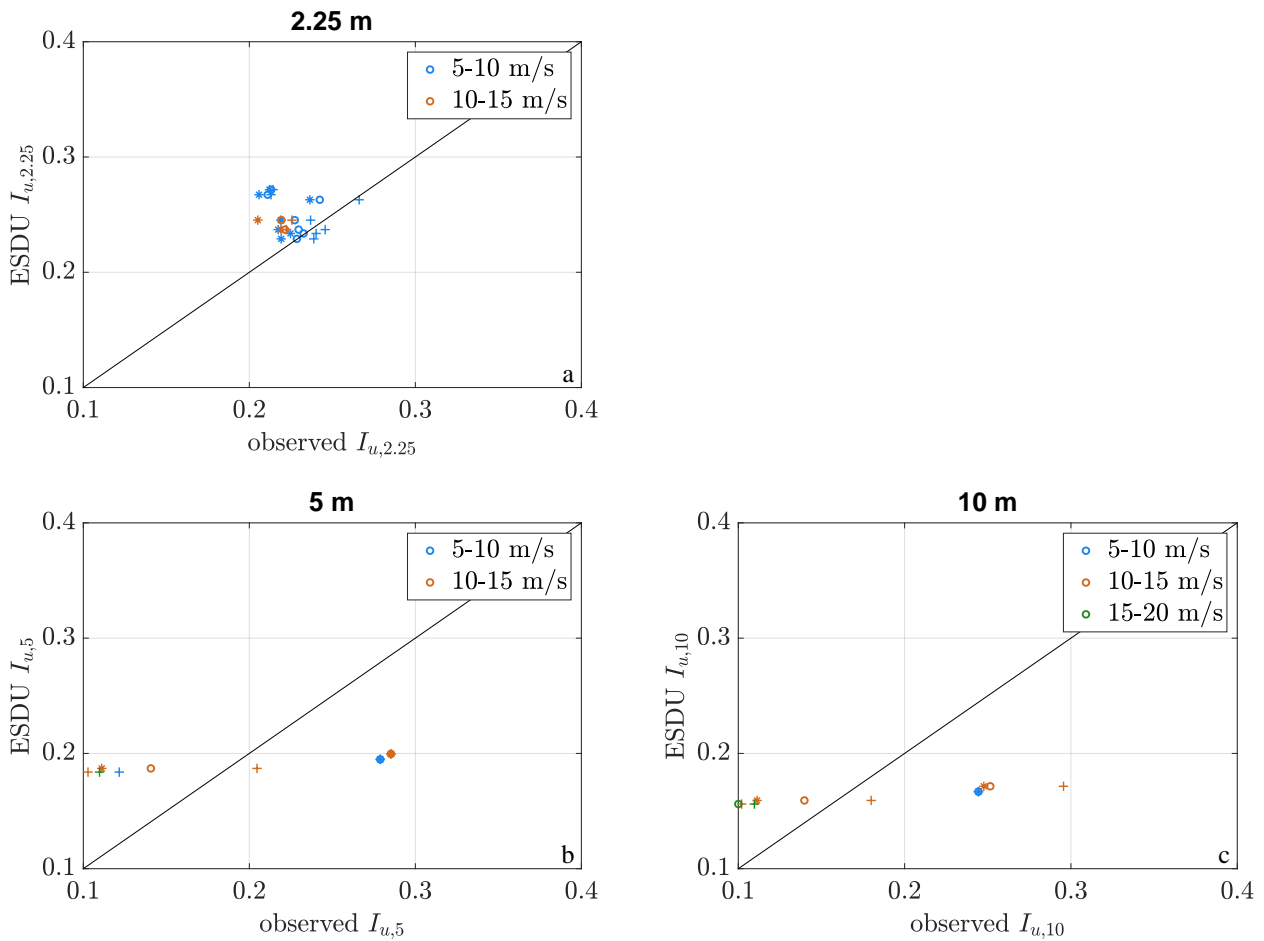
Figure 6.38: Smooth-to-rough transition: Observed I_u medians (circles), 25th and 75th percentiles (plus and stars) against and ESDU model I_u values for 5-10 m/s, 10-15 m/s, 15-20 m/s, and over 20 m/s wind speed bins at a) 2.25 m, b) 5 m, and c) 10 m height.

This is an initial exploration of the data. Future research could explore these data further and dedicated deployments are required that are designed to investigate these transitions.

Chapter 7

Mean Variation with Terrain in Idealised Landfalling Tropical Cyclones

This chapter sets out to investigate how the TCBL responds to different land surface conditions throughout landfall using idealised TC simulations. Idealised TC simulations were run using the HWCM (see Chapter 5.2), which was used to spin up an idealised TC and insert it into a real-world environment. More specifically, a severe TC was generated on a triply nested domain at horizontal grid resolutions of 18 km, 6 km, and 2 km, respectively. The spun up TC was then inserted into a real world environment using nested domains of 10800 x 10800 km, 4800 x 3000 km, and 1200 x 1200 km with 50 vertical levels. Here, the innermost nest is a storm-following domain of 2 km horizontal resolution and 10-min temporal resolution. Initial and boundary conditions were chosen to be favorable for TC development and intensification with high moisture and a constant easterly wind regime throughout the entire TC depth (Chapter 5). In total, the set of four simulations listed in Table 5.3 were carried out, in which the land surface terrain was changed from smooth to rougher terrain using the roughness regimes B-E established in Chapter 4.2. All simulations ran for five days (120 hours) in total to allow a sufficient amount of time for the inserted TC to stabilise before landfall.

7.1   Bulk Storm Characteristics of Simulated Tropical Cyclones

The change of bulk characteristics such as TC track, intensity, radius of maximum winds (RMW), storm size, and TCBL height are explored with regards to their response to different land surface conditions during landfall. The WRF model generates the first two characteristics, i.e. track and intensity, automatically as the center of the storm-following nest (innermost nest) moves in accordance with the translation of the TC center. In 15-min time intervals, the WRF model tracks the position of the TC center, the lowest central pressure at 850 hPa, and the maximum wind speed simulated throughout the entire vortex. Figure 7.1 shows simulated TC tracks for all four simulations in Table 5.3 with the centre of the storm being located approximately 1300 km off the coast at the start of the simulation.
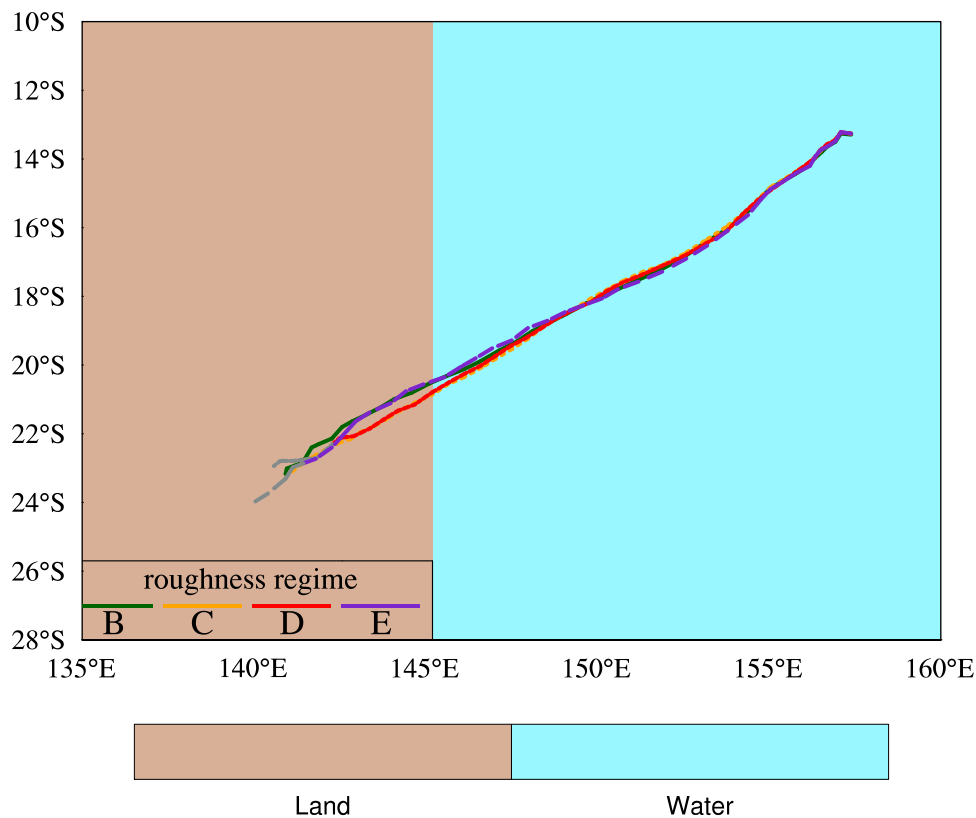
Figure 7.1: Idealised TC tracks transitioning from water (blue-shaded region) to land (brown-shaded region) for simulations B (green line), C (orange line), D (red line) and E (purple line).

All simulated TC tracks exhibit a southwesterly movement throughout the entire TC life cycle, despite an easterly wind regime of 10 kts (5.14 m/s) being imposed on all vertical levels in the initial and boundary conditions. This southwesterly translation occurs because of relatively calm environmental winds and Coriolis parameter variation with latitude such that the β-drift becomes the prevailing driver of TC motion [*Chan*, 2010]. TC landfall occurs between 83 hours in the baserun (simulation B) and 86 hours in the simulation where dense suburban terrain (D) is present. The landfall time was defined as the time of intersect of the TC center with the coastline. Approximately three hours prior to landfall TC tracks start to slightly deviate. Landfall deviations of up to 57 km exist between simulations B and D, and C and E. Surprisingly, TC tracks for the smoothest and the roughest surface were found to make landfall at a similar position. This outcome suggests that the different land surface roughnesses have little impact on TC track prior to landfall, a fact that has also been observed by previous research [e.g. *Ramsay and Leslie*, 2008]. Pronounced TC track deviations prior to landfall are more often associated with the presence of topography instead [*Wu et al.*, 2015]. While TC tracks are unaffected by the tested roughness regimes, considerable differences were observed for the lowest central pressure and the maximum wind speed, as shown in Figure 7.2.
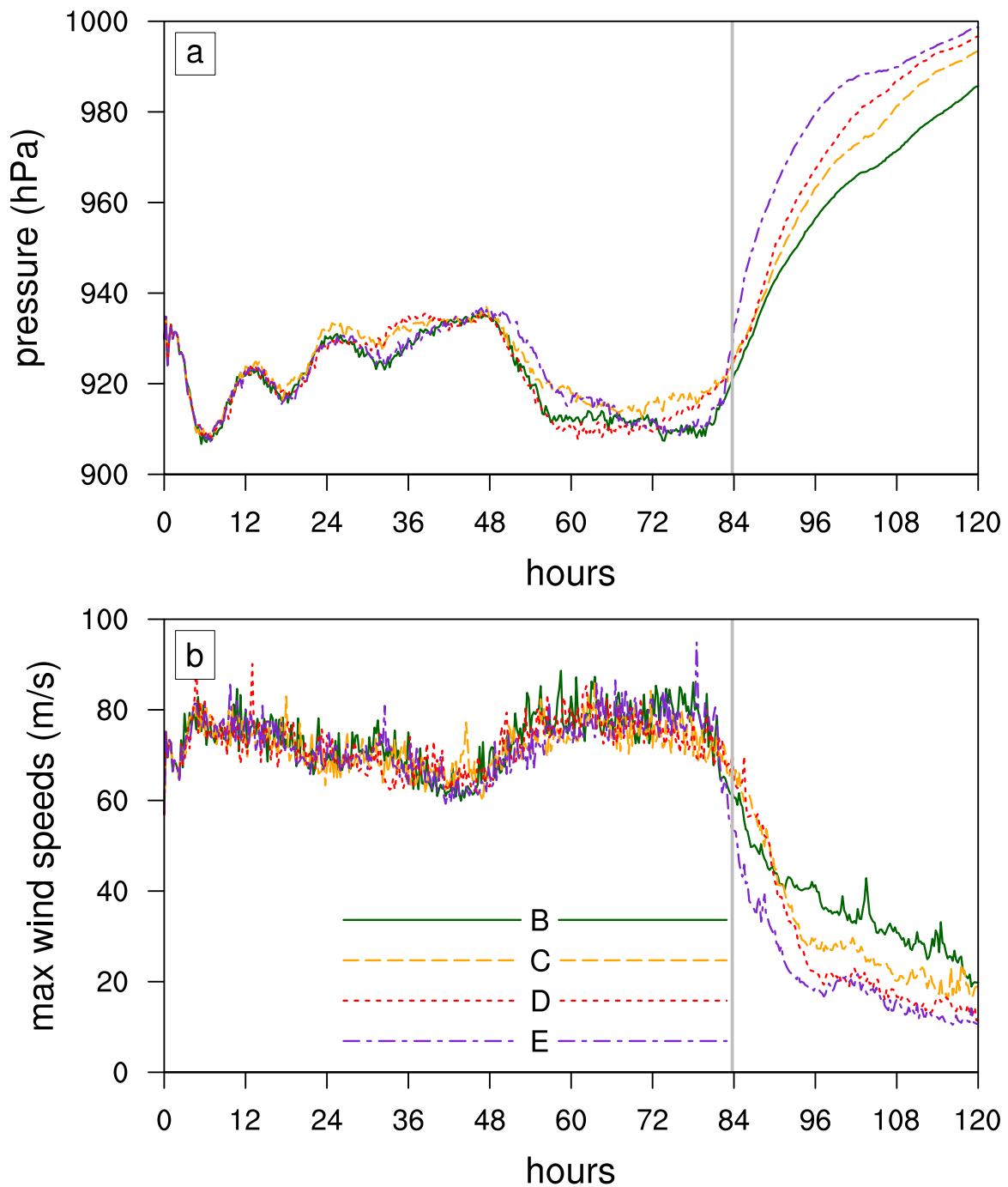
Figure 7.2: a) Lowest central pressure and b) maximum wind speed in idealised TC simulations B (green), C (orange), D (red) and E (purple). TC landfall at 83 hours in the base run (simulation B) is marked with a grey solid line.

It is observed that the rougher the land surface, the greater the reduction of the maximum wind speed and the faster the rise in central pressure after landfall. Changes in the maximum wind speed and central are primarily driven by the increase in surface roughness, which leads to increased frictional dissipation over land. Therefore, the rougher the surface, the stronger the extraction of energy from the TC. Within six hours after landfall, maximum wind speeds over the roughest surface (simulation E, high intensity/forested) drop by approximately 45%. By 12 hours this is 70%. Over the smoothest surface (simulation B, open land), maximum wind speeds decrease by approximately 29% after six hours, and 36% after 12 hours. In the same time frame the minimum central pressure in-

creases by 36.2 hPa (six hours) and 54.2 hPa (12 hours) over high intensity/forested terrain, and 21.6 hPa (siz hours) and 36.4 hPa (12 hours) over open land terrain. In fact, TC intensity appears to start to decrease about two hours prior to landfall as the outer wind field begins to interact with land. How this transition process affects bulk storm characteristics such as the RMW, TC size, and the TCBL height is investigated in subsequent paragraphs.

As the minimum central pressure and maximum wind speed only represent local extrema within the simulated TC, the storm wind field is subsequently broken up into six 60°-wide segments for further investigation of any asymmetries that develop throughout landfall. A storm-relative clockwise coordinate system was developed such that the 0-60° and 300-360° cones refer to the front right and front left side in the direction θ of TC translation, respectively. In each of these cones, instantaneous values of 10-min wind speeds between 300-800 m height are taken into consideration to derive RMW and TC size, whereas the TCBL height is a direct output by the WRF model. The RMW is determined by calculating the distance from the storm centre to the highest average wind maximum within the 300-800 m depth. This follows *Franklin et al.* [2003], who observed TCBL wind maxima at those heights (see Chapter 2.1.1). The TC size is determined as the maximum distance from the center, where a wind speed threshold of at least 17 m/s (general definition of a TC) is satisfied over 300-800 m heights. The estimation of the TCBL height depends on the PBL parameterisation chosen for the simulations. In the selected YSU PBL scheme, the PBL height h represents the level, where minimum flux exists at the inversion level and is determined by

$$h = Ri_{cr} \frac{T_{va}|U(h)|^2}{g\left[T_v(h) - T_s\right]} \tag{7.1}$$

where Ri_{cr} is the critical bulk Richardson number (see also Chapter 2.1.1), $U(h)$ the horizontal wind speed, T_{va} the virtual temperature at the lowest model level, $T_v(h)$ the virtual potential temperature at h, and T_s the temperature near the surface [*Hong et al.*, 2006]. In this analysis, a maximum TCBL height is identified in each 60° cone.

Figures 7.3-7.5 show three-hourly block averages of RMW, storm size, and TCBL height for storm-relative wind cones and all simulations from about 24 hours prior to landfall to 12 hours after landfall. This timeframe was chosen because lowest central pressure and maximum wind speeds in Figure 7.2 suggest that the TC stabilises after 60 hours into the simulation. As the TC structure starts to collapse during landfall, large variations of bulk storm characteristics occur over the first 12 hours after crossing the coastline. Calculated three-hourly mean RMW range between 30 and 40 km prior to landfall in all simulations and TC cones. Similar RMW values were evident in idealised and real WRF simulations conducted by *Nolan et al.* [2014] and *Klotz and Nolan* [2019], who produced hurricane surface wind fields to adequately describe the peak wind speed underestimate during the TC life cycle. After TC landfall, the RMW increases rapidly to 117 km in the front left (300-360°) and two front right sectors (0-120°) of the TC when transitioning over high intensity/forested terrain. The same appears to happen over dense suburban and roughly open terrain with RMW reaching 90 km and 80 km, respectively. Over open land (smoothest surface), the RMW barely expands over 60 km

and appears to exhibit minor differences throughout all TC sectors. These results suggest that the rougher the terrain, the more the RMW expands, which is found to be true for five out of six TC wind cones. While the RMW from 60-360° starts to increase prior to or at land interaction, the RMW in the 0-60° cone does not increase until two to three hours later. As all simulated TCs make landfall at $\theta \approx 235°$, the 0-60° cone is the first part of the storm to interact with land. As such, the delay in RMW increase is counterintuitive. The reason might be related to the 60° cone segregation, in which all RMW are averaged over 300-800 m maximum wind speeds.
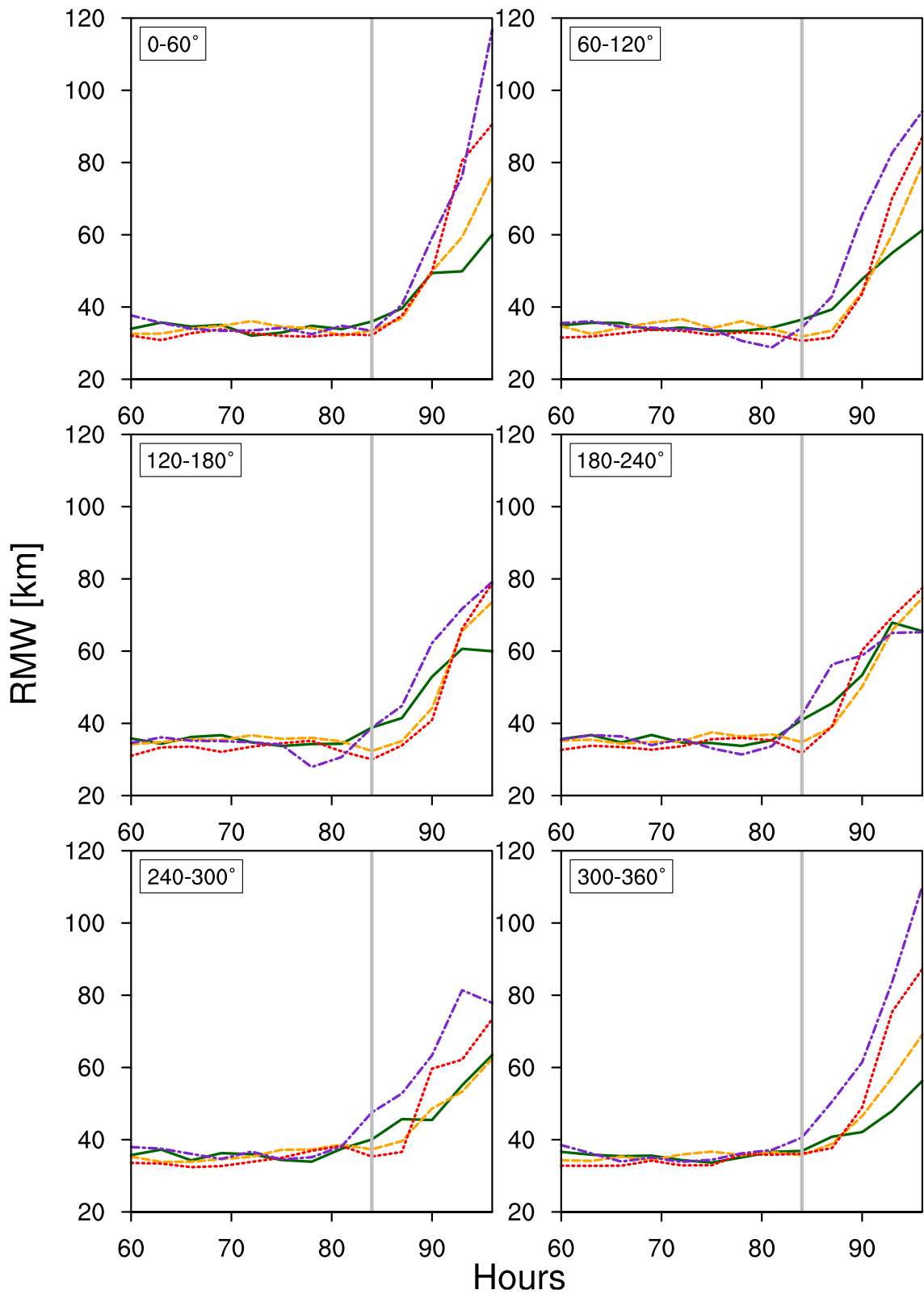
Figure 7.3: Three-hourly RMW for six TC segments with different colors representing the four simulations as in Fig. 7.2. The grey solid line indicates the time the TC center crosses the coastline.
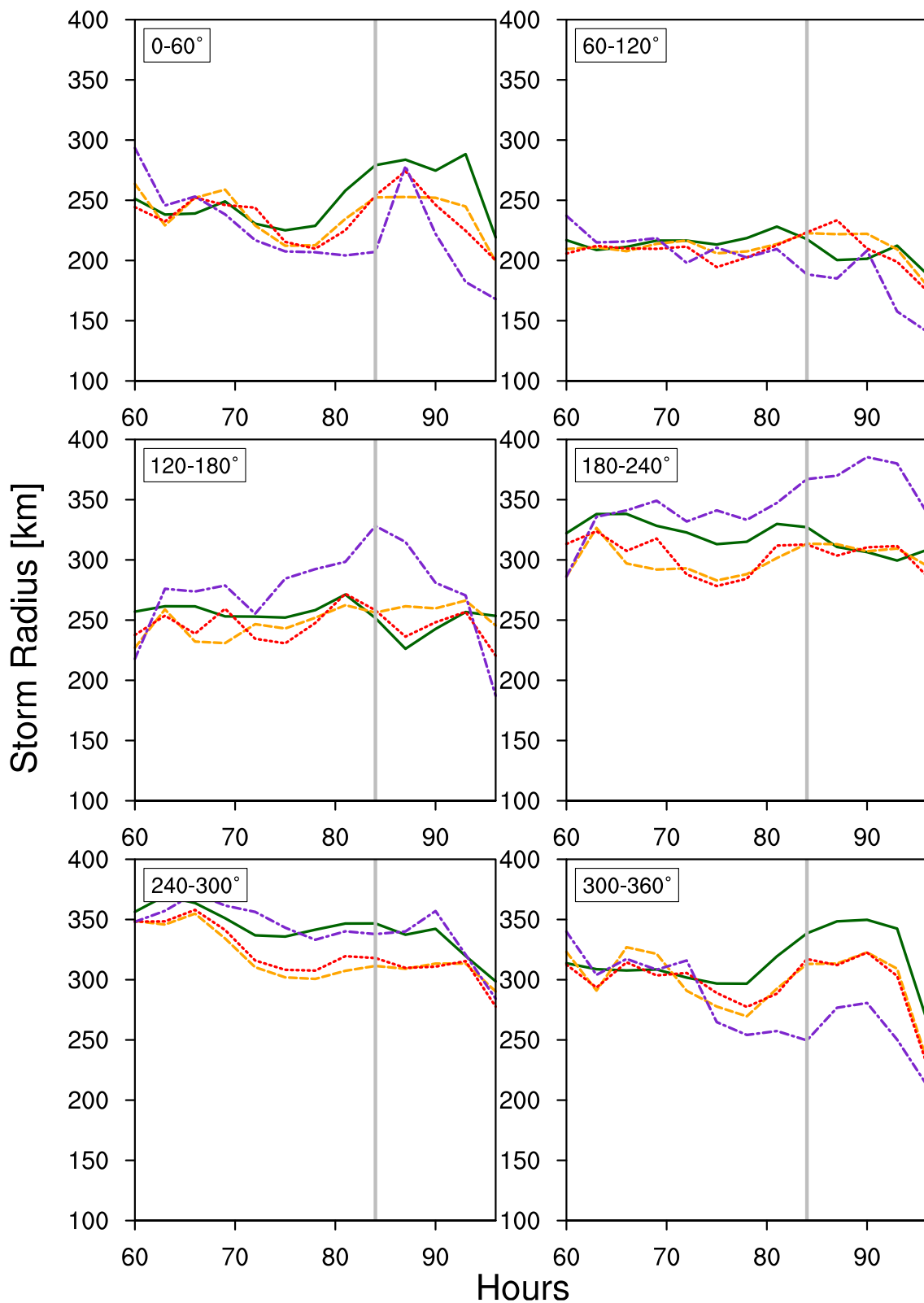
Figure 7.4: Three-hourly TC size for six TC segments with different colors representing the four simulations as in Fig. 7.2. The grey solid line indicates the time the TC center crosses the coastline.

153
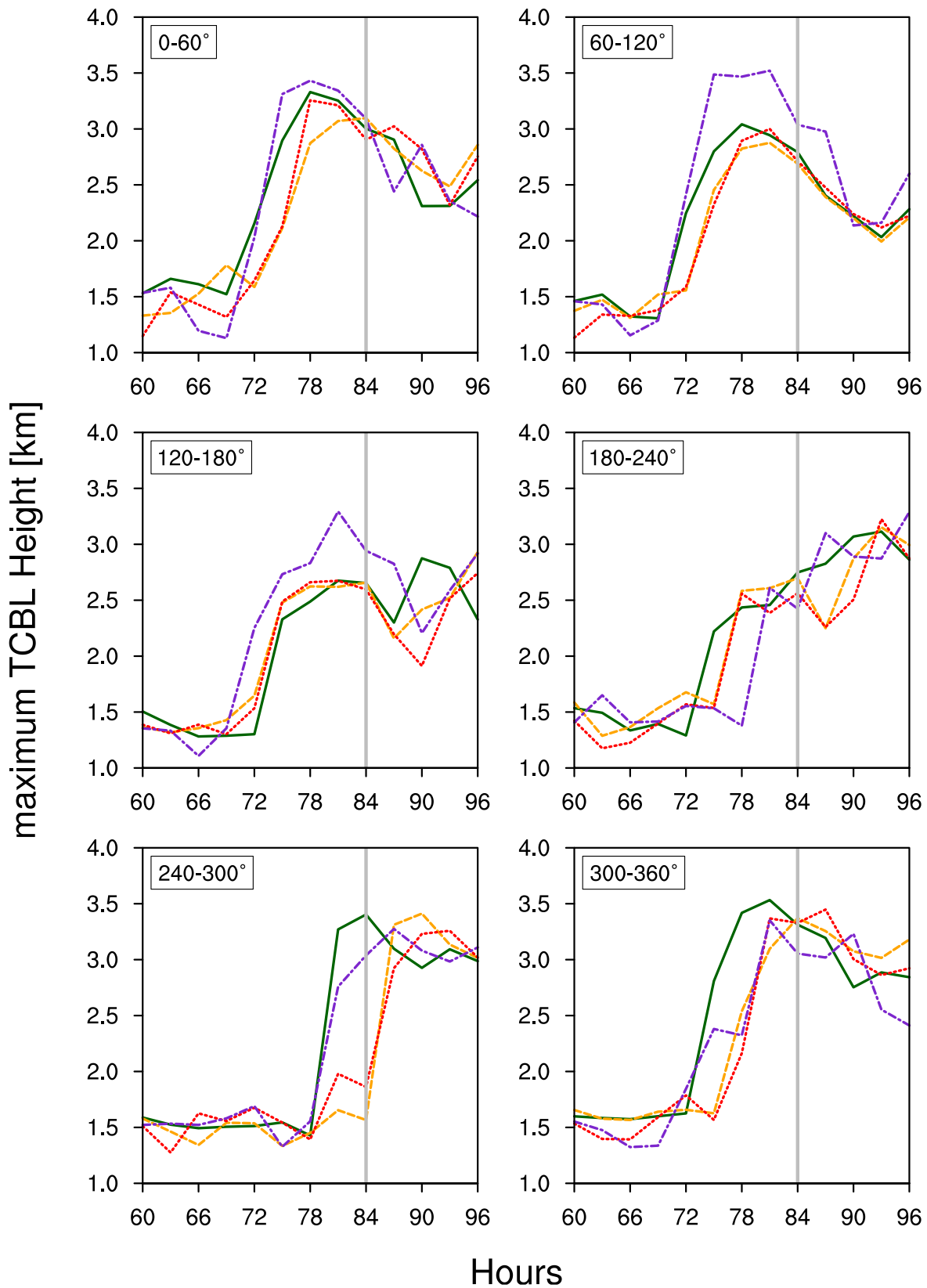
Figure 7.5: Three-hourly TCBL height for six TC segments with different colors representing the four simulations as in Fig. 7.2. The grey solid line indicates the time the TC center crosses the coastline.

The storm size shown in Figure 7.4 exhibits asymmetries with respect to the different wind segments. The TC radius for segments ranging from 0-180° stays well below 300 km, while radii in the remaining segments largely exceed 300 km up until interaction with land occurs. After the TC center crosses

154

the coastline the storm size decreases by up to 20%, whereas the reduction of storm radius is more pronounced in the leading side segments of 300-360°, 0-60°, and 60-120°. However, there is great variability in the storm radius particularly throughout landfall, where wind speeds rapidly decrease due to the increased surface roughness. When the TC transitions from water onto the roughest surface, the TC size tends to be lower than over smoother terrain with only minor differences over roughly open and dense suburban terrain.

Estimated maximum TCBL heights in Figure 7.5 display heights in a range of about 1.2 km to 1.5 km over water in all simulations. Of note is the response of the TCBL height in the vicinity of landfall. When the outermost regions begin to transition over increased surface roughness at around 72 hours, the maximum TCBL height rapidly increases by 70-170% within three hours. The rate of TCBL increase aligns well with the findings by *Powell et al.* [2005] and *Vickery et al.* [2009], who independently found a 60-100% TCBL height increase over land. Maximum TCBL heights appear to be the highest in the leading storm segments and adjacent cones, where TCBL heights reach up to 3.5 km. However, the magnitude of the surface roughness appears to have little influence on the TCBL height across all segments on the south side of the storm, except for high intensity/forested terrain, which tends to lead to the largest TCBL height growth on the north side of the storm. Further analysis of the horizontal wind field and vertical wind profiles in subsequent sections will help explain these findings.

7.2   Surface Winds of Simulated Tropical Cyclones

As previous results show, increased surface roughness during landfall alters TC structure and bulk storm characteristics significantly. When TC structure and bulk storm characteristics change, the TC surface wind field is expected to change also. To investigate how the TC surface wind field changes throughout landfall particularly near the surface, 6 km resolution (second nest) wind speed swaths at 10 m model height were calculated by determining the maximum wind speed at each grid point throughout the entire simulation time. This procedure was applied to all simulations conducted with wind speeds $\geq$ 17 m/s shown in Figure 7.6.
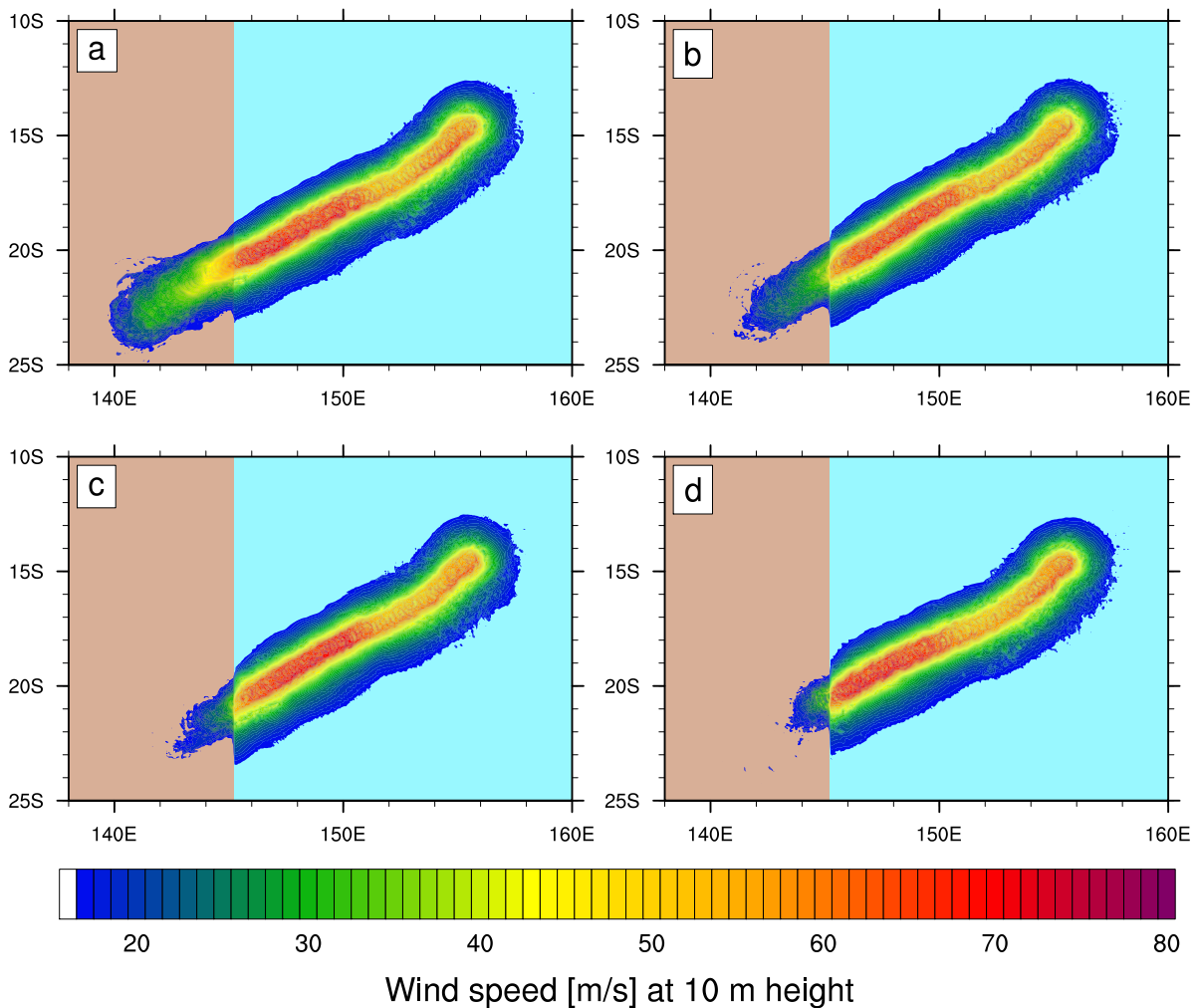
Figure 7.6: Maximum 10 m wind speed swaths transitioning over a) open land, b) roughly open, c) dense suburban, d) high intensity/forested.

Wind speeds of over 70 m/s occur in the center of each swath prior to landfall in all simulations. Post landfall, surface wind speeds over open land decelerate at a slower rate reaching locations over 400 km further inland than over high intensity/forested terrain. While TC wind speeds (> 17 m/s) are still present up to 550 km inland over the smoothest terrain, near-surface wind speeds over the roughest terrain do not exhibit TC strength beyond 125 km inland. Hence, the rougher the terrain, the stronger the deceleration of sustained TC winds following landfall, because of the dampening effect of increased rougher terrain over land (i.e. bushes, houses, trees). Another factor that contributes to the weakening on the TC over land is the lack of moisture and heat supply, which is provided by the ocean. Furthermore, the lack of moisture and heat hinders the production of thunderstorms close to the TC center.

To investigate if rougher terrain leads to a stronger reduction of sustained TC winds holds true for different TC segments from a storm-relative perspective, 10-min surface wind field data from the storm-following nest are analysed with regards to their 10 m wind speed maximum in 2° increments around the storm for all radii up to 500 km. The three-hourly mean TC direction (θ) of translation was calculated throughout the TC life cycle, which allowed the storm relative position of each grid cell

156

within the moving nest to be determined. In general, θ was approximately 235°. Figure 7.7 shows a Hovmöller diagram for maximum wind speeds around the TC and at 10 m height dependent on the surface roughness and simulation time for each of the four simulations. Positive and negative angles represent clockwise and anti-clockwise directions, respectively.
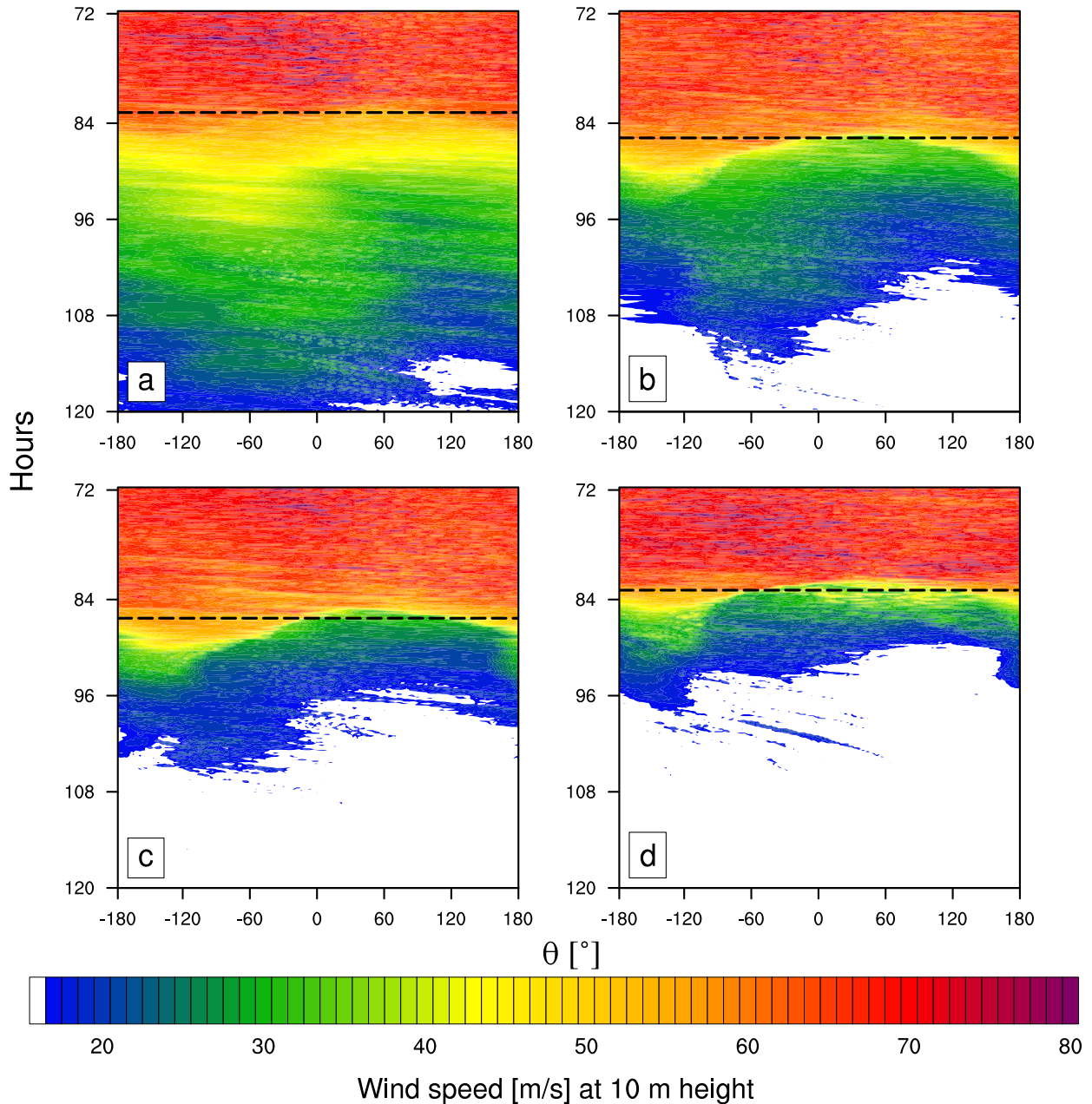
Figure 7.7: Hovmoeller diagram of maximum 10 m wind speeds around the TC when transitioning over a) open land (landfall at 82.67 hours), b) roughly open (landfall at 85.83 hours), c) dense suburban (landfall at 86.33 hours), d) high intensity/forested (landfall at 82.83 hours). Different landfall times are marked with a dashed black line.

Up until landfall surface wind speeds exceed 70 m/s in all simulations and in all directions. Over open land ($z_0 = 0.01$ m) TC-strength wind speeds are evident almost until the end of the simulations for all TC segments. In TC cones between 60-120° surface wind speeds decelerate most rapidly in all simulations with the roughest surface being responsible for the fastest wind reduction. Furthermore, a pro-

longed zone of surface wind speeds between 40-50 m/s exists over open land, which is barely present over rougher terrain ($z_0 > 0.5$ m). In all four simulations, TC asymmetries are evident throughout the landfall process, which persist until decay. More specifically, wind speeds greater than 55 m/s are predominantly visible on the rear side of the vortex ($-180° \leq \theta \leq -120°$, $180° \leq \theta \leq 120°$) up to five hours after landfall (black dashed line in Figure 7.7). While this region of higher wind speeds also extends into the $-120° \leq \theta \leq -60°$ sector over all land surface conditions, it decays within four hours over roughly open (Figure 7.7b), three hours over dense suburban (Figure 7.7c), and one hour over high intensity/forested terrain (Figure 7.7d). These asymmetries are related to the RMW of the different TC sectors crossing land at different times. More specifically, storm-leading sectors exhibit signs of wind speed decay up to an hour prior to landfall, particularly over dense suburban and high intensity/forested terrain. Furthermore, TC asymmetries appear to propagate throughout the entire landfall process. After 120 hours of simulation, surface wind speeds exceed 17 m/s only over open land terrain for $-180° \leq \theta \leq 60°$ segments (Figure 7.7a). Over roughly open terrain, wind speeds decelerate below TC intensity 16 hours after landfall for $\theta \approx 120°$, while 17 m/s are still present at $\theta \approx -60°$ 10 hours later. Similar asymmetries are found over dense suburban and high intensity/forested terrain, where maximum wind speeds fall below TC intensity 10 hours and 8 hours after landfall for $60° \leq \theta \leq 120°$.

Surface wind speed asymmetries shown in Figure 7.7 originate as a response to the sudden change in surface characteristics over land, which induce stronger friction at the surface. Stronger friction at the surface leads to a reduction of the flow over land. Thus, post-landfall inflow is weakened to the right side of the TC associated with the onshore flow, as described by *Wong and Chan* [2007]. The authors further explain that both onshore and offshore flows influence surface wind asymmetries.

7.3 Vertical Structure of Simulated Tropical Cyclones

7.3.1 Vertical Tropical Cyclone Boundary Layer Structure over Water

With changes occurring in bulk storm characteristics as well as the surface wind field during TC landfall, the response of the vertical TC structure throughout the transition to land is investigated. To do this, mean vertical wind speed profiles are extracted for six 60° segments in a storm-relative coordinate system with 0° representing the direction θ of TC translation. In addition, vertical TCBL profiles are averaged for radii bins of 10-30 km, 30-50 km, 50-75 km, 75-100 km, 100-200 km, and > 200 km similar to previous research [*Vickery et al.*, 2009; *Snaiki and Wu*, 2018]. The radial binning is introduced to better understand how different radii in TC segments, such as the inner part of the TC core (10-30 km) and the RMW (30-50 km), are affected by the transition onto land. Vertical TCBL profiles were further examined in a composite framework by normalising these profiles by their individual mean boundary layer (MBL) wind speed following *Powell et al.* [2003] and *Snaiki and Wu* [2018]. The MBL is defined as the mean wind speed averaged over all model levels below 500 m.

To investigate how the TCBL responds throughout the transition process onto land, vertical wind profiles generated in the base run (simulation B, open land) over water are examined first. Figure 7.8 shows normalised 12-hourly TCBL profiles from simulation hour 60-72 before the outermost TC regions begin to cross land. During this 12-hour time frame, the mean direction of the TC is 238° with radii ranging from 210 km to 350 km in the 60-120° and 240-300° segment (Figure 7.4), respectively.
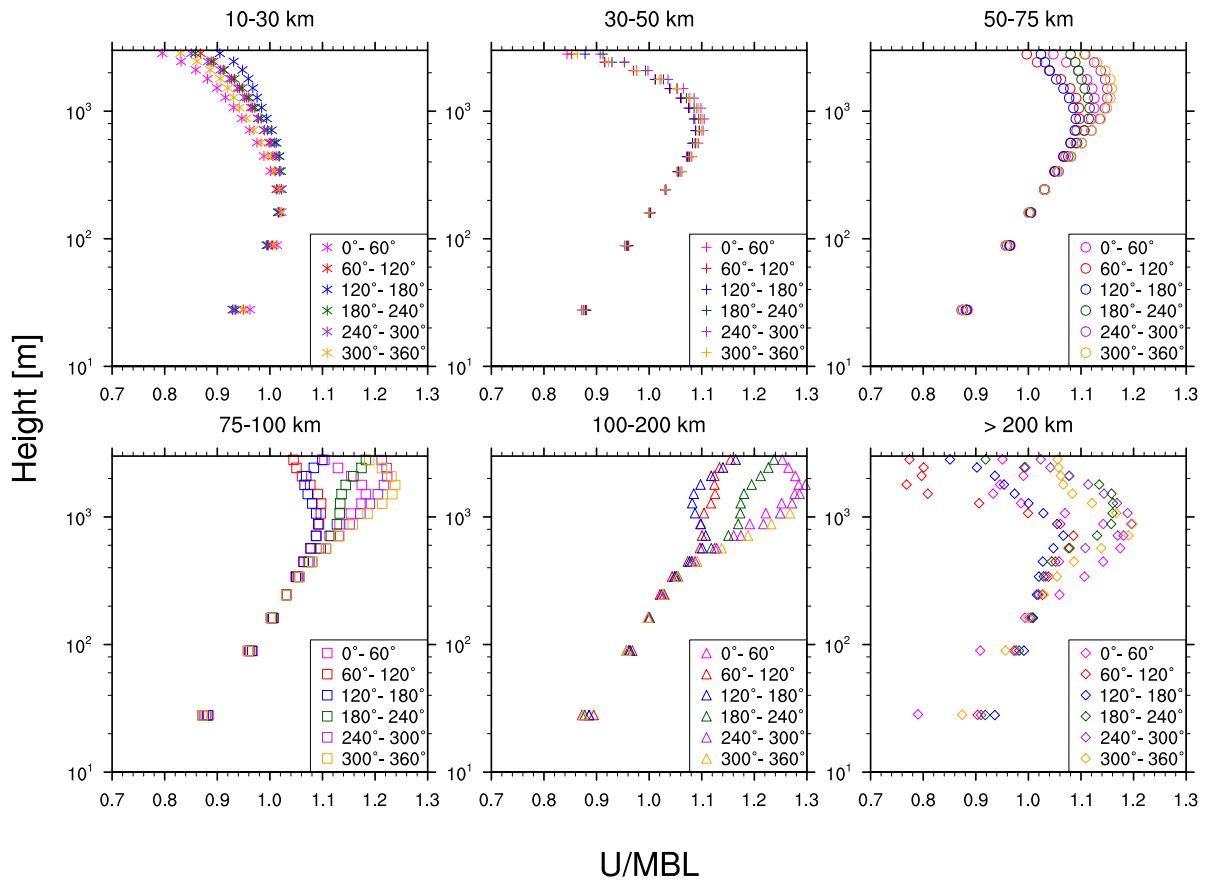
Figure 7.8: 12-hourly mean vertical TCBL profiles generated from the base run (simulation B, open land) for six radii groups and cones.

Time-averaged mean TCBL profiles over water indicate a logarithmic wind profile up to the height of maximum wind speed, which increases with TC radius and MBL. This was also found in previous research [*Powell et al.*, 2003; *Vickery et al.*, 2009; *Snaiki and Wu*, 2018] although these studies do not distinguish between different TC storm segments. Vertical profiles vary for different θ for all radii but the 30-50 km bin. In addition, vertical wind profiles in the RMW (30-50 km) suggest no difference between the different TC segments in the upper regions, while segments at the leading site of the storm tend to exhibit stronger U/MBL ratios than those located on the rear side of the vortex. Below 500-700 m there is almost complete uniformity in vertical profiles out to 200 km from the storm. To validate these simulated vertical TCBL profiles, a comparison with observed dropsonde profiles over water reported by *Snaiki and Wu* [2018] is conducted. Figure 7.9 shows the range of generated profiles from Figure 7.8 as a gray-shaded region along with composite dropwindsonde profiles at similar radii (some observed TCBL profiles appear twice as they fit in more than one radius bin).
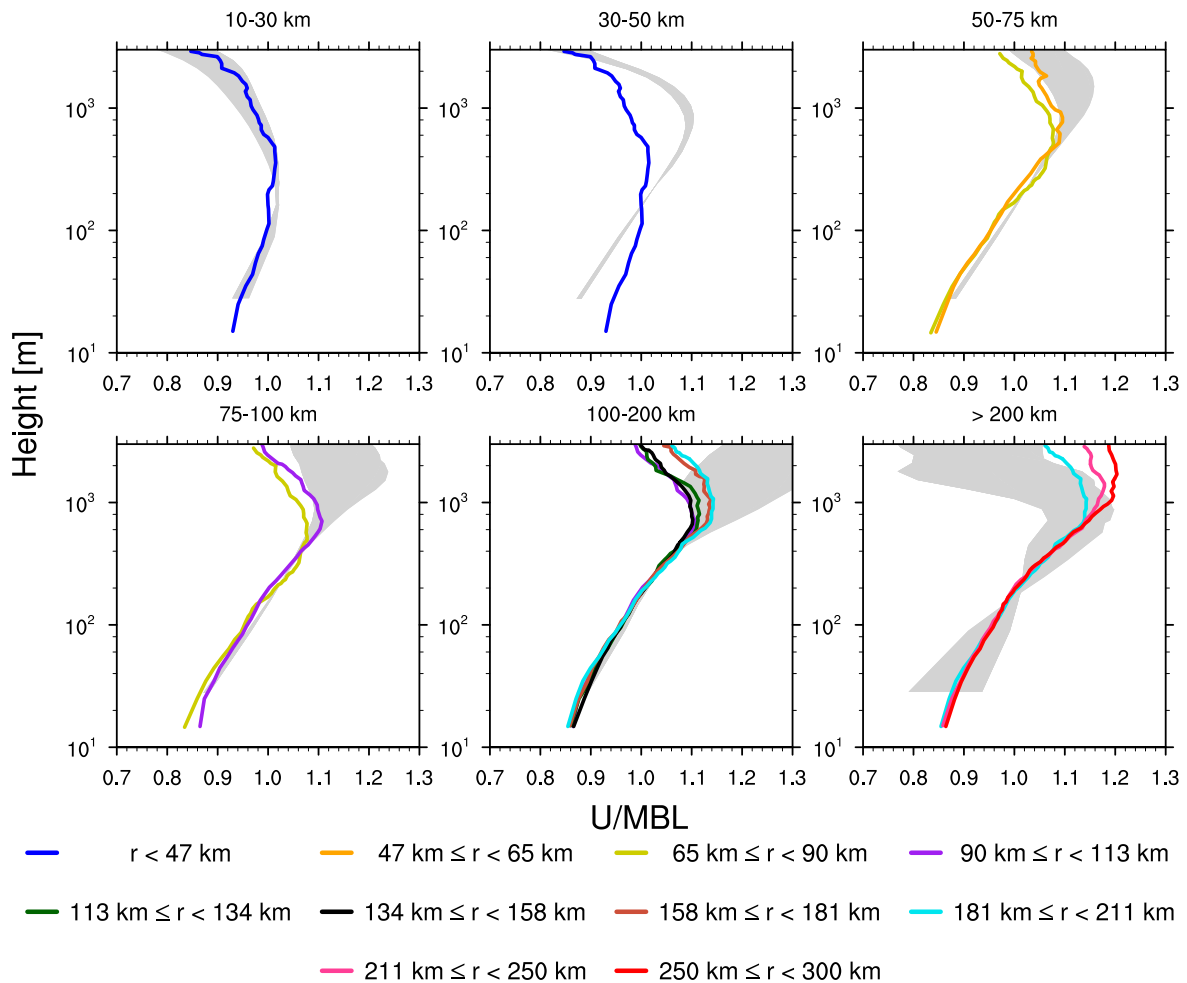
Figure 7.9: Comparison of observed composite dropwindsonde profiles over water (solid lines) [*Snaiki and Wu*, 2018] with ranges of 12-hourly mean vertical TCBL profiles generated from the base run (simulation B, open land) for six radii groups and cones (gray-shaded regions).

Observed TCBL profiles up to the height of the maximum wind speed are generally well-represented in the numerical simulation, with almost identical profiles being noted at 10-30 km and 50-75 km radii. Above the height of the observed maximum wind speed, observed wind profiles are lower than idealised vertical profiles except for radii greater than 200 km. Furthermore, a deviation of observed and modelled TCBL profiles for radii between 30 km and 50 km exists. These differences arise because the mean RMW of the dropsonde measurements may differ from the RMW in the idealised TC simulations. With vertical profiles rapidly changing over short distances from the RMW, the deviation between composite profiles and idealised profiles become large. It is also noted that *Snaiki and Wu* [2018] obtained composite profiles from over 2,000 collected dropsonde measurements for multiple hurricanes occurring between 1996 to 2012, whereas the gray-shaded swaths in Figure 7.9 originate from one simulated storm over a timeframe of 12 hours. Furthermore, the authors do not differentiate between TC segments as opposed to the 60° storm-relative segregation used in present analysis.

Based on these comparisons, simulations are generating physically realistic storms, with well repre-

sented lower level (i.e. below TCBL height).

7.3.2   Vertical Tropical Cyclone Boundary Layer Structure over Land

To better understand how different land surface conditions alter the vertical TCBL structure over land, wind speeds at 50 vertical model levels are extracted for six 60° storm segments over multiple radii bins introduced in Chapter 7.3.1. During this investigation, idealised TCBL profiles are compared with calculated VAD composites recorded by WSR-88D Doppler Radars during 34 hurricanes between 1995 and 2012 [*Krupar*, 2015; *Snaiki and Wu*, 2018]. The comparison between observed and modelled TCBL profiles is important because it attempts to ensure the validity of idealised TCBL profiles when over land. To do so, time-averaged vertical profiles were determined from 6-12 hours after TC landfall for all four simulations, whereas the surface roughness increases from $z_0 = 0.01$ m in the base run (open land) to $z_0 = 0.80$ m over high intensity/forested terrain (simulation E). The choice of 6-12 hours after landfall was to try and get information on how the vertical TCBL looks like once it has adjusted to the land surface conditions.

The comparison of modelled and observed TCBL profiles is shown for each open land ($z_0 = 0.01$ m), roughly open ($z_0 = 0.15$ m), dense suburban ($z_0 = 0.50$ m), and high intensity/forested ($z_0 = 0.80$ m) surface in Figures 7.10, 7.11, 7.12, and 7.13, respectively. Similarly to Figure 7.9, the gray swath represents idealised TCBL profiles for all storm segments.
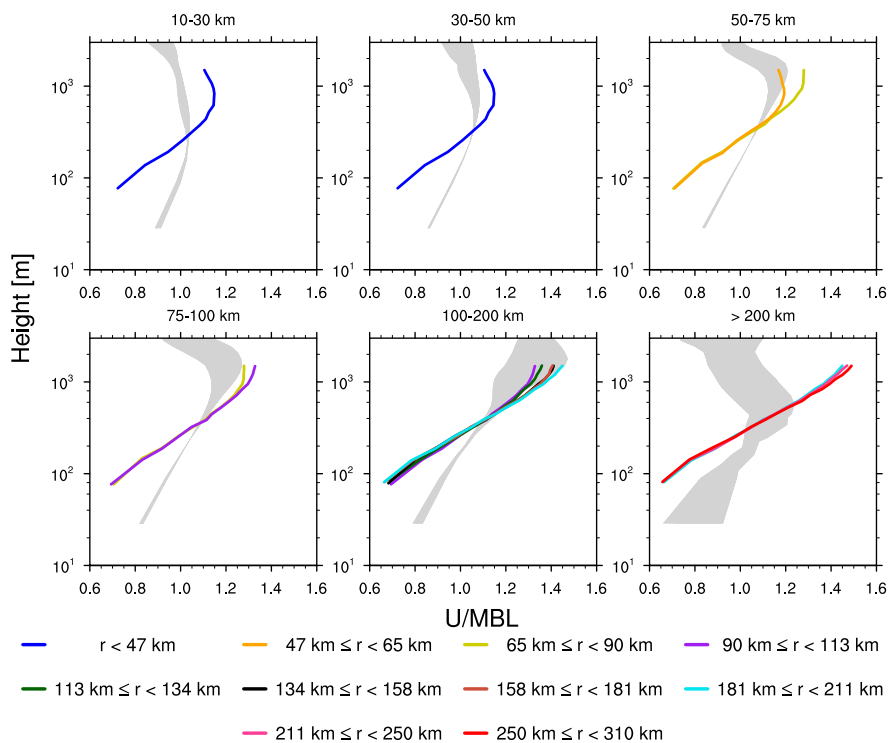
Figure 7.10: Comparison between VAD composite WSR-88D profiles (solid lines) and 6-hourly mean vertical TCBL profiles generated over open land ($z_0 = 0.01$ m) for six radii groups and cones (gray-shaded regions).
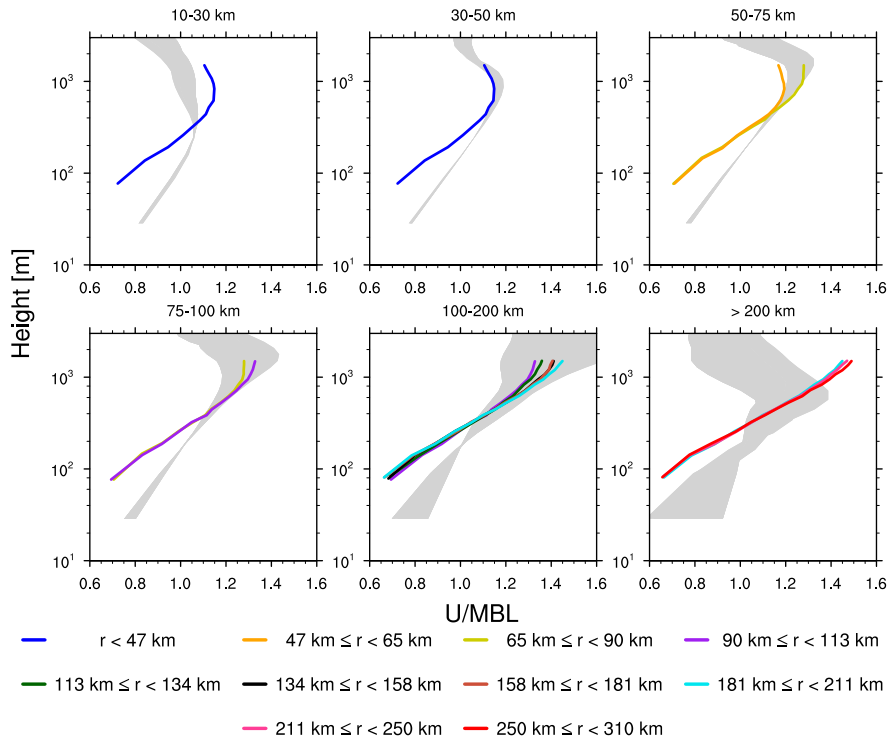
Figure 7.11: Comparison between VAD composite WSR-88D profiles (solid lines) and 6-hourly mean vertical TCBL profiles generated over roughly open ($z_0 = 0.15$ m) for six radii groups and cones (gray-shaded regions).
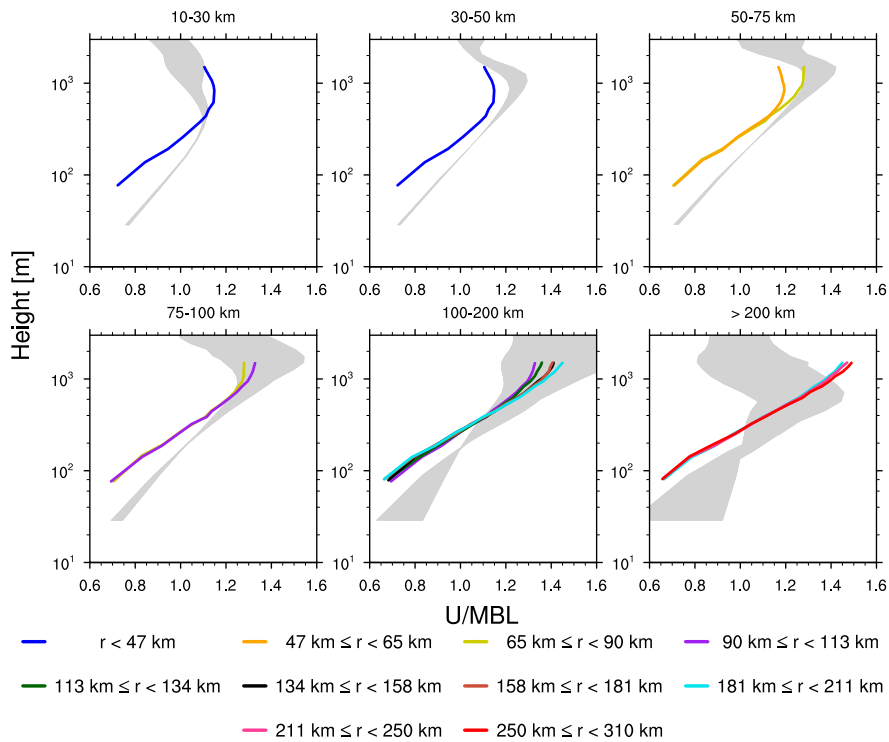
Figure 7.12: Comparison between VAD composite WSR-88D profiles (solid lines) and 6-hourly mean vertical TCBL profiles generated over dense suburban ($z_0 = 0.50$ m) for six radii groups and cones (gray-shaded regions).
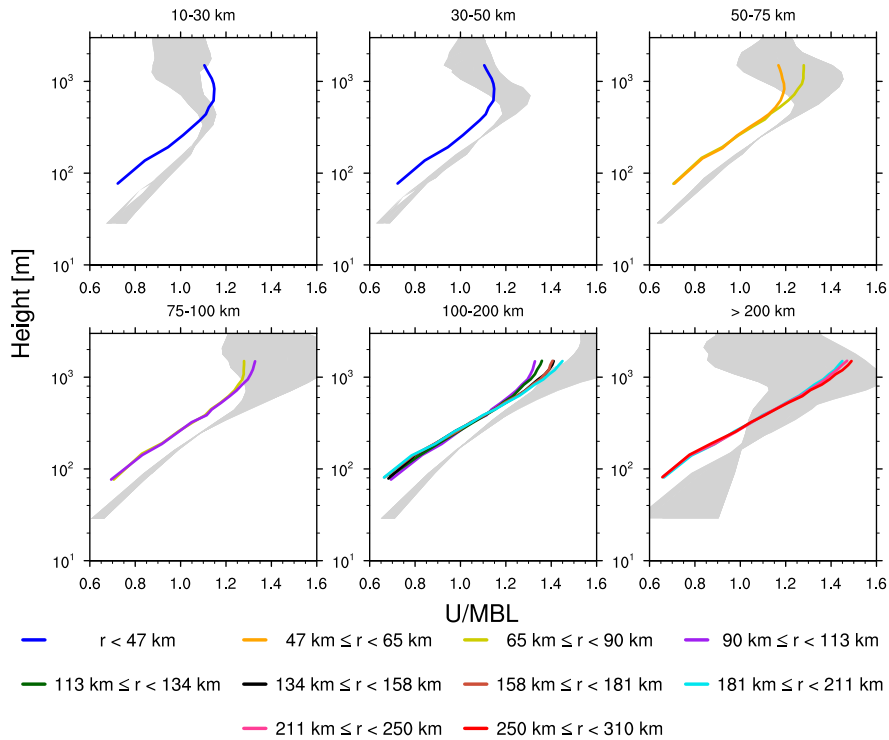
Figure 7.13: Comparison between VAD composite WSR-88D profiles (solid lines) and 6-hourly mean vertical TCBL profiles generated high intensity/forested ($z_0 = 0.80$ m) for six radii groups and cones (gray-shaded regions).

Modelled TCBL profiles over land exhibit a greater wind speed decay particularly closer to the surface with U/MBL ratios of ≥ 0.8 over open land and ≤ 0.7 over high intensity/forested. Observed composite profiles over land do not show a supergradient region for radii > 75 km and agree most with modelled profiles over the roughest surface. Numerical TCBL profiles exhibit a steeper increase in wind with height with increasing surface roughness as would be expected in a traditional ABL. However, the height of the TCBL indicates no dependence on the surface properties, as previously suggested in Figure 7.5. The great deviation of observed composite and modelled vertical profiles may occur because it remains unknown whether Doppler radar systems captured vertical wind profiles exclusively over land. Recorded vertical TCBL profiles over water could influence the composite analysis using the VAD technique. This occurs because the bulk of Doppler radar locations are close to the ocean (Fig. 3 in *Snaiki and Wu* [2018]) and since the VAD technique includes wind speed data from all around a storm these are by default included.

To provide more detail on the TCBL profiles in the gray-shaded regions in Figures 7.10-7.13, subsequent subsections contain investigations of 30-min mean wind speed profiles for available radii, storm segments and land surface conditions.

7.3.2.1 Vertical Wind Speed Profiles near the Inner Core Region

Vertical TCBL profiles near the inner core region (10-30 km) of the TC during landfall were extracted for radii between 10 km and 30 km. Figure 7.14 shows a panel plot of the transition of 30-min

averaged vertical profiles for each angle segment when moving from water to open land (green solid lines), roughly open (orange solid lines), dense suburban (red solid lines), and high intensity/forested (purple solid lines) exposure over the time period of six hours prior to and after landfall. The time of the TC center crossing the coastline is highlighted with a gray-dashed line. The trend to darker colors denotes the time progression, with the lightest color being six hours prior to landfall and the darkest six hours after landfall.
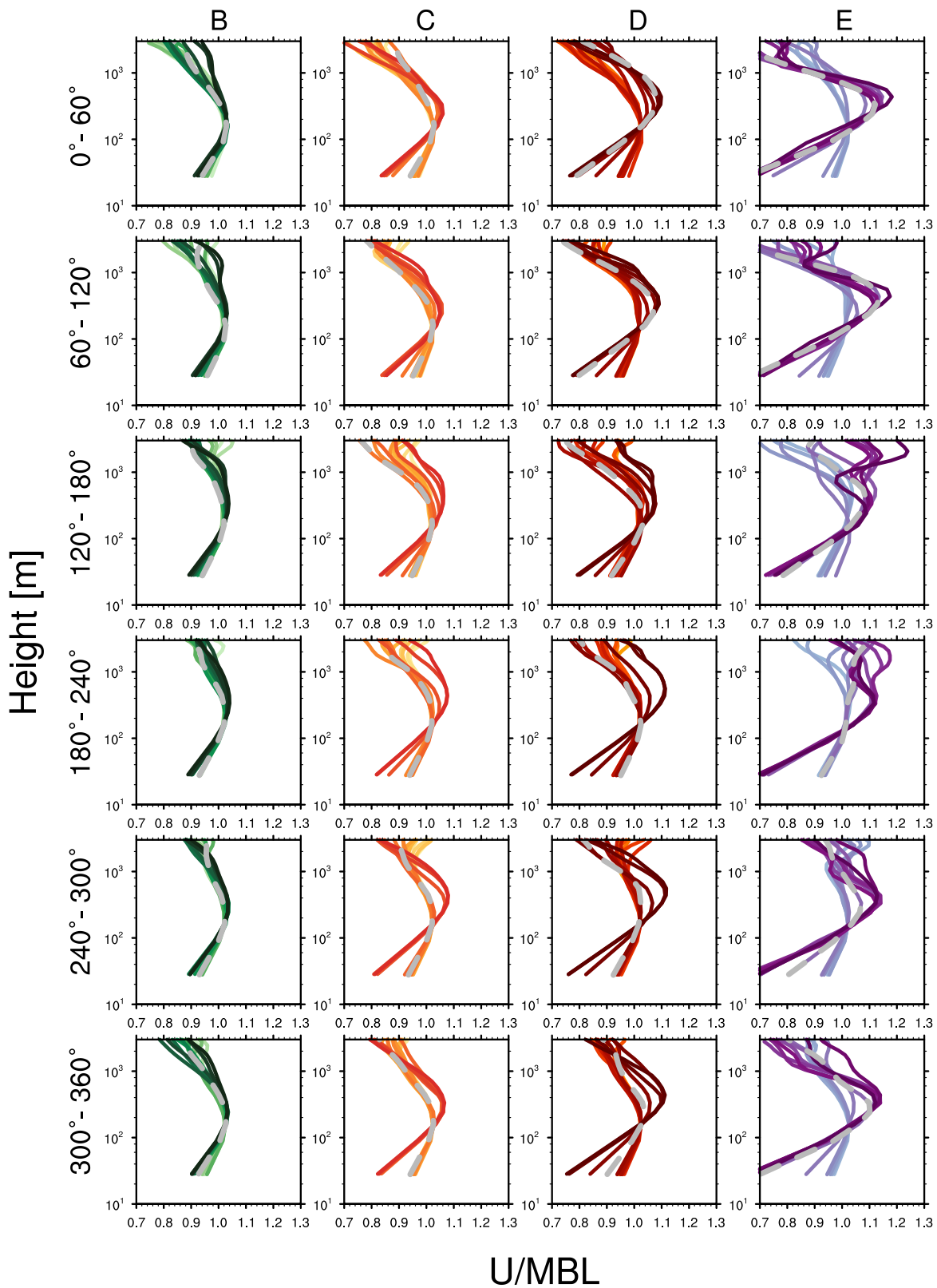
Figure 7.14: Transition of 30-min averaged vertical profiles from water (brighter colors) to open land (green solid lines), roughly open (orange solid lines), dense suburban (red solid lines), and high intensity/forested (purple solid lines) terrain for radii from 10-30 km. The gray-dashed line shows the vertical profile at the landfall time.

TCBL profiles transitioning from water to open land exhibit a similar vertical structure below 1 km before and after landfall, irrespective of the storm segment or time step. However, variations above

this height exist within storm-leading segments of 0-60° and 300-360°. The shape of U/MBL profiles in open land and roughly open remains effectively unchanged as prior to landfall at all segments at the time of landfall. That means that the segments over land have not adjusted to the new profile shape. When the land surface condition changes to roughly open, U/MBL ratios are lower than those over open land and a steeper logarithmic increase to the height of the maximum wind (about 400 m) is evident. This holds also true with respect to the increase in surface roughness. Vertical profiles over dense suburban and high intensity/forested exposures both show lower U/MBL ratios near the surface and a sharper increase to the height of maximum wind than those obtained over smoother terrain. In addition, increased surface roughness shows higher U/MBL ratios at around 500 m height. For vertical U/MBL profiles over dense suburban terrain, as the centre crosses the coast, 0-120° segments have already modified to underlying terrain conditions, but 120-300° segments remain unchanged as over the ocean. Over high intensity/forested terrain, as roughness increases, more segments have transitioned to new profile shape at landfall. This seems to suggest that the higher the roughness, the more the information of this roughness is transferred through the storm - even prior to landfall. In addition, U/MBL ratios greater than 1.1 occur, which aligns well with the processes of increased frictional dissipation over the surface during landfall. This produces a stronger inflow and theoretically a stabilisation of the boundary layer as described in [*Holland*, 1987]. The stronger inflow is evident for 0-120° and 240-360° segments, while remaining cones on the right and left rear of the vortex show slightly smaller maximum U/MBL ratios. The stabilisation of the boundary layer manifests itself through similar-shaped vertical wind profiles after landfall for all roughness regimes. However, the 180-240° TC segment shows greater variations above the height of the maximum wind, which would suggest that this segment transitions last onto land. In general, the variation of vertical wind speed profiles becomes larger, when vertical profiles transition from water to rougher terrain.

These findings align well with explanations by *Chan* [2010], who describes that wind reduction over land (i.e. through) leads to large-scale convergence and divergence asymmetries along the coastline, which affects the TCBL also. Moreover, this asymmetric convergence and divergence in the TCBL leads to the development of an asymmetric flow near the surface because of the creation and reduction of asymmetric vorticity [*Chan*, 2010]. These changes, in turn, influence convection and the diabatic contribution to the potential vorticity tendency *Chan* [2010]. Hence, changes in surface roughness and friction lead to discontinuities in the flow and therefore in the secondary circulation, which affects the vertical structure of the TCBL.

In an attempt to replicate the transition of TCBL profiles (in the inner core) from water onto different land surface conditions, the semi-empirical wind speed profile model by *Snaiki and Wu* [2018] is utilised to generate TCBL profiles for all radii bins and TC segments (see Eq. 2.14 in Chapter 2.1.2). Understanding the performance of this type of empirical/analytical model is important as it will allow risk modellers and forecasters to quickly and accurately assess wind fields in the near coast region. Figure 7.15 contains 30-min TCBL wind profile means (solid lines) and semi-empirical wind speed profiles (dashed lines) six hours prior to and after TC landfall.
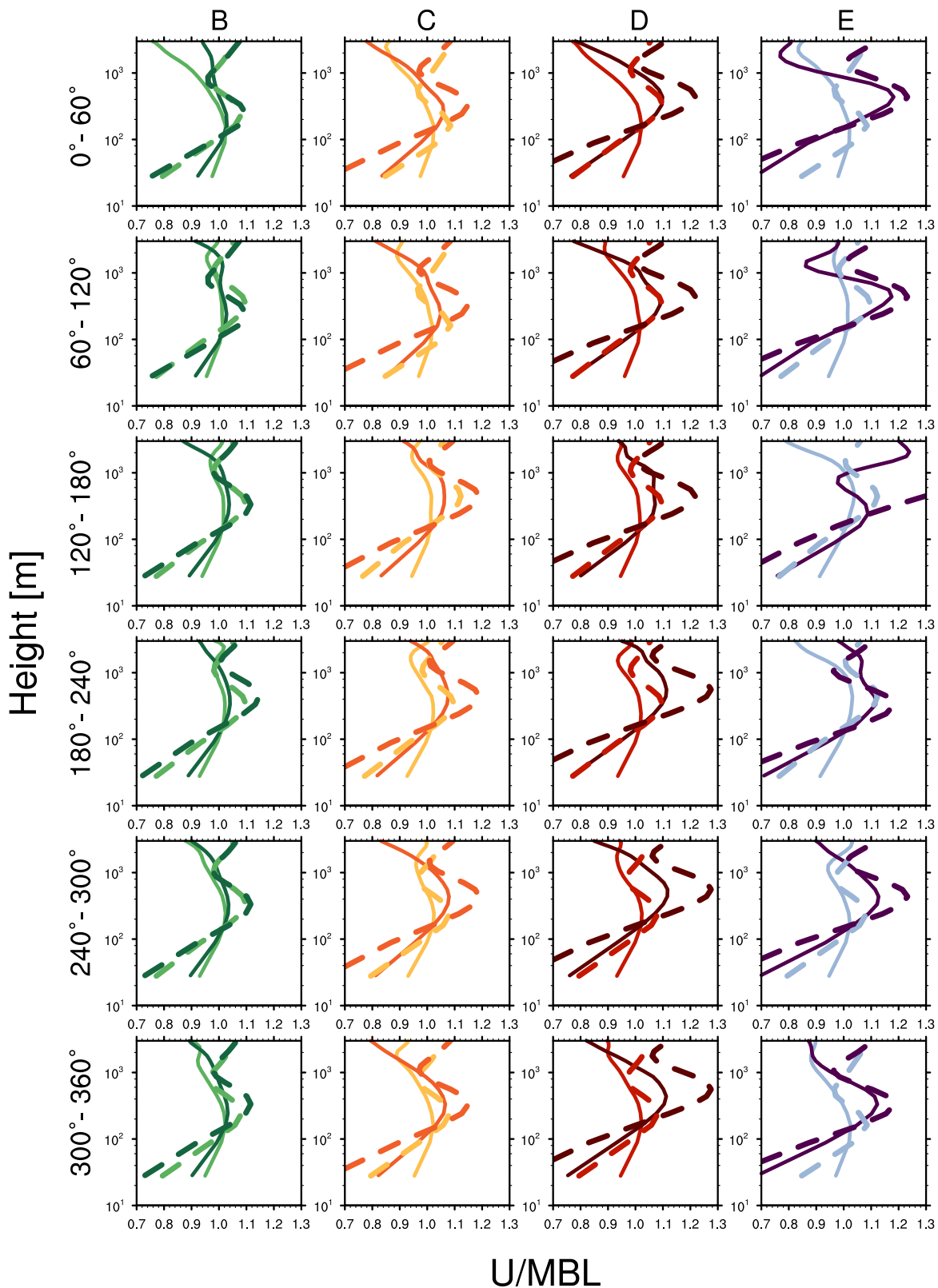
Figure 7.15: Two 30-min averaged vertical profiles at six hours prior to and after the transition from water (brighter colors) to open land (green solid lines), roughly open (orange solid lines), dense suburban (red solid lines), and high intensity/forested (purple solid lines) terrain for radii from 10-30 km. Dashed lines display the semi-empirical model by *Snaiki and Wu* [2018] at the same time.

TCBL wind profiles calculated through the proposed semi-empirical model exhibit lower U/MBL ratios below 200 m and higher U/MBL maxima irrespective of the TC segment. However, the shape

of TCBL profiles by *Snaiki and Wu* [2018] is similar to those generated by WRF over high intensity/forested. In addition the TCBL height aligns well over high intensity/forested terrain profiles after landfall for all TC segments despite 120-180° segment. TCBL heights after landfall over smoother terrain appear to be at the same height, however, U/MBL ratios calculated by the empirical model are up to 0.2 higher than those in the idealised simulations. Although U/MBL ratios exhibit great differences in all segments for $z_0 < 0.8$ m, the empirical model also shows steeper profiles up to the height of maximum wind speed after landfall.

7.3.2.2 Vertical Wind Speed Profiles near Radius of Maximum Winds

Previous analysis showed the RMW to lie within the 30-50 km range. Vertical wind speed profiles for this radius bin were generated in a similar fashion to those described in the previous section and are shown in Figure 7.16. The figure also shows 30-min mean TCBL profiles through the time period of six hours before and after landfall. The behaviour of the TCBL at this radius is of particular importance given it has the greatest impact on people and infrastructure.
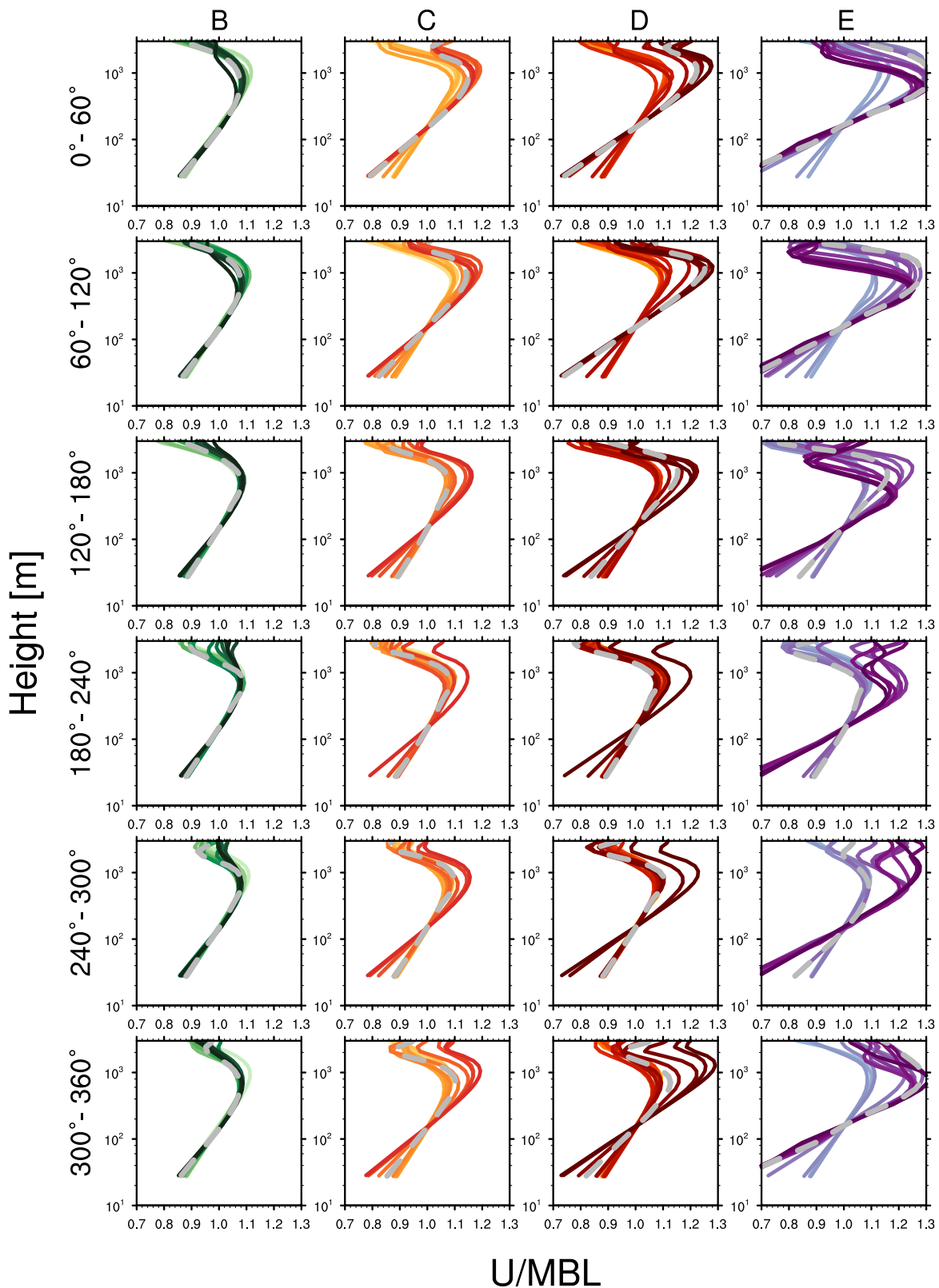
Figure 7.16: Transition of 30-min averaged vertical profiles from water (brighter colors) to open land (green solid lines), roughly open (orange solid lines), dense suburban (red solid lines), and high intensity/forested (purple solid lines) terrain for radii from 30-50 km. The gray-dashed line shows the vertical profile at the landfall time.

Vertical profiles in Figure 7.16 exhibit similar properties to those in the inner core region with respect to their transition over different surface conditions and resulting lower U/MBL ratios near the surface.

Of note is the increased height of the TCBL in all segments compared to those in the inner core region, which was found to increase with radius in Section 7.3.1. However, the TCBL height exhibits variations around the storm which tend to become bigger over rougher terrain. In segments of 120-180° and 180-240° the mean TCBL height is about 500 m over high intensity/forested terrain, with greater TCBL heights noted in remaining TC cones. Furthermore, results suggest that the TCBL height over the roughest terrain becomes lower rather than higher. This finding is contrary to previous research by *Powell et al.* [2005] and *Vickery et al.* [2009], who suggested a TCBL increase of 60-100%. Similar to vertical profiles in the inner core, 120-180° and 180-240° segments appear to transition last, with the rate of change in vertical profiles being reasonably similar around the storm. Over open land exposures, the TCBL seems to stabilise (i.e. equilibrium state) immediately at landfall, while the stabilisation process tends to take at least an hour longer over rougher terrain.

Computed TCBL profiles using the *Snaiki and Wu* [2018] semi-empirical model also indicate a lower TCBL height for rougher terrain, as shown in Figure 7.15. WRF-generated wind speed profiles exhibit stronger wind speeds below 200 m and lower wind speeds above, compared to semi-empirical model profiles.
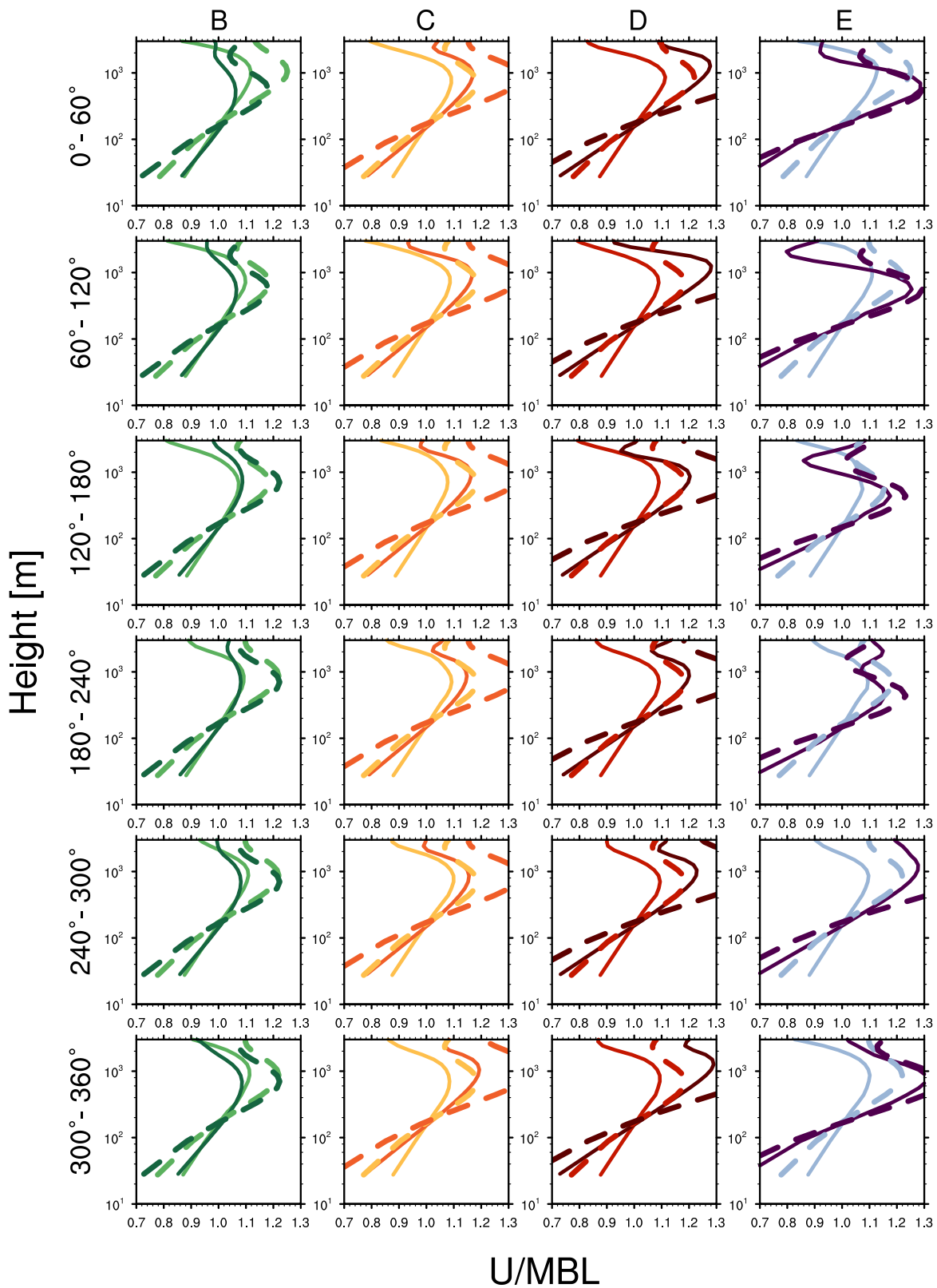
Figure 7.17: Two 30-min averaged vertical profiles at six hours prior to and after the transition from water (brighter colors) to open land (green solid lines), roughly open (orange solid lines), dense suburban (red solid lines), and high intensity/forested (purple solid lines) terrain for radii from 30-50 km. Dashed lines display the semi-empirical model by *Snaiki and Wu* [2018] at the same time.

171

7.3.2.3 Vertical Wind Speed Profiles beyond the Radius of Maximum Winds

TCBL profiles outside of the RMW are investigated for different surface conditions over land. To do this, radii bins examined are 50-75 km, 75-100 km, and 100-200 km. Vertical wind speed profiles for radii greater than 200 km were also generated, however, interpretation of these profiles is a challenging task as regions outside of the TC area are included. The chance of averaging TCBL profiles with profiles outside of the storm is likely and is therefore not further part of the discussion.

Figures 7.18, 7.19, and 7.20 show TCBL profiles similar to the previous sections but for radii bins of 50-75 km, 75-100 km, and 100-200 km, respectively. Of note is the increase of the TCBL with radius irrespective of the underlying terrain. Asymmetries with respect to the TC segments exists with the 180-240° segment exhibiting steeper vertical profiles for high intensity/forested terrain for radii of 50-75 km compared to smoother surfaces. Vertical wind profiles generally become steeper with increasing radius, whereas profiles from 100 km to 200 km are in close agreement with observed profiles over land [*Snaiki and Wu*, 2018] particularly for the leading side of the vortex. Observation-based semi-empirical model profiles by *Snaiki and Wu* [2018] also align well with idealised TCBL profiles as shown in Figure 7.21 for the storm-relative segment of 0-60°.
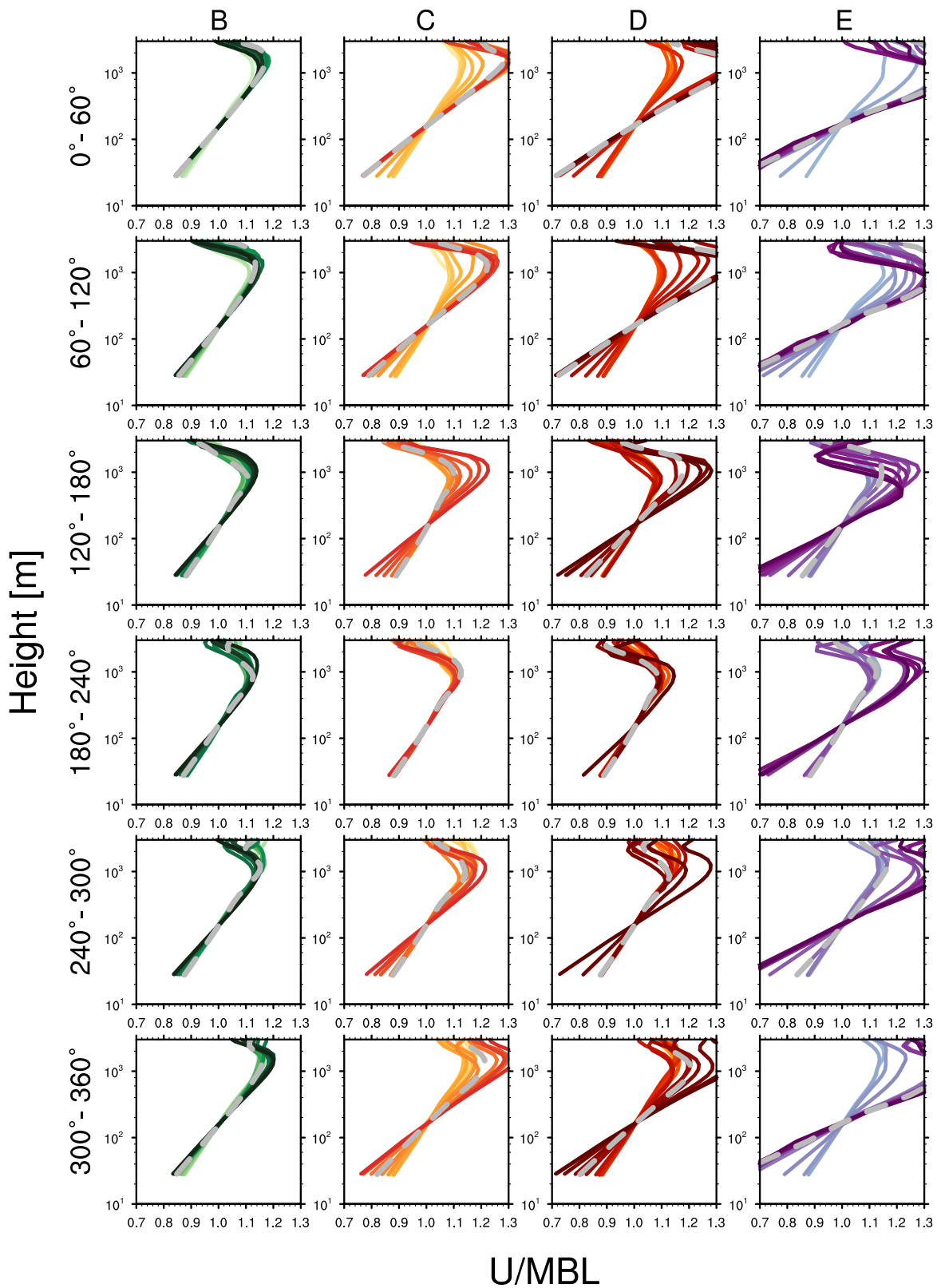
Figure 7.18: Transition of 30-min averaged vertical profiles from water (brighter colors) to open land (green solid lines), roughly open (orange solid lines), dense suburban (red solid lines), and high intensity/forested (purple solid lines) terrain for radii from 50-75 km. The gray-dashed line shows the vertical profile at the landfall time.
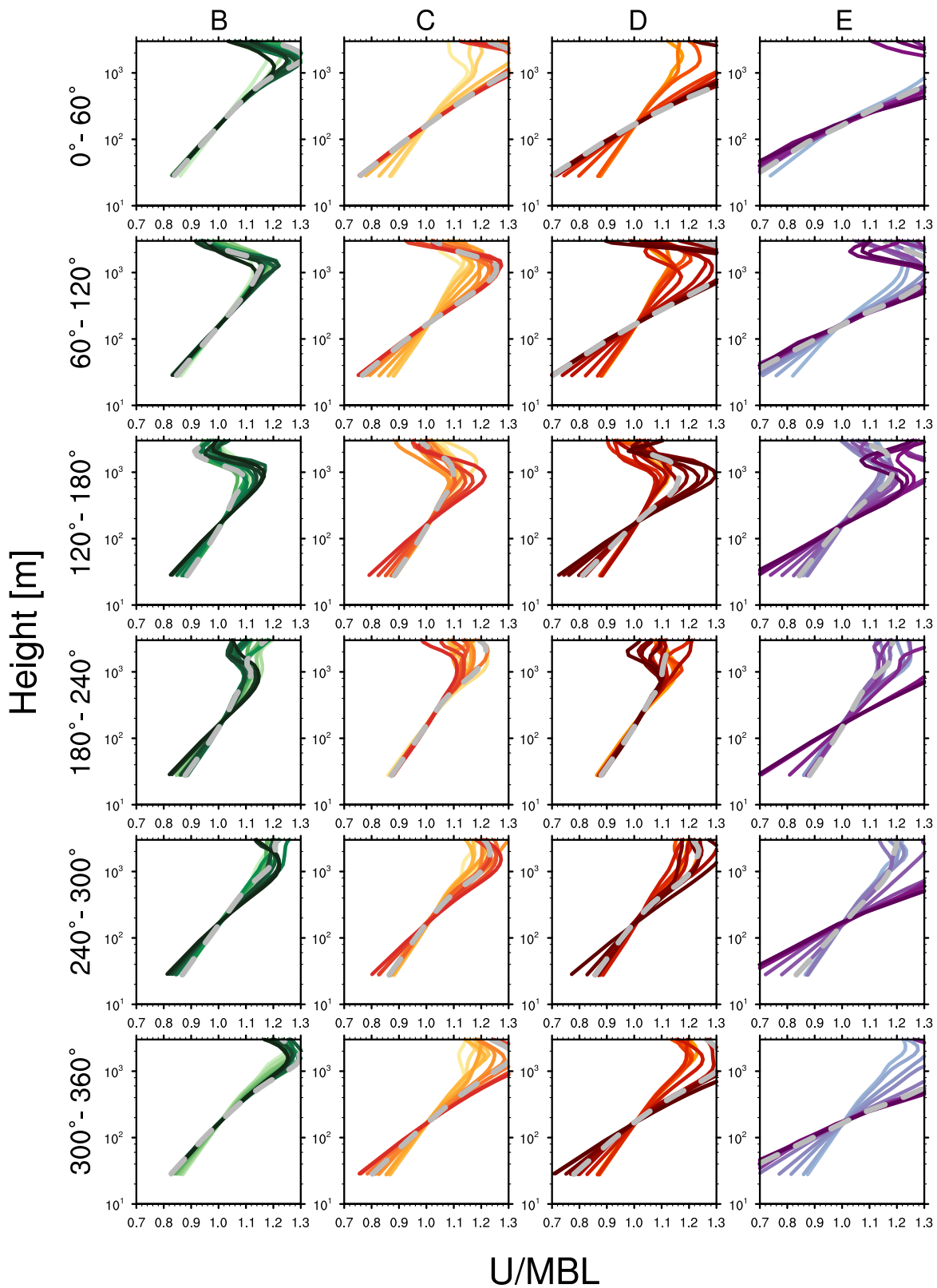
Figure 7.19: Transition of 30-min averaged vertical profiles from water (brighter colors) to open land (green solid lines), roughly open (orange solid lines), dense suburban (red solid lines), and high intensity/forested (purple solid lines) terrain for radii from 75-100 km. The gray-dashed line shows the vertical profile at the landfall time.
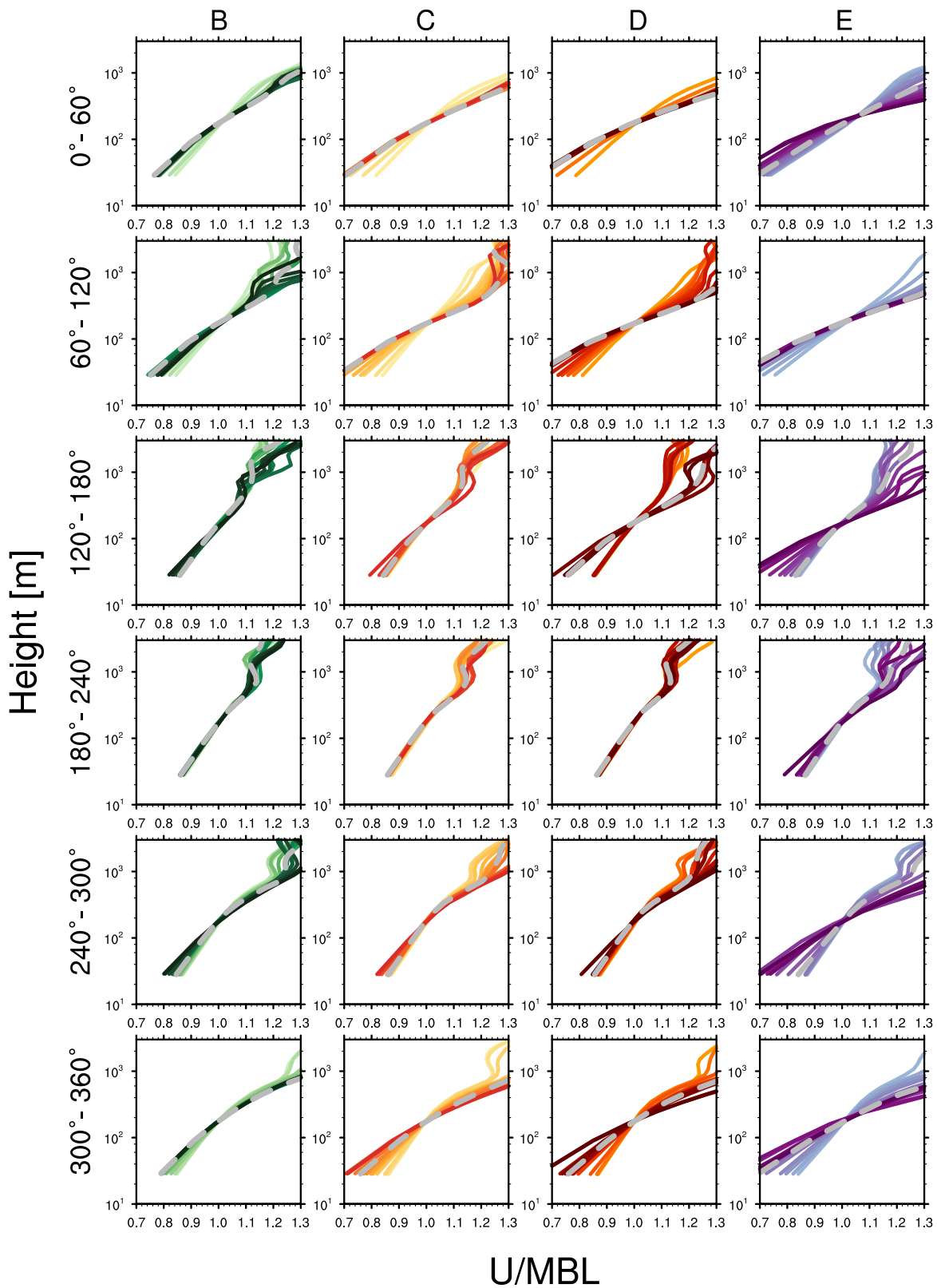
Figure 7.20: Transition of 30-min averaged vertical profiles from water (brighter colors) to open land (green solid lines), roughly open (orange solid lines), dense suburban (red solid lines), and high intensity/forested (purple solid lines) terrain for radii from 100-200 km. The gray-dashed line shows the vertical profile at the landfall time.
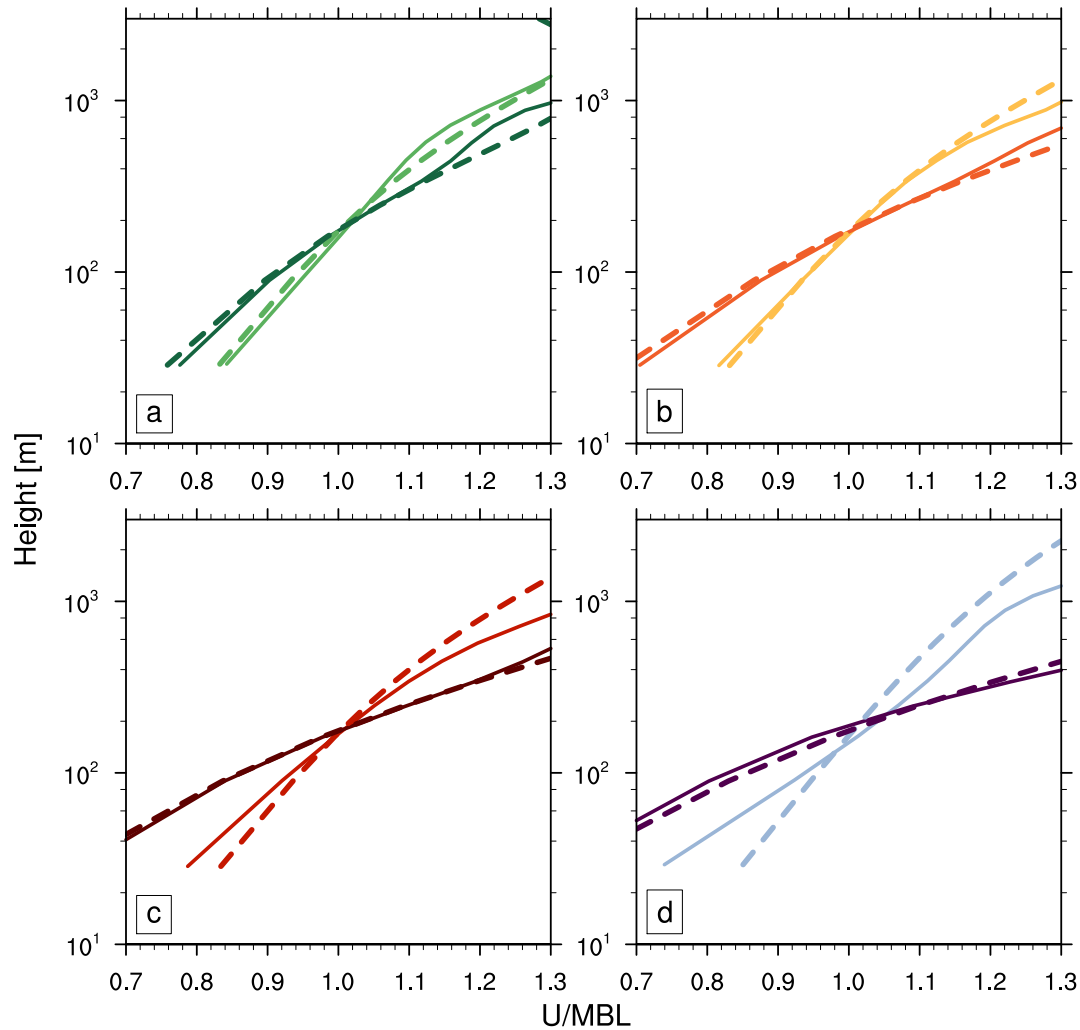
Figure 7.21: Two 30-min averaged vertical profiles at six hours prior to and after the transition from water (brighter colors) to a) open land (green solid lines), b) roughly open (orange solid lines), c) dense suburban (red solid lines), and d) high intensity/forested (purple solid lines) terrain for radii from 100-200 km and in the 0-60° segment. Dashed lines display the semi-empirical model by *Snaiki and Wu* [2018] at the same time.

The empirical model by *Snaiki and Wu* [2018] was found to qualitatively match idealised TCBL profiles after landfall for radii below 75 km and quantitatively above 75 km except for 120-180° and 180-240° segments. Moreover, the empirical model shows a greater difference to TCBL profiles over water than over land.

Chapter 8

Summary and Recommendations

8.1 Summary

Tropical Cyclones (TCs) are rotating low pressure systems characterised by high wind speeds. They pose a major threat to coastal communities and structures that exist within the lowest 2 km in the atmosphere, which is referred to as the tropical cyclone boundary layer (TCBL). To ensure the integrity of structures in the path of landfalling TCs, building design codes and standards must be constantly improved through a better understanding of wind hazards. Understanding this hazard is also true for meteorologists so they can better forecast the impacts of these events. As such, the major objective of this thesis was to contribute to a more detailed understanding of both mean and turbulent TC wind profiles to improve knowledge of surface wind conditions during TC landfall and hence improve the ability of engineers to design effective structures. The particular focus was on how turbulent and mean TCBL profiles respond to abrupt changes in surface roughness, as previous scientific documentation on these aspects were sparse. In order to better understand turbulent and mean TCBL profiles over multiple surface terrain changes, recorded TC near-surface wind field measurements and idealised TC simulations were analysed in this thesis.

Collected wind records from 129 deployed towers at 2.25 m, 3.2 m, 5 m, and 10 m measurement heights were analysed with regards to their upwind terrain and 10-min mean turbulent characteristics, such as turbulence intensity, 3-sec gust and peak factors, skewness and kurtosis, and integral length scale. The upwind terrain was categorised into roughness regimes of water bodies, open land, roughly open, dense suburban, and high intensity/forested. The observational analysis of turbulence statistics with different upwind terrain revealed the following outcomes and conclusions.

1. Turbulence intensity, gust factor, and skewness are the main turbulence characteristics to show a dependence on the upstream terrain.

2. Peak factor, kurtosis, and integral length scale exhibit little to no dependence on the upstream terrain.

3. Turbulence intensities measured at $z \leq 10$ m are found to reach equilibrium around 1000-2000 m downwind from a roughness change irrespective of measurement height or upstream roughness. Consequently, the prevailing belief that an upwind distance of $x \approx 100z$ is sufficient for turbulence characteristics to reach equilibrium is not supported by the observations made within landfalling TCs assessed here.

4. The assumption that the vertical I_u profile follows a logarithmic pattern in the lowest 10 m appears to break down in a TC environment.

5. A transition model is proposed that describes how I_u transitions from an upwind terrain to a new roughness regime for $z \leq 10$ m. In addition, the transition model incorporates a new empirical description of equilibrium I_u profiles for all investigated roughness regimes below 10 m elevation.

6. Traditional engineering terrain transition models AS/NZS1170.2 and ESDU were shown to overestimate equilibrium turbulence intensities in a TC environment.

During TC landfall onto four different land surfaces, bulk storm characteristics such as RMW and TC size, a horizontal surface wind field, and mean TCBL profiles were studied using idealised TC simulations. A set of four TC simulations was conducted utilising the Hybrid WRF Cyclone Model (HWCM) approach, which involves the spin up of an idealised TC over a water surface and then placed into a real world environment. With these four parametric tests the way sudden changes in terrain, i.e. sea to open land, roughly open, dense suburban, and high intensity/forested, influence the mean surface wind field and structure of the TCBL was systematically explored. Simulations were set up on a triply nested domain of 10800 x 10800 km with horizontal grid resolutions of 18 km, 6 km, and 2 km. To ensure enough time for the TC to stabilise before translating onto land, the storm was placed about 1300 km off the coastline. The meteorological environment, within which the storm was placed, was provided through a 30-year climatological mean atmospheric sounding with idealised wind speeds of 10 kts (5.14 m/s) from 90 degree direction. Numerical results of simulated TCBL profiles over different surface conditions are summarised below.

1. Idealised TCBL profiles over water generally match observed TCBL profiles by dropwindsondes, which validates the simulation approach.

2. Increased surface roughness over land lowers TC intensity during landfall (in some cases prior to) but the change in roughness does not lead to track deflections.

3. Maximum TC wind speeds were found to drop by up to 70% within 12-hours after landfall over very rough terrain ($z_0 = 0.8$ m).

4. TCBL profiles follow a logarithmic wind profile up to the height of maximum wind speed, which was shown to increase with TC radius and MBL.

5. Idealised TCBL profiles over land appear to deviate from those obtained from Doppler radars for $z_0 < 0.8$ m.

6. When idealised TCs transition onto land, vertical TCBL respond with lower U/MBL ratios near the surface and greater ratios at the height of maximum wind. Over very rough terrain (i.e. $z_0 \geq 0.8$ m), the TCBL height appears to reduce down to 500 m for radii below 75 km from the TC centre.

8.2 Recommendations

Based on the summary and conclusions in the previous sections, several recommendations for future research arise:

Observations

1. Substantially more near-surface wind field data at heights $z \leq 10$ m need to be collected and analysed with regards to their turbulence characteristics to more adequately understand highly complex wind fields in landfalling TCs.

2. Targeted tower deployments in landfalling TCs should be set up as lines of towers following terrain changes in order to understand turbulence transition better and to confirm $x \approx 2000$ m. This will allow an investigation of velocity magnitude change and would allow detailed exploration of the influence of multiple terrain changes as well.

3. Further model approaches that describe multiple terrain changes should be developed to better assess how the turbulent flow is modified.

Numerical Simulations

1. Future idealised simulations need to include TCs of categories 1 to 5 in order to better understand how the strength of the TC is affected by different land surface conditions.

2. A broader spectrum of underlying z_0 values over land is required to better understand the influence of different land surface conditions on the TC surface wind field and vertical TCBL profiles.

References

Anthes, R. A., Development of Asymmetries in a Three-Dimensional Numerical Model of the Tropical Cyclone, *Monthly Weather Review*, *100*(6), 461–476, 1972.

Anthes, R. A., A cumulus parameterization scheme utilizing a one-dimensional cloud model, *Monthly Weather Review*, *105*(3), 270–286, 1977a.

Anthes, R. A., Hurricane model experiments with a new cumulus parameterization scheme, *Monthly Weather Review*, *105*(3), 287–300, 1977b.

Anthes, R. A., *Tropical Cyclones: Their Evolution, Structure and Effects*, no. 41, v. 19 in Meteorological Monographs, American Meteorological Society, 1982.

Anthes, R. A., and D. Keyser, Tests of a Fine-Mesh Model over Europe and the United States, *Monthly Weather Review*, *107*(8), 963–984, doi:10.1175/1520-0493(1979)107⟨0963:TOAFMM⟩2.0.CO;2, 1979.

Anthes, R. A., and T. T. Warner, Prediction of Mesoscale Flows over Complex Terrain, *Tech. Rep. ECOM-5532*, Atmos. Sci. Lab., White Sands Missle Range, 1974.

Anthes, R. A., and T. T. Warner, Development of Hydrodynamic Models Suitable for Air Pollution and Other Mesometerological Studies, *Monthly Weather Review*, *106*(8), 1045–1078, doi:10.1175/1520-0493(1978)106⟨1045:DOHMSF⟩2.0.CO;2, 1978.

Anthes, R. A., and T. T. Warner, Description of the Penn State/NCAR Mesoscale Model Version 4 (MM4). NCAR Tech. Note, *Tech. rep.*, NCAR/TN-282+ STP, 66 pp.[Available from NCAR, PO Box 3000, Boulder, CO 80303], 1987.

Anthes, R. A., Y.-H. Kuo, S. G. Benjamin, and Y.-F. Li, The evolution of the mesoscale environment of severe local storms: Preliminary modeling results, *Monthly Weather Review*, *110*(9), 1187–1213, 1982.

Anthes, R. A., Y.-H. Kuo, and J. R. Gyakum, Numerical Simulations of a Case of Explosive Marine Cyclogenesis, *Monthly Weather Review*, *111*(6), 1174–1188, doi:10.1175/1520-0493(1983) 111⟨1174:NSOACO⟩2.0.CO;2, 1983.

Arakawa, A., and V. R. Lamb, Computational design of the basic dynamical processes of the ucla general circulation model, in *General Circulation Models of the Atmosphere*, *Methods in Computational Physics: Advances in Research and Applications*, vol. 17, edited by J. Chang, pp. 173 – 265, Elsevier, doi:https://doi.org/10.1016/B978-0-12-460817-7.50009-4, 1977.

Arakawa, A., and W. H. Schubert, Interaction of a Cumulus Cloud Ensemble with the Large-Scale Environment, Part I, *Journal of the Atmospheric Sciences*, *31*(3), 674–701, doi:10.1175/1520-0469(1974)031⟨0674:IOACCE⟩2.0.CO;2, 1974.

ASCE 7, *Minimum Design Loads for Buildings and Other Structures*, sei/asce 7-02 ed., American Society of Civil Engineers, doi:10.1061/9780784406243, 2003.

AS/NZS 1170.2:2011, *Structural design actions, Part 2: Wind actions*, Standards Australia, 2011.

Balderrama, J., F. Masters, K. Gurley, D. Prevatt, L. Aponte-Bermúdez, T. Reinhold, J.-P. Pinelli, C. Subramanian, S. Schiff, and A. Chowdhury, The Florida Coastal Monitoring Program (FCMP): A review, *Journal of Wind Engineering and Industrial Aerodynamics*, *99*(9), 979 – 995, doi:http://dx.doi.org/10.1016/j.jweia.2011.07.002, 9th UK Conference on Wind Engineering (September, 2010), 2011.

Balderrama, J., F. Masters, and K. Gurley, Peak factor estimation in hurricane surface winds, *Journal of Wind Engineering and Industrial Aerodynamics*, *102*, 1–13, 2012.

Barthelmie, R. J., J. P. Palutikof, and T. D. Davies, Estimation of sector roughness lengths and the effect on prediction of the vertical wind speed profile, *Boundary-Layer Meteorology*, *66*(1), 19–47, doi:10.1007/BF00705458, 1993.

Beljaars, A. C., The Measurement of Gustiness at Routine Wind Stations: A Review, *KNMI Rep. WR87-11, 50 pp., [Available online at* http://library.wmo.int/pmb_ged/iom_31.pdf*]*, 1987.

Bender, M. A., R. E. Tuleya, and Y. Kurihara, A Numerical Study of the Effect of a Mountain Range on a Landfalling Tropical Cyclone, *Monthly Weather Review*, *113*(4), 567–583, doi:10.1175/1520-0493(1985)113⟨0567:ANSOTE⟩2.0.CO;2, 1985.

Benjamin, S. G., and T. N. Carlson, Some effects of surface heating and topography on the regional severe storm environment. Part I: Three-dimensional simulations, *Monthly Weather Review*, *114*(2), 307–329, 1986.

Bergeron, T., Review of modern Meteorology — 12. The problem of tropical hurricanes, *Quarterly Journal of the Royal Meteorological Society*, *80*(344), 131–164, 1954.

Blackadar, A., High resolution models of the planetary boundary layer, *Advances in environmental science and engineering*, *1*(1), 50–85, 1978.

Braham, R. R., and P. Squires, Cloud physics, *Bulletin of the American Meteorological Society*, *55*(6), 543–586, doi:10.1175/1520-0477(1974)055⟨0543:CP⟩2.0.CO;2, 1974.

Bretherton, C. S., *Entrainment, Detrainment and Mixing in Atmospheric Convection*, pp. 211–230, Springer Netherlands, Dordrecht, doi:10.1007/978-94-015-8828-7_8, 1997.

Brooks, F. A., Need for measuring horizontal gradients in determining vertical eddy transfers of heat and moisture, *Journal of Meteorology*, *18*(5), 589–596, doi:10.1175/1520-0469(1961)018⟨0589: NFMHGI⟩2.0.CO;2, 1961.

Browning, K. A., and R. Wexler, The determination of kinematic properties of a wind field using doppler radar, *Journal of Applied Meteorology*, *7*(1), 105–113, doi:10.1175/1520-0450(1968) 007⟨0105:TDOKPO⟩2.0.CO;2, 1968.

Bruyere, C. L., G. J. Holland, B. Buckley, M. Leplastrier, P. Chan, M. Tingley, and A. Dyer, Hybrid Real-Idealized Tropical Cyclones as a New Loss Tool, *AMOS National Conference*, 2016.

Busch, N. E., S. W. Chang, and R. A. Anthes, A multi-level model of the planetary boundary layer suitable for use with mesoscale dynamic models, *Journal of Applied Meteorology*, *15*(9), 909–919, 1976.

Businger, J. A., Evaluation of the Accuracy with Which Dry Deposition Can Be Measured with Current Micrometeorological Techniques, *Journal of Climate and Applied Meteorology*, *25*(8), 1100–1124, doi:10.1175/1520-0450(1986)025⟨1100:EOTAWW⟩2.0.CO;2, 1986.

Chan, J. C. L., Movement of Tropical Cyclones, in *Global Perspectives on Tropical Cyclones*, vol. 4, pp. 133–148, World Scientific Series on Asia-Pacific Weather and Climate, 2010.

Chang, S. W.-J., The Mutual Response of the Tropical Cyclone and the Ocean as Revealed by AN Interacting Atmospheric and Oceanic Model, Ph.d. thesis, The Pennsylvania State University, 1977.

Chang, S. W.-J., The Orographic Effects Induced by an Island Mountain Range on Propagating Tropical Cyclones, *Monthly Weather Review*, *110*(9), 1255–1270, doi:10.1175/1520-0493(1982) 110⟨1255:TOEIBA⟩2.0.CO;2, 1982.

Charney, J., The Use of the Primitive Equations of Motion in Numerical Prediction, *Tellus*, *7*(1), 22–26, doi:10.1111/j.2153-3490.1955.tb01138.x, 1955.

Charney, J. G., and A. Eliassen, On the Growth of the Hurricane Depression, *Journal of the Atmospheric Sciences*, *21*(1), 68–75, doi:10.1175/1520-0469(1964)021⟨0068:OTGOTH⟩2.0.CO;2, 1964.

Chen, Y., and M. K. Yau, Asymmetric structures in a simulated landfalling hurricane, *Journal of the Atmospheric Sciences*, *60*(18), 2294–2312, doi:10.1175/1520-0469(2003)060⟨2294:ASIASL⟩2.0. CO;2, 2003.

Choi, E., Characteristics of typhoons over the South China Sea, *Journal of Wind Engineering and Industrial Aerodynamics*, *3*(4), 353 – 365, doi:http://dx.doi.org/10.1016/0167-6105(78)90038-7, 1978.

Cohen, A. E., S. M. Cavallo, M. C. Coniglio, and H. E. Brooks, A Review of Planetary Boundary Layer Parameterization Schemes and Their Sensitivity in Simulating Southeastern U.S. Cold Season Severe Weather Environments, *Weather and Forecasting*, *30*(3), 591–612, doi:10.1175/WAF-D-14-00105.1, 2015.

Cook, N., The designer's guide to wind loading on building structures. Part I: Background, damage survey, wind data, and structural classification, *Building Research Establishment, Watford*, 1985.

Craig, G. C., and S. L. Gray, CISK or WISHE as the mechanism for tropical cyclone intensification, *Journal of the Atmospheric Sciences*, *53*(23), 3528–3540, 1996.

Davenport, A. G., Rationale for determining design wind velocities, *Tech. rep.*, National Rresearch Council of Canada Ottawa (Ontario) Div of Building Research, 1960.

Davenport, A. G., The spectrum of horizontal gustiness near the ground in high winds, *Quarterly Journal of the Royal Meteorological Society*, *87*(372), 194–211, doi:10.1002/qj.49708737208, 1961.

Davenport, A. G., Note on the distribution of the largest value of a random function with application to gust loading., in *ICE Proceedings*, vol. 28, pp. 187–196, Thomas Telford, 1964.

Deacon, E., Wind gust speed: averaging time relationship, *Australian Meteorological Magazine*, *51*, 11–14, 1965.

Deaves, D., Computations of wind flow over two-dimensional hills and embankments, *Journal of Wind Engineering and Industrial Aerodynamics*, *6*(1), 89 – 111, doi:https://doi.org/10.1016/0167-6105(80)90024-0, 1980.

Deaves, D. M., Computations of wind flow over changes in surface roughness, *Journal of Wind Engineering and Industrial Aerodynamics*, *7*(1), 65–94, 1981.

DeMaria, M., The Effect of Vertical Shear on Tropical Cyclone Intensity Change, *Journal of the Atmospheric Sciences*, *53*(14), 2076–2088, doi:10.1175/1520-0469(1996)053⟨2076:TEOVSO⟩2.0.CO;2, 1996.

Dodla, V. B., S. Desamsetti, and A. Yerramilli, A Comparison of HWRF, ARW and NMM Models in Hurricane Katrina (2005) Simulation, *International Journal of Environmental Research and Public Health*, *8*(6), 2447, doi:10.3390/ijerph8062447, 2011.

Dorst, N. M., The National Hurricane Research Project: 50 Years of Research, Rough Rides, and Name Changes, *Bulletin of the American Meteorological Society*, *88*(10), 1566–1588, doi:10.1175/BAMS-88-10-1566, 2007.

Dudhia, J., Numerical study of convection observed during the winter monsoon experiment using a mesoscale two-dimensional model, *Journal of the Atmospheric Sciences*, *46*(20), 3077–3107, 1989.

Dudhia, J., A nonhydrostatic version of the Penn State-NCAR mesoscale model: Validation tests and simulation of an Atlantic cyclone and cold front, *Monthly Weather Review*, *121*(5), 1493–1513, 1993.

Dudhia, J., WRF Modeling System Overview, *Presentation at the 2016 WRF Winter Tutorial*, Mesoscale and Microscale Meteorology Laboratory / NCAR, 2016a.

Dudhia, J., Overview of WRF Physics, *Presentation at the 2016 wrf winter tutorial*, Mesoscale and Microscale Meteorology Laboratory / NCAR, 2016b.

Dudhia, J., D. Gill, K. Manning, W. Wang, and C. Bruyere, PSU/NCAR Mesoscale Modeling System Tutorial Class Notes and User's Guide: MM5 Modeling System Version 3, *MM5 Modeling System Version 3*, 1999.

Dudhia, J., D. Gill, K. Manning, W. Wang, and C. Bruyere, PSU/NCAR Mesoscale Modeling System (MM5 version 3) Tutorial Class Notes and User's Guide, *Available from the National Center for Atmospheric Research, Boulder, Colorado, USA*, 2002.

Dudhia, J., D. Gill, K. Manning, W. Wang, C. Bruyere, S. Kelly, and K. Lackey, PSU/NCAR Mesoscale Modeling System, *Tutorial Class Notes and User's Guide: MM5 Modeling System Version*, *3*, 2005.

Durst, C. S., Wind speeds over short periods of time, *The Meteorological Magazine*, *89*(1056), 181–186, 1960.

Eliassen, A., The quasi-static equations of motion with pressure as independent variable, *Geoj. Publ.*, *17*(3), 44 pp., 1949.

Eliassen, A., and M. Lystad, The Ekman layer of a circular vortex - A numerical and theoretical study, *Geophysica Norvegica*, *31*, 1–16, 1977.

Elliott, W. P., The growth of the atmospheric internal boundary layer, *Eos, Transactions American Geophysical Union*, *39*(6), 1048–1054, doi:10.1029/TR039i006p01048, 1958.

Elsberry, R. L., Tropical Cyclone Motion, *A global view of tropical cyclones*, pp. 91–131, 1987.

Emanuel, K. A., An Air-Sea Interaction Theory for Tropical Cyclones. Part I: Steady-State Maintenance, *Journal of the Atmospheric Sciences*, *43*(6), 585–605, doi:10.1175/1520-0469(1986)043⟨0585:AASITF⟩2.0.CO;2, 1986.

Emanuel, K. A., 100 Years of Progress in Tropical Cyclone Research, *Meteorological Monographs*, *59*, 15.1–15.68, doi:10.1175/AMSMONOGRAPHS-D-18-0016.1, 2018.

ESDU, *Strong Winds in the Atmospheric Boundary Layer: Part 1: Hourly-mean Wind Speeds*, ESDU series on wind engineering, 2003-03 ed., Engineering Sciences Data Unit, 1982.

ESDU, *Strong Winds in the Atmospheric Boundary Layer: Part 2: Discrete Gust Speeds*, ESDU series on wind engineering, 2003-03 ed., Engineering Sciences Data Unit, 1983.

Etling, D., *Theoretische Meteorologie: Eine Einführung*, chap. Die atmosphärische Grenzschicht, pp. 297–340, Springer Berlin Heidelberg, Berlin, Heidelberg, doi:10.1007/978-3-540-75979-9_21, 2008.

Fernández-Cabán, P., and F. Masters, Near surface wind longitudinal velocity positively skews with increasing aerodynamic roughness length, *Journal of Wind Engineering and Industrial Aerodynamics*, *169*, 94 – 105, doi:https://doi.org/10.1016/j.jweia.2017.06.007, 2017.

Ferrier, B. S., A Double-Moment Multiple-Phase Four-Class Bulk Ice Scheme. Part I: Description, *Journal of the Atmospheric Sciences*, *51*(2), 249–280, doi:10.1175/1520-0469(1994)051⟨0249: ADMMPF⟩2.0.CO;2, 1994.

Finocchio, P. M., S. J. Majumdar, D. S. Nolan, and M. Iskandarani, Idealized Tropical Cyclone Responses to the Height and Depth of Environmental Vertical Wind Shear, *Monthly Weather Review*, *144*(6), 2155–2175, doi:10.1175/MWR-D-15-0320.1, 2016.

Foken, T., *Micrometeorology*, Springer, Heidelberg, 2008.

Franklin, J. L., M. L. Black, and K. Valde, GPS Dropwindsonde Wind Profiles in Hurricanes and Their Operational Implications, *Weather and Forecasting*, *18*(1), 32–44, doi:10.1175/1520-0434(2003) 018⟨0032:GDWPIH⟩2.0.CO;2, 2003.

Freeman, B. E., Mathematical modeling of mesoscale meteorology over complex terrain, *Tech. rep.*, Available from Science Applications, Inc., P.O. Box 2351, LaJolla Calif. 92037., 1974.

Gash, J. H. C., Observations of turbulence downwind of a forest-heath interface, *Boundary-Layer Meteorology*, *36*(3), 227–237, doi:10.1007/BF00118661, 1986.

Gentry, M. S., and G. M. Lackmann, Sensitivity of simulated tropical cyclone structure and intensity to horizontal resolution, *Monthly Weather Review*, *138*(3), 688–704, 2010.

Giammanco, I. M., J. L. Schroeder, and M. D. Powell, Observed characteristics of tropical cyclone vertical wind profiles, *Wind and Structures*, *15*(1), 65, 2012.

Giammanco, I. M., J. L. Schroeder, and M. D. Powell, GPS Dropwindsonde and WSR-88D Observations of Tropical Cyclone Vertical Wind Profiles and Their Characteristics, *Weather and Forecasting*, *28*(1), 77–99, doi:10.1175/WAF-D-11-00155.1, 2013.

Giammanco, I. M., J. L. Schroeder, F. J. Masters, P. J. Vickery, R. J. K. III, and J.-A. Balderrama, Influences on Observed Near-Surface Gust Factors in Landfalling U.S. Gulf Coast Hurricanes: 2004–08, *Journal of Applied Meteorology and Climatology*, *55*(12), 2587–2611, doi:10.1175/ JAMC-D-16-0053.1, 2016.

Haltiner, G., and R. Williams, Numerical Prediction and Dynamic Meteorology (2nd ed.), *Wiley*, 1980.

Haque, S. M. A., The initiation of cyclonic circulation in a vertically unstable stagnant air mass, *Quarterly Journal of the Royal Meteorological Society*, *78*(337), 394–406, doi:10.1002/qj.49707833710, 1952.

Harper, B., J. Kepert, and J. Ginger, Guidelines for converting between various wind averaging periods in tropical cyclone conditions, *World Meteorological Organization, WMO/TD*, *1555*, 2010.

Harrison, E. J., and R. L. Elsberry, A method for incorporating nested finite grids in the solution of systems of geophysical equations, *Journal of the Atmospheric Sciences*, *29*(7), 1235–1245, 1972.

Henderson, D., M. Mason, and J. Ginger, SWIRLnet : portable anemometer network for wind speed measurements of land-falling tropical cyclones, in *The 12th Americas Conference on Wind Engineering (12ACWE)*, Seattle, Washington, USA, 2013.

Hill, K. A., and G. M. Lackmann, Analysis of Idealized Tropical Cyclone Simulations Using the Weather Research and Forecasting Model: Sensitivity to Turbulence Parameterization and Grid Spacing, *Monthly Weather Review*, *137*(2), 745–765, doi:10.1175/2008MWR2220.1, 2009.

Hirth, B. D., J. L. Schroeder, C. C. Weiss, D. A. Smith, and M. I. Biggerstaff, Research Radar Analyses of the Internal Boundary Layer over Cape Canaveral, Florida, during the Landfall of Hurricane Frances (2004), *Weather and Forecasting*, *27*(6), 1349–1372, doi:10.1175/WAF-D-12-00014.1, 2012.

Holland, G. J., Mature Structure and Structure Change, *A global view of tropical cyclones*, pp. 13–52, 1987.

Holland, G. J., The Maximum Potential Intensity of Tropical Cyclones, *Journal of the Atmospheric Sciences*, *54*(21), 2519–2541, doi:10.1175/1520-0469(1997)054⟨2519:TMPIOT⟩2.0.CO;2, 1997.

Holmes, J. D., *Strong wind characteristics and turbulence*, chap. 3, pp. 57–82, CRC Press, doi:10.1201/b18029-4, 0, 2015.

Hong, S.-Y., Overview of Physical Parameterizations , *Power point slides presented at the January 2015 basic WRF tutorial*, NCAR/KIAPS, 2015.

Hong, S.-Y., J. Dudhia, and S.-H. Chen, A Revised Approach to Ice Microphysical Processes for the Bulk Parameterization of Clouds and Precipitation, *Monthly Weather Review*, *132*(1), 103–120, doi:10.1175/1520-0493(2004)132⟨0103:ARATIM⟩2.0.CO;2, 2004.

Hong, S.-Y., Y. Noh, and J. Dudhia, A new vertical diffusion package with an explicit treatment of entrainment processes, *Monthly Weather Review*, *134*(9), 2318–2341, doi:10.1175/MWR3199.1, 2006.

Houze, R. A., Mesoscale convective systems, *Reviews of Geophysics*, *42*(4), doi:10.1029/ 2004RG000150, rG4003, 2004.

Hsie, E.-Y., and R. A. Anthes, Simulations of frontogenesis in a moist atmosphere using alternative parameterizations of condensation and precipitation, *Journal of the Atmospheric Sciences*, *41*(18), 2701–2716, 1984.

Hubert, L. F., Distribution of surface friction in hurricanes, *Journal of Meteorology*, *16*(4), 393–404, doi:10.1175/1520-0469(1959)016⟨0393:DOSFIH⟩2.0.CO;2, 1959.

Hupfer, P., Zur Abschätzung der Schubspannung des Windes an der Meeresoberfläche bei kurzen Windwirklängen, *Gerlands Beitr. Geophys., Leipzig*, *87*, 263–266, 1978.

Ishizaki, H., Wind profiles, turbulence intensities and gust factors for design in typhoon-prone regions, *Journal of Wind Engineering and Industrial Aerodynamics*, *13*(1), 55 – 66, doi:http://dx.doi.org/ 10.1016/0167-6105(83)90128-9, 1983.

Islam, T., P. K. Srivastava, M. A. Rico-Ramirez, Q. Dai, M. Gupta, and S. K. Singh, Tracking a tropical cyclone through WRF–ARW simulation and sensitivity of model physics, *Natural Hazards*, *76*(3), 1473–1495, doi:10.1007/s11069-014-1494-8, 2015.

Janjić, Z. I., The Step-Mountain Eta Coordinate Model: Further Developments of the Convection, Viscous Sublayer, and Turbulence Closure Schemes, *Monthly Weather Review*, *122*(5), 927–945, doi:10.1175/1520-0493(1994)122⟨0927:TSMECM⟩2.0.CO;2, 1994.

Janjic, Z., A nonhydrostatic model based on a new approach, *Meteorology and Atmospheric Physics*, *82*(1-4), 271–285, 2003.

Jegede, O. O., and T. Foken, A study of the internal boundary layer due to a roughness change in neutral conditions observed during the linex field campaigns, *Theoretical and Applied Climatology*, *62*(1), 31–41, doi:10.1007/s007040050072, 1999.

Johnson, R. E., Estimation of friction of surface winds in the August 1949, Florida hurricane, *Monthly Weather Review*, *82*(3), 73–79, doi:10.1175/1520-0493(1954)082⟨0073:EOFOSW⟩2.0. CO;2, 1954.

Jorgensen, D. P., Mesoscale and Convective-Scale Characteristics of Mature Hurricanes. Part II. Inner Core Structure of Hurricane Allen (1980), *Journal of the Atmospheric Sciences*, *41*(8), 1287–1311, doi:10.1175/1520-0469(1984)041⟨1287:MACSCO⟩2.0.CO;2, 1984.

Kain, J. S., The Kain–Fritsch Convective Parameterization: An Update, *Journal of Applied Meteorology*, *43*(1), 170–181, doi:10.1175/1520-0450(2004)043⟨0170:TKCPAU⟩2.0.CO;2, 2004.

Kain, J. S., and J. M. Fritsch, A One-Dimensional Entraining/Detraining Plume Model and its Application in Convective Parameterization, *Journal of the Atmospheric Sciences*, *47*(23), 2784–2802, doi:10.1175/1520-0469(1990)047⟨2784:AODEPM⟩2.0.CO;2, 1990.

Kain, J. S., and J. M. Fritsch, *Convective Parameterization for Mesoscale Models: The Kain-Fritsch Scheme*, pp. 165–170, American Meteorological Society, Boston, MA, doi:10.1007/978-1-935704-13-3_16, 1993.

Kaplan, J., and M. DeMaria, A simple empirical model for predicting the decay of tropical cyclone winds after landfall, *Journal of Applied Meteorology*, *34*(11), 2499–2512, doi:10.1175/1520-0450(1995)034⟨2499:ASEMFP⟩2.0.CO;2, 1995.

Kareem, A., and J. Zhao, Analysis of non-gaussian surge response of tension leg platforms under wind loads, *Journal of Offshore Mechanics and Arctic Engineering*, *116*(3), 137–144, doi:10.1115/1.2920142, 1994.

Kepert, J. D., The Dynamics of Boundary Layer Jets within the Tropical Cyclone Core. Part I: Linear Theory, *Journal of the Atmospheric Sciences*, *58*(17), 2469–2484, doi:10.1175/1520-0469(2001)058⟨2469:TDOBLJ⟩2.0.CO;2, 2001.

Kepert, J. D., *The wind-field structure of the tropical cyclone boundary-layer*, Monash University, Department of Mathematics and Statistics, 2002.

Kepert, J. D., Observed Boundary Layer Wind Structure and Balance in the Hurricane Core. Part I: Hurricane Georges, *Journal of the Atmospheric Sciences*, *63*(9), 2169–2193, doi:10.1175/JAS3745.1, 2006a.

Kepert, J. D., Observed Boundary Layer Wind Structure and Balance in the Hurricane Core. Part II: Hurricane Mitch, *Journal of the Atmospheric Sciences*, *63*(9), 2194–2211, doi:10.1175/JAS3746.1, 2006b.

Kepert, J. D., Slab- and height-resolving models of the tropical cyclone boundary layer. Part I: Comparing the simulations, *Quarterly Journal of the Royal Meteorological Society*, *136*(652), 1686–1699, doi:10.1002/qj.667, 2010a.

Kepert, J. D., Tropical cyclone structure and dynamics, in *Global Perspectives on Tropical Cyclones*, vol. 4, pp. 3–53, World Scientific Series on Asia-Pacific Weather and Climate, 2010b.

Kepert, J. D., Choosing a Boundary Layer Parameterization for Tropical Cyclone Modeling, *Monthly Weather Review*, *140*(5), 1427–1445, doi:10.1175/MWR-D-11-00217.1, 2012.

Kepert, J. D., and Y. Wang, The Dynamics of Boundary Layer Jets within the Tropical Cyclone Core. Part II: Nonlinear Enhancement, *Journal of the Atmospheric Sciences*, *58*(17), 2485–2501, doi:10.1175/1520-0469(2001)058⟨2485:TDOBLJ⟩2.0.CO;2, 2001.

Kepert, J. D., J. Schwendike, and H. Ramsay, Why is the Tropical Cyclone Boundary Layer Not "Well Mixed"?, *Journal of the Atmospheric Sciences*, *73*(3), 957–973, doi:10.1175/JAS-D-15-0216.1, 2016.

Klotz, B. W., and D. S. Nolan, SFMR Surface Wind Undersampling over the Tropical Cyclone Life Cycle, *Monthly Weather Review*, *147*(1), 247–268, doi:10.1175/MWR-D-18-0296.1, 2019.

Knapp, K. R., M. C. Kruk, D. H. Levinson, H. J. Diamond, and C. J. Neumann, The International Best Track Archive for Climate Stewardship (IBTrACS), *Bulletin of the American Meteorological Society*, *91*(3), 363–376, doi:10.1175/2009BAMS2755.1, 2010.

Knievel, J., Numerical Weather Prediction (NWP) and the WRF Model, in *ATEC Forecasters' Conference*, available at http://ral.ucar.edu/projects/armyrange/references/forecastconf_06/02_wrf.pdf, 2006.

Knupp, K. R., J. Walters, and E. W. McCaul, Doppler Profiler Observations of Hurricane Georges at landfall, *Geophysical Research Letters*, *27*(20), 3361–3364, doi:10.1029/1999GL011260, 2000.

Knupp, K. R., J. Walters, and M. Biggerstaff, Doppler Profiler and Radar Observations of Boundary Layer Variability during the Landfall of Tropical Storm Gabrielle, *Journal of the Atmospheric Sciences*, *63*(1), 234–251, doi:10.1175/JAS3608.1, 2006.

Kogan, Y. L., The Simulation of a Convective Cloud in a 3-D Model with Explicit Microphysics. Part I: Model Description and Sensitivity Experiments, *Journal of the Atmospheric Sciences*, *48*(9), 1160–1189, doi:10.1175/1520-0469(1991)048⟨1160:TSOACC⟩2.0.CO;2, 1991.

Kolmogorov, A., The Local Structure of Turbulence in Incompressible Viscous Fluid for Very Large Reynolds' Numbers, *Akademiia Nauk SSSR Doklady*, *30*, 301–305, 1941.

Kosiba, K., J. Wurman, F. J. Masters, and P. Robinson, Mapping of Near-Surface Winds in Hurricane Rita Using Finescale Radar, Anemometer, and Land-Use Data, *Monthly Weather Review*, *141*(12), 4337–4349, doi:10.1175/MWR-D-12-00350.1, 2013.

Krupar, R. J., Improving surface wind estimates in tropical cyclones using WSR-88D derived wind profiles, Ph.D. thesis, Texas Tech University, 2015.

Krupar, R. J., J. L. Schroeder, D. A. Smith, S.-L. Kang, and S. Lorsolo, A Comparison of ASOS Near-Surface Winds and WSR-88D-Derived Wind Speed Profiles Measured in Landfalling Tropical Cyclones, *Weather and Forecasting*, *31*(4), 1343–1361, doi:10.1175/WAF-D-15-0162.1, 2016.

Kurihara, Y., and R. E. Tuleya, Structure of a Tropical Cyclone Developed in a Three-Dimensional Numerical Simulation Model, *Journal of the Atmospheric Sciences*, *31*(4), 893–919, doi:10.1175/1520-0469(1974)031⟨0893:SOATCD⟩2.0.CO;2, 1974.

Lange, H., *Die Physik des Wetters und des Klimas: ein Grundkurs zur Theorie des Systems Atmosphäre*, Reimer, 2002.

Laprise, R., The Euler Equations of Motion with Hydrostatic Pressure as an Independent Variable, *Monthly Weather Review*, *120*(1), 197–207, doi:10.1175/1520-0493(1992)120⟨0197:TEEOMW⟩2.0.CO;2, 1992.

Li, Y., K. K. W. Cheung, and J. C. L. Chan, Numerical study on the development of asymmetric convection and vertical wind shear during tropical cyclone landfall, *Quarterly Journal of the Royal Meteorological Society*, *140*(683), 1866–1877, doi:10.1002/qj.2259, 2014.

Lin, N., J. A. Smith, G. Villarini, T. P. Marchok, and M. L. Baeck, Modeling Extreme Rainfall, Winds, and Surge from Hurricane Isabel (2003), *Weather and Forecasting*, *25*(5), 1342–1361, doi: 10.1175/2010WAF2222349.1, 2010.

Lin, Y.-L., R. D. Farley, and H. D. Orville, Bulk Parameterization of the Snow Field in a Cloud Model, *Journal of Climate and Applied Meteorology*, *22*(6), 1065–1092, doi:10.1175/1520-0450(1983) 022⟨1065:BPOTSF⟩2.0.CO;2, 1983.

Lin, Y.-L., J. Han, D. W. Hamilton, and C.-Y. Huang, Orographic Influence on a Drifting Cyclone, *Journal of the Atmospheric Sciences*, *56*(4), 534–562, doi:10.1175/1520-0469(1999)056⟨0534: OIOADC⟩2.0.CO;2, 1999.

Liu, C., M. W. Moncrieff, and W. W. Grabowski, Explicit and Parameterized Realizations of Convective Cloud Systems in TOGA COARE, *Monthly Weather Review*, *129*(7), 1689–1703, doi: 10.1175/1520-0493(2001)129⟨1689:EAPROC⟩2.0.CO;2, 2001.

Lorsolo, S., J. A. Zhang, F. M. Jr., and J. Gamache, Estimation and Mapping of Hurricane Turbulent Energy Using Airborne Doppler Measurements, *Monthly Weather Review*, *138*(9), 3656–3670, doi: 10.1175/2010MWR3183.1, 2010.

Mallik, M., M. Ahasan, and M. Chowdhury, Simulation of Track and Landfall of Tropical Cyclone Viyaru and Its Associated Storm Surges Using NWP Models, *American Journal of Marine Science*, *3*(1), 11–21, 2015.

Marks, F. D., and R. A. Houze, Airborne Doppler Radar Observations in Hurricane Debby, *Bulletin of the American Meteorological Society*, *65*(6), 569–582, doi:10.1175/1520-0477(1984)065⟨0569: ADROIH⟩2.0.CO;2, 1984.

Marks, F. D., and R. A. Houze, Inner Core Structure of Hurricane Alicia from Airborne Doppler Radar Observations, *Journal of the Atmospheric Sciences*, *44*(9), 1296–1317, doi:10.1175/ 1520-0469(1987)044⟨1296:ICSOHA⟩2.0.CO;2, 1987.

Mason, M., and D. Henderson, Deployment of the Surface Weather Information Relay and Logging Network (SWIRLnet) during Tropical Cyclone Ita (2014), *17th Australasian Wind Engineering Society Workshop*, 2015.

Masters, F. J., H. W. Tieleman, and J. A. Balderrama, Surface wind measurements in three gulf coast hurricanes of 2005, *Journal of Wind Engineering and Industrial Aerodynamics*, *98*(10–11), 533 – 547, doi:http://dx.doi.org/10.1016/j.jweia.2010.04.003, 2010.

McFarquhar, G. M., H. Zhang, G. Heymsfield, J. B. Halverson, R. Hood, J. Dudhia, and F. Marks, Factors Affecting the Evolution of Hurricane Erin (2001) and the Distributions of Hydrometeors: Role of Microphysical Processes, *Journal of the Atmospheric Sciences*, *63*(1), 127–150, doi:10. 1175/JAS3590.1, 2006.

Milbrandt, J. A., M. K. Yau, J. Mailhot, and S. Bélair, Simulation of an Orographic Precipitation Event during IMPROVE-2. Part I: Evaluation of the Control Run Using a Triple-Moment Bulk Microphysics Scheme, *Monthly Weather Review*, *136*(10), 3873–3893, doi:10.1175/2008MWR2197.1, 2008.

Miller, B. I., On the Filling of Tropical Cyclones over Land, *Tech. rep.*, NHRP Rep. No. 66, U.S. Dept. Commerce, 82 pp. [NOAA/NHRL, 1320 S. Dixie Hwy., Coral Gables, FL 33146], 1963.

Miller, B. I., A Study of the Filling of Hurricane Donna (1960) over Land, *Monthly Weather Review*, *92*(9), 389–406, doi:10.1175/1520-0493(1964)092⟨0389:ASOTFO⟩2.3.CO;2, 1964.

Miller, C., J.-A. Balderrama, and F. Masters, Aspects of observed gust factors in landfalling tropical cyclones: Gust components, terrain, and upstream fetch effects, *Boundary-Layer Meteorology*, *155*(1), 129–155, doi:10.1007/s10546-014-9989-0, 2015.

Miller, C. A., Revisiting the Durst gust factor curve, *Canadian Journal of Civil Engineering*, *38*(9), 998–1001, 2011.

Miyake, M., *Transformation of the Atmospheric Boundary Layer Over Inhomogeneous Surfaces*, Scientific report, Department of Atmospheric Sciences, University of Washington, 1965.

Miyakoda, K., and A. Rosati, One-way nested grid models: The interface conditions and the numerical accuracy, *Monthly Weather Review*, *105*(9), 1092–1107, 1977.

Montgomery, M. T., and R. K. Smith, Paradigms for tropical cyclone intensification, *Aust. Meteor. Oceanogr. J*, *64*, 1–30, 2014.

Montgomery, M. T., H. D. Snell, and Z. Yang, Axisymmetric Spindown Dynamics of Hurricane-like Vortices, *Journal of the Atmospheric Sciences*, *58*(5), 421–435, doi:10.1175/1520-0469(2001)058⟨0421:ASDOHL⟩2.0.CO;2, 2001.

Montgomery, M. T., M. M. Bell, S. D. Aberson, and M. L. Black, Hurricane Isabel (2003): New Insights into the Physics of Intense Storms. Part I: Mean Vortex Structure and Maximum Intensity Estimates, *Bulletin of the American Meteorological Society*, *87*(10), 1335–1347, doi: 10.1175/BAMS-87-10-1335, 2006.

Morrison, H., An overview of cloud and precipitation microphysics and its parameterization in models. , *Presentation at the WRF Workshop 2010*, NCAR/NESL/MMM, 2010.

Morrison, H., J. A. Curry, and V. I. Khvorostyanov, A New Double-Moment Microphysics Parameterization for Application in Cloud and Climate Models. Part I: Description, *Journal of the Atmospheric Sciences*, *62*(6), 1665–1677, doi:10.1175/JAS3446.1, 2005.

Myers, V. A., Surface friction in a Hurricane, *Monthly Weather Review*, *82*, 307–311, 1959.

NCEP, NCEP FNL Operational Model Global Tropospheric Analyses, continuing from July 1999, National Centers for Environmental Prediction, National Weather Service, NOAA, U.S. Department of Commerce: Research Data Archive at the National Center for Atmospheric Research, Computational and Information Systems Laboratory, Boulder, CO. [Available online at http://dx.doi.org/10.5065/D6M043C6.], 2000.

NCEP, NCEP GDAS/FNL 0.25 Degree Global Tropospheric Analyses and Forecast Grids, National Centers for Environmental Prediction/National Weather Service/NOAA/U.S. Department of Commerce (2015), NCEP GDAS/FNL 0.25 Degree Global Tropospheric Analyses and Forecast Grids, https://doi.org/10.5065/D65Q4T4Z, Research Data Archive at the National Center for Atmospheric Research, Computational and Information Systems Laboratory, Boulder, CO [Available online at http://dx.doi.org/10.5065/D65Q4T4Z.], 2015.

NOAA, C-CAP Regional Land Cover and Change, National Oceanic and Atmospheric Administration, Office for Coastal Management. "C-CAP Regional Land Cover and Change". Coastal Change Analysis Program (C-CAP) Regional Land Cover. Charleston, SC: NOAA Office for Coastal Management. [Accessed May 2018 at www.coast.noaa.gov/ccapftp.], 2010.

Nolan, D. S., J. A. Zhang, and D. P. Stern, Evaluation of Planetary Boundary Layer Parameterizations in Tropical Cyclones by Comparison of In Situ Observations and High-Resolution Simulations of Hurricane Isabel (2003). Part I: Initialization, Maximum Winds, and the Outer-Core Boundary Layer, *Monthly Weather Review*, *137*(11), 3651–3674, doi:10.1175/2009MWR2785.1, 2009.

Nolan, D. S., J. A. Zhang, and E. W. Uhlhorn, On the limits of estimating the maximum wind speeds in hurricanes, *Monthly Weather Review*, *142*(8), 2814–2837, doi:10.1175/MWR-D-13-00337.1, 2014.

Oke, T. R., *Boundary layer climates*, Routledge, 1978.

O'Lenic, E. A., Mesoscale interactions between a cold front and the planetary boundary layer, M.s. thesis, The Pennsylvania State University, 1976.

Oliger, J., and A. Sundström, Theoretical and practical aspects of some initial boundary value problems in fluid dynamics, *SIAM Journal on Applied Mathematics*, *35*(3), 419–446, 1978.

Ooyama, K. V., A dynamical model for the study of tropical cyclone development, *Geofis. Int.*, *4*, 187—-198, 1964.

Ooyama, K. V., Numerical Simulation of the Life Cycle of Tropical Cyclones, *Journal of the Atmospheric Sciences*, *26*(1), 3–40, doi:10.1175/1520-0469(1969)026⟨0003:NSOTLC⟩2.0.CO;2, 1969.

Ooyama, K. V., Theory on parameterization of cumulus convection, *Bulletin of the American Meteorological Society*, *52*(8), 783, 1971.

Ooyama, K. V., A Thermodynamic Foundation for Modeling the Moist Atmosphere, *Journal of the Atmospheric Sciences*, *47*(21), 2580–2593, doi:10.1175/1520-0469(1990)047⟨2580:ATFFMT⟩2.0.CO;2, 1990.

Osuri, K. K., U. Mohanty, A. Routray, M. A. Kulkarni, and M. Mohapatra, Customization of WRF-ARW model with physical parameterization schemes for the simulation of tropical cyclones over North Indian Ocean, *Natural Hazards*, *63*(3), 1337–1359, doi:10.1007/s11069-011-9862-0, 2012.

Otte, T. L., Using MMS Version 2 with Models-3/CMAQ, *Epa-600/r-99/065*, Office of Research and Development Washington, D.C. 20460, 1999.

Palmen, E., On the formation and structure of tropical hurricanes, *Geophysica*, *3*(1), 26–38, 1948.

Parker, C., A. Lynch, and M. Tsukernik, Evaluating WRF-ARW v3.4.1 Simulations of Tropical Cyclone Yasi, *WRF users workshop WS2013*, 2013.

Parker, M. D., and R. H. Johnson, Organizational Modes of Midlatitude Mesoscale Convective Systems, *Monthly Weather Review*, *128*(10), 3413–3436, doi:10.1175/1520-0493(2001)129⟨3413:OMOMMC⟩2.0.CO;2, 2000.

Paulsen, B., and J. Schroeder, An examination of tropical and extratropical gust factors and the associated wind speed histograms, *Journal of Applied Meteorology*, *44*(2), 270–280, 2005.

Phillips, N. A., and J. Shukla, On the strategy of combining coarse and fine grid meshes in numerical weather prediction, *Journal of Applied Meteorology*, *12*(5), 763–770, 1973.

Powell, M., G. Soukup, S. Cocke, S. Gulati, N. Morisseau-Leroy, S. Hamid, N. Dorst, and L. Axe, State of florida hurricane loss projection model: Atmospheric science component, *Journal of Wind Engineering and Industrial Aerodynamics*, *93*(8), 651 – 674, doi:https://doi.org/10.1016/j.jweia.2005.05.008, 2005.

Powell, M. D., The Transition of the Hurricane Frederic Boundary-Layer Wind Field from the Open Gulf of Mexico to Landfall, *Monthly Weather Review*, *110*(12), 1912–1932, doi:10.1175/1520-0493(1982)110⟨1912:TTOTHF⟩2.0.CO;2, 1982.

Powell, M. D., Changes in the Low-Level Kinematic and Thermodynamic Structure of Hurricane Alicia (1983) at Landfall, *Monthly Weather Review*, *115*(1), 75–99, doi:10.1175/1520-0493(1987)115⟨0075:CITLLK⟩2.0.CO;2, 1987.

Powell, M. D., Boundary Layer Structure and Dynamics in Outer Hurricane Rainbands. Part I: Mesoscale Rainfall and Kinematic Structure, *Monthly Weather Review*, *118*(4), 891–917, doi:10.1175/1520-0493(1990)118⟨0891:BLSADI⟩2.0.CO;2, 1990.

Powell, M. D., and S. H. Houston, Hurricane Andrew's Landfall in South Florida. Part II: Surface Wind Fields and Potential Real-Time Applications, *Weather and Forecasting*, *11*(3), 329–349, doi:10.1175/1520-0434(1996)011⟨0329:HALISF⟩2.0.CO;2, 1996.

Powell, M. D., P. P. Dodge, and M. L. Black, The Landfall of Hurricane Hugo in the Carolinas: Surface Wind Distribution, *Weather and Forecasting*, *6*(3), 379–399, doi:10.1175/1520-0434(1991)006⟨0379:TLOHHI⟩2.0.CO;2, 1991.

Powell, M. D., S. H. Houston, and T. A. Reinhold, Hurricane Andrew's Landfall in South Florida. Part I: Standardizing Measurements for Documentation of Surface Wind Fields, *Weather and Forecasting*, *11*(3), 304–328, doi:10.1175/1520-0434(1996)011⟨0304:HALISF⟩2.0.CO;2, 1996.

Powell, M. D., P. J. Vickery, and T. A. Reinhold, Reduced drag coefficient for high wind speeds in tropical cyclones, *Nature*, *422*, 279–283, article, 2003.

Raju, P., J. Potty, and U. Mohanty, Sensitivity of physical parameterizations on prediction of tropical cyclone Nargis over the Bay of Bengal using WRF model, *Meteorology and Atmospheric Physics*, *113*(3-4), 125–137, doi:10.1007/s00703-011-0151-y, 2011.

Ramsay, H. A., and L. M. Leslie, The Effects of Complex Terrain on Severe Landfalling Tropical Cyclone Larry (2006) over Northeast Australia, *Monthly Weather Review*, *136*(11), 4334–4354, doi:10.1175/2008MWR2429.1, 2008.

R.M. Young, *Wind Monitor-MA Model 05106 User Manual*, R.M. Young Company, available at http://www.youngusa.com/Manuals/05106-90(K).pdf, 2000.

Črnivec, N., and R. K. Smith, Mean radiosonde soundings for the Australian monsoon/cyclone season, *International Journal of Climatology*, *37*(1), 66–78, doi:10.1002/joc.4687, 2017.

Rotunno, R., and K. A. Emanuel, An Air–Sea Interaction Theory for Tropical Cyclones. Part II: Evolutionary Study Using a Nonhydrostatic Axisymmetric Numerical Model, *Journal of the Atmospheric Sciences*, *44*(3), 542–561, doi:10.1175/1520-0469(1987)044⟨0542:AAITFT⟩2.0.CO;2, 1987.

Schneider, R., and G. M. Barnes, Low-Level Kinematic, Thermodynamic, and Reflectivity Fields Associated with Hurricane Bonnie (1998) at Landfall, *Monthly Weather Review*, *133*(11), 3243–3259, doi:10.1175/MWR3027.1, 2005.

Schroeder, J. L., and D. A. Smith, Hurricane Bonnie wind flow characteristics as determined from WEMITE, *Journal of Wind Engineering and Industrial Aerodynamics*, *91*(6), 767 – 789, doi:http://dx.doi.org/10.1016/S0167-6105(02)00475-0, 2003.

Schroeder, J. L., D. A. Smith, and R. E. Peterson, Variation of turbulence intensities and integral scales during the passage of a hurricane, *Journal of Wind Engineering and Industrial Aerodynamics*, *77–78*, 65 – 72, doi:http://dx.doi.org/10.1016/S0167-6105(98)00132-9, 1998.

Schroeder, J. L., M. Conder, and J. Howard, Additional insights into hurricane gust factors, in *Proc. 25 th Conf. Hurricane and Tropical Meteorology, AMS, San Diego*, 2002.

Schroeder, J. L., B. P. Edwards, and I. M. Giammanco, Observed tropical cyclone wind flow characteristics, *Wind and Structures*, *12*(4), 349–381, 2009.

Schwendike, J., and J. D. Kepert, The Boundary Layer Winds in Hurricanes Danielle (1998) and Isabel (2003), *Monthly Weather Review*, *136*(8), 3168–3192, doi:10.1175/2007MWR2296.1, 2008.

Sempreviva, A. M., S. E. Larsen, N. G. Mortensen, and I. Troen, Response of neutral boundary layers to changes of roughness, *Boundary-Layer Meteorology*, *50*(1), 205–225, doi:10.1007/BF00120525, 1990.

Siegel, S., and N. J. Castellan, *Nonparametric statistics for the behavioral sciences*, 2nd ed ed., New York: McGraw-Hill, 1988.

Simiu, E., and R. H. Scanlan, *Wind effects on structures: An introduction to wind engineering*, 2nd ed ed., New York : Wiley, ”A Wiley-Interscience publication.”, 1986.

Sitkowski, M., and G. M. Barnes, Low-Level Thermodynamic, Kinematic, and Reflectivity Fields of Hurricane Guillermo (1997) during Rapid Intensification, *Monthly Weather Review*, *137*(2), 645–663, doi:10.1175/2008MWR2531.1, 2009.

Skamarock, W. C., J. B. Klemp, J. Dudhia, D. O. Gill, D. M. Barker, W. Wang, and J. G. Powers, A description of the advanced research WRF version 2, *Tech. rep.*, NCAR Tech Note, NCAR-/TN–468+STR, 88 pp. [Available from UCAR Communications, P.O. Box 3000, Boulder, CO, 80307]. Available online at http://box.mmm.ucar.edu/wrf/users/docs/arw_v2.pdf), 2005.

Skamarock, W. C., J. B. Klemp, J. Dudhia, D. O. Gill, D. M. Barker, M. Duda, X.-Y. Huang, J. G. Powers, and W. Wang, A description of the advanced research WRF version 3, *Tech. rep.*, NCAR Technical Note NCAR/TN-475+STR, DOI: 10.5065/D68S4MV, 2008.

Smith, R. K., and M. T. Montgomery, Hurricane boundary-layer theory, *Quarterly Journal of the Royal Meteorological Society*, *136*(652), 1665–1670, doi:10.1002/qj.679, 2010.

Smith, R. K., and M. T. Montgomery, Toward Clarity on Understanding Tropical Cyclone Intensification, *Journal of the Atmospheric Sciences*, *72*(8), 3020–3031, doi:10.1175/JAS-D-15-0017.1, 2015.

Snaiki, R., and T. Wu, A semi-empirical model for mean wind velocity profile of landfalling hurricane boundary layers, *Journal of Wind Engineering and Industrial Aerodynamics*, *180*, 249 – 261, doi: https://doi.org/10.1016/j.jweia.2018.08.004, 2018.

Sobel, J. P., Nested Grids in Numerical Weather Prediction and AN Application to a Mesoscale Jet Streak, Ph.d. thesis, The Pennsylvania State University, 1976.

Song, L., W. Chen, B. Wang, S. Zhi, and A. Liu, Characteristics of wind profiles in the landfalling typhoon boundary layer, *Journal of Wind Engineering and Industrial Aerodynamics*, *149*, 77 – 88, doi:http://dx.doi.org/10.1016/j.jweia.2015.11.008, 2016.

Stensrud, D. J., An Overview of Convection Parameterization, *Presentation at the WRF Workshop 2012*, NOAA/National Severe Storms Laboratory, 2012.

Stull, R. B., *An Introduction to Boundary Layer Meteorology*, Kluwer Academic Publishers, The Netherlands, 1988.

Sumner, H. C., North Atlantic Hurricanes and Tropical Disturbances 1943, *Monthly Weather Review*, *71*(11), 179–183, doi:10.1175/1520-0493(1943)71⟨179:NAHATD⟩2.0.CO;2, 1943.

Syono, S., On the Formation of Tropical Cyclones, *Tellus*, *5*(2), 179–195, doi:10.1111/j.2153-3490.1953.tb01047.x, 1953.

Szyrmer, W., S. Laroche, and I. Zawadzki, A Microphysical Bulk Formulation Based on Scaling Normalization of the Particle Size Distribution. Part I: Description, *Journal of the Atmospheric Sciences*, *62*(12), 4206–4221, doi:10.1175/JAS3620.1, 2005.

Taylor, G. I., The spectrum of turbulence, *Proceedings of the Royal Society of London: A Mathematical, Physical and Engineering Sciences*, *164*(919), 476–490, doi:10.1098/rspa.1938.0032, 1938.

Trier, S. B., M. A. LeMone, F. Chen, and K. W. Manning, Effects of Surface Heat and Moisture Exchange on ARW-WRF Warm-Season Precipitation Forecasts over the Central United States, *Weather and Forecasting*, *26*(1), 3–25, doi:10.1175/2010WAF2222426.1, 2011.

Troen, I., N. Mortensen, and E. Petersen, WASP Wind Analysis and Application Programme (User's Guide), Rise Nation, *Lab., Denmark*, 1987.

Tuleya, R. E., and Y. Kurihara, A numerical simulation of the landfall of tropical cyclones, *Journal of the Atmospheric Sciences*, *35*(2), 242–257, doi:10.1175/1520-0469(1978)035⟨0242:ANSOTL⟩2.0.CO;2, 1978.

Tuleya, R. E., M. A. Bender, and Y. Kurihara, A Simulation Study of the Landfall of Tropical Cyclones, *Monthly Weather Review*, *112*(1), 124–136, doi:10.1175/1520-0493(1984)112⟨0124:ASSOTL⟩2.0.CO;2, 1984.

Vickery, P. J., D. Wadhera, M. D. Powell, and Y. Chen, A Hurricane Boundary Layer and Wind Field Model for Use in Engineering Applications, *Journal of Applied Meteorology and Climatology*, *48*(2), 381–405, doi:10.1175/2008JAMC1841.1, 2009.

Wang, W., C. Bruyère, M. Duda, J. Dudhia, D. Gill, M. Kavulich, K. Keene, H.-C. Lin, J. Michalakes, S. Rizvi, X. Zhang, J. Berner, K. Fossell, J. D. Beezley, J. L. Coen, J. Mandel, H.-Y. Chuang, N. McKee, T. Slovacek, and J. Wolff, ARW Version 3 Modeling System User's Guide July 2015, *Tech. rep*, Mesoscale and Microscale Meteorology Division / National Center for Atmospheric Research, 2015.

Warner, T. T., R. A. Anthes, and A. L. McNab, Numerical Simulations with a Three-Dimensional Mesoscale Model, *Monthly Weather Review*, *106*(8), 1079–1099, doi:10.1175/1520-0493(1978)106⟨1079:NSWATD⟩2.0.CO;2, 1978.

Weiss, C. C., and J. L. Schroeder, StickNet - A new portable, rapidly-deployable, surface observation system, *Bulletin of the American Meteorological Society*, *89*(10), 1502–1503, 2008.

Wieringa, J., An objective exposure correction method for average wind speeds measured at a sheltered location, *Quarterly Journal of the Royal Meteorological Society*, *102*(431), 241–253, doi: 10.1002/qj.49710243119, 1976.

Wieringa, J., Description requirements for assessment of non-ideal wind stations — for example aachen., *Journal of Wind Engineering and Industrial Aerodynamics*, *11*(1), 121 – 131, doi:https://doi.org/10.1016/0167-6105(83)90094-6, 1983.

Wieringa, J., Updating the davenport roughness classification, *Journal of Wind Engineering and Industrial Aerodynamics*, *41*(1), 357 – 368, doi:https://doi.org/10.1016/0167-6105(92)90434-C, 1992.

Wieringa, J., Representative roughness parameters for homogeneous terrain, *Boundary-Layer Meteorology*, *63*(4), 323–363, doi:10.1007/BF00705357, 1993.

Wilks, D., *Statistical Methods in the Atmospheric Sciences 2nd Edition*, Elsevier Academic Press, 2005.

Willoughby, H. E., F. D. Marks, and R. J. Feinberg, Stationary and Moving Convective Bands in Hurricanes, *Journal of the Atmospheric Sciences*, *41*(22), 3189–3211, doi:10.1175/1520-0469(1984)041⟨3189:SAMCBI⟩2.0.CO;2, 1984.

Wong, M. L. M., and J. C. L. Chan, Tropical cyclone motion in response to land surface friction, *Journal of the Atmospheric Sciences*, *63*(4), 1324–1337, doi:10.1175/JAS3683.1, 2006.

Wong, M. L. M., and J. C. L. Chan, Modeling the Effects of Land–Sea Roughness Contrast on Tropical Cyclone Winds, *Journal of the Atmospheric Sciences*, *64*(9), 3249–3264, doi:10.1175/JAS4027.1, 2007.

Wood, C., A simplified calculation method for gust factors, *Journal of Wind Engineering and Industrial Aerodynamics*, *12*(3), 385 – 387, doi:https://doi.org/10.1016/0167-6105(83)90060-0, 1983.

Wu, C.-C., and A. N. Chiu, Comparison of some ambient and typhoon instantaneous wind speed characteristics, *Journal of Wind Engineering and Industrial Aerodynamics*, *13*(1), 43 – 53, doi: http://dx.doi.org/10.1016/0167-6105(83)90127-7, 1983.

Wu, C.-C., T.-H. Li, and Y.-H. Huang, Influence of Mesoscale Topography on Tropical Cyclone Tracks: Further Examination of the Channeling Effect, *Journal of the Atmospheric Sciences*, *72*(8), 3032–3050, doi:10.1175/JAS-D-14-0168.1, 2015.

Yu, B., and A. Gan Chowdhury, Gust factors and turbulence intensities for the tropical cyclone environment, *Journal of applied Meteorology and Climatology*, *48*(3), 534–552, 2009.

Yu, B., A. G. Chowdhury, and F. J. Masters, Hurricane wind power spectra, cospectra, and integral length scales, *Boundary-layer meteorology*, *129*(3), 411–430, 2008.

Zhang, D.-L., Y. Liu, and M. K. Yau, Surface Winds at Landfall of Hurricane Andrew (1992) — A Reply, *Monthly Weather Review*, *127*(7), 1711–1721, doi:10.1175/1520-0493(1999)127⟨1711:SWALOH⟩2.0.CO;2, 1999.

Zhang, J. A., W. M. Drennan, P. G. Black, and J. R. French, Turbulence Structure of the Hurricane Boundary Layer between the Outer Rainbands, *Journal of the Atmospheric Sciences*, *66*(8), 2455–2467, doi:10.1175/2009JAS2954.1, 2009.

Zhang, J. A., R. F. Rogers, D. S. Nolan, and F. D. M. Jr., On the Characteristic Height Scales of the Hurricane Boundary Layer, *Monthly Weather Review*, *139*(8), 2523–2535, doi:10.1175/MWR-D-10-05017.1, 2011.

Zhu, P., Simulation and parameterization of the turbulent transport in the hurricane boundary layer by large eddies, *Journal of Geophysical Research: Atmospheres*, *113*(D17), doi:10.1029/2007JD009643, d17104, 2008.

Appendices

Appendix A

Turbulence Statistics Plots

Figures A.1 and A.2 show the along- and across-wind components for I_u and I_v, G_{u3} and G_{v3}, g_{u3} and g_{v3}, γ_{su} and γ_{sv}, γ_{ku} and γ_{kv}, and L_u and L_v, at 3.2 m elevation for towers deployed in open land.
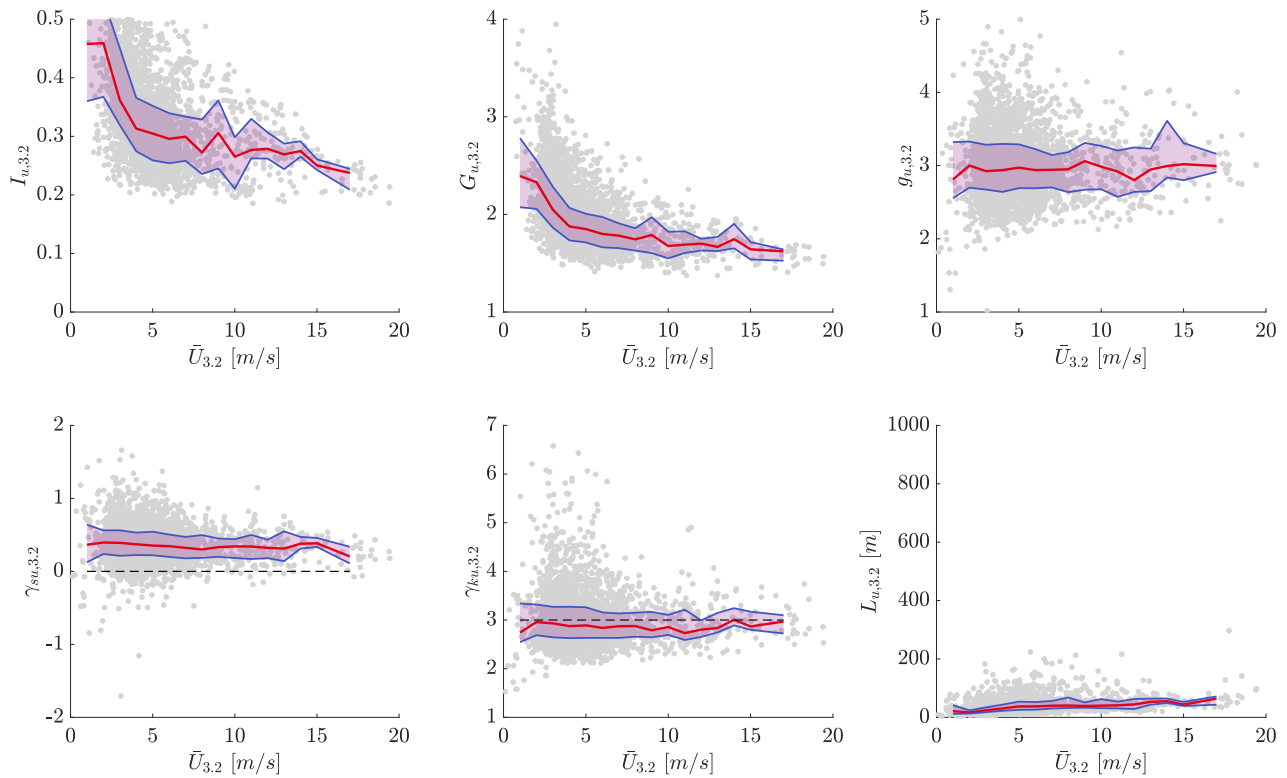
Figure A.1: Along-wind component of turbulent characteristics in open land at 3.2 m measurement height. Grey scattering reflects 10-minute turbulent means, 1 m/s binned median and area between 25th and 75th percentile are represented by the red solid line and the shaded region, respectively.
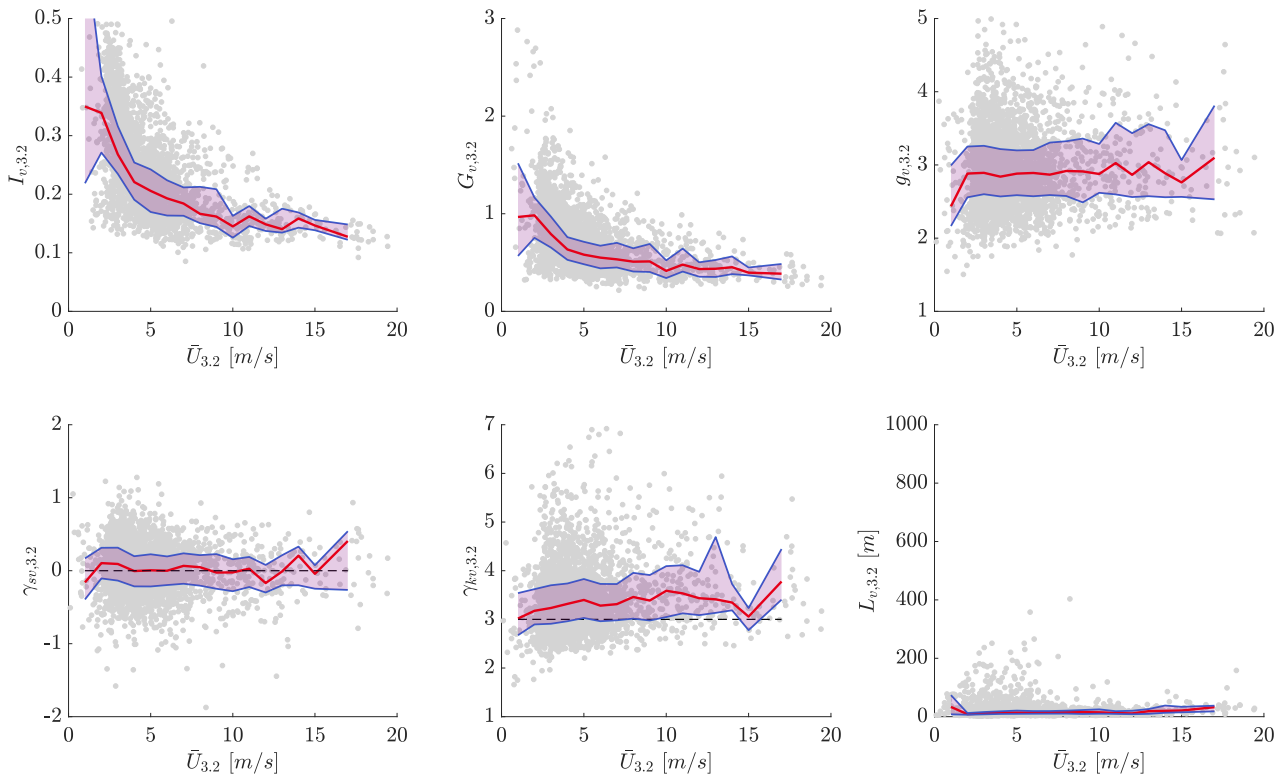
Figure A.2: Across-wind component of turbulent characteristics in open land at 3.2 m measurement height. Grey scattering reflects 10-minute turbulent means, 1 m/s binned median and area between 25th and 75th percentile are represented by the red solid line and the shaded region, respectively.

Figures A.3-A.6 show the along- and across-wind components for I_u and I_v, G_{u3} and G_{v3}, g_{u3} and g_{v3}, γ_{su} and γ_{sv}, γ_{ku} and γ_{kv}, and L_u and L_v, at 5 m elevation for towers deployed in open land and roughly open.
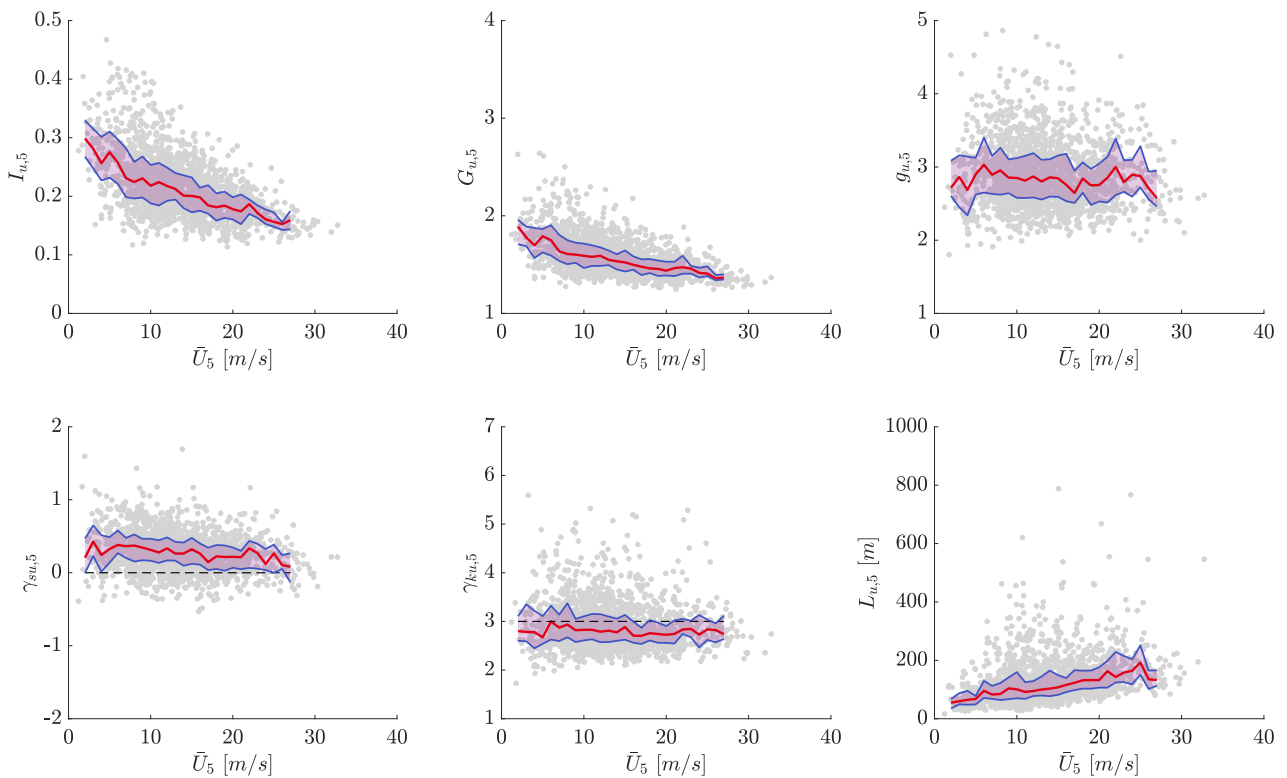
Figure A.3: Along-wind component of turbulent characteristics in open land at 5 m measurement height. Grey scattering reflects 10-minute turbulent means, 1 m/s binned median and area between 25th and 75th percentile are represented by the red solid line and the shaded region, respectively.
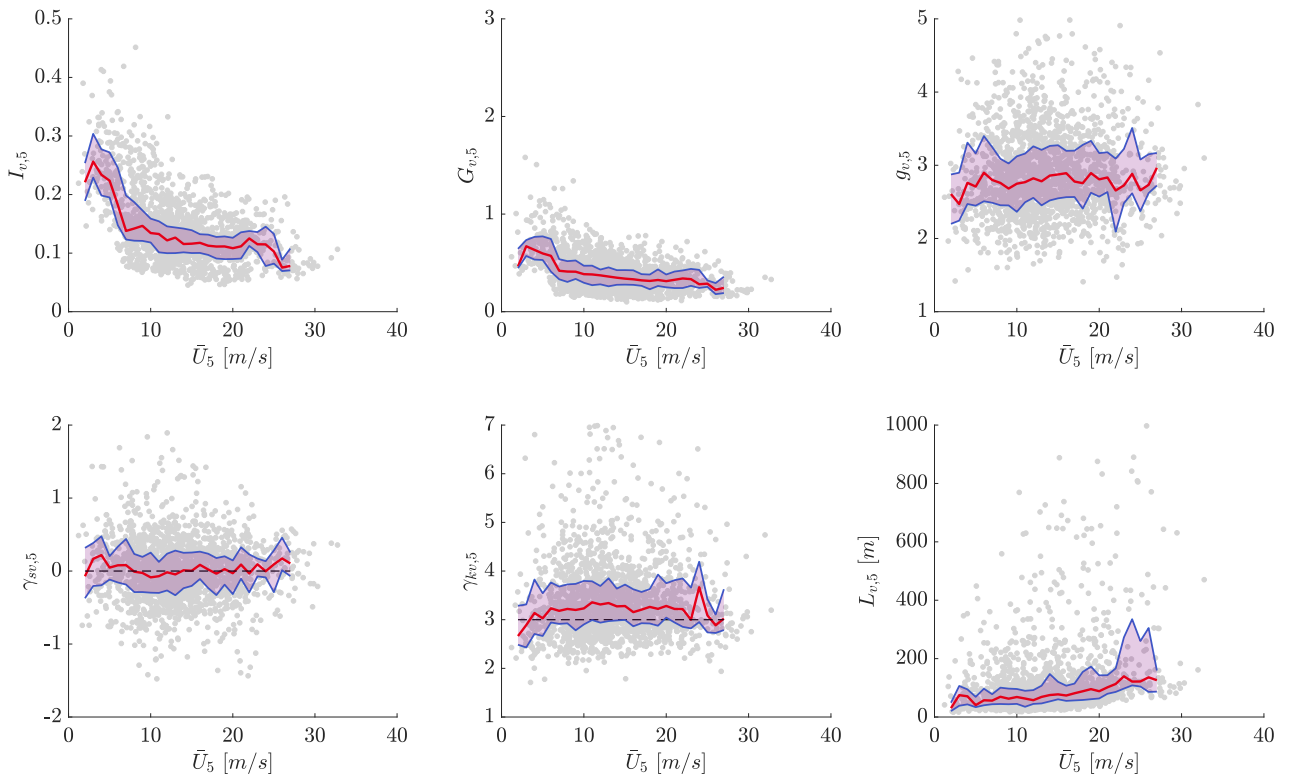
Figure A.4: Across-wind component of turbulent characteristics in open land at 5 m measurement height. Grey scattering reflects 10-minute turbulent means, 1 m/s binned median and area between 25th and 75th percentile are represented by the red solid line and the shaded region, respectively.
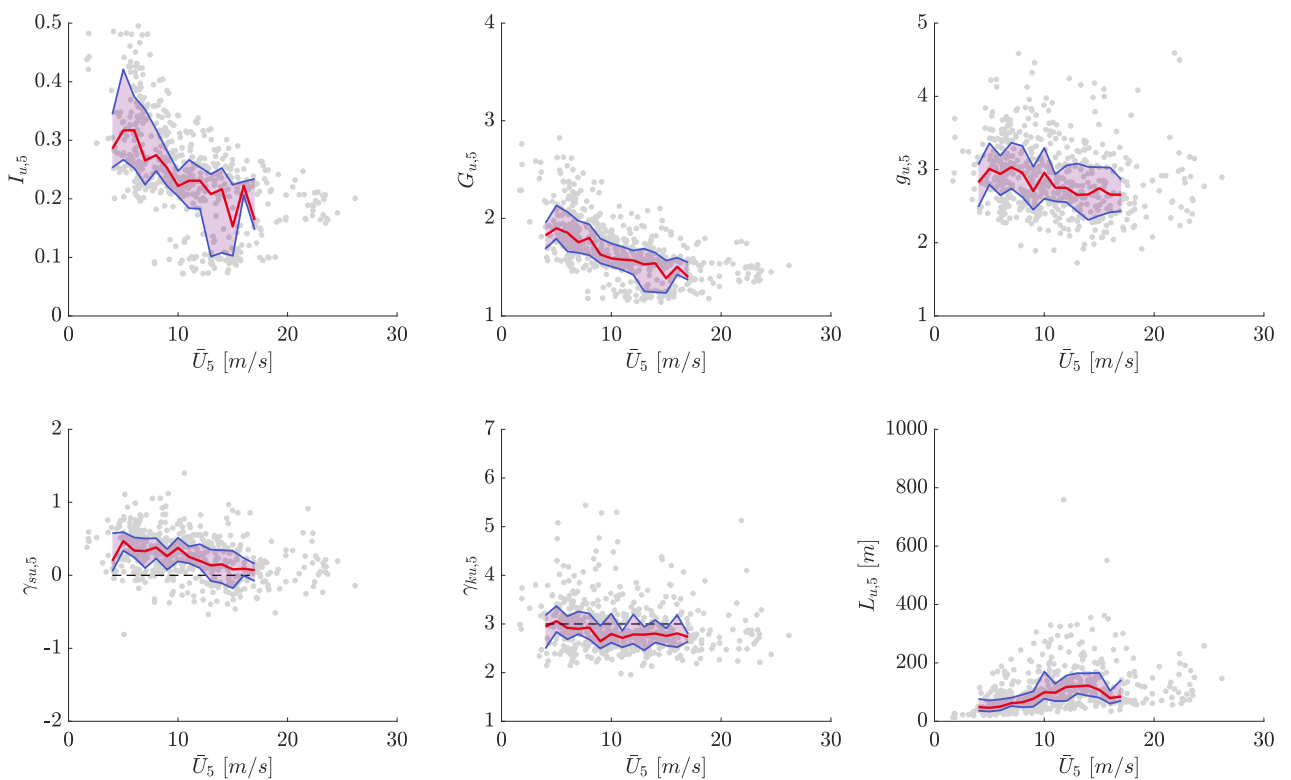
Figure A.5: Along-wind component of turbulent characteristics in roughly open at 5 m measurement height. Grey scattering reflects 10-minute turbulent means, 1 m/s binned median and area between 25th and 75th percentile are represented by the red solid line and the shaded region, respectively.
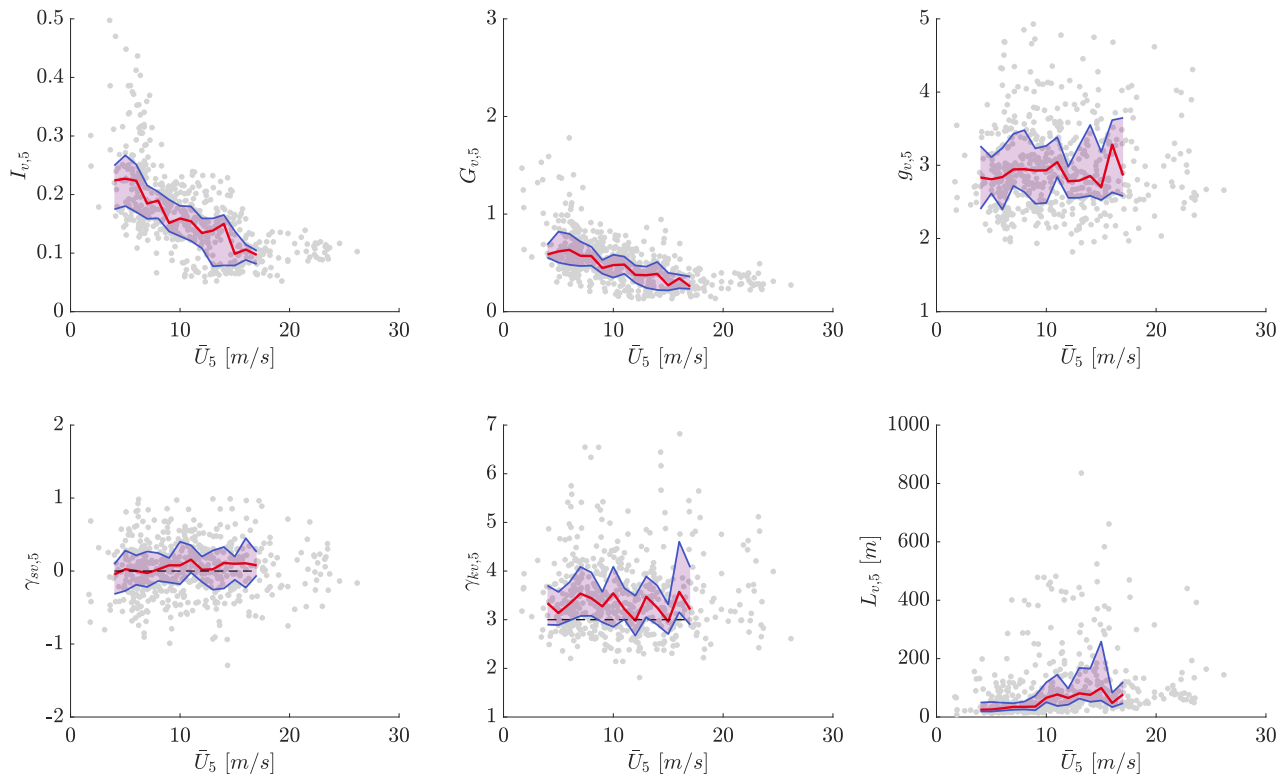
Figure A.6: Across-wind component of turbulent characteristics in roughly open at 5 m measurement height. Grey scattering reflects 10-minute turbulent means, 1 m/s binned median and area between 25th and 75th percentile are represented by the red solid line and the shaded region, respectively.

Figures A.7-A.10 show the along- and across-wind components for I_u and I_v, G_{u3} and G_{v3}, g_{u3} and g_{v3}, γ_{su} and γ_{sv}, γ_{ku} and γ_{kv}, and L_u and L_v, at 10 m elevation for towers deployed in open land and roughly open.
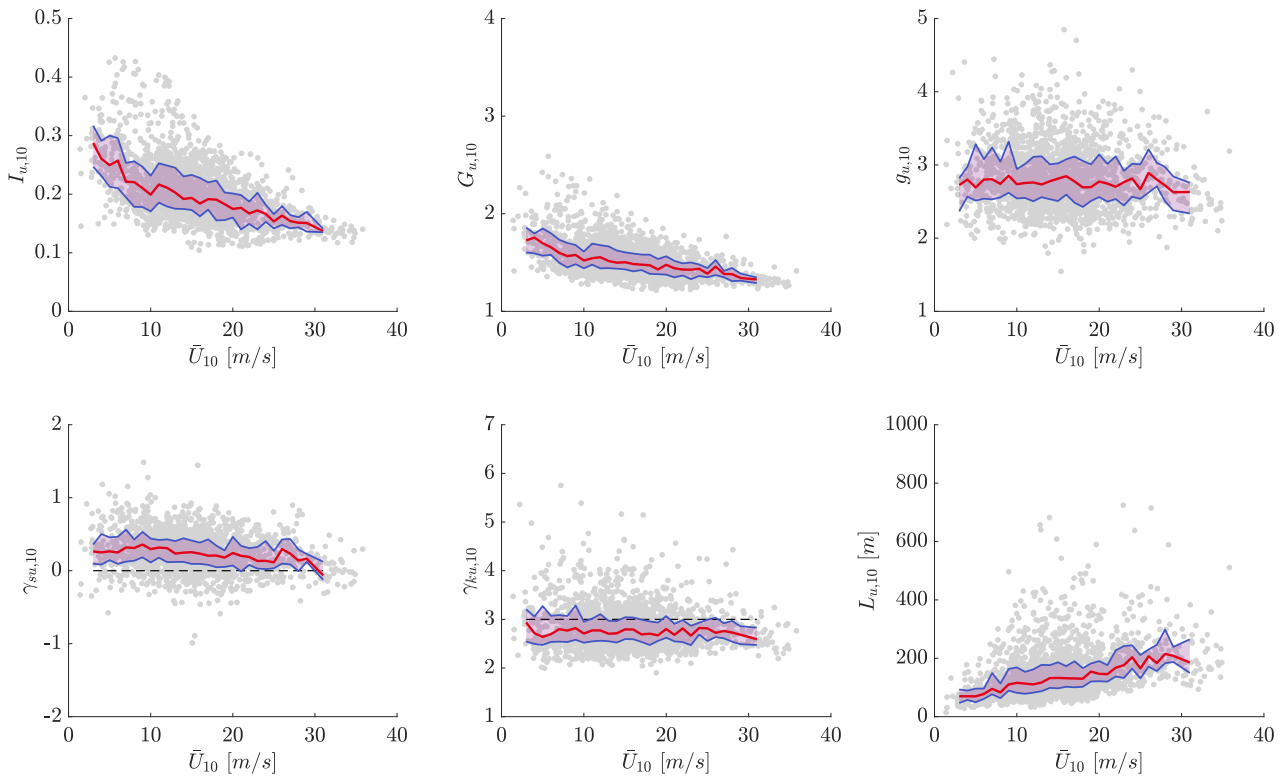
Figure A.7: Along-wind component of turbulent characteristics in open land at 10 m measurement height. Grey scattering reflects 10-minute turbulent means, 1 m/s binned median and area between 25th and 75th percentile are represented by the red solid line and the shaded region, respectively.
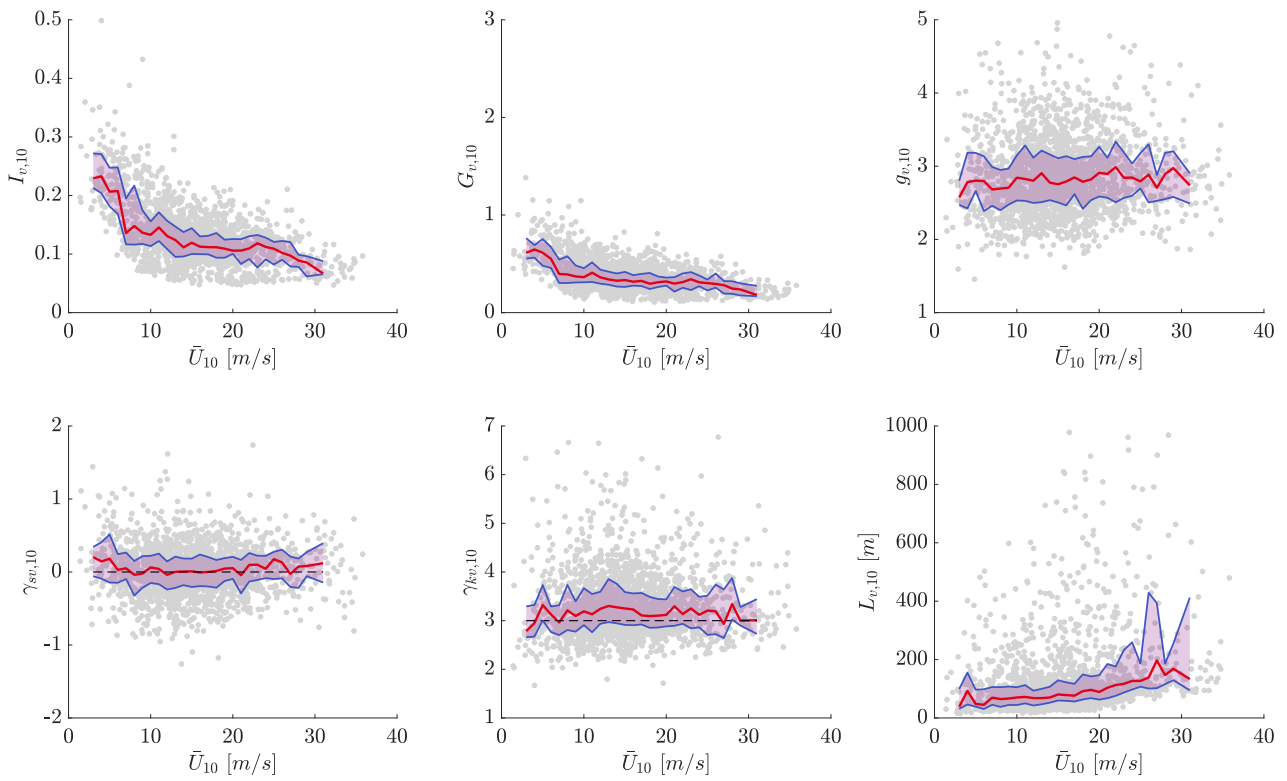
Figure A.8: Across-wind component of turbulent characteristics in open land at 10 m measurement height. Grey scattering reflects 10-minute turbulent means, 1 m/s binned median and area between 25th and 75th percentile are represented by the red solid line and the shaded region, respectively.
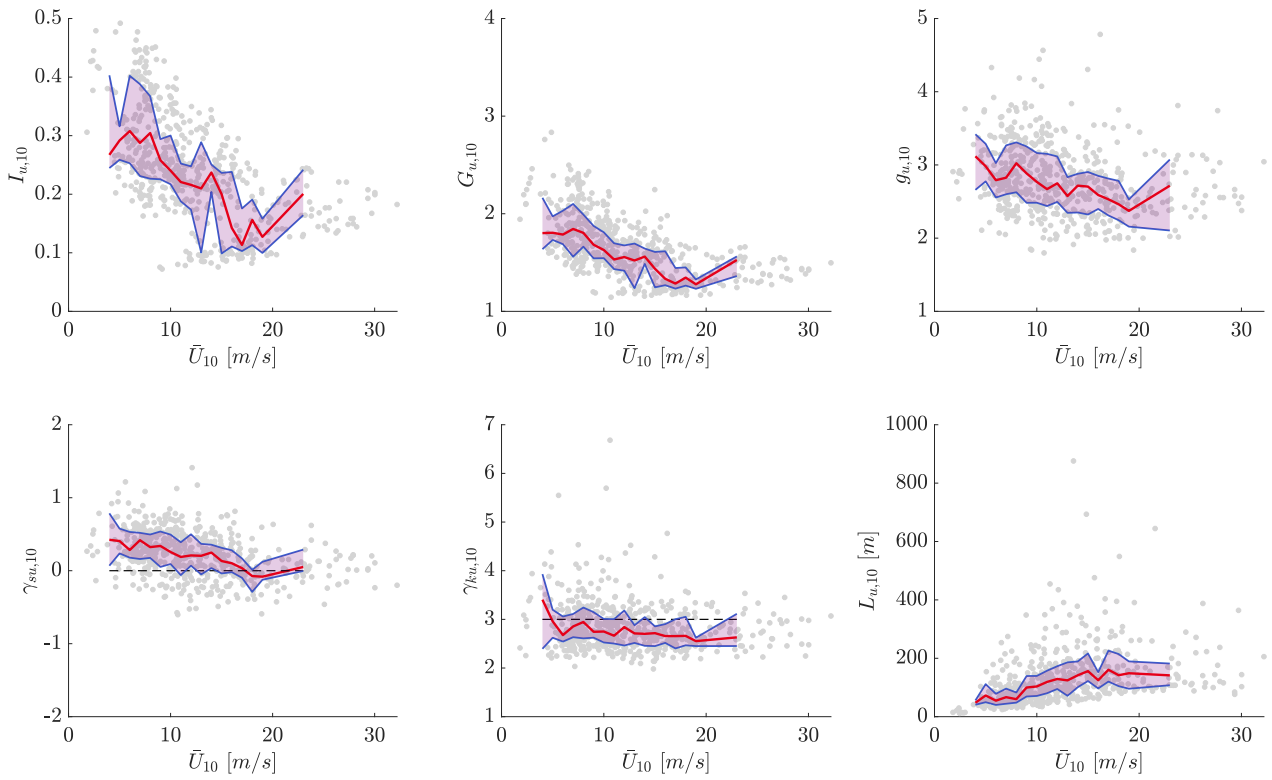
Figure A.9: Along-wind component of turbulent characteristics in roughly open at 5 m measurement height. Grey scattering reflects 10-minute turbulent means, 1 m/s binned median and area between 25th and 75th percentile are represented by the red solid line and the shaded region, respectively.
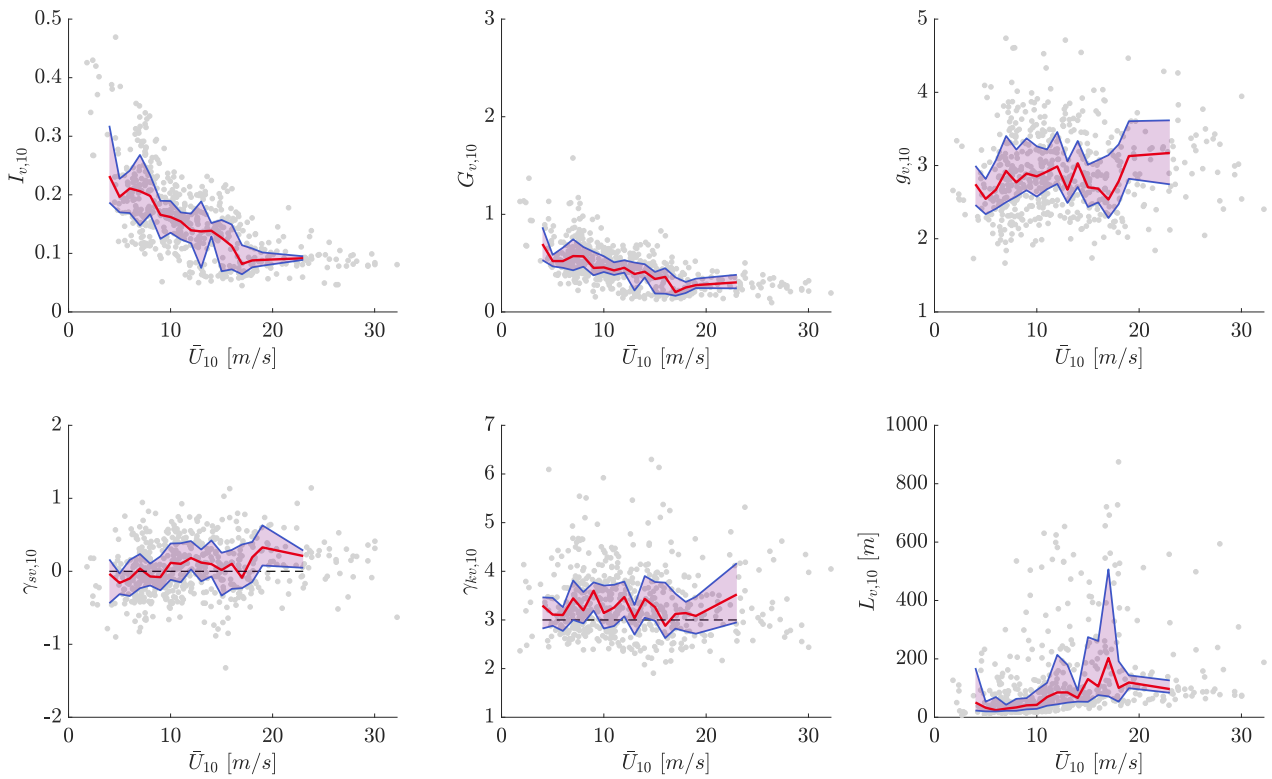
Figure A.10: Across-wind component of turbulent characteristics in roughly open at 5 m measurement height. Grey scattering reflects 10-minute turbulent means, 1 m/s binned median and area between 25th and 75th percentile are represented by the red solid line and the shaded region, respectively.

Figures A.11-A.15 show the variation of turbulence statistics with increasing $\bar{U}$ at all elevations and

terrain exposures.
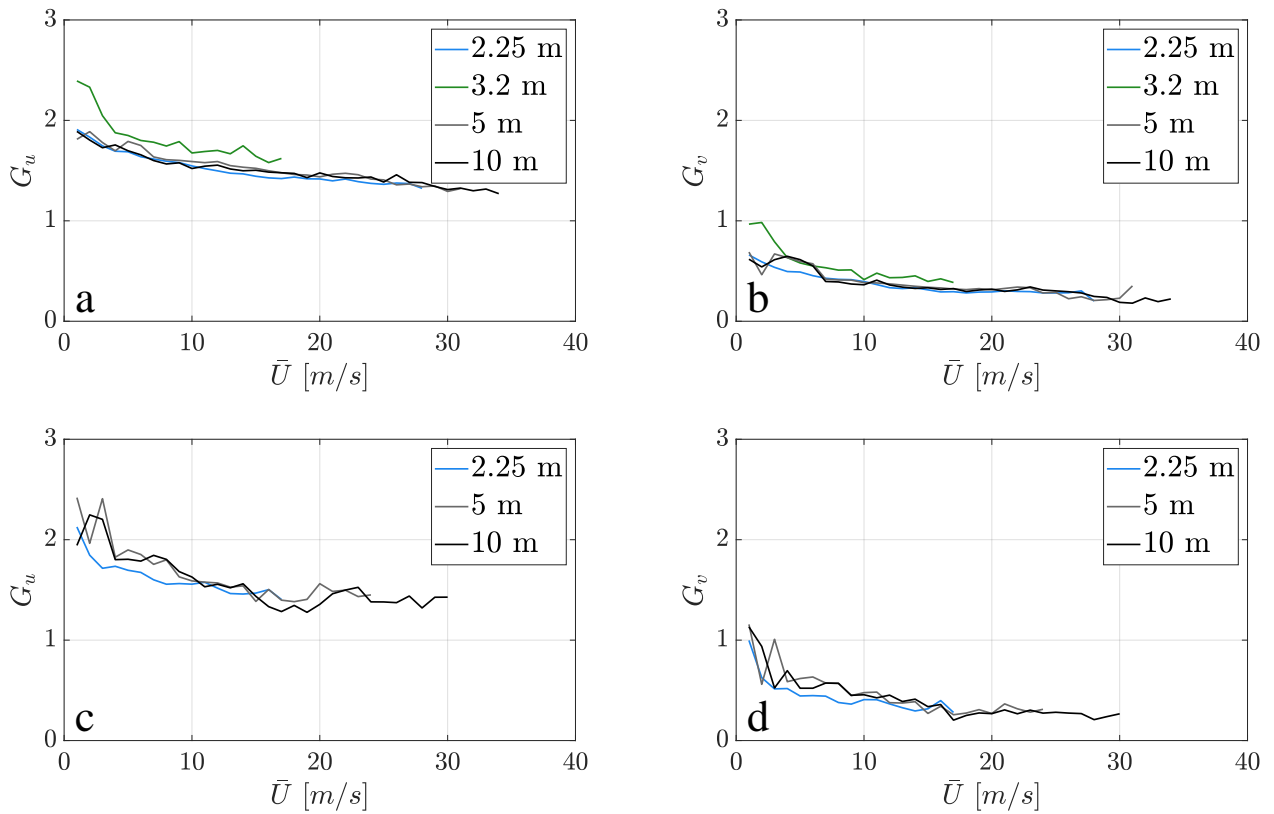
Figure A.11: Variation of a) G_u and b) G_v medians in open land, and c) G_u and d) G_v medians in roughly open terrain at elevations of 2.25 m, 3.2 m, 5 m, and 10 m.
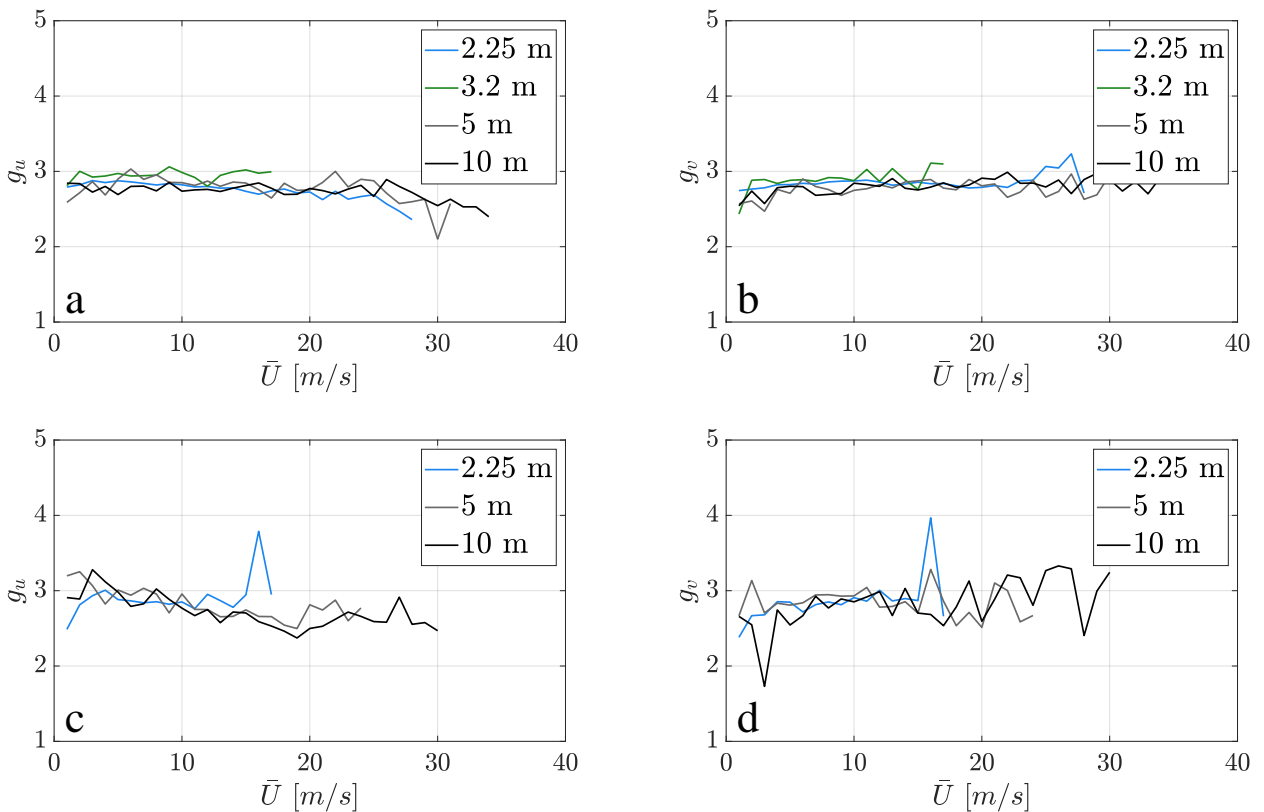
Figure A.12: Variation of a) g_u and b) g_v medians in open land, and c) g_u and d) g_v medians in roughly open terrain at elevations of 2.25 m, 3.2 m, 5 m, and 10 m.
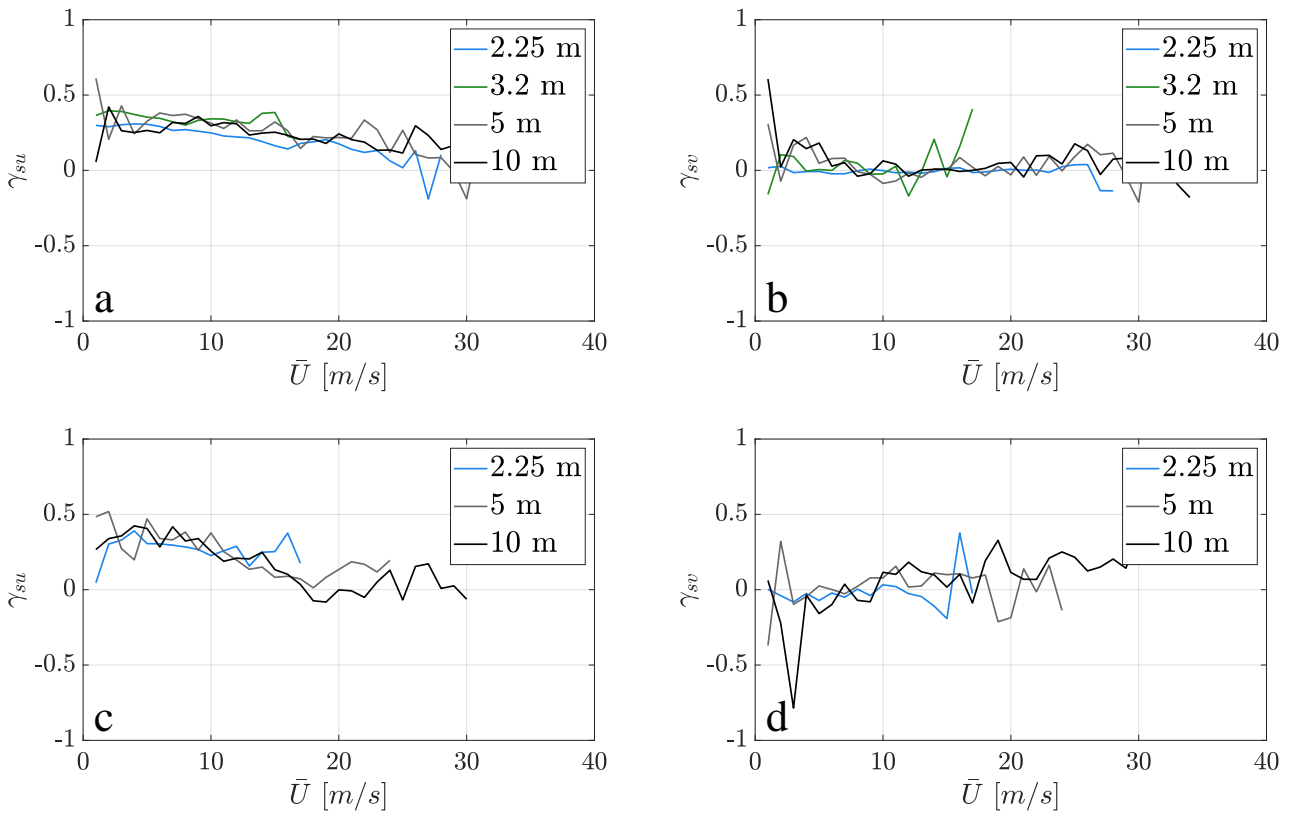
Figure A.13: Variation of a) γ_{su} and b) γ_{sv} medians in open land, and c) γ_{su} and d) γ_{sv} medians in roughly open terrain at elevations of 2.25 m, 3.2 m, 5 m, and 10 m.
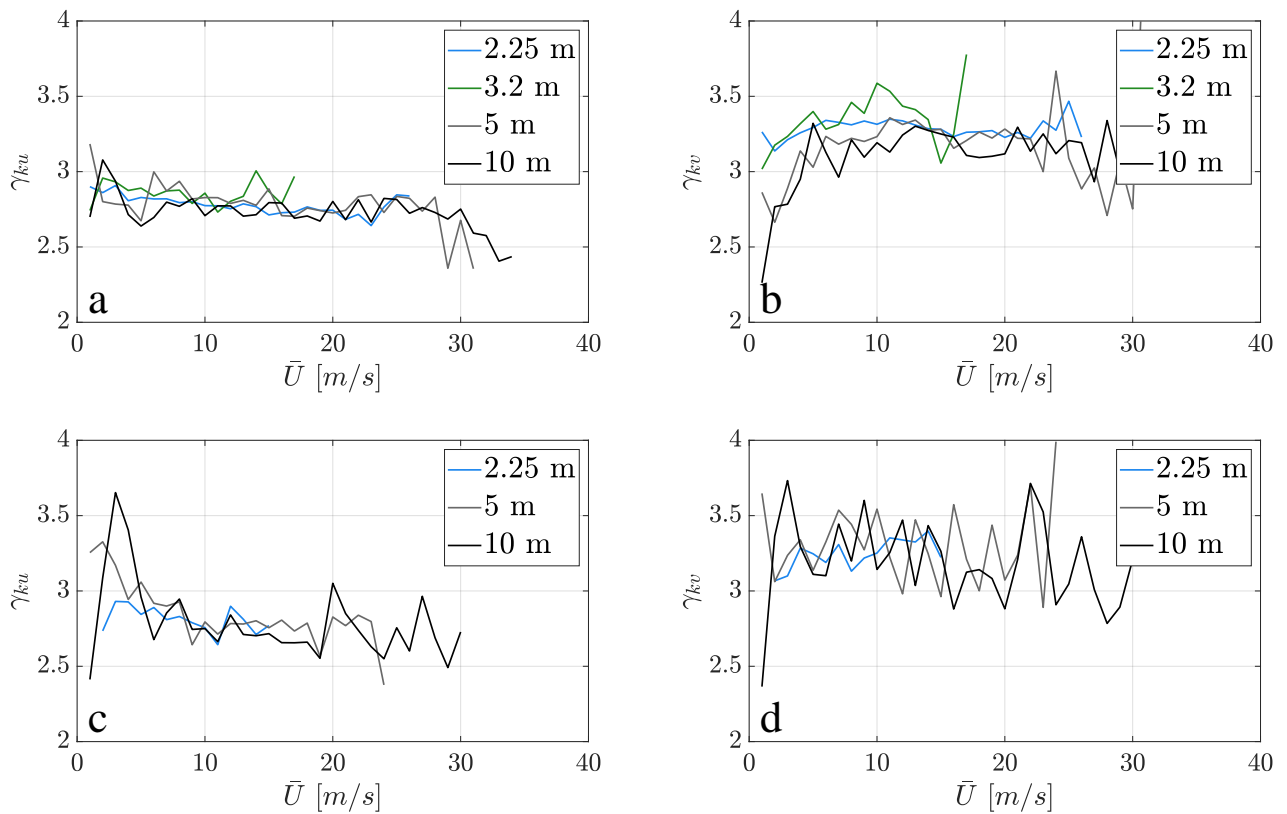
Figure A.14: Variation of a) γ_{ku} and b) γ_{kv} medians in open land, and c) γ_{ku} and d) γ_{kv} medians in roughly open terrain at elevations of 2.25 m, 3.2 m, 5 m, and 10 m.
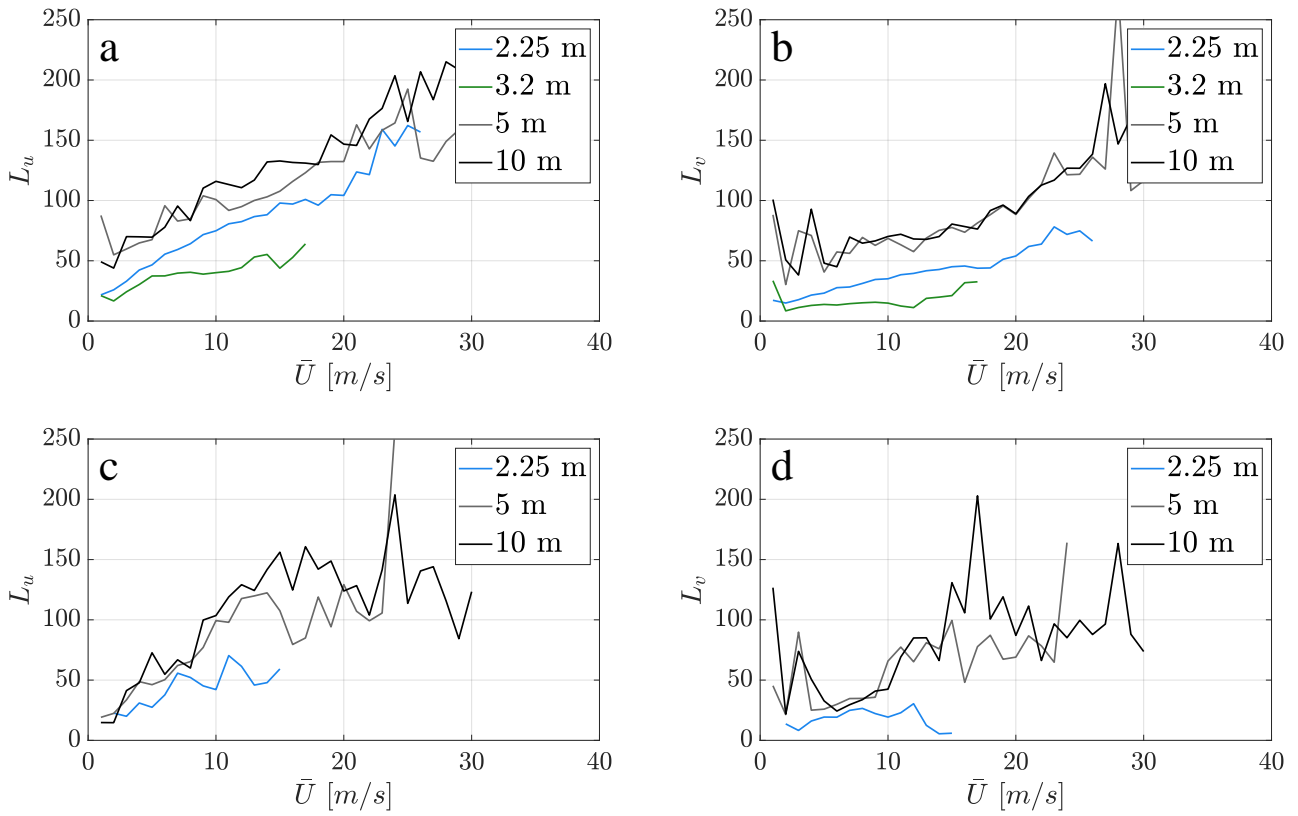
Figure A.15: Variation of a) L_u and b) L_v medians in open land, and c) L_u and d) L_v medians in roughly open terrain at elevations of 2.25 m, 3.2 m, 5 m, and 10 m.

Figures A.16-A.20 shows the variation of turbulent statistics with $\bar{U}$. The 25th to 75th percentile range at 5 m and 10 m height including all open land and roughly open towers with smooth-to-rough (blue-shaded area) and rough-to-smooth (black-shaded area) transitions is shown for wind speeds ≥ 5 m/s, where $x_1 > 200$ m.
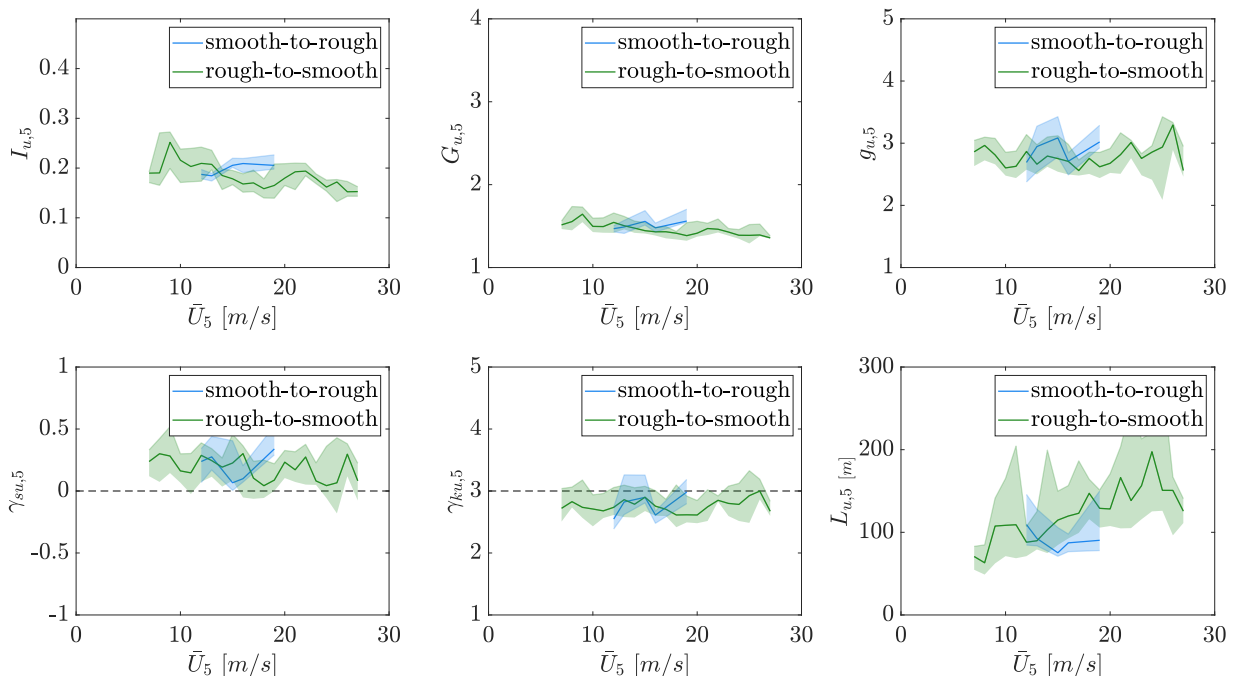
Figure A.16: Smooth-to-rough (blue-shaded area) and rough-to-smooth (green-shaded area) transitions of along-wind turbulence statistics in open land at 5 m.

208
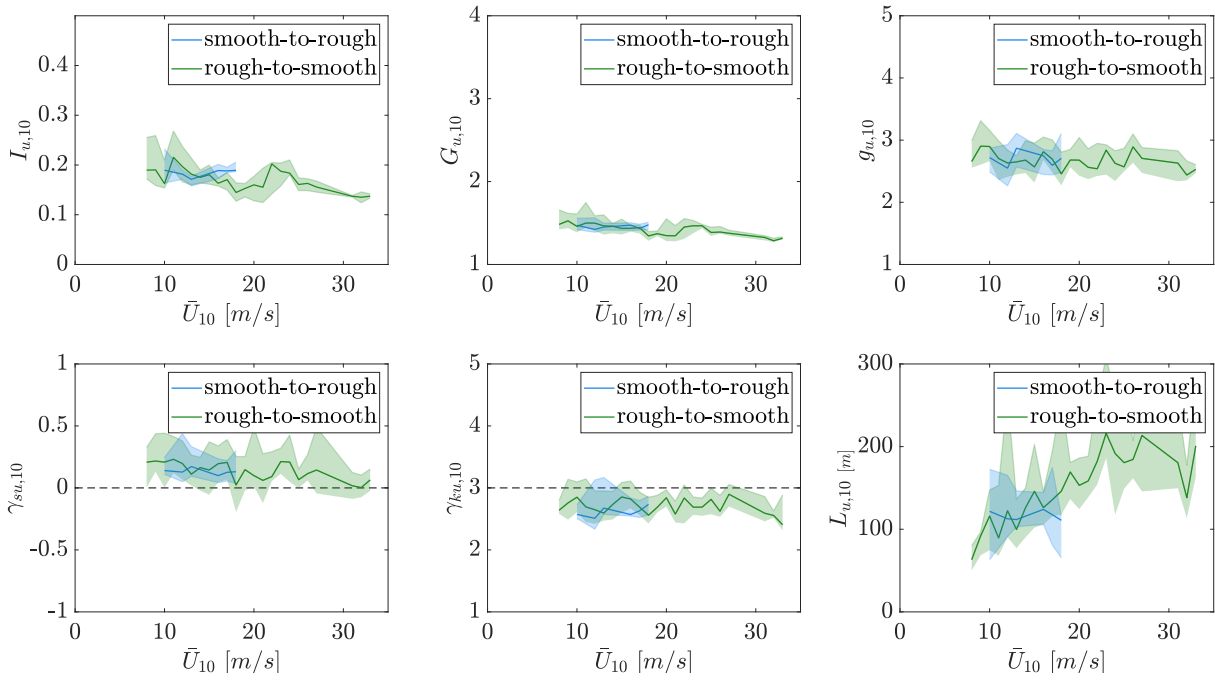
Figure A.17: Smooth-to-rough (blue-shaded area) and rough-to-smooth (green-shaded area) transitions of along-wind turbulence statistics in open land at 10 m.
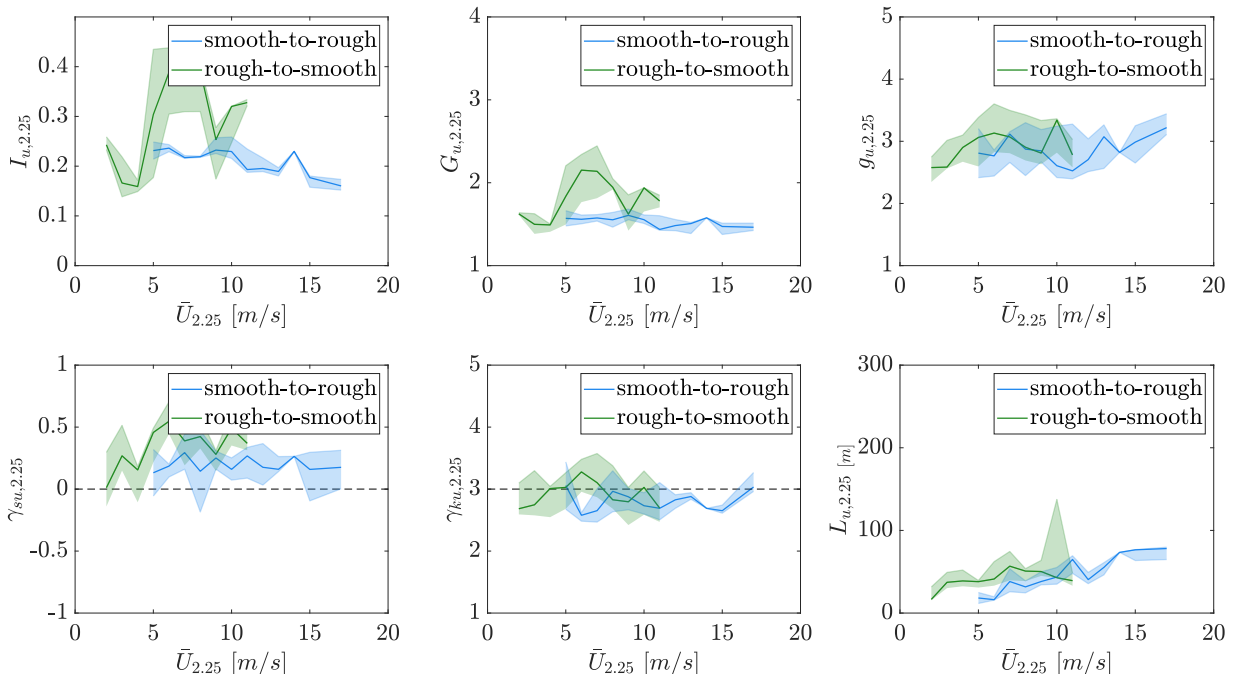
Figure A.18: Smooth-to-rough (blue-shaded area) and rough-to-smooth (green-shaded area) transitions of along-wind turbulence statistics in roughly open at 2.25 m.
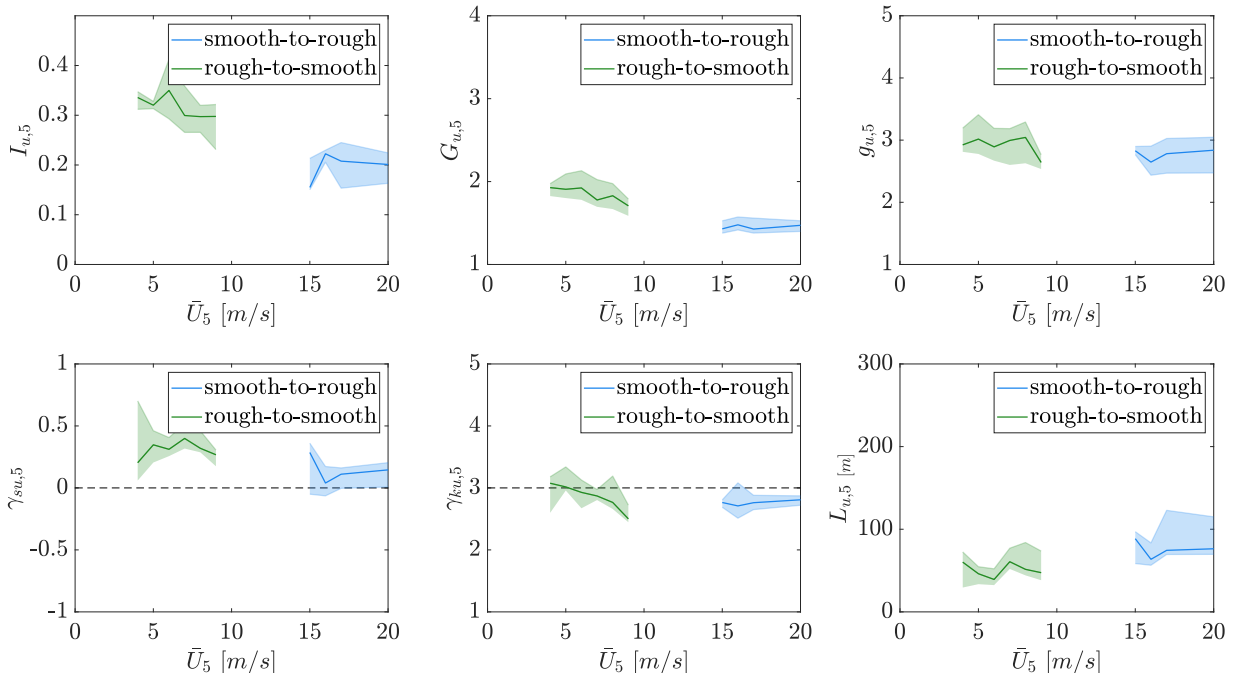
Figure A.19: Smooth-to-rough (blue-shaded area) and rough-to-smooth (green-shaded area) transitions of along-wind turbulence statistics in roughly open at 5 m
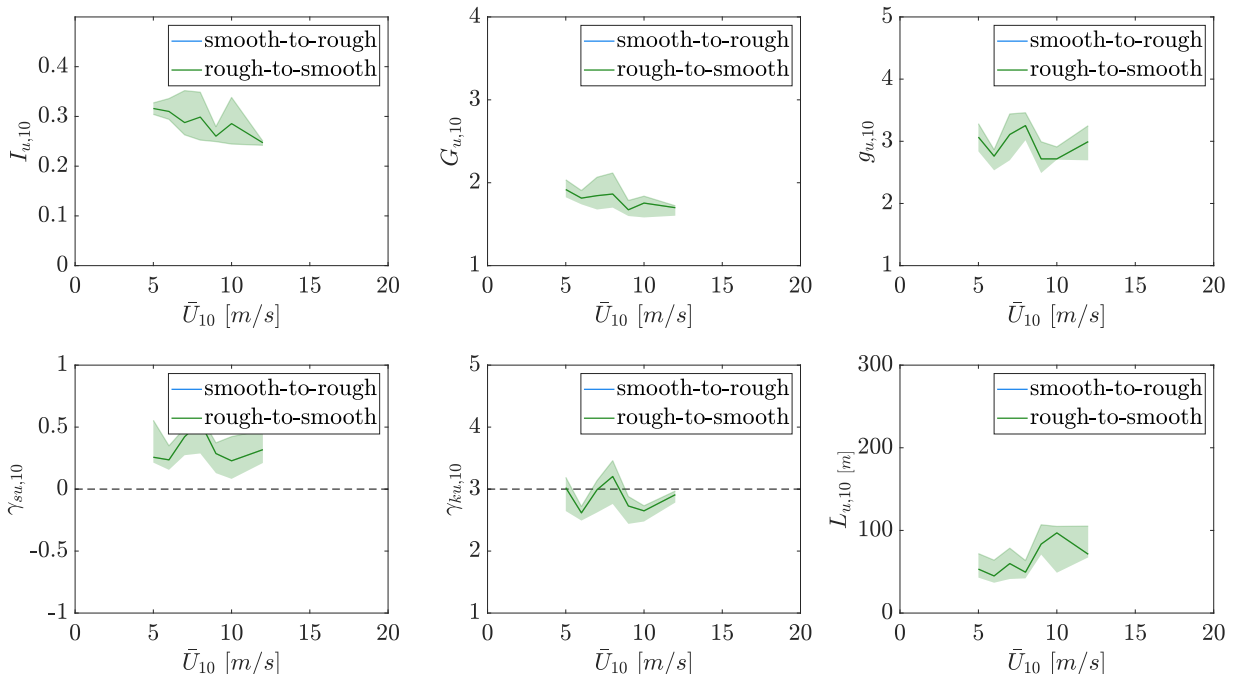
Figure A.20: Smooth-to-rough (blue-shaded area) and rough-to-smooth (green-shaded area) transitions of along-wind turbulence statistics in roughly open at 10 m

Appendix B

WRF Quality Testing

This appendix Chapter examines the quality of the WRF model through an investigation of how physical parameterisation schemes such as cumulus schemes, microphysics schemes, and PBL schemes effect TC track and intensity in a numerical simulation. Here, the International Best Track Archive for Climate Stewardship (IBTrACS) was used as validation data for numerical model reconstructions.

B.1 Data Sources

B.1.1 Tropical Cyclone Track Data

The International Best Track Archive for Climate Stewardship (IBTrACS) is an internationally recognized TC track archive [*Knapp et al.*, 2010]. The IBTrACS version used is v03r10 with updates to 2017. This global database is compiled through the collaboration of Regional Specialized Meteorological Centers (RSMCs) and other international centres including:

- Australian Bureau of Meteorology

- China Meteorological Administration - Shanghai Typhoon Institute

- Hong Kong Observatory

- Joint Typhoon Warning Center

- RSMC Honolulu, HI, USA (NOAA's Central Pacific Hurricane Center)

- RSMC La Reunion

- RSMC Miami, FL, USA (NOAA's Tropical Prediction Center)

- RSMC Nadi, Fiji

- RSMC New Delhi, India

- RSMC Tokyo, Japan

- TCWC Wellington, New Zealand

The entire collection of TC observations are merged into one archive for free public use. The data origin is recorded, as well as all observations and corrections made during the quality control or user feedback processes. To satisfy the diversity of the research groups, the output is provided in various formats, e.g. CSV, WMO, cXML, netcdf, and HURDAT.

Typically, the IBTrACS database reports 27 TC characteristics in 6-hourly intervals for the seven different TC basins: the North Atlantic (NA), eastern Pacific (EP), western North Pacific (WP), northern Indian Ocean (NI), southern Indian Ocean (SI), South Pacific (SP), and South Atlantic (SA). Figure B.1 illustrates observed TCs in the different basins between 1979 and 2007 coloured by their intensity on the Saffir-Simpson Hurricane Wind Scale.
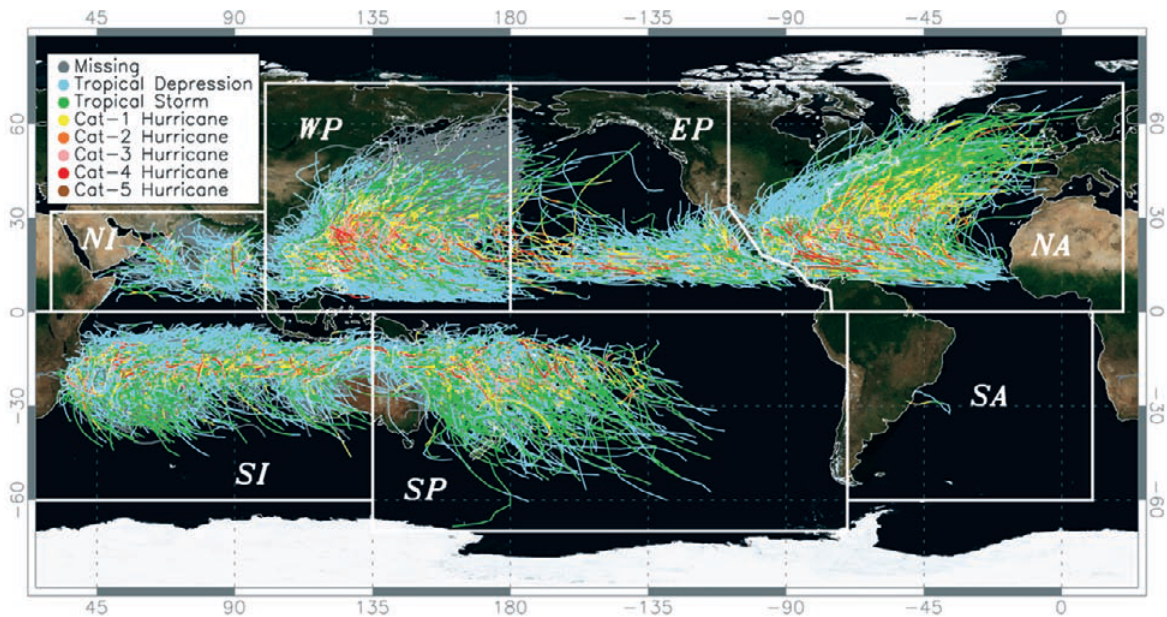
Figure B.1: All IBTrACS storm tracks by basin (1979-2007). The colors indicate the respective intensity on the Saffir-Simpson Hurricane Scale [*Knapp et al.*, 2010].

Available storm attributes used to compare TC reconstructions are the latitude and longitude position, the mean sea level pressure, and the maximum wind speed. The derived data from IBTrACS is crucial for TC investigation regarding their characteristics and impacts. In particular, this chapter utilises the best track data to compare the observed track with the WRF-ARW model output.

B.1.2 Reanalyses Datasets

The concept of reanalysis involves the worldwide assimilation of recent observations into one dataset. It is primarily used for climate monitoring and research. All available observations are collected from

weather stations, radiosondes, satellites, buoys, aircrafts and ship reports every 6-12 hours. In the present study, the National Center for Environmental Prediction (NCEP) data is used to create an initialisation file for the HWCM (Chapter 5.2) and to test the quality of the WRF model.

B.1.2.1 NCEP Final Datasets

The initial and boundary conditions used in WRF-ARW sensitivity simulations are provided by the reanalysis dataset titled NCEP FNL Operational Model Global Tropospheric Analyses [*NCEP*, 2000]. NCEP, National Weather Service, NOAA and U.S. Department of Commerce store the reanalyses datafiles in WMO GRIB1 and WMO GRIB2 formats on a $1° \times 1°$ grid ranging from 0E to 359E and 90N to 90S (360 x 181 Longitude/Latitude). Meteorological output variables are available every six hours from the surface up to 10 hPa at 26 vertical levels. Specifically, parameters such as surface pressure, sea level pressure, geopotential height, temperature, sea surface temperature, soil values, ice cover, relative humidity, u- and v- winds, vertical motion, vorticity and ozone are contained in the reanalyses dataset.

The FNL analyses dataset incorporates around 10% more observational data than the GFS analyses and are derived from the Global Data Assimilation System (GDAS) [*NCEP*, 2000]. The GDAS continuously records observations from the Global Telecommunications System (GTS). In general, the FNL reanalyses package is created with the same model which NCEP uses in the Global Forecast System (GFS).

Idealised WRF-ARW simulations are driven with the NCEP GDAS/FNL 0.25 Degree Global Tropospheric Analyses and Forecast Grids [*NCEP*, 2015], continuing from early July 2015. Analysed meteorological parameters are available in a 6-hourly cycle at 26 vertical levels ranging from 1000 hPa to 10 hPa. Similar to the previous mentioned NCEP FNL dataset, NCEP GDAS/FNL 0.25 contains surface pressure, sea level pressure, geopotential height, temperature, sea surface temperature, soil values, ice cover, relative humidity, u- and v- winds, vertical motion, vorticity, and ozone.

B.2 Tropical Cyclone Reconstruction Methodology

TC Ita affected the northeastern coastal areas of Queensland in 2014. Modelling the track and intensity of such events has been a major research challenge for decades. Part of the reason for this is that numerical simulation techniques require that different physical parameterisation schemes be used to model small scale processes unable to be directly simulated. Amongst others, results from *Raju et al.* [2011], *Parker et al.* [2013], and *Islam et al.* [2015] demonstrate how these schemes influence TC track and intensity throughout the entire life of the storm, showing that choice of cumulus (CU), microphysics (MP) and PBL physics schemes significantly change track and intensity properties of a simulated storm. Hence, one of the first challenges when attempting to numerically reconstruct a TC is choosing a suitable combination of physics schemes.

For this reason a sensitivity study to investigate how choice of CU, MP and PBL schemes influence storm characteristics when attempting to numerically reconstruct TC Ita within WRF-ARW was conducted. To explore grid resolution and initial condition dependency influence, a limited number of sensitivity tests were also undertaken. The aim of these model tests was to identify an optimal combination for the reconstruction of TC Ita and its wind field at landfall.

B.2.1 Model Configuration

In order to test how the choice of parameterisation schemes changes TC track and intensity, version 3.7.1 of the WRF-ARW model [*Skamarock et al.*, 2008] is used to reconstruct TC Ita. Two domains, d01 and d02 (Figure B.2), are set up with grid and time step ratios of 1:3 with 30 vertical height levels. Domain d02 is a moving nest with the vortex-following option turned on, which tracks the lowest pressure value at the 850 hPa pressure to identify the storm. Once the TC has been captured within the moving nest TC track position, central pressure and highest wind speed both at the surface are generated every 15 minutes. The outer domain (d01) consists of 230×230 grid points with a 10 km horizontal resolution, whereas the moving nest (d02) has a grid spacing of 3.3 km on a 220×220 grid. Figure B.2 illustrates the spatial domain extent of d01 and the position within this domain of d02 on 9 April at 12 UTC, two days prior to landfall. A high-resolution version of these grids is also discussed in the results (Chapter B.3), where d01 grid spacing is reduced to 3 km and d02 to 1 km.
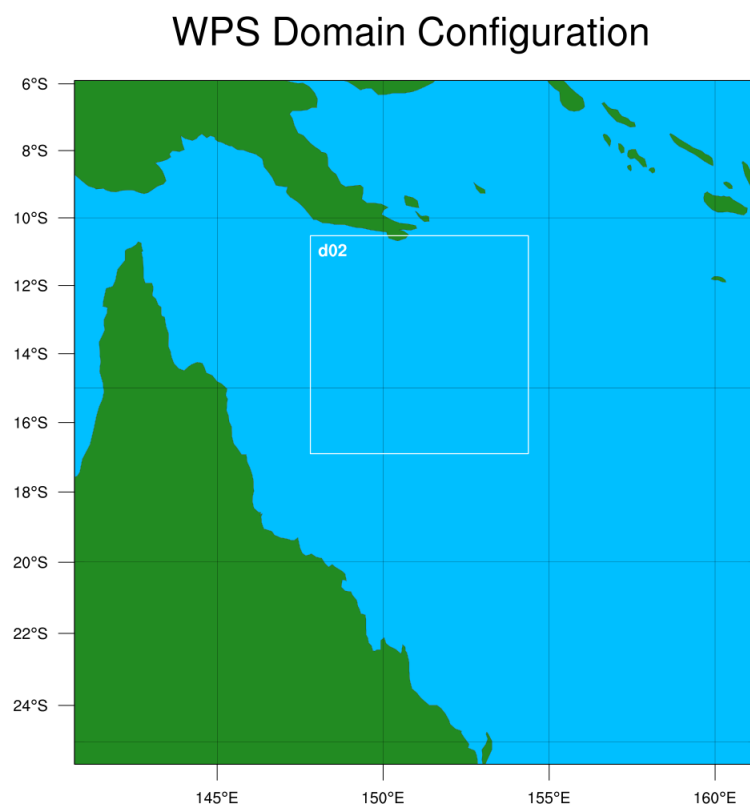
Figure B.2: WRF-ARW pre-processing domain configuration with horizontal grid spacing of 10 km (d01) and 3.3 km (d02) for model runs starting on 9 April 12 UTC.

The time range between 9 April, 12 UTC to 14 April, 12 UTC, or 5 April, 00 UTC to 14 April, 12 UTC, was used for all model runs resolved in three-hourly time steps. All initial and boundary conditions are sourced from the $1° \times 1°$ NCEP final operational model global tropospheric analyses data [*NCEP*, 2000].

B.2.2   Model Initialisation and Grid Dependency Testing

In a first attempt the modelled track's dependency on the model initialisation date and grid resolution was tested without changing the default physics scheme configuration. Starting from 5 April at 12 UTC, two simulations were conducted with a resolution of 10 km and 3.3 km (*lowres*) and 3 km and 1 km (*highres*) each for domains d01 and d02, respectively (see also Figure B.4 in Chapter B.3). However, further model initialisation dates were the 9 and 10 April at 12 UTC with the coarser grid resolution mentioned above. Initial testing was necessary to figure out a suitable grid resolution and model start date that included the smallest track position deviation compared to the observed track (best track) of TC Ita. Obtaining these information led to a further examination of various physics schemes combinations with a fixed model initialisation time and grid resolution.

B.2.3   Sensitivity Study

A sensitivity study was carried out to evaluate the suitability of combinations of physics schemes on the reconstruction of TC Ita. Resulting bias in track position and storm intensity (i.e. minimum central pressure) has been calculated with reference to TC Ita's track in the IBTrACS database [*Knapp et al.*, 2010].

Although tremendous physics variations are available in WRF-ARW, this study focuses on testing CU, MP, and PBL parameterisations as they are known to influence TC track and intensity that already have been considered in previous studies [e.g. *Raju et al.*, 2011; *Parker et al.*, 2013; *Islam et al.*, 2015]. Starting from 9 April at 12 UTC, 27 combinations in total were analysed using three of each CU, MP, and PBL schemes.

- CU schemes: KF, modified Tiedtke (MF), Betts–Miller–Janjic (BM)

- MP schemes: WRF Single-Moment 3 class (WSM3) and WSM6, Eta Ferrier (EF)

- PBL schemes: Yonsei University (YSU), Mellor–Yamada–Janjic (MYJ), MYNN Level 2.5

The default configuration (Run 1, KF_wsm3_YSU) uses the Kain Fritsch (KF) CU, WSM3 MP, and YSU PBL physics schemes. Apart from changes in CU, MP, and PBL schemes all simulations utilise the default WRF-ARW physics options unless stated otherwise.

B.3 Numerical sensitivity tests

The first WRF-ARW simulation to numerically reproduce TC Ita was carried out with default physics configuration (*KF_wsm3_YSU*) on a defined grid of 10 km for the outer domain and 3.3 km for the moving nest, starting on 5 April. Figure B.3 shows the track and intensity of TC Ita for the simulation along with the best track (observed track). Table B.1 demonstrates the TC category related wind speeds in km/h.
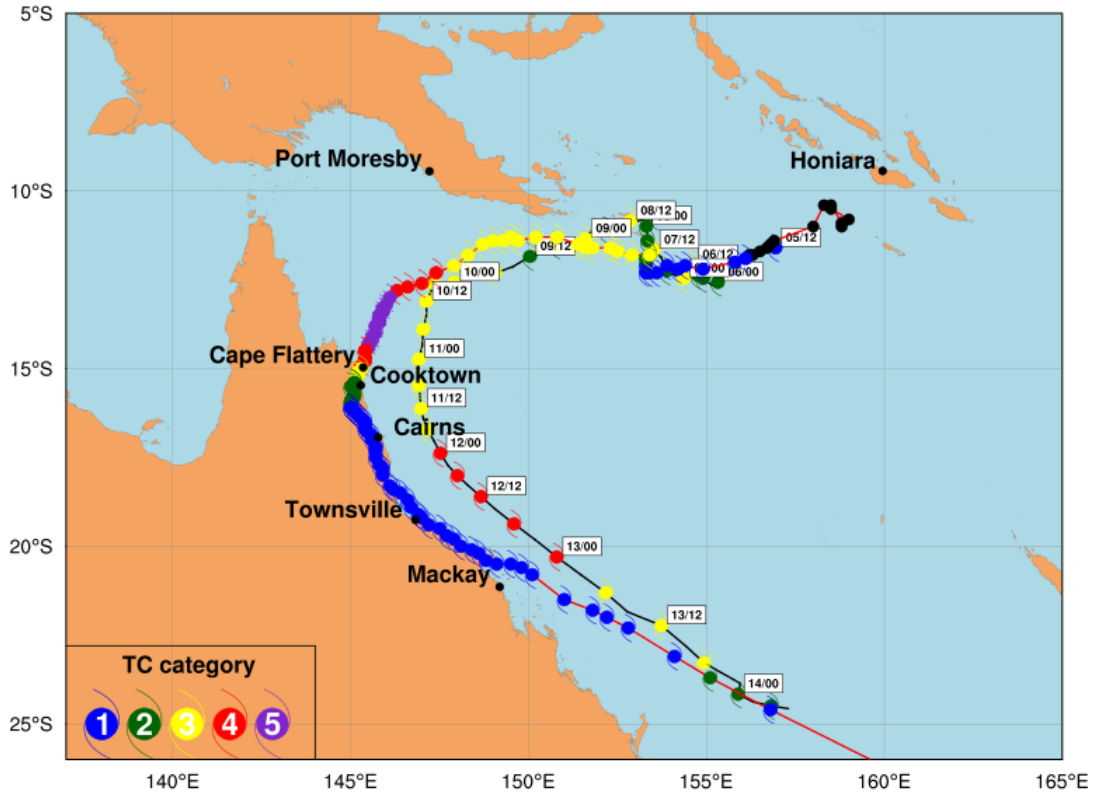
Figure B.3: IBTrACS best track (red line) and intensity along with WRF-ARW (black line) modelled track and intensity for TC Ita

Name	Category	wind speeds [km/h]
tropical cyclone	1	90-125
tropical cyclone	2	125-164
severe tropical cyclone	3	165-224
severe tropical cyclone	4	225-279
severe tropical cyclone	5	> 280

Table B.1: Tropical Cyclone Category System (Australian Bureau of Meteorology).

The modelled track and observed track are reasonably well aligned in the beginning of the life cycle. However, tracks start to diverge on 7 April when the simulation takes a sharp northerly deviation

caused by a northward directed steering flow. After 27 hours the simulated track returns to a more westerly heading in-line with the observed best track. The WRF-ARW simulation then moves closer to the coastline and intensifies at a rate similar to the best track, but shifts south of the observed track. The simulated track then slowly intensifies over the next 36 hours to a minimum central pressure of 952.5 hPa, and remains approximately 150 km offshore. This is in contrast to the observed event, which makes landfall at Cape Flattery and reaches a minimum central pressure of 930 hPa. Hence, the model configuration with default physics initiated six days prior landfall underestimates the storm central pressure by approximately 22 hPa and largely misrepresents the storm track.

B.3.1   Model Initialisation and Grid Dependency Tests

Two modelling parameters that are known to influence simulated storm behaviour are grid resolution and model initialisation date. To investigate the influence of model resolution further, a higher resolution grid (d01 = 3 km, d02 = 1 km) was implemented. Figure B.4 illustrates the track of the high resolution run starting on 5 April (*05_highres*, green line, which can be compared with the lower resolution run discussed previously (*05_lowres*, blue dashed line). Although both tracks behave similarly during the first three to four days, the high resolution run shows no significant improvement to the track behaviour and in fact stays further off the coast than the default run. Both simulations exhibit similar minimum pressure traces throughout their life cycles (Figure B.5). Of note is the pressure offset of about 20 hPa as the beginning of initialised tracks on 5 April. Within the following three and a half days their pressure shape varies between 980 hPa and 1000 hPa, whereas the observed track starts intensifying after one and a half day. Both *05_lowres* and *05_highres* are unable to capture the rapid intensification phase on 10 April between 0 and 12 UTC. Instead, simulated tracks exhibit their lowest central pressure after the observed landfall time (11 April, 12 UTC) because both *05_lowres* and *05_highres* stay offshore and maintain gradual intensification. It was therefore decided that the default grid resolution was appropriate for progressing this research forward.
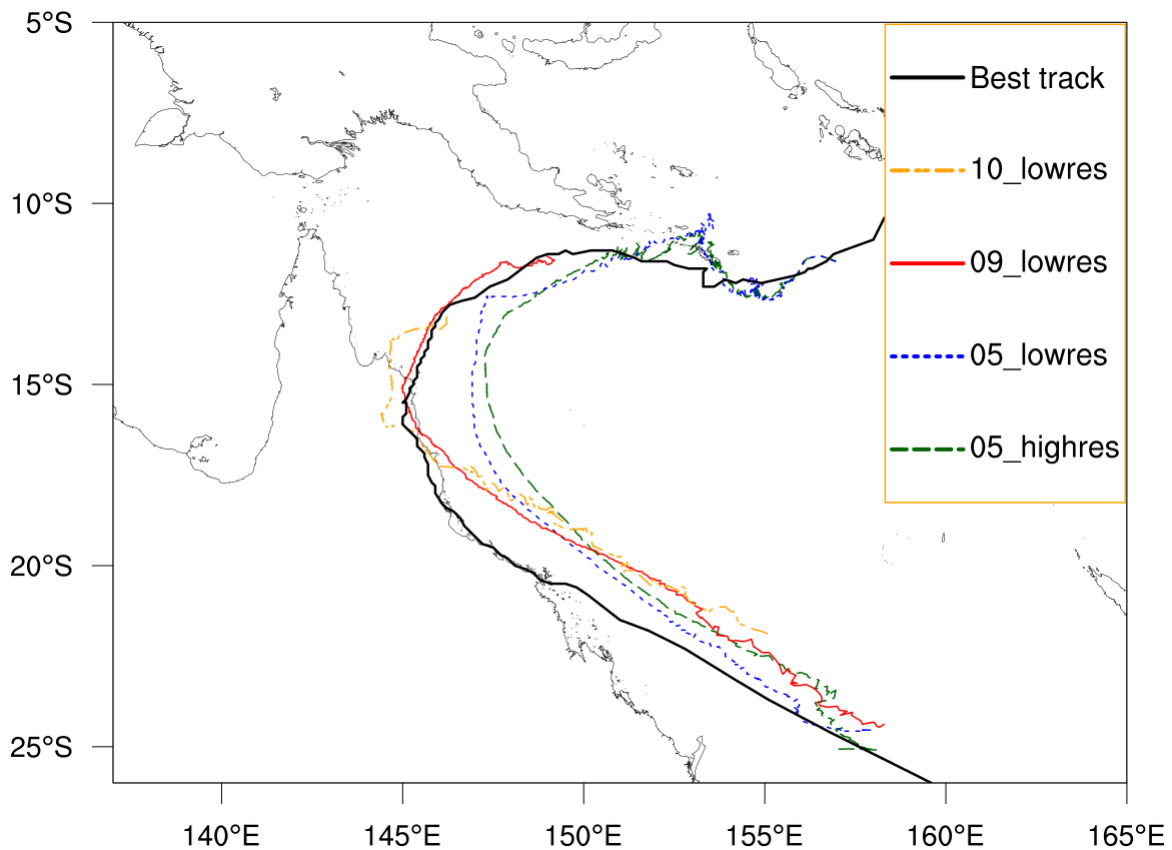
Figure B.4: WRF-ARW modelled tracks and best track (black) of TC Ita for different starting times and grid size.
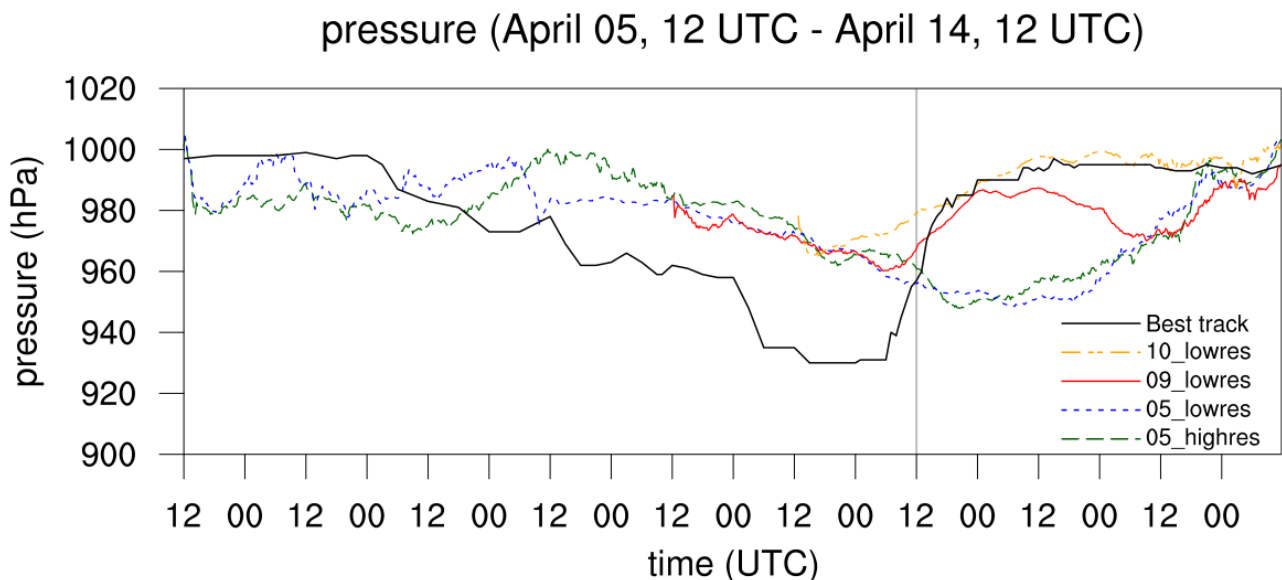
Figure B.5: Simulated (coloured) and observed (black) central pressures along the tracks in Figure B.4.

A second component that can influence TC track behaviour is linked with the choice of the model initialisation date. The poor replication of TC Ita's track and intensity (Figure B.3) was hypothesised to be linked to a poor representation of the steering flow and the TC vortex itself in the initial and boundary conditions drawn from the coarse NCEP reanalysis data. Hence, three different model initialisation dates were tested, in particular 5, 9 and 10 April each at 12 UTC. Modelled tracks and

intensity for these simulations are also shown in Figures B.4 and Figure B.5, respectively. The simulation initialised on 9 April (*09_lowres*, red line) was found to exhibit closer agreement to Ita's path, with a track position error of approximately 27 km at landfall (11 April, 12 UTC). Again, *09_lowres* starts with a 20 hPa central pressure offset and does not capture the rapid intensification phase prior to landfall. However, this simulation exhibits a reasonable timing of the central pressure rise a few hours before moving onshore, which results in a pressure difference of 10.5 hPa at landfall. Of note is the decrease in *09_lowres* central pressure beginning on 12 April around 12 UTC being associated with re-intensification as the storm moves offshore. For the WRF-ARW simulation initiated on 10 April (*10_lowres*, orange line) large differences in track and intensity were observed even before making landfall. In this case, it is hypothesised that the model spin-up time is too short for the storm to fully develop. Based on these simulation results, all subsequent simulations were initiated from 9 April at 12 UTC as they are expected to match the best track more closely.

Figures B.6 and B.7 display all subsequently simulated tracks and central pressure shapes with detailed information about name, landfall position error, mean position error along the track, minimum central pressure error along the track, and central pressure error at landfall provided in Table B.2.
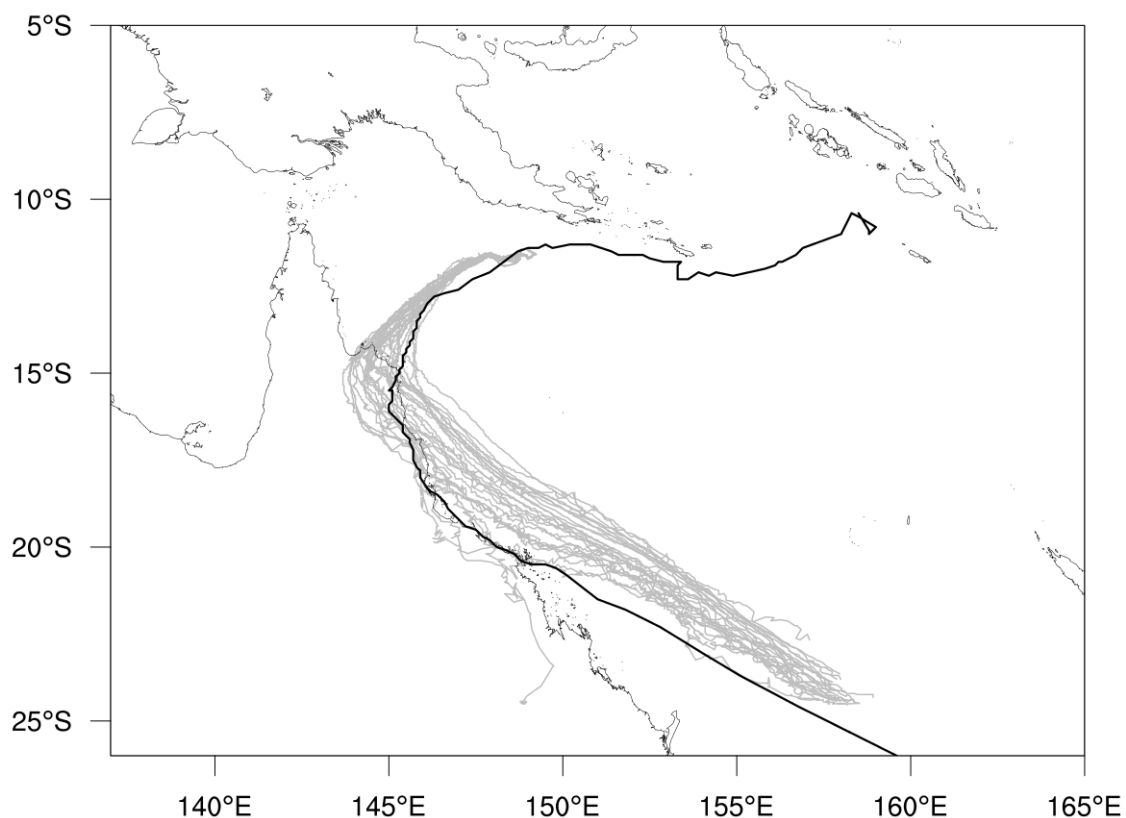
Figure B.6: WRF-ARW modelled tracks (grey) and best track (black) of TC Ita starting at 9 April 12 UTC.
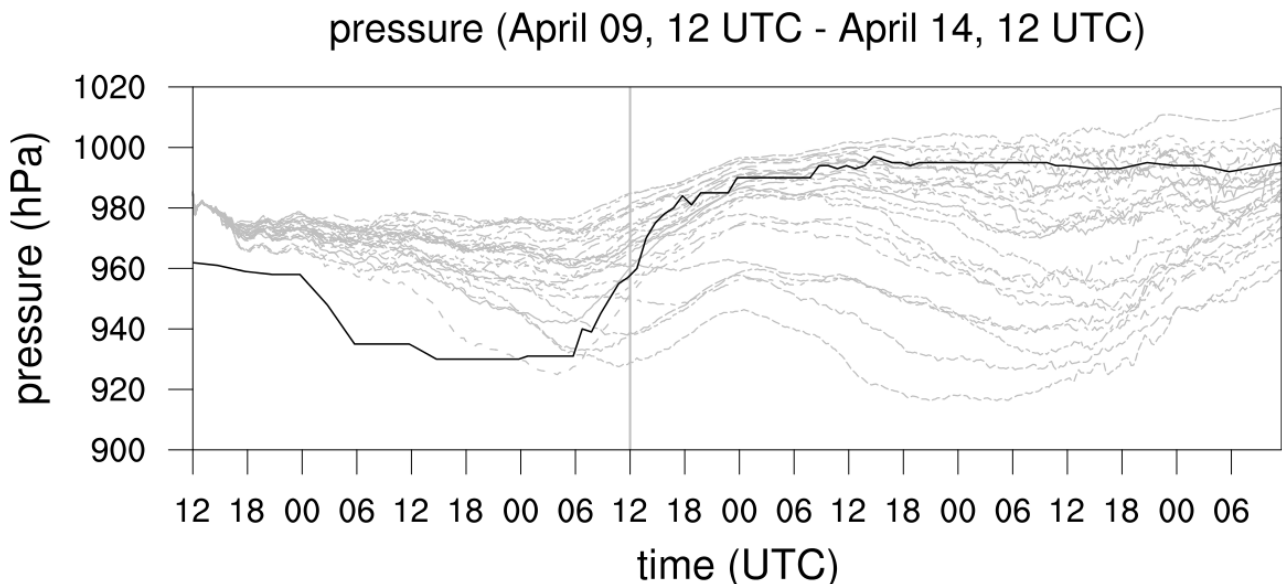
Figure B.7: Simulated (grey) and observed (black) central pressures along the tracks in Figure B.4.

The output of all sensitivity runs in Figures B.6 and B.7 demonstrates similar storm behaviour across each of the physics schemes, but also shows a wide spread of results from test to test. For example, most simulations show a sharp change in track direction (south-westerly to south-easterly) when approaching the coast. Although the shift in tracks occurs at different times, it is consistently simulated. This is hypothesised to be caused by the poor representation of the environmental conditions (e.g. steering flow), which largely drive the TC direction. Simulated WRF-ARW storms were weaker regarding their central pressure and might be more influenced by the steering flow. Considering all 27 conducted simulations for the entire simulation period, a mean track error of approximately 110 km is computed. Due to the different physics options, a spread exists in the simulated tracks, which becomes greater as the storm approaches landfall. At landfall (11 April, 12 UTC), the mean track error was found to be about 93.5 km while 11% of all tracks failed to encounter land.

Overall, a mean root mean square error (RMSE) of about 24.4 hPa is calculated for the storm central pressure throughout its life cycle. This error is not consistent along the entire storm track and was reduced down to 14.2 hPa at landfall. However, none of the simulations captured the best track's lowest central pressure, which was observed at 930 hPa. The KF_FE_MYNN simulation (Table B.2) depicts a low central pressure at 931.6 hPa but it was estimated after the observed landfall. The bulk of the simulations stay around one day over land before they move offshore. This behaviour explains the poor representation of the central pressure after landfall. Part of the reason for the poor replication of central pressure is believed to be linked with the initial 20 hPa offset in central pressure introduced because simulations are initiated from course reanalysis data. This might lead to the inability of the simulated storm to rapidly intensify. Moreover, a large spread in central pressures was observed in the latter part of simulated tracks (Figure B.7), which is believed to be caused by the storm interactions with land that will be explored further in Chapter 7. For those simulations that kept storms well offshore, prolonged, and in some cases re-intensifying periods of low central pressures were observed.

Name	landfall position error [km]	mean position error [km]	min. central pressure [hPa]	central pressure error (landfall) [hPa]
KF_wsm3_YSU	26.93	64.67	960.3	10.5
KF_wsm3_MYJ	91.99	77.46	970.9	23.2
KF_wsm3_MYNN	44.38	70.66	950.0	3.5
KF_wsm6_YSU	48.51	110.44	939.4	7.0
KF_wsm6_MYJ	44.46	87.69	952.8	0.7
KF_wsm6_MYNN	25.27	101.91	916.4	28.7
KF_FE_YSU	56.62	108.91	939.9	3.5
KF_FE_MYJ	41.48	77.28	967.9	14.9
KF_FE_MYNN	33.98	97.30	931.6	19.0
MT_wsm3_YSU	149.79	118.13	965.9	23.6
MT_wsm3_MYJ	171.18	143.33	972.5	27.6
MT_wsm3_MYNN	150.13	115.12	953.0	14.9
MT_wsm6_YSU	104.71	105.38	955.3	7.8
MT_wsm6_MYJ	138.15	93.80	958.4	16.7
MT_wsm6_MYNN	103.45	80.36	925.2	6.6
MT_FE_YSU	87.97	83.75	957.0	8.8
MT_FE_MYJ	131.97	85.63	965.9	17.7
MT_FE_MYNN	100.96	69.25	942.3	2.4
BM_wsm3_YSU	109.06	157.96	972.8	21.4
BM_wsm3_MYJ	133.67	158.44	973.0	27.2
BM_wsm3_MYNN	97.96	130.27	960.9	12.0
BM_wsm6_YSU	98.88	145.64	946.6	4.7
BM_wsm6_MYJ	124.63	145.65	954.0	11.0
BM_wsm6_MYNN	98.02	132.77	926.6	18.9
BM_FE_YSU	95.47	139.29	956.6	17.5
BM_FE_MYJ	117.59	128.44	971.3	21.8
BM_FE_MYNN	97.31	130.55	947.9	10.5

Table B.2: Sensitivity run statistics for all simulations starting from 9 April 12 UTC.

B.3.2 Cumulus (CU) schemes

Figures B.8 and B.9 illustrate track position and pressure of three selected CU schemes (KF, MT, BM) while MP and PBL parameterisations were held constant. Results indicate that the run including the KF scheme have smaller track position errors, with respect to the best track, than the MF or BM cumulus options. This is confirmed when considering all sensitivity runs, and it is found that KF simulations exhibit a mean track position error of 88.5 km, while the MF and BM cumulus parameterisations generate errors of 99.4 km and 141 km, respectively. At landfall, MP and PBL schemes exhibit a mean landfall point around 117.3 km northwest of the best track position, whereas parameterisations using the KF scheme only have a mean landfall position error of approximately 46 km.

The most reasonable performance was delivered by the the KF_wsm3_YSU that exhibit the lowest mean track error of around 65 km and 27 km at landfall. The KF_wsm6_MYJ combination shows the smallest deviation of 0.7 hPa in terms of central pressure error at landfall, whereas the landfall position was located about 44.5 km northwest of the observed track.
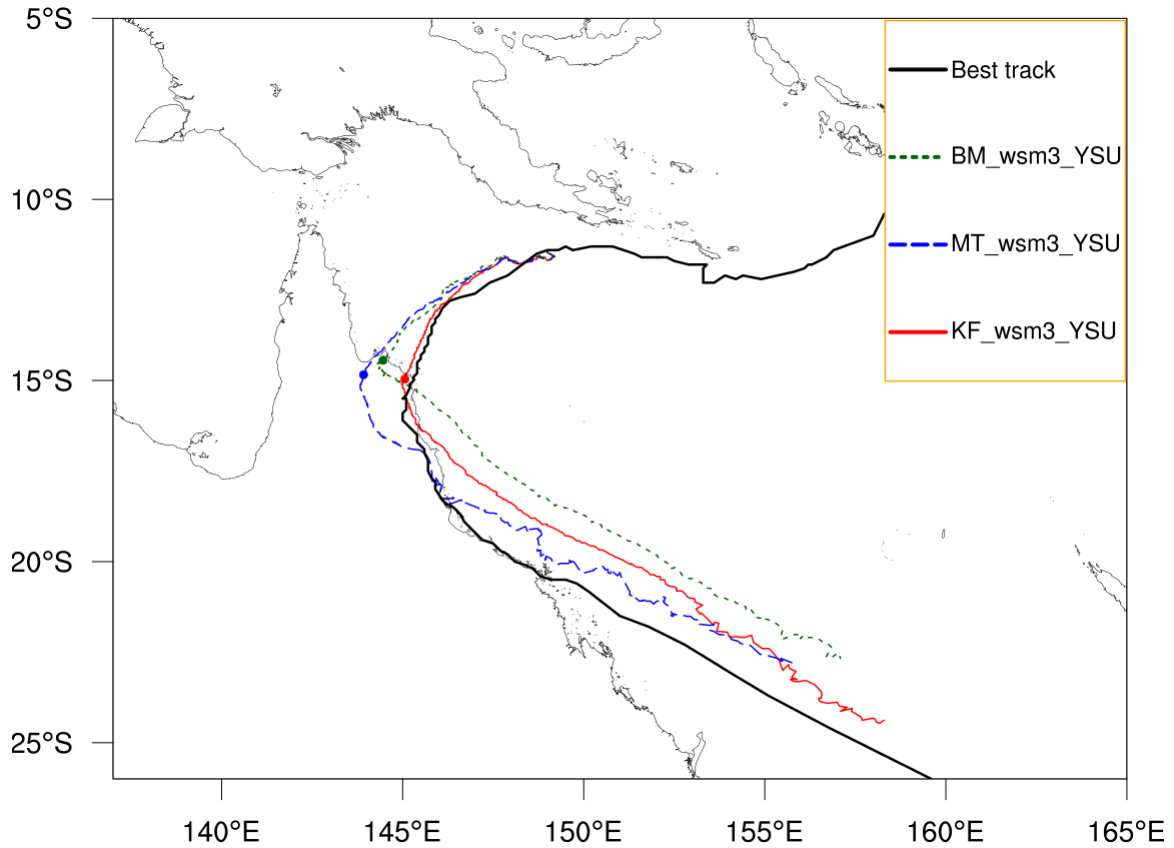
Figure B.8: WRF-ARW modelled tracks and best track (black) of TC Ita for different CU schemes
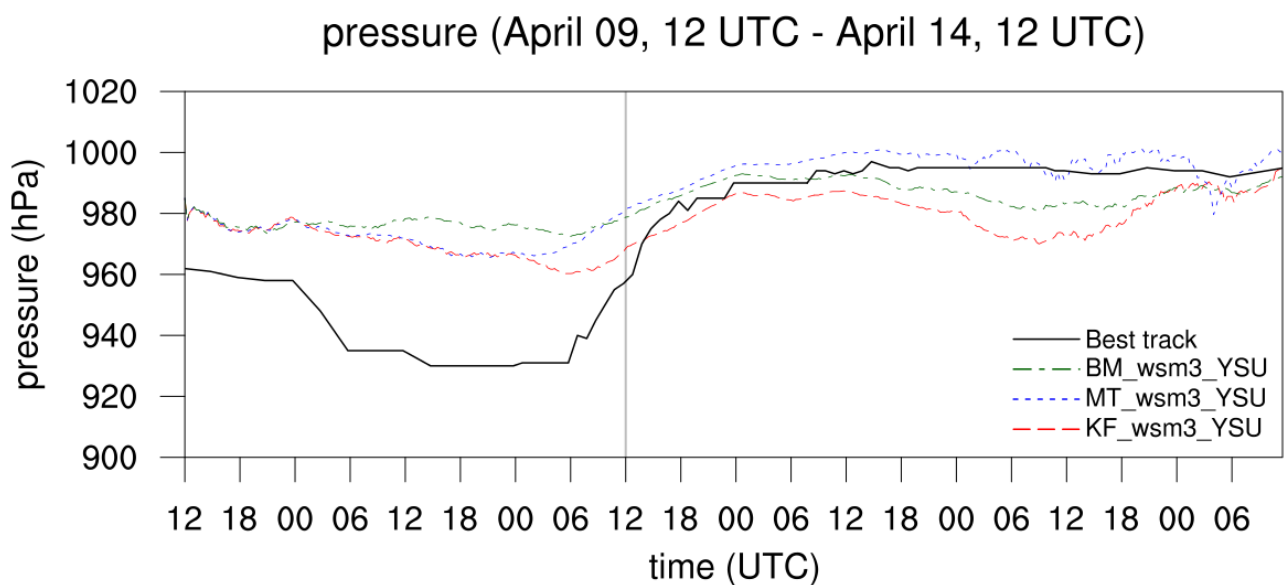
Figure B.9: Simulated (coloured) and observed (black) central pressures along the tracks in Figure B.8.

B.3.3 Microphysics (MP) Schemes

Incorporating the variation of MP schemes largely leads to changes in the simulated storm intensity (i.e. pressure). As illustrated in Figures B.11 and B.10, the tracks remain spatially close to each other up to landfall but the minimum central pressure varies by up to 20 hPa over this period. Considering all 27 simulations, the WSM6 scheme was found to produce the lowest pressure values and the highest wind speeds. However, no simulations were found to capture the sharp drop in pressure that occurs 36 hours prior to landfall, and none were able to rectify the 20 hPa deficit introduced by the initial conditions. Where events made landfall, the increase in pressure seen in the best track was reasonably simulated.
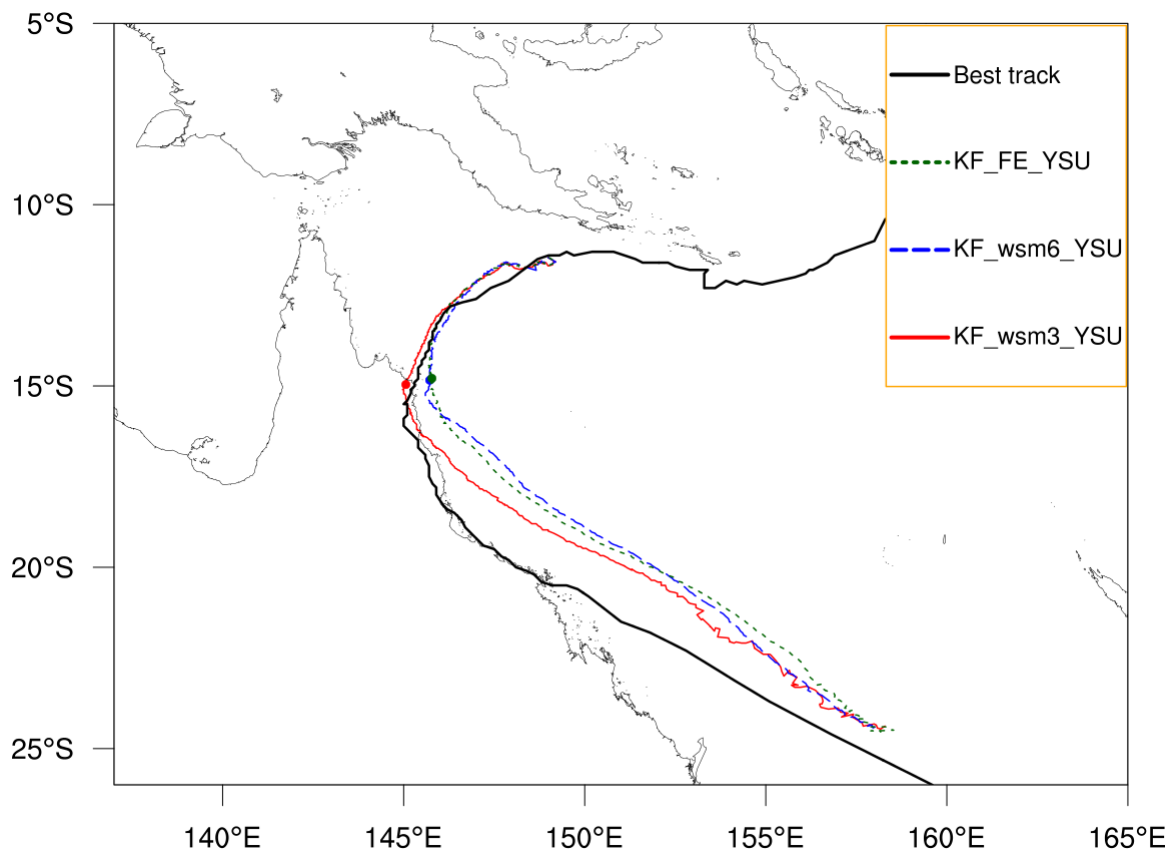
Figure B.10: WRF-ARW modelled tracks (coloured) and best track (black) of TC Ita for different MP schemes.
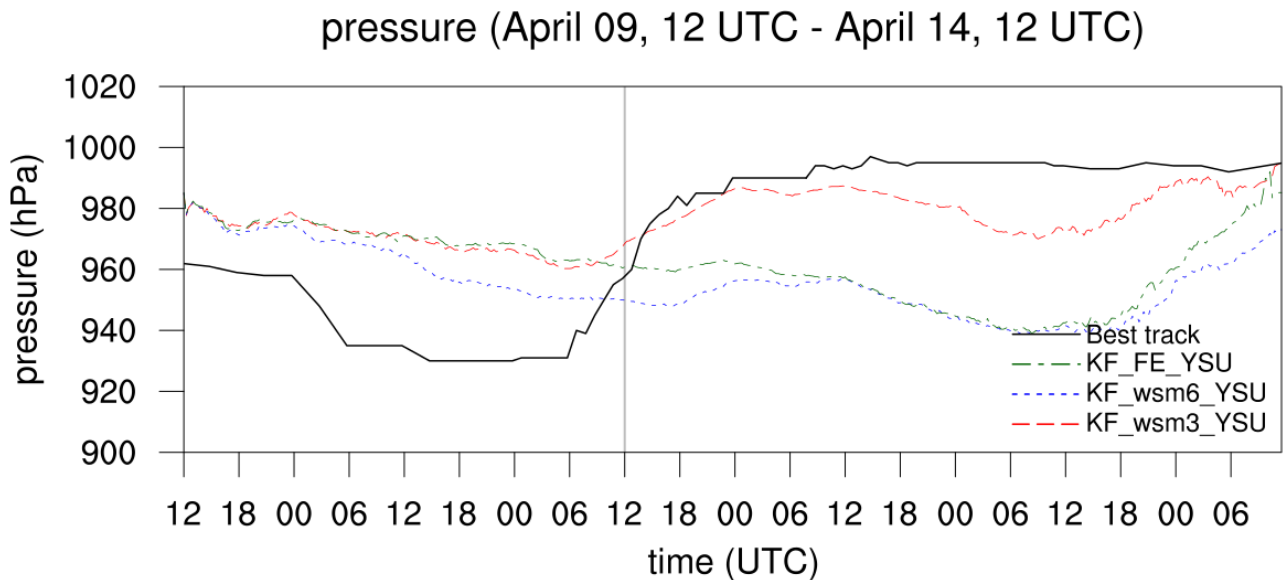
Figure B.11: Simulated (coloured) and observed (black) central pressures along the tracks in Figure B.10

B.3.4 Planetary Boundary Layer (PBL) Schemes

Similar to the MP schemes variation, PBL parameterisations largely influence the simulated intensity (Figure B.13). The simulated tracks with PBL scheme variation show only small deviations, as illustrated in Figure B.12. Overall, the MYNN PBL scheme was found to produce the lowest central pressure values and highest wind speeds compared to the other simulations, while the combination of MT_FE_MYNN exhibit the lowest central pressure error over the entire track of about 10.4 hPa.

Figure B.13: Simulated (coloured) and observed (black) central pressures along the tracks in Figure B.12

According to Table B.2, the WRF-ARW default physics combination including KF_wsm3_YSU shows reasonable results regarding track position at landfall and over the full storm's life cycle. Additionally, the pressure error at landfall is comparably small, although it fails to capture TC Ita's rapid intensification phase. However, considering all 27 simulations this was found to be a common phenomenon.